

Particle separation and fractionation by microfiltration

Promotor: Prof. Dr. Ir. R.M. Boom
Hoogleraar Levensmiddelenproceskunde, Wageningen Universiteit

Copromotoren: Dr. Ir. C.G.P.H. Schroën
Universitair docent, sectie Proceskunde, Wageningen Universiteit

Dr. Ir. R.G.M. van der Sman
Universitair docent, sectie Proceskunde, Wageningen Universiteit

Promotiecommissie: Prof. Dr. Ir. J.A.M. Kuipers
Universiteit Twente

Prof. Dr. Ir. M. Wessling
Universiteit Twente

Dr. Ir. A. van der Padt
Royal Friesland Foods

Prof. Dr. M.A. Cohen Stuart
Wageningen Universiteit

Janneke Kromkamp

Particle separation and fractionation by microfiltration

Scheiding en fractionering
van deeltjes
middels microfiltratie

Proefschrift

Ter verkrijging van de graad van doctor
op gezag van de rector magnificus
van Wageningen Universiteit,
Prof.dr. M.J. Kropff,
in het openbaar te verdedigen
op dinsdag 6 september 2005
des namiddags te vier uur in de Aula.

Particle separation and fractionation by microfiltration

Janneke Kromkamp

Thesis Wageningen University, The Netherlands, 2005 - with Dutch summary

ISBN: 90-8504-239-9

Contents

1	Introduction	1
1.1	Membrane filtration	2
1.2	Microfiltration	2
1.3	Mass transport	5
1.4	Shear-induced diffusion	7
1.5	Research aim and outline	9
2	Lattice Boltzmann simulation of 2D and 3D non-Brownian suspensions in Couette flow	13
2.1	Introduction	14
2.2	Computer simulation method	15
2.2.1	Simulation of the fluid	15
2.2.2	Fluid-particle interactions	17
2.2.3	Accuracy of particle representation and particle-particle interactions	18
2.3	Single and pair particles in Couette flow	20
2.3.1	Wall effects on a single particle	20
2.3.2	Two colliding particles in shear flow	21
2.4	2D and 3D multiparticle suspensions in Couette flow	23
2.4.1	Wall effects	23
2.4.2	Viscosity	25
2.4.3	Shear-induced diffusion	27
2.5	Conclusions	33
2.6	Lubrication force in a 2D suspension	34
2.7	Analytical model for shear-induced diffusion	36
2.7.1	The collision frequency of the particle in 3D	36
2.7.2	The collision frequency of a particle in 2D	38
2.7.3	The displacement of the particle in a collision	38
2.7.4	The self-diffusion tensor	40
3	Shear-induced self-diffusion and microstructure in non-Brownian suspensions at non-zero Reynolds numbers	41
3.1	Introduction	42
3.2	Computer simulation method	45
3.3	Effects of hydrodynamics and inertia in particle suspensions	48
3.4	Shear-induced diffusion at non-zero Reynolds numbers	55
3.5	Shear-induced changes in microstructure	61
3.6	Conclusions	63

3.7	Lubrication force in a 2D suspension	65
4	Shear-induced self-diffusion in bidisperse suspensions	69
4.1	Introduction	70
4.2	Computer simulation method	73
4.3	Rheology and microstructure of bidisperse particle suspensions at non-zero Reynolds numbers	76
4.4	Shear-induced self-diffusion in bidisperse suspensions	79
4.5	Conclusions	86
5	Shear-induced diffusion model for microfiltration of polydisperse suspensions	89
5.1	Introduction	90
5.2	Shear-induced migration model for polydisperse suspensions	91
5.3	Materials and methods	92
5.4	Results and discussion	92
5.4.1	Predicted steady-state fluxes	92
5.4.2	Experimental results	95
5.5	Conclusions	96
6	Effects of particle size segregation on crossflow microfiltration performance: control mechanism for concentration polarisation and particle fractionation	99
6.1	Introduction	100
6.2	Shear-induced diffusion in polydisperse suspensions	101
6.2.1	Particle back-transport as determined by shear-induced migration	101
6.2.2	Shear-induced particle segregation in channel flow	102
6.3	Materials and methods	103
6.3.1	CSLM experiments	103
6.3.2	Fractionation of milk fat globules	105
6.4	Results	106
6.4.1	Kinetics of particle deposition	106
6.4.2	Shear-induced diffusive particle behaviour	107
6.4.3	Fractionation of milk fat globules	112
6.5	Conclusions	114
7	Differential analysis of particle deposition layers from micellar casein and milk fat globule suspensions	117
7.1	Introduction	118
7.2	Materials and methods	120
7.2.1	Preparation of colloidal suspensions	120
7.2.2	Viscosity of micellar casein suspensions	121
7.2.3	Dead-end filtration	122
7.2.4	Analysis of cake properties	122
7.3	Results	124
7.3.1	Latex suspensions	124
7.3.2	Micellar casein suspensions	126
7.3.3	Milk fat globule suspensions	129

7.4	Conclusions	131
8	A suspension flow model for hydrodynamics and concentration polarisation in crossflow microfiltration	137
8.1	Introduction	138
8.2	Computer simulation method	140
8.2.1	Suspension flow model	140
8.2.2	Lattice Boltzmann method for hydrodynamics and convection-diffusion	141
8.2.3	Initial and boundary conditions	144
8.3	Results	147
8.3.1	Simulation of microfiltration with the suspension flow model	147
8.3.2	Effect of transmembrane pressure on flux and cake layer formation	147
8.3.3	Position-dependence of flux and cake layer thickness	150
8.3.4	Microfiltration in systems with different geometries	152
8.4	Conclusions	155
9	References	161
	Summary	169
	Samenvatting	173
	Nawoord	177
	Curriculum vitae	181
	List of publications	183

1

Introduction

1.1 Membrane filtration

In the field of separation processes, two groups can be distinguished, techniques to separate phases and techniques to separate components [1, 2]. Phase separation techniques take advantage of differences in particle size (sieving, filtration) or density (sedimentation, centrifugation). Component separation techniques are based on differences in vapour pressure (distillation, stripping), freezing point (crystallization), charge (ion exchange, electrolysis), affinity (absorption, extraction), or chemical nature (leaching, complexation).

Membrane filtration is a separation technique in which the flow through a membrane is used to separate different components from each other. In pressure-driven membrane filtration processes, such as microfiltration, ultrafiltration, nanofiltration and reverse osmosis, these components are present in a fluid and their separation is driven by a pressure gradient over the membrane. These processes can be classified based on the separation property of the process and on the membrane pore size (Table 1). Consequently, some belong to the group of phase separation techniques and others to the group of component separation techniques.

Table 1.1: Pressure-driven membrane filtration processes

Process	Separation property	Membrane pore size	Operating pressure
Microfiltration	size	0.05 - 5 μm	≤ 3 bar
Ultrafiltration	size	2 nm - 0.05 μm	1 - 10 bar
Nanofiltration	size and/or affinity and/or charge	0.5 - 2 nm	5 - 40 bar
Reverse osmosis	affinity and/or charge	- *	10 - 100 bar

* *subject of debate; often considered not to have pores*

In general, advantageous aspects of pressure-driven membrane filtration processes are their high selectivity and the possibilities for operation without a phase change. Further they are operated at ambient temperatures, without the need for additives and with relatively low energy consumption. Besides that, membrane filtration processes offer the advantages of continuous and automatic operation, modular construction and simple integration in existing production processes, as well as relatively low capital and running costs.

1.2 Microfiltration

Microfiltration (MF) is one of the pressure-driven membrane filtration processes. As stated in table 1.1, MF membranes are size-selective, have relatively large pores and are operated at pressures below 3 bar. In general, the size of the particles that are retained during MF ranges from 0.02 to 20 μm .

Some of the particles in the feed solution may be small compared to the membrane pores and are consequently able to pass the membrane. In this case, not only a fluid-particle but also a size-selective particle-particle separation may be accomplished (see

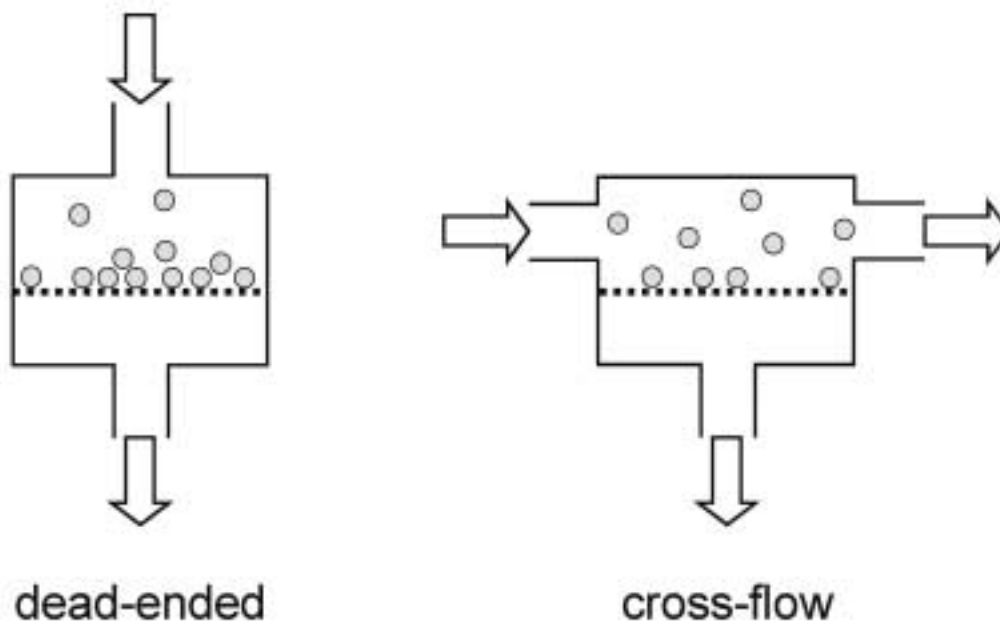


Figure 1.1: Schematic representation of “dead-ended flow” (left) and “cross-flow” (right) MF.

e.g. Chapter 6).

MF is one of the oldest membrane filtration processes. In 1929 the process was first commercialised by Sartorius Werke GmbH in Gottingen, Germany as a bacteriological assay to rapidly determine the safety of drinking water. Application on an industrial scale started in the late sixties. An important factor for the industrial application was the development of cross-flow membrane filtration systems. In such a system, the feed suspension flow is directed parallel or tangential to the membrane with inlet and outlet ports (Figure 1.1). Compared to “dead-ended flow” or “impact flow” with a perpendicular direction of the feed suspension flow to the membrane, a “cross-flow” flow pattern results in much higher permeation fluxes. This is due to re-entrainment of polarised and deposited particles by wall shear stresses along the membrane. Control over this re-entrainment process is of key importance for process operation as is discussed in Chapters 5-8 for the applications under study in this thesis.

Nowadays MF has a broad application range in industries such as the biotechnological, food, electronic and automobile industry. The applications are diverse, but to mention a few:

- **biotechnological applications:** bacterial, yeast and mammalian cell harvesting; clarification of antibiotics and virus containing solutions; sterilisation of solutions containing antibiotics, valuable biological molecules and DNA, and tissue culture media;
- **food applications:** wine, juice and beer clarification, sterilisation, protein separation in milk;
- **medical applications:** blood oxygenators, plasma separation from blood;
- **water treatment:** production of ultrapure water, oil-water separations, wastewater treatment.

This thesis is targeted at future membrane separation processes for dairy applications.

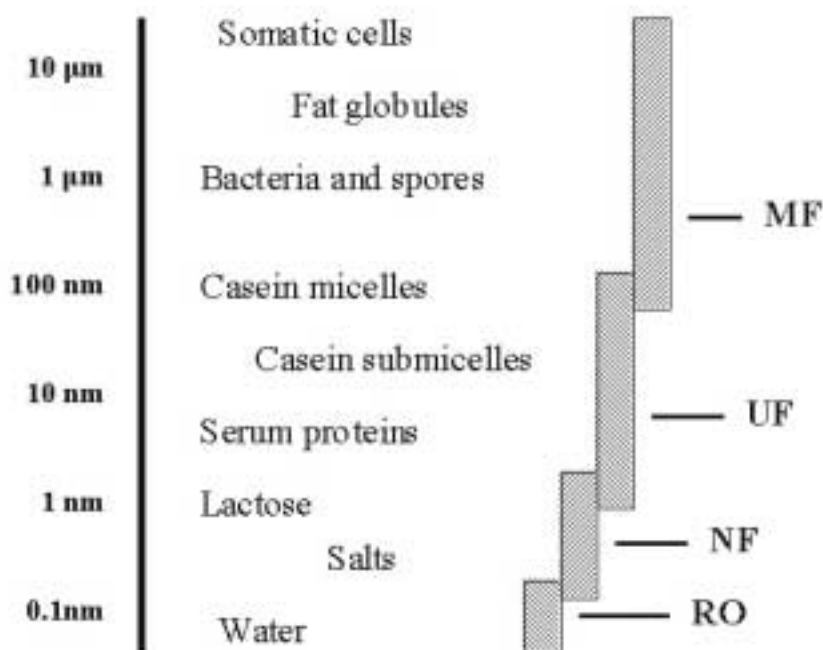


Figure 1.2: Components in milk: size indication and membrane processes [3].
 MF=microfiltration UF=ultrafiltration NF=nanofiltration RO=reverse osmosis.

Milk consists of a wide variety of constituents with different functionalities. The functionality of these constituents could be used more effectively if they were available separately. Because these constituents often have different sizes (Figure 1.2), membrane separation technology is in general very suited to accomplish this separation. However, milk is also a very complex feed for membrane separation, because of the broad particle size distribution (1 nm-20 μ m), high volume fractions of dispersed components ($\pm 15\%$ in total) and different properties of the feed constituents (deformability, charge, hydrophilicity, etc.). As a consequence, current membrane processes for milk have either a rather low capacity, due to strong particle accumulation at the membrane surface, or are energy demanding, because of the high cross-flow velocity that has to be applied to control particle accumulation. Also the selectivity of the membrane separation processes is affected negatively by the complexity of milk, an effect that is often related to particle accumulation. Practical application of many promising separation steps of milk, such as the separation and fractionation of fat globules, the reduction of bacteria and spores, and the separation of casein micelles and serum proteins, is currently limited because of the low capacity and selectivity. The main issue that has to be resolved for membrane separation to be applied on industrial scale milk separation is control of particle accumulation at the membrane. In order to do so, more detailed information on particle behaviour is required. This thesis studies various aspects of this particle behaviour, in order to obtain better understanding of the phenomena playing a role during MF of milk.

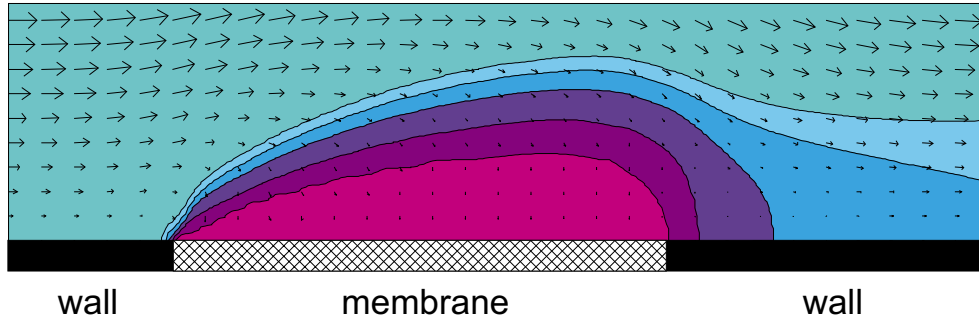


Figure 1.3: Example of a concentration polarisation layer formed during MF. The colors indicate the concentration, ranging from 0-0.1 v/v (light grey) to 0.5-0.6 v/v (dark grey). The arrows indicate the flow velocity. This figure shows a result of the suspension flow model, which is described in detail in Chapter 8.

1.3 Mass transport

During MF, the rejected particles usually form a cake layer on the membrane surface. The pressure-driven permeate flux through this cake layer and the membrane may be described by Darcy's law:

$$J \equiv \frac{1}{A} \frac{dV}{dt} = \frac{\Delta p}{\eta_0 (R_m + R_c)} \quad (1.1)$$

where J is the permeate flux, V is the total volume of permeate, A is the membrane area, t is the filtration time, Δp is the pressure drop imposed across the cake and membrane, η_0 is the viscosity of the permeate, R_m is the membrane resistance (which can increase with time due to membrane fouling and compaction), and R_c is the cake resistance (which can increase with time due to cake buildup and compression).

Cross-flow MF results in a (partial) re-entrainment of particles from the layer near the membrane to the bulk phase. As a consequence of this re-entrainment, the cake layer grows and reduces the permeate flux until a steady state is reached. At steady state, the convection of particles toward the cake layer by the permeate flow is balanced by back-transport of the particles away from the cake layer by diffusion and inertial lift. A concentration-polarisation boundary layer is positioned adjacent to the cake layer in which there is a rapid decrease in particle concentration from that at the edge of the cake layer to that in the bulk suspension (Figure 1.3).

The flux during MF can be predicted by means of modelling of the particle accumulation process including concentration polarisation. In models originally developed for ultrafiltration, the re-entrainment or back-transport of particles is assumed to be governed by *Brownian diffusion*. The Brownian diffusivity D_b of a particle of radius a is given by the Stokes-Einstein relationship:

$$D_b = \frac{kT}{6\pi\eta_0 a} \quad (1.2)$$

where k is the Boltzmann constant and T the absolute temperature.

These models predict the flux through a thin boundary layer where the mass transfer coefficient is based on theoretical or empirical correlations developed for convective heat

or mass transfer in tubes or channels having nonporous walls [4]. When this model is however used for MF, the predicted fluxes are much lower than those observed in practice. This discrepancy is often referred to as the “flux paradox for colloidal suspensions” [5]. The explanation for this flux paradox has been found in other back-transport mechanisms that supplement or even exceed the Brownian back-diffusion away from the membrane.

One of the other proposed back-transport mechanisms is *inertial lift*, which leads to the so-called “tubular-pinch effect”. Inertial lift is experienced by an isolated, neutrally buoyant particle in a duct under laminar flow conditions as a result of complex interactions with the flow field and the duct walls. When the channel Reynolds number is much larger than unity, the maximum lift velocity $v_{L,0}$ for a spherical particle near the wall of a two-dimensional channel is [6]:

$$v_{L,0} = 0.577 \frac{\rho_0 a^3 \dot{\gamma}_0^2}{16\eta_0} \quad (1.3)$$

where ρ_0 is the density of the suspending fluid and $\dot{\gamma}_0$ is the wall shear rate. With the basic premise that particles are carried to the membrane walls only if the permeate flux exceeds the maximum inertial lift velocity, the flux model can be (numerically) solved. The numerical solutions showed that the inertial lift velocity is often much lower than the permeation velocity in typical cross-flow MF systems, and therewith this mechanism is clearly not the solution for the flux paradox.

An alternative back-transport mechanism is *shear-induced diffusion*, also called hydrodynamic diffusion. This diffusion is the result of particle displacements from the streamlines in a shear flow as they interact with and tumble over other particles. The shear-induced diffusivity is proportional to the square of the particle size multiplied by the shear rate. Davis and Leighton [7] and Romero and Davis [8, 9] have developed an integral MF theory, including both cake resistance and membrane resistance, that uses concentration-dependent shear-induced diffusivities and shear viscosities appropriate for particulate suspensions. The shear-induced diffusivity \hat{D}^s is given by:

$$\hat{D}^s(\phi) = 0.33\phi^2 (1 + 0.5e^{8.8\phi}) \quad (1.4)$$

The diffusivity \hat{D}^s is a dimensionless parameter that is obtained by normalising for $\dot{\gamma}a^2$ (see also Equation 1.6). Obviously, the volume fraction of particles ϕ is of influence on \hat{D}^s . The shear-induced diffusive behaviour of particulate suspensions is evaluated in great detail in Chapters 2-4.

In Figure 1.4, the three back-transport mechanisms (*Brownian diffusion*, *inertial lift*, *shear-induced diffusion*) are compared by calculation of the steady state flux as a function of the particle size. MF is normally used for the separation of particles in the size range of 0.02 - 20 μm . From Figure 1.4, it can be concluded that shear-induced diffusion is the predominant back-transport mechanism for particles of this size. Therefore, our main focus is on shear-induced diffusion in this thesis. The basics are explained in the next section.

Other back-transport mechanisms that have been proposed for MF are for instance scouring [11], turbulent burst [12] and friction forces [13]. Because these back-transport mechanisms are more intuitive rather than theoretically founded, they are only mentioned here but are not part of this thesis.

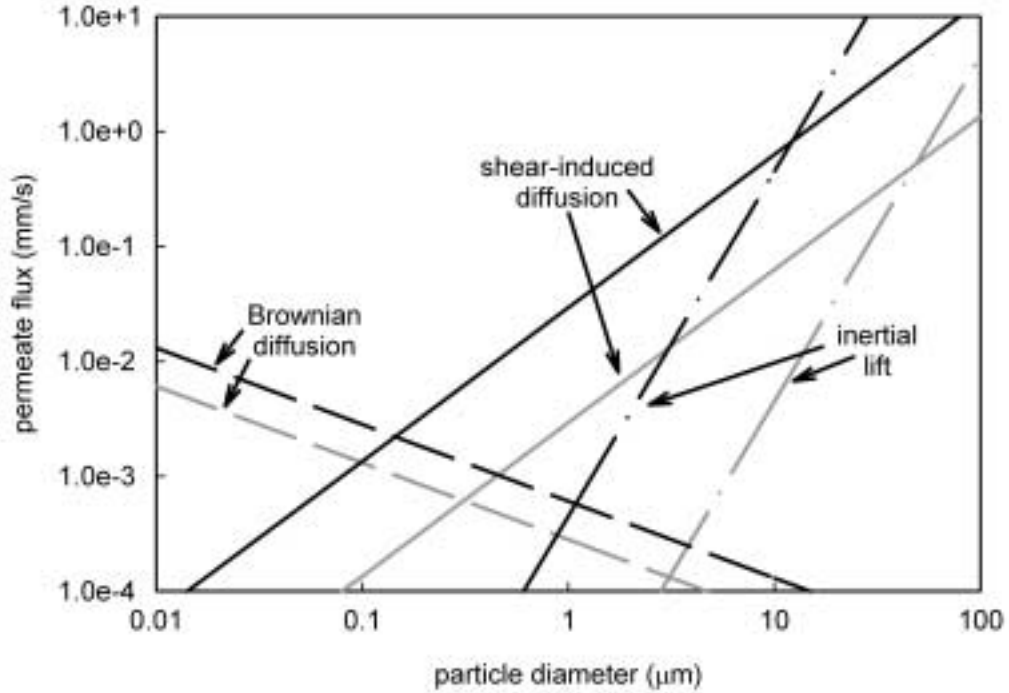


Figure 1.4: Permeate flux as a function of particle size as predicted by models based on three different back-transport mechanisms: Brownian diffusion, inertial lift, shear-induced diffusion (modified version of the figure published by Belfort and co-workers [10]). The permeate flux is indicated for shear rates ranging between 1000 (lower grey line) and 10000 (upper black line) s^{-1} .

1.4 Shear-induced diffusion

Shear-induced diffusion is the result of particle displacements from the streamlines in a shear flow as these particles interact with and tumble over other particles (Figure 1.5). In a suspension where the particles are homogeneously distributed, these displacements give rise to a diffusive behaviour called shear-induced self-diffusion. The shear-induced self-diffusion coefficient can be deduced from the individual particle displacements following:

$$\mathbf{D}^s \equiv \lim_{t \rightarrow \infty} \frac{1}{2} \frac{d}{dt} \langle \mathbf{x}(t) \mathbf{x}(t) \rangle \quad (1.5)$$

where $d\mathbf{x}(t)$ is the particle displacement vector, dt the time step and \mathbf{D}^s the associated diffusion tensor. A tensor is needed since the motion of particles is anisotropic due to the anisotropy of shear flow. The motion of a non-Brownian particle is in principle purely deterministic and the displacement of a given particle only depends on the external velocity field and its interactions with all other particles in the system. To obtain the random displacements that are a characteristic of diffusive motion, the initial particle configuration also needs to be changed. As a consequence, shear-induced diffusion is to be characterised as a long-time diffusion process.

The relevant time and length scales in the system are the shear rate $\dot{\gamma}$ and the particle radius a , respectively. Because \mathbf{D}^s has the dimension [length²/time], it scales as $\dot{\gamma} a^2$ and

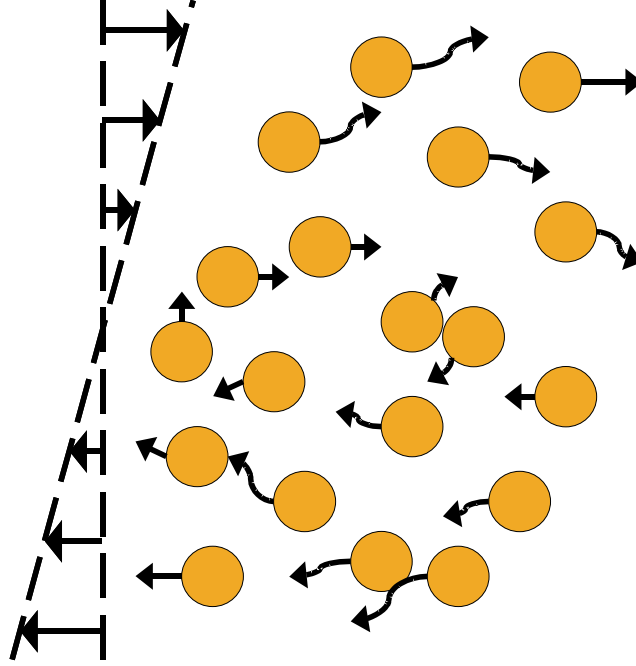


Figure 1.5: Schematic representation of shear-induced self-diffusion.

a dimensionless diffusivity \hat{D}^s can be defined:

$$\hat{D}^s = \frac{D^s}{\dot{\gamma}a^2} \quad (1.6)$$

The dimensionless diffusivity still depends on dimensionless parameters like the particle volume fraction ϕ .

In 1977, Eckstein, Bailey and Shapiro [14] were the first authors that reported about diffusive-like behaviour of particles in shear flow. Since then, the phenomenon of shear-induced diffusion has been studied experimentally [15–19], theoretically [20–24] and computationally [25–27]. In general, it is technically complex to monitor individual particle displacements or other particle behaviour on a microscopic scale in an experimental set-up, therefore computer simulations play an important role in research on shear-induced diffusion. In recent years, Acrivos and co-workers [25, 26] and Brady and co-workers [27] have carried out extensive research on shear-induced self-diffusion, making use of the Stokesian Dynamics computer simulation technique. As a result, shear-induced self-diffusion in monodisperse suspensions and at Stokes flow conditions can be considered well-understood.

In MF systems, rather than shear-induced self-diffusion solely, the collective process of gradient diffusion plays a role, leading to net migration of particles on the macroscopic level. In one of their very recent papers, Brady and co-workers [28] present a technique to determine migratory diffusion coefficients in homogeneous suspensions. The results were in excellent agreement with available experimental results. It was postulated by the authors that the gradient diffusivity D^∇ may be approximated by:

$$D^\nabla \approx \frac{D^s}{S^{\text{eq}}(0)} \quad (1.7)$$

where $S^{\text{eq}}(0)$ is the static structure factor corresponding to the hard-sphere suspension at thermodynamic equilibrium.

1.5 Research aim and outline

In this thesis, factors affecting the efficiency of MF processes for milk separation are studied on various levels of detail. The main focus is on concentration polarisation and its effects, because this can be considered the key factor for the process efficiency.

For monodisperse suspensions of ideal hard spheres, concentration polarisation is a relatively well-known process, but for suspensions with a complex composition like milk, concentration polarisation can be considered an unexplored area because the diffusive behaviour of suspensions is not yet sufficiently understood.

It is chosen to start at the basic level of shear-induced self-diffusion, because this diffusive behaviour can be considered the basis for microfiltration (Figure 1.6: particle dynamics). Up to now, computer simulations have been the most successful research method for shear-induced self-diffusion, since it is hard to experimentally monitor individual particle trajectories in concentrated suspensions in shear flow. Presently, these computer simulation studies were exclusively carried out with the Stokesian dynamics technique, which resulted in a good knowledge of shear-induced self-diffusion of monodisperse suspensions at Stokes flow conditions. In this study, the Lattice Boltzmann (LB) method is used to study shear-induced diffusion by computer simulation. The LB method for suspension flow is a well-established technique, which was originally developed by Ladd [29, 30]. Compared to Stokesian dynamics, the LB method has the advantage that it is not limited to the Stokes flow regime, which for instance facilitates computations on suspension flow at non-zero Reynolds numbers, in the vicinity of walls and with multi-sized particles. These are all conditions that are relevant to membrane separation systems. The LB method was preferred because it is considered better suited for these complex conditions than the Stokesian dynamics technique. Although the LB method is a well-established technique for suspension flow, the application to shear-induced self-diffusion is new.

The LB computer simulation results are validated by means of experiments on microfiltration processes, where different aspects of suspension composition have been investigated (Figure 1.6: particle accumulation and deposition, particle separation and fractionation). Part of the experimental research is carried out on so-called microsieve membranes [31]. In comparison with conventional MF membranes, they have exemplary properties, such as a smooth and flat surface, a narrow pore size distribution, and a membrane thickness in the order of μm , resulting in an extremely high permeability. Although these membranes are not yet used for large-scale applications, they seem to be promising for MF of complex suspensions. The success of these microsieves is however expected to depend heavily on a proper control of concentration polarisation. This is an important reason to take them into account in this thesis.

Chapters 2, 3 and 4 of this thesis focus on shear-induced diffusion, which is the predominant transport mechanism for particles in the size range under study (0.02-20 μm). This phenomenon is studied by means of computer simulations following the LB method (Figure 1.6). First (Chapter 2), the flow behaviour of 2D and 3D suspensions in a Couette system is studied, which resulted in a modelling approach for computer simulation of shear-induced self-diffusion. Following this modelling approach, shear-induced dif-

fusion at non-Stokesian conditions has been studied in Chapter 3. In Chapter 4, a study of the mutual influence of different-sized particles on their shear-induced diffusivity is presented.

The research described in Chapter 2, 3 and 4 lays the foundation for the research in the next chapters, which focus on concentration polarisation in MF systems (Figure 1.6). In Chapter 5, the effect of the presence of different-sized particles in the feed suspension on the steady-state flux is investigated. Chapter 6 focuses on different-sized particles as well, but here, the effect of these particles on the deposition of particles onto the membrane and on the fractionation of particles is investigated. In Chapter 7, a step is made towards actual milk ingredients. The properties of deposited casein micelles and fat globules from bovine milk are studied. Finally (Chapter 8), a computer simulation model is developed for suspension flow in MF systems, which allows the complete solution of the flow field in systems with complex geometries and for polydisperse suspensions (Figure 1.6: particle separation and fractionation). The computer simulation model is meant as a design tool for microfiltration membranes, systems and processes.

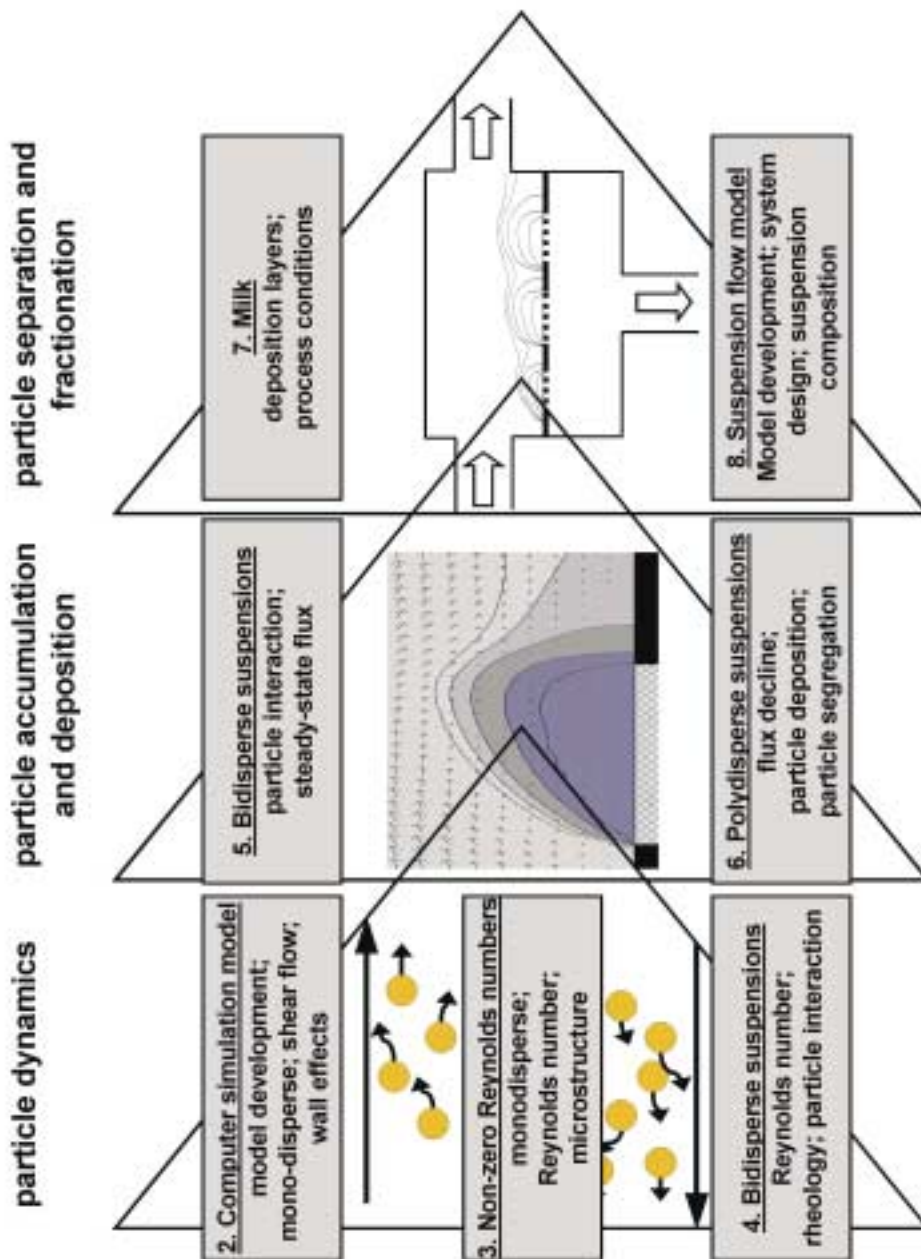


Figure 1.6: Outline per chapter, indicating the various levels of detail in this thesis.

**Lattice Boltzmann simulation of 2D
and 3D non-Brownian suspensions in
Couette flow**

In this study, the Lattice Boltzmann (LB) method is applied for computer simulation of suspension flow in Couette systems. Typical aspects of Couette flow such as wall effects and non-zero Reynolds numbers can be studied well with the LB method because of its time-dependent character. Couette flow of single, two and multi-particle systems was studied, where two-dimensional (2D) systems were compared with three-dimensional (3D) systems.

Computations on multi-particle 3D suspensions, for instance to assess the viscosity or shear-induced diffusivity, were found to be very intensive. This was only partly a consequence of the 3D system size. The critical particle grid size, necessary for accurate results, was found to be relatively large, increasing the system to impractical sizes.

It is however demonstrated that it is possible to carry out computer simulations on 2D suspensions and use relatively simple, linear scaling relations to translate these results to 3D suspensions, in this way avoiding intensive computations. By doing so, the LB method is shown to be well-suited for study of suspension flow in Couette systems, particularly for aspects as particle layering near solid walls, hydrodynamic particle interactions and viscous stresses at non-zero Reynolds numbers, which cannot be easily solved with alternative methods. It also opens the way to employ the LB method for other unexplored aspects, such as particle polydispersity and high Reynolds number flow, with large relevance to practical processing of suspensions.

2.1 Introduction

Since many manufacturing processes involve the transport of suspensions such as slurries, colloids, polymers and ceramics, knowledge of the flow behaviour of suspensions is of general interest. Not only the behaviour in shear flow but also in the presence of rigid boundaries, such as a pipe wall, is important, because these rigid boundaries can induce effects such as structuring, demixing and wall slip [32]. In experimental research as well as theoretical research, Couette flow is often used as a means to investigate the suspension flow behaviour in simple shear flow and in the presence of walls.

In the recent years, computer simulation models for colloidal suspension flow have developed into powerful research tools [33]. These numerical models take explicit account of the hydrodynamic forces between the suspended particles, although the various models do this in different ways. In Brownian and Stokesian dynamics, the hydrodynamic interactions are assumed to be fully developed. This virtually means that the time scales between the fluid dynamics and the motion of the solid particles are completely separated. These methods are however not suited for suspensions bounded by walls, and are therewith also not suited for Couette flow. Time-dependent models do not assume fully developed hydrodynamic interactions, but take into account the development of hydrodynamic interactions in time and space from purely local stresses generated at the solid-fluid surface. These models, including Lattice Boltzmann (LB) and finite-element methods, as well as particle-based schemes such as dissipative particle dynamics, are suited for describing Couette flow. In comparison to the LB method, finite-element methods require much more computing power, while dissipative particle dynamics is less often used for hydrodynamics. Therefore, the Lattice-Boltzmann method can be considered the best-

developed of the time-dependent models for multi-particle suspensions.

In the time-dependent methods, the solid-fluid surface is explicitly present in the system. This mostly means that the solid particles are represented on a numerical grid, which introduces inaccuracy not only in the shape of the particle but also in the fluid flow around the particle. The degree of inaccuracy is dependent on the particle grid size and this brings up limitations in the range of conditions where accurate results can be obtained. One obvious limitation is the volume fraction of particles in the system. Dependent on the particle size, there will be a limiting volume fraction above which the accuracy will be insufficient.

An advantage of computer modelling is that very detailed knowledge on the particle dynamics and structure can be gained, such as the translational and rotational velocities of the individual particles in the suspension. In spite of the large progress in computational power, these computer modelling techniques still require a large computing effort, which limits the system size in the computations. This is particularly the case when the particle grid size needs to be relatively large in order to have sufficient accuracy. One way to reduce the computing power can be to carry out simulations on two-dimensional (2D) instead of three-dimensional (3D) suspensions. Adequate 2D-3D scaling relations are then required to be able to translate the 2D results to predictions for 3D suspensions.

In this paper, we present a study on the use of the LB method for computer simulation of 2D and 3D suspensions in Couette flow, with the aim to investigate whether computer simulations on 2D suspensions can (partly) replace computer simulations on 3D suspensions, especially when the latter are computationally intensive. Hereto, we compare different aspects of the flow behaviour of 2D and 3D suspensions in Couette systems in order to find 2D-3D scaling relations. Furthermore we investigate the accuracy of the results in relation to the particle size and the volume fraction, as related to the explicit presence of the solid-fluid surface in the system. Therewith, this paper demonstrates the use and the limitations of LB computations on 2D suspensions in Couette flow as compared to 3D real suspensions.

2.2 Computer simulation method

For general information about the LB method, we refer to literature (see e.g. [34]). In this section, the emphasis is on the suspended particles, their incorporation in the fluid and their interactions.

2.2.1 Simulation of the fluid

The LB method is based on the well-established connection between the dynamics of a dilute gas and the Navier-Stokes equations [35]. In the LB method, the discretised Boltzmann equation is solved for fictitious fluid particles, that are constrained to move on a lattice. The state of the fluid is characterised by the single-particle distribution function $f_i(\mathbf{x}, t)$, describing the average number of particles at a particular node of the lattice \mathbf{x} , at a time t , with the discrete velocity c_i , which brings the fluid particles in one time step to an adjacent lattice node. It is known that only a small set of discrete velocities is necessary to simulate the Navier-Stokes equations [36]. In the simulations described in this paper, the fluid dynamics were solved with a D2Q9 or a D3Q19 LB scheme, which is respectively defined on a 2D square lattice with rest particles and 8 non-zero particle

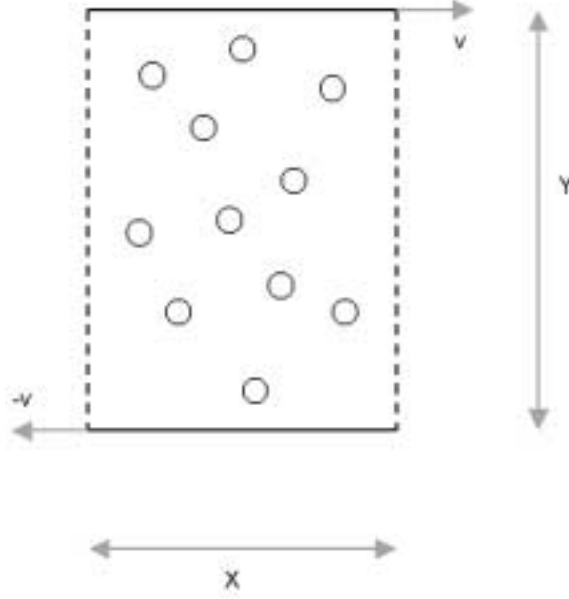


Figure 2.1: Schematic representation of the 2D Couette system. The solid box lines represent rigid walls and the dashed lines periodic boundaries. The 3D Couette system is similar, but has an extra dimension Z , which is bounded by periodic boundaries.

velocities or on a 3D square lattice with rest particles and 18 non-zero particle velocities. The velocity directions link lattice sites to its nearest and next-nearest neighbours. The hydrodynamic field's mass density ρ , momentum density \mathbf{j} , and the momentum flux density Π are moments of this velocity distribution:

$$\rho = \sum_i f_i, \mathbf{j} = \sum_i f_i \mathbf{c}_i, \Pi = \sum_i f_i \mathbf{c}_i \mathbf{c}_i \quad (2.1)$$

The fictitious fluid particles and their interactions evolve by collisions and subsequent propagation to neighbouring lattice sites. In a collision step, the distribution function is relaxed towards the local equilibrium distribution according to:

$$f_i(\mathbf{x} + \Delta \mathbf{x}_i, t + \Delta t) = f_i(\mathbf{x}, t) - \frac{f_i(\mathbf{x}, t) - f_i^{eq}(\mathbf{x}, t)}{\tau} \quad (2.2)$$

The relaxation time τ controls the relaxation of the viscous stress in the fluid and is linked to the kinematic viscosity ν via:

$$\nu = c_s^2 \left(\tau - \frac{1}{2} \right) \Delta t \quad (2.3)$$

where the speed of sound c_s is defined by $c_s^2 = c^2/3$. In our simulations we applied $\tau = 1.0$ (in lattice units), which corresponds to a kinematic viscosity ν of the fluid of $1/6$ (in lattice units). The equilibrium distribution $f_i^{eq}(\mathbf{x}, t)$ is chosen such that the Navier-Stokes equations for a weakly compressible system are obtained [37].

The 2D Couette system consists of a rectangular box with a width X and a height Y (Figure 2.1). Periodic boundaries were applied at the left and right side of the box, while the upper and lower boundaries consist of a rigid wall. The rigid walls move with a constant velocity v in a horizontal but opposite direction in order to create a shear flow. The 3D Couette system is similar to the 2D system, but has an extra dimension Z , which is bounded by periodic boundaries.

2.2.2 Fluid-particle interactions

In the LB scheme for particulate suspensions as developed by Ladd [29, 30], the solid particles are defined by a boundary surface, which can be of any size or shape. The spherical (3D) or circular (2D) particles are projected on the lattice, where the boundary surface cuts off some of the links between lattice nodes. Fluid particles moving along the boundary surface interact with the surface at boundary nodes that are located at the lattice nodes nearest to the boundary surface of the solid particles, following an alternative method to Ladd's, that was developed by Behrend [38]. In this method, called relaxed bounce back conditions at the nodes, the LB collisions are carried out at every node, including the boundary nodes. The method of Behrend avoids some complications of Ladd's method, where additional information is to be passed between lattice nodes because the boundary nodes are placed in between instead of on lattice nodes. The resolution of the particles on the grid is better for Ladd's method, although Behrend showed that the translational friction of the particles agreed well with results of Ladd and with independent numerical results. The rotational friction however, agreed less well, due to the worse resolution. Comparable results were obtained for the hydrodynamic interactions between pairs of spheres, where the parallel friction coefficients were in excellent agreement with independent numerical solutions, whereas the agreement of the perpendicular friction coefficients was less. Results for three different transport coefficients were all again very accurate. In this study, we have chosen for Behrend's method because of its relative simplicity.

The collision rules at the boundary surface enforce a stick boundary condition on the fluid, which means that the fluid velocity is matched to the local solid-body velocity \mathbf{u}_b . This local solid-body velocity \mathbf{u}_b (at position \mathbf{x}_b) is determined by the solid-particle velocity \mathbf{U} , its angular velocity Ω and the position of its center of mass \mathbf{R} :

$$\mathbf{u}_b = \mathbf{U} + \Omega \times (\mathbf{x}_b - \mathbf{R}) \quad (2.4)$$

After the collision phase, the boundary nodes are updated in the following way:

$$f_i(\mathbf{x} + \Delta\mathbf{x}_i, t + \Delta t) = f'_{-i}(\mathbf{x}, t) + \frac{2\rho w_i}{c_s^2} \mathbf{u}_b \cdot \mathbf{c}_i \quad (2.5)$$

$$f_i(\mathbf{x} - \Delta\mathbf{x}_i, t + \Delta t) = f'_i(\mathbf{x}, t) - \frac{2\rho w_i}{c_s^2} \mathbf{u}_b \cdot \mathbf{c}_i \quad (2.6)$$

Here $f'_i(\mathbf{x}, t)$ is the post-collisional distribution function. For moving suspension particles, in this update, momentum is exchanged between the incoming particles from the fluid and the solid side (the combined momentum of the fluid and the solid phase is however conserved). From this momentum exchange the force and torque exerted on a suspension particle is calculated. Hereafter the kinematic properties of the suspension particles themselves are updated with a simple Euler forward integration of Newton's second law.

The calculations on spherical (3D) and circular (2D) particles follow essentially the same method. Only the mass M and the moment of inertia I in Newton's second law differ. For 3D particles, they are given by:

$$M = \rho_s \frac{4}{3} \pi a^3 \quad (2.7)$$

$$I = 0.4 M a^2 \quad (2.8)$$

where ρ and ρ_s are the density of the fluid and the solid particle respectively, and a is the particle radius. For 2D particles, M and I are given by:

$$M = \rho_s \pi a^2 \quad (2.9)$$

$$I = 0.5 M a^2 \quad (2.10)$$

Since a suspended particle is essentially simulated by the introduction of a boundary surface, separating the interior of the particle from the exterior, the interior of the particle also consists of fluid. The particles thus comprise a solid shell of given mass and inertia, filled with fluid of the same mass density as the bulk fluid. Ladd [30] examined the effects of the interior fluid on the behaviour of the particle. Dynamically, the particle behaves as if its mass is the sum of the shell mass and the mass of the interior fluid. With a sufficiently high effective mass of the shell, the contribution of the interior fluid to the inertial force is negligibly small. Our computations were carried out in this regime, with an effective mass ρ_s/ρ of 10. Since our computations are carried out in the Stokes flow regime, inertial effects do not play a role (see also Kromkamp and others [39]).

2.2.3 Accuracy of particle representation and particle-particle interactions

By the projection of the suspended particles on the lattice, a discrete representation of the surface is obtained, which becomes more and more precise as the surface curvature gets smaller and which is exact for surfaces parallel to lattice planes. Together with the choice of the location of the boundary nodes and the boundary update rules, the discretisation of the particle surface onto the lattice induces a hydrodynamic particle diameter that is slightly larger than the diameter based on the number of occupied lattice nodes [30]. It is therefore often proposed that the particle diameter should be corrected for this hydrodynamic effect. The magnitude of the correction is mostly based on the particle behaviour in the Stokes flow regime and at low particle concentrations. As also presented in an earlier paper [39], we have seen that in suspensions in shear flow, particles can approach each other very closely, such that particles would largely overlap when the hydrodynamic particle size would be taken into account. The closest approach distance is moreover found to be dependent on conditions such as the particle concentration and the shear rate. Since assessment of the hydrodynamic particle diameter in these systems is virtually impossible, while the corrections would probably be very small, we did not apply this correction but used the input particle diameter in our calculations.

Since the suspension flow behaviour in Couette systems is mainly governed by hydrodynamic particle-particle or particle-wall interactions, these interactions need to be accurately resolved in the computations. When two suspension particles come into close contact with each other, the lubrication force becomes important. This force is caused by the attenuation of the fluid film in the gap between the two particles and is repulsive upon approach and attractive upon separation of the particles. When the gap width between two particles is in the order of one lattice spacing, the lubrication force is however not exactly resolved with the LB method. This is due to the discretisation of the particles and fluid on a grid and is a problem that is encountered by all numerical methods. This lubrication breakdown leads to a so-called “depletion force” that pushes particles into each other. To overcome this problem we applied a lubrication correction method based on an explicit

calculation of the lubrication force F [40]. For a 3D system F is given by [40]:

$$\begin{aligned} F &= -6\pi\eta\mathbf{U}_{12}\cdot\hat{\mathbf{R}}_{12}\frac{a_1a_2}{(a_1+a_2)^2}\left(\frac{1}{h}-\frac{1}{h_c}\right), h < h_c \\ F &= 0, h > h_c \end{aligned} \quad (2.11)$$

where η is the viscosity, $\mathbf{U}_{12} = \mathbf{U}_1 - \mathbf{U}_2$ and $h = |\mathbf{R}_{12}| - (a_1 + a_2)$ is the gap (distance between the particle surfaces). The unit vector $\hat{\mathbf{R}}_{12} = \mathbf{R}_{12}/|\mathbf{R}_{12}|$. For a 2D system the lubrication force per unit cylinder length F is given by (see appendix 2.6):

$$\begin{aligned} F &= -\frac{1}{2}\eta\mathbf{U}_{12}\cdot\hat{\mathbf{R}}_{12}\left(\left(\frac{a_1+a_2}{h}\right)^{\frac{3}{2}}\left(F_0 + \frac{h}{a_1+a_2}F_1\right) - \left(\frac{a_1+a_2}{h_c}\right)^{\frac{3}{2}}\right. \\ &\quad \left.(F_0 + \frac{h_c}{a_1+a_2}F_1)\right), h < h_c \\ F &= 0, h > h_c \end{aligned} \quad (2.12)$$

where F_0 is the numerical constant $\frac{3}{4}\pi\sqrt{2} = 3.3322$ and F_1 is the first order correction for the lubrication limit $h/2a \ll 1$ with a value of $\frac{231}{80} \cdot \pi \cdot \sqrt{2} = 12.829$. In accordance with Ladd and Verberg [33], we applied a correction on the lubrication force to account for the lubrication force that is already resolved in the computations of the fluid dynamics. This was done by subtracting the lubrication force at a cut-off distance h_c from the total lubrication force, as indicated in Equations 2.11 and 2.12. The cut-off distance h_c represents the cut-off distance between the particle surfaces for the added lubrication force and was chosen equal to 1.1 lattice units for a 3D system and to 2.0 lattice units for a 2D system (as was found optimal in our simulations). For 3D systems, Nguyen and Ladd [40] showed that this correction leads to more accurate results for particle interactions at short interparticle distances, even with neutrally buoyant particles very near to contact and without causing instabilities in the particle dynamics.

Since tangential lubrication has a weaker logarithmic divergence and its breakdown does not lead to serious problems, we have not included this correction in our simulations.

We have noticed before, that in suspensions with relatively high particle fractions or at high particle Reynolds number, particle clustering and overlap can occur, which greatly affects the diffusive behaviour of the particles [39]. This behaviour seems to be correlated with the lubrication breakdown of concentrated colloids, that was reported by Ball and Melrose [41]. As suggested by these authors, we applied a Hookean spring force between the particles to avoid this clustering and overlap. This Hookean spring force was applied for gaps h smaller than a thickness δ and was applied in the direction of the line of particle centres, according to:

$$F_h = F_0 - \left(\frac{F_0}{\delta}\right)h \quad (2.13)$$

with a maximal Hookean spring force F_0 of $2.5 \cdot 10^{-6}$ (in lattice units) for a 3D system and 10.0 (in lattice units) for a 2D system. The Hookean spring force is active in a layer around the particle with a thickness $\delta/2$ of 0.025 lattice units for a 3D system and 0.05 lattice units for a 2D system.

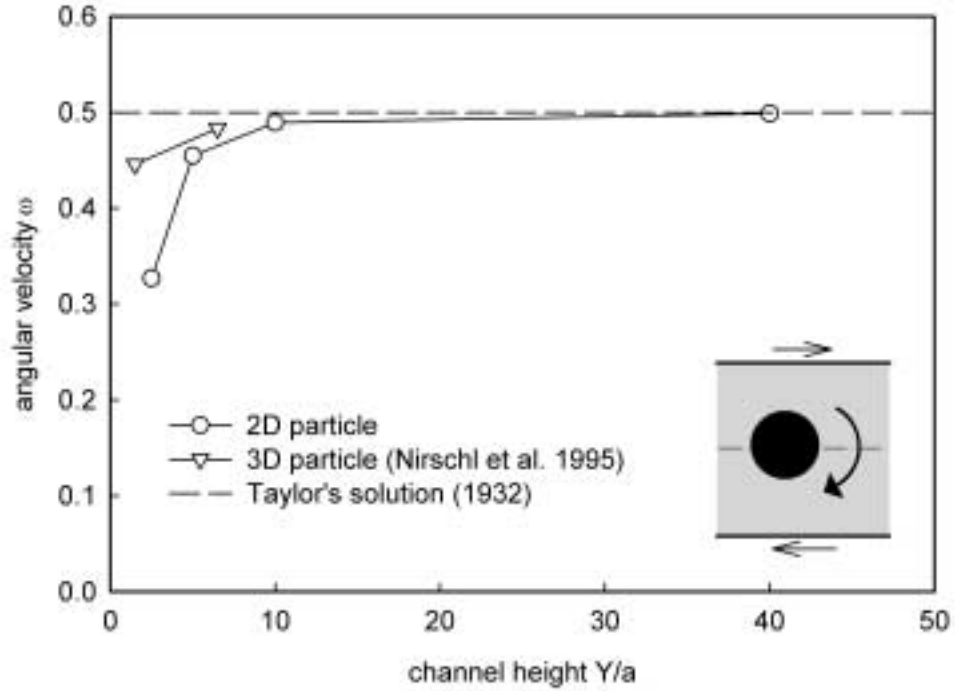


Figure 2.2: The angular velocity ω as a function of the relative channel height Y/a for a single cylinder with radius a in shear flow ($Re_{\text{shear,p}} = 0.058$, $a=8$ lattice units). The distance between the solid walls of the Couette system was varied between $2.5a$ and $40a$. The results are compared to results of Nirschl and co-workers [42] for a 3D system. The line represents Taylor's solution for $Y/a = \infty$ [43] and the inset shows a scheme of the simulated situation.

2.3 Single and pair particles in Couette flow

2.3.1 Wall effects on a single particle

In order to compare wall effects between a single suspended 2D particle and a 3D particle in shear flow, the rotation was studied in Couette systems with varying ratio of channel height to particle radius Y/a . For 3D particles, we take the data from Nirschl and others [42], who used a finite volume numerical scheme. We studied the rotation of 2D particles with our LB model.

The LB calculations were carried out for a 2D particle with a radius a of 8 lattice units. The distance X/a between the periodic boundaries was 80, which was verified to give results corresponding to a system with an infinitely large distance X/a . The channel height Y/a varied between 2.5 and 40. The shear rate $\dot{\gamma}$ was 3.75×10^{-5} per time step, which was verified to give results corresponding to Stokes flow. The shear-based particle Reynolds number $Re_{\text{shear,p}} = 4\dot{\gamma}a^2/\nu$, where ν is the kinematic viscosity, was equal to 0.058. The 2D particle was placed at the horizontal centerline of the Couette system. We assessed the equilibrium angular velocity ω of the 2D particle, which is normalised for the shear rate.

For a channel height Y/a larger than 10, the angular velocity ω was close to the analytical solution of Taylor [43] for a rotating particle in simple shear (Figure 2.2). For

smaller channel heights, the angular velocity ω starts to decrease due to interaction with the walls. The decrease starts earlier and is most pronounced for the 2D particle, where the angular velocity ω decreased from the maximum value of 0.50 to a value of 0.33 at a channel height Y/a of 2.5. This effect can be understood because the intensity of the flow field around a 2D particle is larger than around a 3D particle. As a result, for 2D particles, wall effects start at a channel height Y/a , which is about 3 units higher than for 3D particles, while the wall effects for 2D particles are more intense as well. The results suggest that a scaling relation can be obtained between 2D and 3D results by normalisation of the channel height. For the 2D results, the channel height should be multiplied with a factor of about 0.33.

2.3.2 Two colliding particles in shear flow

The hydrodynamic interactions between particles in a 2D and a 3D system can be compared from the flow trajectory of two interacting particles. Batchelor and Green [44] have derived an analytical solution for 3D particles, but a solution for 2D particles is not yet available. Therefore, we calculated the flow trajectories with the LB model for 2D as well as 3D particles, at equivalent conditions.

For 2D particles, two equal-sized particles ($a=8$ lattice units) were placed at equidistant heights above and under the horizontal centerline. The initial horizontal distance $(x - x_{\text{midpoint}})/a$ from the midpoint between the particles was 5, while the initial vertical distance was varied. Both the channel height ($Y/a=40$) and the distance between the periodic boundaries ($X/a=80$) were chosen such that they did not affect the particle trajectories. $Re_{\text{shear,p}}$ was equal to 0.058, which was verified to give results in accordance with Stokes flow. For 3D particles, virtually the same conditions are applied, except for the particle radius, which was chosen as 11 lattice units.

The resulting flow trajectories are presented in figure 2.3. When the two particles pass each other, they move away from the horizontal centerline upon approach and move back to their original height upon separation, as is described by Batchelor and Green [44]. When comparing 2D and 3D particles, it is clear that the 3D particles move closer around each other: the minimal gap between the 2D particles is equal to $0.27a$ and $0.11a$ for initial vertical distances from the midpoint of respectively $0.44a$ and $0.25a$, while the minimal gap between 3D particles is respectively $0.01a$ and $0.00a$.

These differences between the inter-particle distances are caused by differences between the ratio of drag to lubrication force for 2D and 3D particles, which causes the fluid to move less easily out of or into the gap for 2D particles. A consequence of the observed behaviour is that the range of hydrodynamic interactions is longer for 2D particles. In 2D multi-particle systems, this may lead to more intense hydrodynamic interactions at a similar particle fraction.

A full scaling of the particle trajectories would at least require a numerical solution of the lubrication force, but here we apply an analytical scaling by simply rescaling of the X -axis and Y -axis in figure 2.3. The X -axis is rescaled by normalising X for X^* , the X -value where the particle has reached a distance $Y^* = 0.5(Y_{\text{max}} - Y_{\text{initial}})$. The Y -axis is rescaled by normalising Y for the factor $Y_{\text{max}}(Y - Y_{\text{initial}})/(Y_{\text{max}} - Y_{\text{initial}}) + 1.0(Y_{\text{max}} - Y)/(Y_{\text{max}} - Y_{\text{initial}})$. Obviously, this rescaling can only be applied when X^* and Y_{max} are already known. The result is presented in figure 2.4.

The rescaling lead to 2D and 3D trajectories with a good resemblance. This indicates

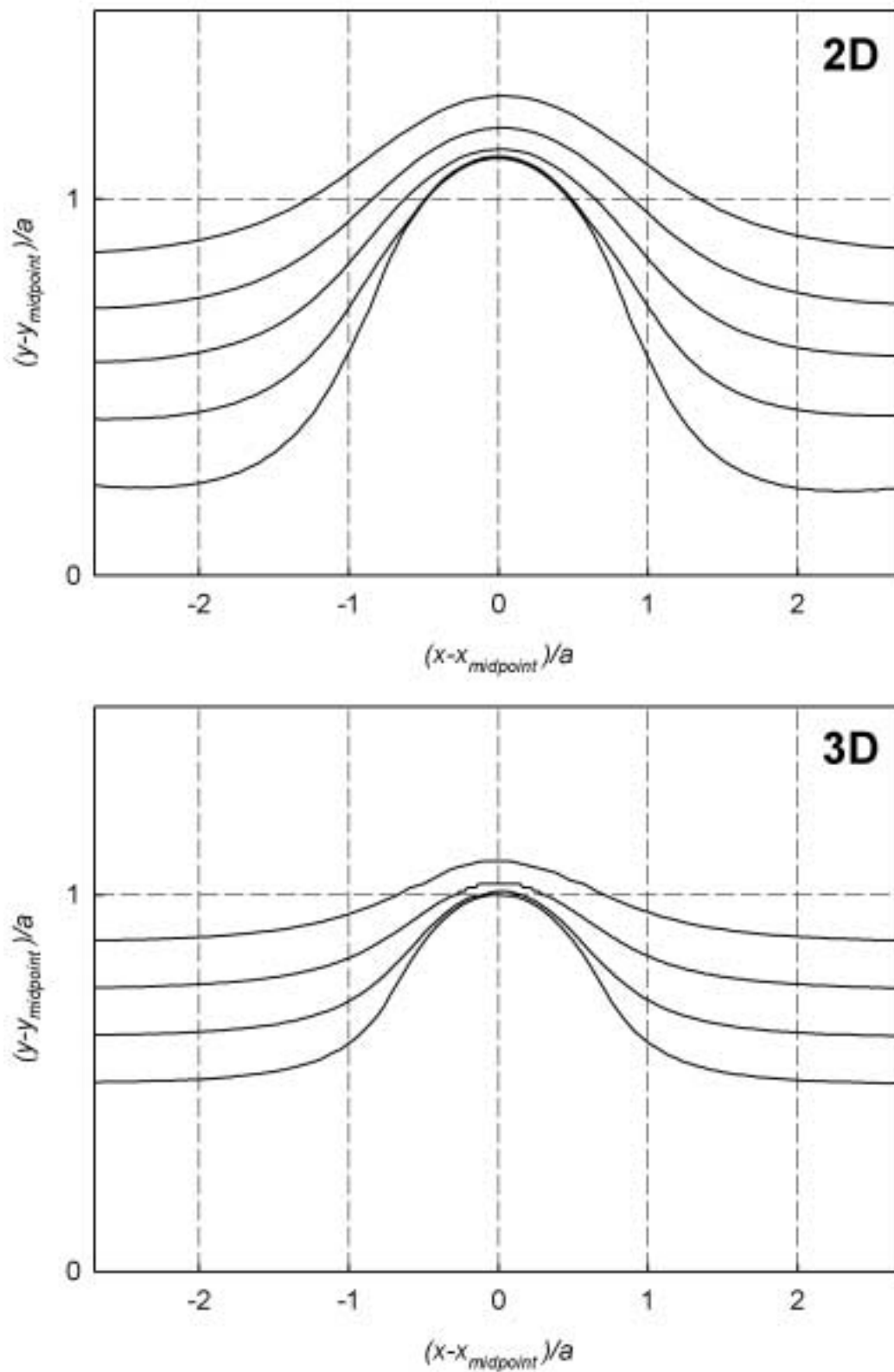


Figure 2.3: Cylinder or sphere trajectory during interaction of two cylinders ($a=8.0$ lattice units (2D)) or two spheres ($a=11.0$ lattice units (3D)) in a linear shear field ($Re_{\text{shear},p} = 0.058$) between two walls, for varying initial positions of the cylinders and spheres.

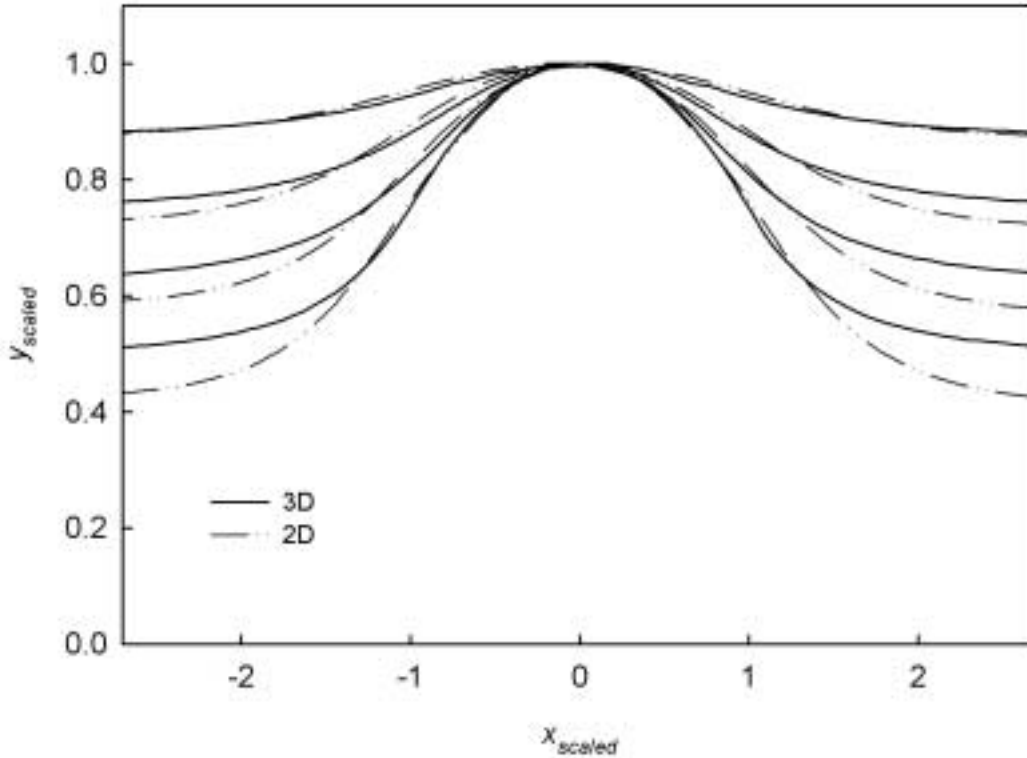


Figure 2.4: Cylinder or sphere trajectory during interaction of two cylinders ($a=8.0$ lattice units (2D)) or two spheres ($a=11.0$ lattice units (3D)) in a linear shear field ($Re_{\text{shear},p} = 0.058$) between two walls, for varying initial positions of the cylinders and spheres. The values for X and Y are scaled as explained in the text (section 2.3.2).

that the trajectories of 2D and 3D systems can be scaled with the parameters X^* and Y_{max} , which can thus be considered characteristic for this system. Only when the particles are relatively far apart discrepancies occur but these long-range effects are often less relevant in concentrated suspensions.

2.4 2D and 3D multiparticle suspensions in Couette flow

2.4.1 Wall effects

The 2D multiparticle system consists of a rectangular box with $X : Y = 1 : 2$. The total number of particles (particle radius 8 lattice units) was equal to 200. $Re_{\text{shear},p}$ was equal to 0.023. In the 3D multiparticle system, the particle radius and $Re_{\text{shear},p}$ were similar to the 2D system. The box size was $X : Y : Z = 1 : 1.5 : 1$ and the total number of particles 400.

Walls can induce effects as particle structuring, demixing and wall slip. In order to analyse these effects, we compare the time-averaged concentration distribution and the particle velocity profile as a function of the distance to the wall for 2D and 3D systems (Figure 2.5). In the 2D system, a layer near the walls with a height close to a was depleted

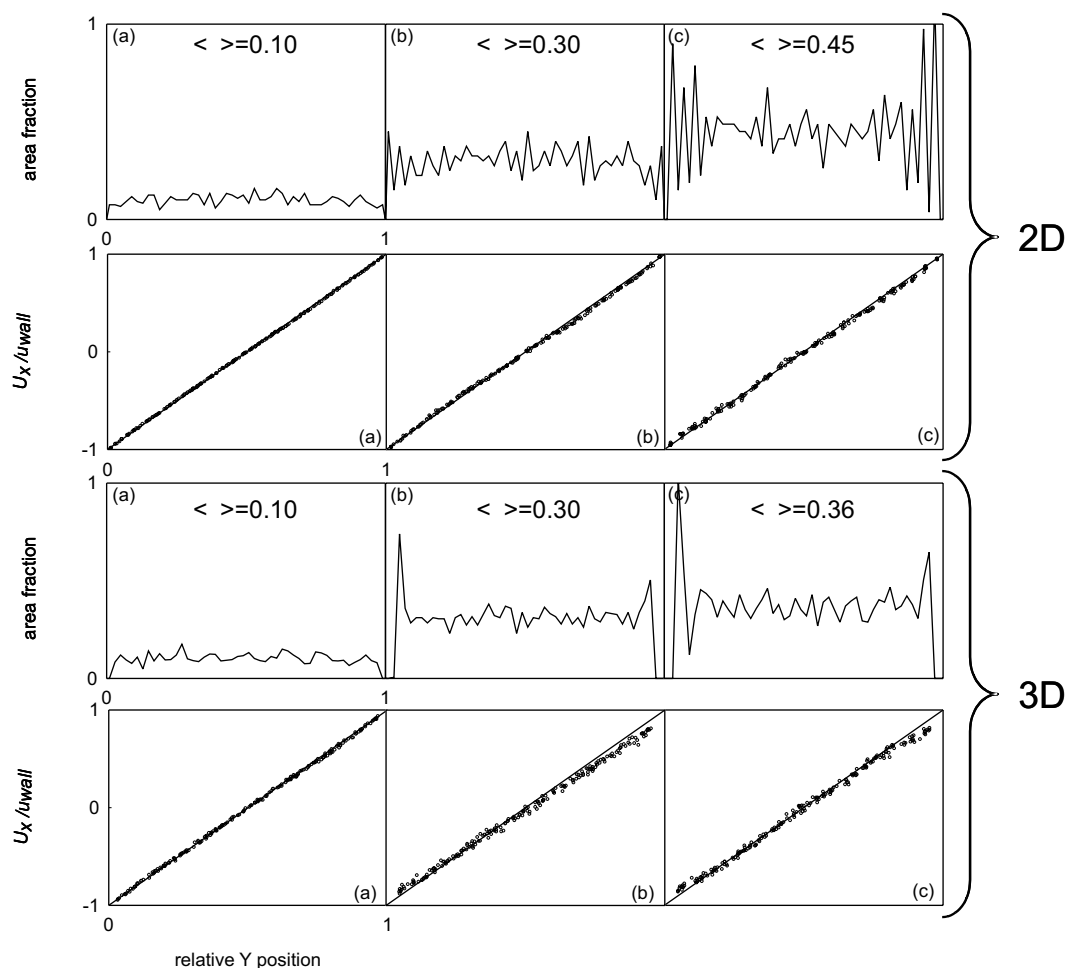


Figure 2.5: The time-averaged area (2D, cylinders) or volume (3D, spheres) fraction ϕ across the channel width Y for a 2D suspension (top) with mean area fractions $\langle \phi \rangle$ of 0.10 (a), 0.30 (b) and 0.45 (c) and a 3D suspension (bottom) with mean volume fractions $\langle \phi \rangle$ of 0.10 (a), 0.30 (b) and 0.36 (c).

of particles, as can be expected based on the particle size. No additional wall depletion was however found. For $\phi > 0.10$, strong structuring effects are found near the walls, which is clear from the concentration fluctuations. For $\phi = 0.3$, the first concentration peak appears at a distance from the wall between 0 and $1.3a$ and between $1.1a$ and $2.1a$ for $\phi = 0.45$. For $\phi = 0.45$ at least two distinct particle layers are visible, at a distance between $1.1a$ and $2.1a$ and between $3.2a$ and $4.2a$ from the wall respectively. From the particle velocity profile in the 2D system, it is clear that the shear profile deviates slightly from perfectly linear, but that, even for $\phi = 0.45$ where the particle velocity near the walls was up to 5% smaller than expected, this effect of wall slip is of minor importance.

In a 3D system, the situation was slightly different (figure 2.5). The height of the layer near the walls that was depleted of particles, was again close to a . Structuring effects were found to differ from 2D systems. In 3D systems, for volume fractions higher than 0.10, only one concentration peak was visible, which was more pronounced than in 2D systems. For $\phi = 0.3$, and 0.36 this concentration peak appears at a distance from the wall between $0.93a$ and $1.40a$ and between $0.88a$ and $1.09a$ respectively. As in accordance with wall

effects in a 2D and 3D single particle system, where these effects were only evident at small channel heights for 3D spheres, the concentration peak was closer to the wall in a 3D system (at the highest concentration). As a consequence of this more pronounced structuring in 3D systems, the particle velocity profile was also found to deviate more from perfectly linear. The profile exhibited a tendency towards a sigmoid shape. The velocity of particles near the walls deviated around 10% from the velocity expected for a linear velocity profile.

2.4.2 Viscosity

The viscosity of a concentrated suspension is a characteristic that strongly depends on hydrodynamic interactions. By calculation of the squeezing flow contribution, the viscosity can be calculated as a function of the particle fraction, as is done for 3D particles by Frankel and Acrivos [45]. The result is practically identical to the semi-empirical model of Krieger and Dougherty [46], which is valid for both 2D and 3D suspensions:

$$\eta_r = \left(1 - \frac{\langle \phi_s \rangle}{\phi_{\max}}\right)^{-[\eta]\phi_{\max}} \quad (2.14)$$

where η_r is the relative viscosity, $\langle \phi_s \rangle$ is the averaged particle fraction and ϕ_{\max} , the maximum packing fraction. The dimensionless factor $[\eta]$ is the intrinsic relative viscosity of the suspension. It is often suggested that the factor $[\eta]\phi_{\max}$ is similar for 2D and 3D suspensions [47]. Here we will use $[\eta]\phi_{\max}=1.82$, as derived from the values for ϕ_{\max} and $[\eta]$ of 0.68 and 2.68 respectively, that are reported by Phillips and co-workers [16] for 3D suspensions. The value for ϕ_{\max} in the denominator of Equation 2.14 followed from a subsequent fit of the simulation results.

Because the viscosity simply evolves from the lubrication force as a function of the mean distance between the particles, the scaling relation between 2D and 3D systems directly follows from this derivation. Therefore, we only determined the viscosity as a function of the particle fraction to compare the accuracy between 2D and 3D systems. In our simulations, the viscosity is determined from the stress at the walls in a multiparticle Couette system. For a 2D system, the height Y/a and width X/a of the Couette system are equal to respectively 64.75 and 32.38. The particle fraction was varied by varying the number of particles up to a maximum of 365. $Re_{\text{shear,p}}$ was equal to 0.012, which was verified to give results in accordance with Stokes flow. For a 3D system, the system properties were as described in section 2.4.1.

Figure 2.6 presents the results. There is a good agreement between the 2D computer simulation results and the Krieger-Dougherty model for $\phi_{\max}=0.88$. At a particle fraction ϕ exceeding 0.49 however, the viscosity is slightly lower than according to the Krieger-Dougherty model. Also the 3D computer simulation results show a good agreement with the Krieger-Dougherty model ($\phi_{\max}=0.69$). Similar to the 2D system, at higher concentrations, the viscosity starts to get lower than the Krieger-Dougherty model. This occurs however at a particle fraction ϕ exceeding 0.3 instead of 0.49 for a 2D system. Moreover, from Figure 2.6, it is clear that an appropriate scaling is obtained when the particle fractions of both 2D and 3D suspensions are related to ϕ_{\max} .

From comparison of our 2D viscosity data with LB results from literature (see e.g. [47] for an overview), it is clear that our data do not significantly differ from these data.

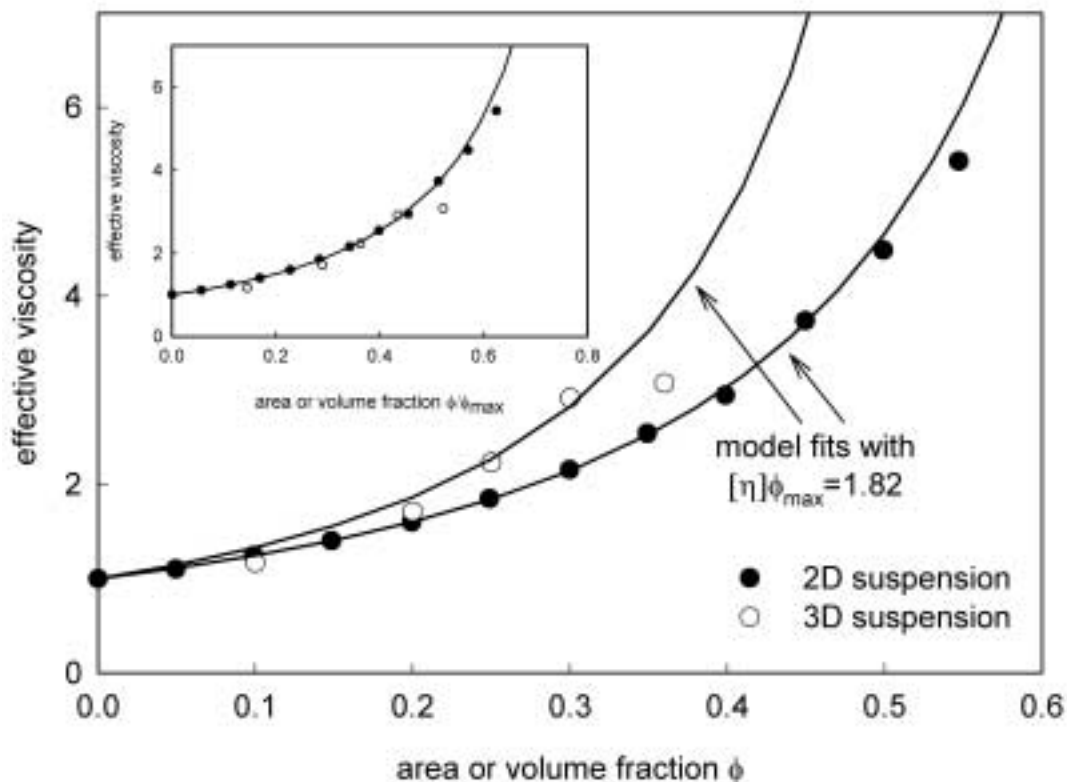


Figure 2.6: Effective viscosity of a 2D and a 3D suspension as a function of the area (cylinders) or volume (spheres) fraction. The lines represent fits of the results to the Krieger-Dougherty model with a value of 1.82 for $[\eta]_{\phi_{\max}}$, both for 2D and for 3D suspensions (the fit result for ϕ_{\max} was 0.88 for 2D and 0.69 for 3D). The inset shows the viscosity as a function of ϕ/ϕ_{\max} .

3D viscosity data are amongst others given by Heemels and others [48]. These authors could accurately describe the viscosity up to a volume fraction of at least 0.45, making use of the similar LB method as Ladd, but adapted in order to simulate truly solid particles. They also showed that when the original LB method of Ladd is used [29, 30], the internal fluid in the particles contributes to the effective density, which leads to an underestimation of the viscosity over the total volume fraction regime. A leveling off at higher volume fractions, as occurs in our simulations, is however not observed. Because this behaviour is found at lower volume fractions in 3D suspensions, where the particles come into closer contact, we hypothesize that the inaccuracy in the viscosity has to do with this close contact. It may therefore be that the less accurate particle representation, that is associated with Behrend's boundary rules as used in this study, is the main reason for the inaccuracy at higher particle fractions. The viscosity results indicate that particle radii in concentrated 3D suspensions should be relatively large in order to obtain sufficient accuracy. Since 3D suspensions require much computing power, this is a clear disadvantage of the method followed.

2.4.3 Shear-induced diffusion

Computer simulation

Another interesting phenomenon in multiparticle suspensions in shear flow is shear-induced diffusion, a phenomenon that arises from the hydrodynamic interactions between the particles. As can be seen in Figure 2.3, apart from the displacement caused by the affine flow, two-particle interactions do not lead to permanent displacements of these particles. In a concentrated multi-particle suspension however, simultaneous interactions between more than two particles can lead to permanent displacements, which can have a diffusive character on a sufficiently large timescale. The shear-induced self-diffusivity is thus defined as the time rate of change of one half times the mean-square displacement:

$$D_{xx} \equiv \lim_{t \rightarrow \infty} \frac{1}{2} \frac{d}{dt} \langle x(t)x(t) \rangle \quad (2.15)$$

Sierou and Brady [27] have done extensive computer simulation work on shear-induced self-diffusion, using the Stokesian dynamics technique. As far as we know, they have not published any results from 2D simulations. In contrast to Stokesian dynamics, our LB method enables research on shear-induced diffusion at non-Stokesian conditions, such as in the presence of walls and at non-zero Reynolds number. Here, we investigate 2D-3D scaling relations for shear-induced diffusion because this knowledge may enable the use of computationally less intensive 2D simulations.

The 2D and 3D systems were as described in section 2.4.1. For a 2D system, the shear-induced diffusivity is determined over a strain range between 18 and 60. In order to evaluate the effect of the initial particle configuration on the diffusion coefficient, we splitted the displacement curve of one simulation run into several curves which start at different times of the simulation run (and consequently at different particle configurations). In each separate curve, the mean square displacement was monitored over a strain of 30. The final diffusion coefficient is the mean value of the diffusion coefficients that were determined from the individual mean square displacement curves. Dependent on the particle volume fraction, the 2D calculations required between 70 and 650 h CPU time. With a similar particle radius, the 3D system requires much more computational power per simulated particle than a 2D system. For 3D systems, a particle number of 400 is found to be sufficiently high to obtain results that are representative for an infinitely large system. This particle number was twice as high as in a 2D system, which results in an improved statistical reliability of the 3D simulations. In order to limit the computational effort, the shear-induced diffusivity is determined over a strain range between 4.5 and 15, which was verified to give results representative for the long-range diffusive regime. In this way, the 3D simulations required about 40 times more CPU time than the 2D simulations (with equal particle radius).

For a 3D system and $\phi \geq 0.20$, our simulations generated shear-induced diffusivities that are smaller than the results found by Sierou and Brady [27]. In order to try to elucidate these differences, we assessed the influence of the particle radius on the shear-induced diffusivity at $\phi = 0.10, 0.20$ and 0.30 (figure 2.7). The shear-induced diffusivity increased with the particle radius, but seems to have reached a plateau value for $\phi = 0.10$ at a particle radius of 8 lattice units. For $\phi = 0.20$ and 0.30 , even at a particle radius of 10 lattice units, a plateau value was not reached. The values for $\phi = 0.30$ were furthest away from the values presented by Sierou and Brady [27].

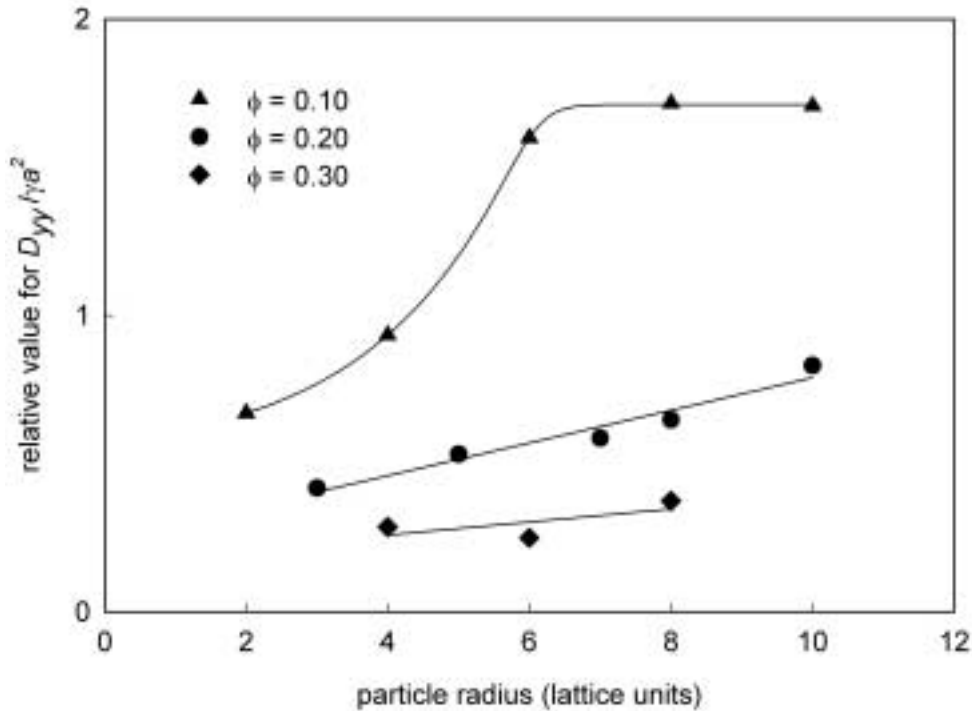


Figure 2.7: Component D_{yy} of the shear-induced self-diffusion coefficient, as related to the values found with Stokesian dynamics by Sierou and Brady [27], in a 3D suspension as a function of the particle radius for $\phi = 0.10, 0.20$ and 0.30 ($N = 400, Re_{shear,p} = 0.023$). The lines are drawn as a guide to the eye.

One hypothesis for the cause of the differences could be that a jammed state of hydrodynamic clusters is formed, as for instance put forward by Farr and co-workers [49]. Because the particles have more or less fixed positions in such system-spanning clusters, the particle displacements may be smaller than in an unjammed state. It can be expected that system size will be of large influence on the jamming transition. We did however not find these effects when varying the distance between the two moving walls. Therewith, this hypothesis is less likely to be the cause for the differences in shear-induced diffusivity.

Another reason might be in the occurrence of short-range multi-particle interactions. In our code, multi-particle interactions are solved by pair-wise calculation of the interaction effects, which are successively calculated for all particle pairs. The problem does not seem to be in the pair-wise calculation itself, because this would not lead to an effect of the particle radius as shown in Figure 2.7. It may however be that the solution of the short-range multi-particle interactions in our code is too inaccurate because of the ragged particle surface. This explanation is in line with the observed effect of the particle radius and our hypothesis based on the viscosity results. Because of the relative close approach of particles in 3D systems, this problem might be more pronounced in 3D than in 2D systems.

Since the inaccuracy is found to increase with ϕ , it can be expected that for volume fractions higher than 0.20, even larger particles are required. However, a particle radius of 14 would already require about 2000 times more CPU time than 2D simulations, while

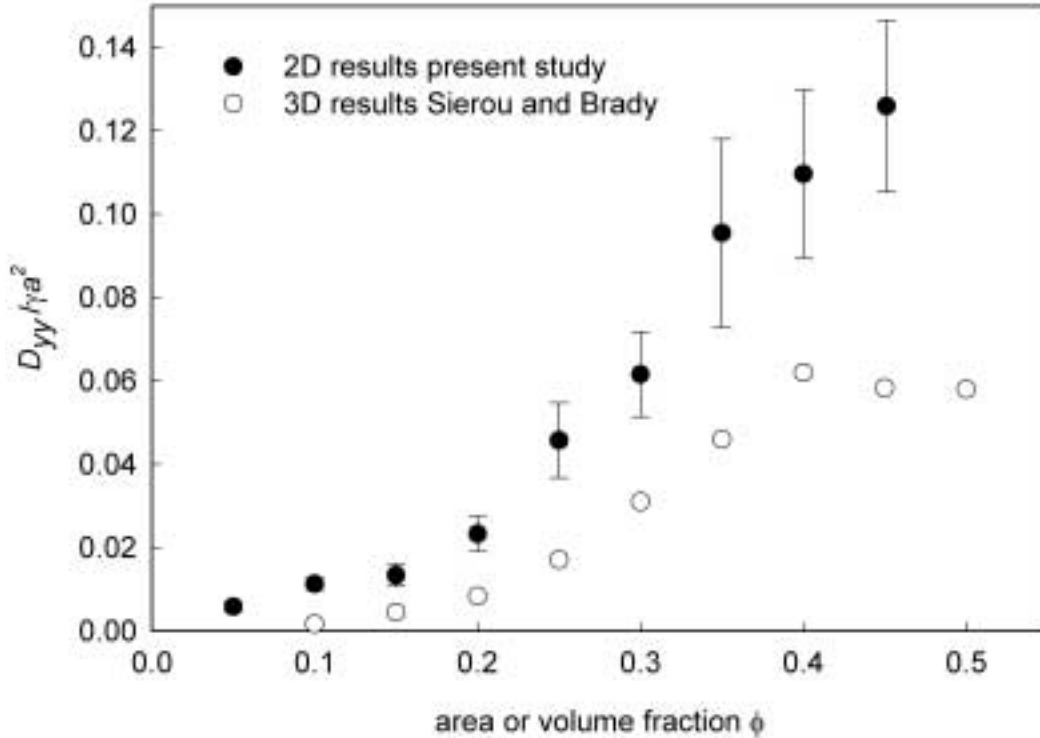


Figure 2.8: Component D_{yy} of the shear-induced self-diffusion coefficient as a function of the cylinder area fraction for a 2D suspension ($N = 200$) in shear flow at $Re_{shear,p} = 0.023$. The open symbols represent the relation found by Sierou and Brady [27] for a 3D system with spheres instead of cylinders.

the CPU time would increase with a factor of about 25000 for a particle radius of 20. Even on advanced supercomputers, one would run into problems with these requirements.

The 2D results on shear-induced diffusivity are presented in figure 2.8. These results were not found to be dependent on the particle size within a range of plus or minus 25%. We can thus conclude that, similar to the viscosity results, the 2D results for shear-induced diffusion are less sensitive to inaccuracy in the particle representation on the grid. At area fractions higher than 0.45 however, very large standard deviations were found, which may be caused by comparable reasons as mentioned above for 3D systems, namely formation of a jammed state or inaccuracies in the calculation of the short-range multi-particle interactions. Therefore, we limited the results up to an area fraction of 0.45.

The relation between shear-induced diffusivity and ϕ is clearly different from the 3D relation. For volume fractions lower than 0.25, the 2D shear-induced diffusivity was around three times higher, and at higher fractions around two times. In order to better understand these differences and to be able to translate 2D results into 3D results, we have developed an analytical model for shear-induced diffusivity. This model is discussed in the next section.

Analytical model for 2D-3D scaling

We used an analytical model for shear-induced diffusion (an adapted version of the model that was originally published by Breedveld [50]), which is based on a simple collision mechanism.

Our simple collision model, described in appendix 2.7, approaches self-diffusion in a similar way as Leighton and Acrivos [15] did. It describes the movement of individual particles in a homogeneous suspension and shear field under the action of excluded volume effects that are caused by interactions with neighbouring particles on different streamlines in the shear flow. The particle motion during each encounter is described as a deterministic process, but it is assumed that this can lead to diffusive behaviour in systems with many particles and random initial positions. An encounter of particles is modelled as an effective two-particle collision process, which proceeds unhindered until it is terminated by the presence of a third neighbouring particle. Without the presence of a third neighbouring particle, the collision is ended when the angle $\theta = \pi$ is reached (see figure in appendix 2.7), which does not result in a net displacement of the colliding particle. This is consistent with the shear flow trajectories that are obtained in the symmetric problem of two colliding ideal hard spheres [21]. When particle concentrations are high, the average time between subsequent collisions is shorter than the time needed to complete the interaction and then the collisions end when interaction with a third incoming particle occurs. Under these model assumptions, in a following step, particle trajectories are calculated as a function of initial particle positions and finally, averaging the displacements over all configurations provides a measure for shear-induced self-diffusion. It is clear that the model will be valid for a restricted range of particle fractions. This range is determined by factors such as the presence of two-particle interactions and the homogeneity of the suspension. In previous work [39], we have seen that particles in an inhomogeneous suspension can have an increased shear-induced diffusivity. But, although the model is simplistic in that it does not at all consider complex hydrodynamics, it provides interesting insights into the nature of the microscopic processes that could be responsible for shear-induced self-diffusion, even more because the model does not contain adjustable parameters.

With our collision model, the components D_{xx} , D_{yy} , D_{zz} and D_{xy} of the diffusion tensor have been calculated for a 3D system (figure 2.9). The calculated values for the components D_{yy} and D_{zz} are almost a factor 4 lower than most experimental data (see e.g. [17, 18]). The latest numerical results, calculated with ASD, are however a factor 2 lower than experimental data; it was postulated by the authors that discrepancies are due to analysing over too short strains in the experiments [27].

A feature that seems to be captured well by the collision model is the volume fraction dependence. D_{yy} and D_{zz} level off for volume fractions above 25%. In the model, this is due to the fact that above this critical concentration, the average duration of an interaction is shorter than needed for the completion of the trajectory to $\theta = \pi$. The diffusion components D_{yy} and D_{zz} reach a plateau value at a volume fraction of 25%. This is due to the fact that the decrease in displacement at a higher volume fraction is exactly balanced by the increase in collision frequency, resulting in constant diffusion coefficients. Such a plateau value for D_{yy} and D_{zz} is also found in experiments, although at a somewhat higher volume fraction of around $\phi = 0.35$. Only Sierou and Brady [27] found a plateau value for D_{yy} as well as D_{zz} in their latest model calculations with the ASD technique.

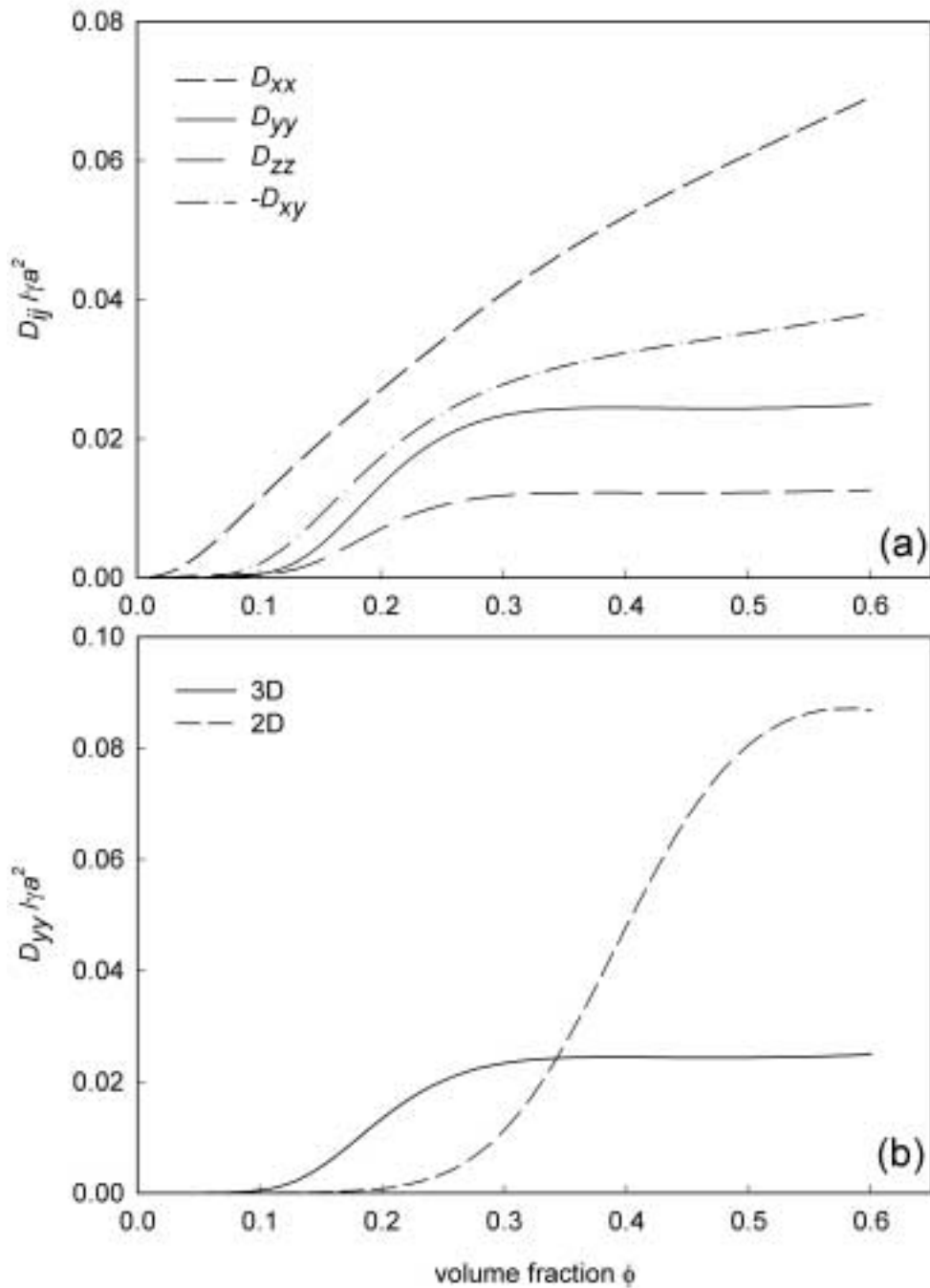


Figure 2.9: The components D_{xx} , D_{yy} , D_{zz} and D_{xy} of the diffusion tensor for a 3D system, as calculated from the collision model (part a) and D_{yy} for a 2D system as compared to a 3D system (part b).

Most model predictions however do not show a plateau value at all.

The anisotropy D_{yy}/D_{zz} between the velocity gradient and vorticity direction is equal to 2 in our model. The value of 2 agrees well with experimentally observed values for the anisotropy D_{yy}/D_{zz} . Although only a limited number of results on D_{xx} and D_{xy} is available in literature, the results of our collision model exhibit large differences with these results. Particularly the volume fraction dependence is different in our model results. The negative sign of D_{xy} is however correctly predicted. Since considerable debate still exists on the magnitudes of D_{xx} and D_{xy} , it is hard to assess the accuracy of the model predictions; more elucidation is needed.

For a 2D system, the collision model predicts a different volume fraction dependence of D_{yy} than for a 3D system (figure 2.9b). For 2D, D_{yy} starts to increase at an area fraction between 0.2 and 0.3. After it has started increasing however, the diffusion component D_{yy} not only increases faster with the area/volume fraction, but it also reaches its plateau value at a critical area fraction, which is two times higher than for a 3D system. Moreover, at area fractions above the critical value, the diffusion component shows a decrease instead of staying at a constant level. A relevant factor for these differences is the collision rate per particle. In a 2D system, the collision rate per particle at a certain fraction is two times smaller than in a 3D system. On the other hand, the average displacement during a collision is larger because the angle φ is equal to 0 in 2D systems, resulting in the maximal value of 1 for $\cos(\varphi)$. The combination of these two effects leads to a somewhat steeper increase of D_{yy} with the area/volume fraction than in 3D systems, although the difference is not large. The lower collision rate per particle in 2D systems is also relevant for the onset concentration of D_{yy} and the critical concentration where levelling off occurs. The onset concentration is directly related to the collision rate, because it is determined by the point where a two particle collision starts to be disturbed by a third particle. For the critical concentration, the average collision time is also important. Since the average time needed for a collision does not differ much between 2D and 3D systems, the smaller collision rate causes a shift of the critical concentration from 0.25 to about 0.50 in 2D systems. At higher concentrations in 2D systems, the effect of decreasing displacement is larger than the effect of increasing collision rate, leading to a net decrease of D_{yy} .

Based on this understanding, our expectations for 2D systems are that at relatively low area fractions, the shear-induced diffusion component D_{yy} is smaller than for 3D systems. At area fractions above 0.25, the 2D diffusion component can become up to a factor 3.5 higher, due to the difference in area/volume fraction dependence. A normalisation was carried out by dividing the area or volume fraction by ϕ^* , the fraction where the diffusivity has reached half of the maximal value ($0.5D_{\max}$), and by dividing the diffusivity by its maximal value (D_{\max}) (Figure 2.10). As a result, the normalised 2D and 3D values of the collision model nicely coincide with each other. The same procedure has been carried out on the 2D and 3D simulation results, but here, because the collision model did not capture the $D_{yy} - \phi$ relation well, the normalisation parameters were derived from the simulation results itself. In this way, a good agreement is found between the normalised data of our 2D LB simulations and the 3D Stokesian dynamics simulations of Sierou and Brady [27]. This indicates that the 2D-3D scaling relation as determined from the collision model, is suited for the translation of (future) 2D simulation results to 3D. In this way, computationally intensive 3D simulations can be avoided.

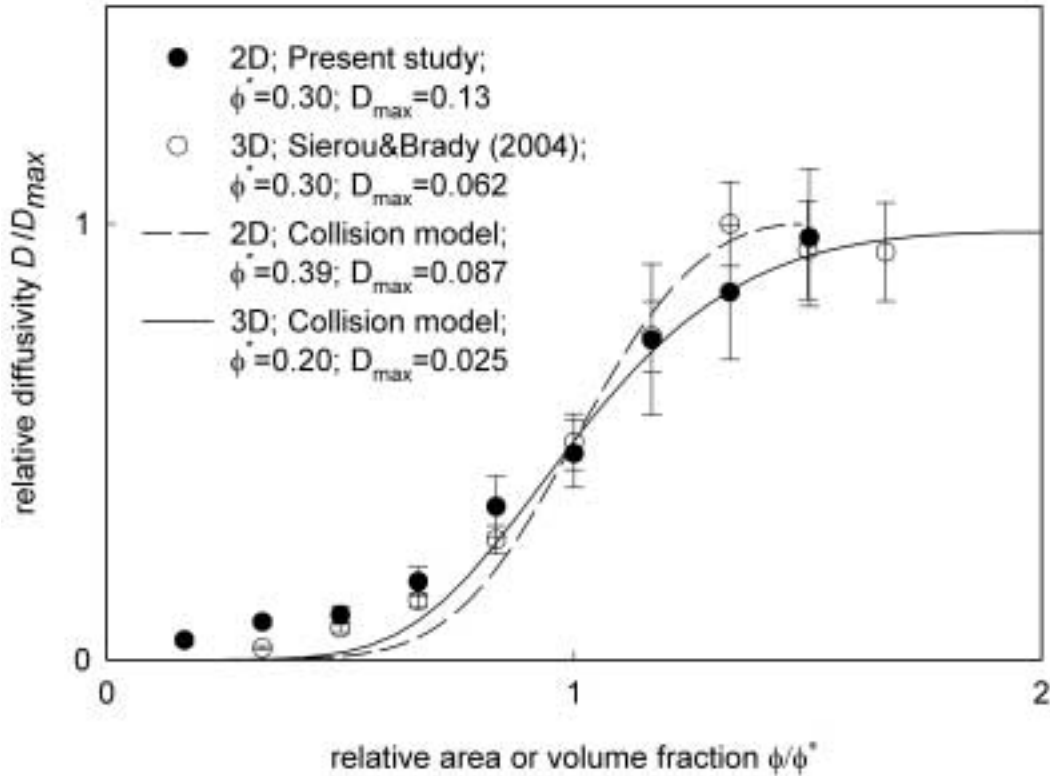


Figure 2.10: Comparison of the shear-induced diffusivity as predicted by the collision model and by computer simulation. The shear-induced diffusivity D_{yy} and the area or volume fraction ϕ are normalised following scaling rules derived from the results of the collision model. The values for ϕ^* and D_{max} are determined separately for each curve from the results presented in Figure 2.7 and 2.9. For the 2D results of the present study, the value for D_{max} is derived from D_{yy} at ϕ^* .

2.5 Conclusions

In this study, we have analysed the flow behaviour of suspensions subjected to Couette flow, making use of the LB method. The focus was on a comparison of the flow behaviour of 2D and 3D suspensions. Since computations on 3D suspensions can computationally be very intensive, it is investigated whether and when it is advantageous to carry out computations on 2D suspensions and translate these results to 3D suspensions with the help of scaling relations.

We have found particle structuring near the walls in both 2D and 3D suspensions. The thickness of the structuring layer was thinner for 3D suspensions, which is in accordance with wall effects in 2D and 3D single particle systems. Wall slip was found in both systems as well, and was more intensive in 3D systems and at higher concentrations. An important consequence of the differences between 2D and 3D is that when one is interested in the bulk particle behaviour, in the 2D system, a larger system size should be chosen than in a 3D system.

For computation of the viscosity and shear-induced diffusion, limitations are found in

the maximum volume fraction of particles that gives accurate results; these limitations are found to be related to the grid size of the suspended particles. In 3D systems, for a particle radius of 8 lattice units, the inaccuracy became evident at ϕ larger than 0.30 (viscosity) or larger than 0.15 (shear-induced diffusion), which is at much lower concentrations than in 2D systems. This sensitivity of 3D systems to inaccuracy is probably related to the closer approach distance of two interacting particles in shear flow and may be caused by inaccuracy, introduced by the particle discretisation on the grid.

Because of the very large particle grid sizes, necessary to obtain accurate results for 3D systems, only advanced supercomputers are currently suited for LB computations on 3D systems, while the computations on 2D systems can be carried out well on a single processor or on small computer clusters. Therefore, adequate scaling relations would be helpful to translate 2D simulation results to 3D systems. For the viscosity, such scaling relations are already known, and we were able to reproduce those in our LB simulations. For shear-induced diffusion, we have developed an analytical collision model, which is able to predict qualitatively correct shear-induced diffusivities, and which captures the scaling between 2D and 3D well.

This study shows that the feasibility of 3D LB simulations is restricted to smaller parameter domains than 2D simulations. With the use of relatively simple, linear scaling rules, it proved possible to translate 2D simulation results to 3D real systems, which opens the way to employ the LB method for unexplored aspects of suspension flow in Couette systems, such as particle polydispersity and high Reynolds number flow, with large relevance to practical processing of suspensions.

Acknowledgements

Friesland Foods is greatly acknowledged for supporting this research. Prof Dr Mike Cates and Dr Kevin Stratford from Edinburgh University are greatly thanked for fruitful discussions. The authors would like to acknowledge the support of the Dutch Ministries of Economic Affairs, Education, Culture and Sciences and of Housing, Spatial Planning and the Environment through a grant of the Dutch Program Economy, Ecology and Technology and the support of the European Commission through grant number HPRI-CT-1999-00026 (the TRACS Programme at EPCC).

2.6 Lubrication force in a 2D suspension

We apply lubrication theory to calculate the hydrodynamic force between two cylinders in a 2D suspension. For small gaps (i.e. rim to rim distances) $2h$ the force between two adjacent cylinders can be calculated, solving the flow field in the gap upto first order in $\epsilon = h/a$. In the calculation two cylinders are considered, approaching each other with a velocity $2U$. A Cartesian coordinate system ($\mathbf{e}_x, \mathbf{e}_z$) was used with the origin at the center of the gap. The z -coordinate, taken along the line of centers, was scaled on h and the x -coordinate was scaled on \sqrt{ah} ; the z -component of the velocity was scaled on U , the x -component on $\sqrt{a/h}U$. The pressure was scaled on $a\eta U/h^2$. Under these conditions

the differential equation for the dimensionless stream function ψ becomes:

$$\frac{\partial^4 \psi}{\partial z^4} + 2\epsilon \frac{\partial^4 \psi}{\partial x^2 \partial z^2} + \epsilon^2 \frac{\partial^4 \psi}{\partial x^4} = 0 \quad (2.6.1)$$

The rim of both disks is described by $z = \pm b(x)$ with

$$b(x) = 1 + \frac{1}{2}x^2 + \epsilon \frac{1}{8}x^4 + \epsilon^2 \frac{1}{16}x^6 + \dots \quad (2.6.2)$$

and the boundary conditions on these rims read:

$$v_z = - \frac{\partial \psi}{\partial x} = \mp 1, \quad (2.6.3)$$

$$v_x = \frac{\partial \psi}{\partial z} = 0, \quad (2.6.4)$$

For convenience $\psi = 0$ is chosen at $z = 0$, so ψ is odd in z . This equation can be solved assuming

$$\psi = \psi_0 + \epsilon \psi_1 + \dots \quad (2.6.5)$$

where ψ_0 fulfills the boundary conditions (2.6.3) and (2.6.4) and $\partial \psi_1 / \partial x = \partial \psi_1 / \partial z = 0$ on the rim of the particle. The solution is given by:

$$\psi_0 = \frac{1}{2}x \left(3 \left(\frac{z}{b} \right) - \left(\frac{z}{b} \right)^3 \right) \quad (2.6.6)$$

$$\psi_1 = \frac{3}{20}g(x) \left(\frac{z}{b} \right) \left(1 - \left(\frac{z}{b} \right)^2 \right)^2 \quad (2.6.7)$$

where $g(x) = 4x(b')^2 - 2bb' - xbb''$ and b' , b'' are the first and second derivative of $b = b(x)$, respectively. The pressure along the line $z = 0$ can be calculated by integrating:

$$\left(\frac{\partial p}{\partial x} \right)_{z=0} = -3b^{-3} \left(x + \epsilon \left(\frac{3}{5}g(x) - \frac{1}{2}f(x) \right) \right) \quad (2.6.8)$$

where $f(x) = 2x(b')^2 - 2bb' - xbb''$. The zz -component of the total stress tensor (the superfix $^{[D]}$ indicates the dimensional form)

$$T_{zz}^{[D]} = -p^{[D]} + 2\eta \frac{\partial v_z^{[D]}}{\partial z^{[D]}}$$

reads in dimensionless form

$$T_{zz} = -p + 2\epsilon \frac{\partial v_z}{\partial z} = -p - 2\epsilon \frac{\partial^2 \Psi}{\partial x \partial z}$$

where also T_{zz} has been scaled on $p_0 = a\eta U/h^2$. The (dimensionless) force per unit length, F , on the particle is calculated by integrating T_{zz} along the line $z = 0$ (with swapping the order of integration of the $\partial p / \partial x$ term):

$$\begin{aligned} F(\epsilon) &= 2 \int_0^\infty (T_{zz})_{z=0} dx \quad (2.6.9) \\ &= 2 \int_0^\infty x \left(\frac{\partial p}{\partial x} \right)_{z=0} dx - 4\epsilon \int_0^\infty \left(\frac{\partial^2 \Psi}{\partial x \partial z} \right)_{z=0} dx \\ &= \int_0^\infty \frac{3x}{b^3(x)} \left(2x + \epsilon \left(\frac{6}{5}g(x) - f(x) \right) \right) dx - 4\epsilon \int_0^\infty \frac{3}{2b^2}(b - xb') dx \end{aligned}$$

This expression can be rewritten as:

$$F(\epsilon) = F_0 + \epsilon(F_1 - F_2)$$

where

$$\begin{aligned} F_0 &= \int_0^\infty \frac{6x^2}{(1 + \frac{1}{2}x^2)^3} dx = \frac{3}{4}\pi\sqrt{2} = 3.3322 \\ F_1 &= \int_0^\infty \frac{3x}{(1 + \frac{1}{2}x^2)^3} \left(\left(\frac{25}{10}x^3 - \frac{3}{5}x - \frac{6x^5}{(8 + 4x^2)} \right) \right) dx = \frac{207}{80}\pi\sqrt{2} = 11.496 \\ F_2 &= \int_0^\infty 6 \frac{(1 - \frac{1}{2}x^2)}{(1 + \frac{1}{2}x^2)^2} dx = 0.0 \end{aligned}$$

are numerical constants. In our simulations, we have erroneously used a value of $F_1 = 12.829$, which lead to about 1% overestimation of the lubrication force. The lubrication force per unit length in dimensional form, $F^{[D]} = p_0\sqrt{ah}F$, follows from Equation 2.6.10 as:

$$F^{[D]} = \left(\frac{h}{a}\right)^{-3/2} \eta U F(h/a) = \left(\frac{h}{a}\right)^{-3/2} \eta U \left(F_0 + \frac{h}{a}F_1\right) \quad (2.6.10)$$

which expression is correct to the first order of ϵ .

2.7 Analytical model for shear-induced diffusion

2.7.1 The collision frequency of the particle in 3D

Consider a simple shear field in which the velocity of the fluid (in Cartesian coordinates) is given by:

$$\mathbf{v} = \dot{\gamma}y\mathbf{e}_x \quad (2.7.1)$$

so the x-direction is the velocity direction, the y-direction along the gradient and the z-direction along the vorticity direction. A collision takes place when two particles touch each other: $r_{ij} = p = a_i + a_j$, where a_i is the radius of particle (i).

Using spherical coordinates (r, ϑ, φ) (see Figure 2.11) and the unit vectors:

$$\begin{aligned} \mathbf{e}_r &= -\cos \vartheta \mathbf{e}_x + \sin \vartheta \mathbf{e}_s \\ \mathbf{e}_\vartheta &= \sin \vartheta \mathbf{e}_x + \cos \vartheta \mathbf{e}_s \\ \mathbf{e}_\varphi &= -\sin \varphi \mathbf{e}_y + \cos \varphi \mathbf{e}_z \end{aligned} \quad (2.7.2)$$

where \mathbf{e}_s is defined by:

$$\mathbf{e}_s = \cos \varphi \mathbf{e}_y + \sin \varphi \mathbf{e}_z \quad (2.7.3)$$

the relative position between two particles is given by:

$$\mathbf{r}_{rel} = p(-\cos \vartheta \mathbf{e}_x + \sin \vartheta \mathbf{e}_s) \quad (2.7.4)$$

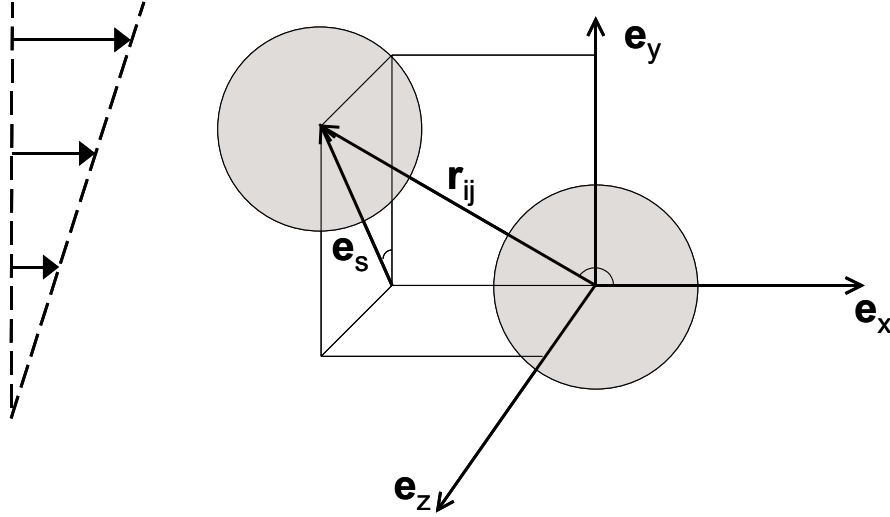


Figure 2.11: Geometry for describing a typical collision.

and the relative velocity before collision by:

$$\mathbf{v}_{rel} = \dot{\gamma} p \sin \vartheta \cos \varphi \mathbf{e}_x \quad (2.7.5)$$

We consider a monodisperse suspension with volume fraction ϕ of particles with radius a . The particle flux onto the surface of a tagged particle can be estimated as:

$$\mathbf{j} = n \mathbf{v}_{rel} = 2na\dot{\gamma} \sin \vartheta_o \cos \varphi_o \mathbf{e}_x \quad (2.7.6)$$

where n is the number density of the particles in the suspension. ϑ_o and φ_o define the orientation of the colliding particles. The collision rate in a certain space angle $d\dot{N}_c/d\Omega$ is given by:

$$d\dot{N}_c = -n \mathbf{v}_{rel} \cdot (2a)^2 d\Omega \mathbf{e}_r \quad (2.7.7)$$

$$\frac{d\dot{N}_c}{d\Omega} = 8na^3 \dot{\gamma} \cos \varphi_o \sin \vartheta_o \cos \vartheta_o \quad (2.7.8)$$

and the total collision rate:

$$\begin{aligned} \dot{N}_c &= 2 \int_{\Omega^{(1)}} \frac{d\dot{N}_c}{d\Omega} d\Omega \\ &= \frac{12}{\pi} \phi \dot{\gamma} \int_0^{\pi/2} \sin^2 \vartheta_o \cos \vartheta_o d\vartheta_o \int_{-\pi/2}^{\pi/2} \cos \varphi_o d\varphi_o \\ &= \frac{8}{\pi} \dot{\gamma} \phi \end{aligned} \quad (2.7.9)$$

where $\Omega^{(1)}$ is the space angle for which $0 < \vartheta < \pi/2$ and $-\pi/2 < \varphi < \pi/2$. The probability that a given collision occurs with orientation (ϑ_o, φ_o) or $(\pi - \vartheta_o, \pi + \varphi_o)$ is given by the function $\Phi(\vartheta_o, \varphi_o)$:

$$\Phi(\vartheta_o, \varphi_o) = \frac{\left(\frac{d\dot{N}_c}{d\Omega} \right)}{\int_{\Omega^{(1)}} \left(\frac{d\dot{N}_c}{d\Omega} \right) d\Omega} = \frac{3}{2} \cos \varphi_o \cos \vartheta_o \sin \vartheta_o \quad (2.7.10)$$

and the mean time, τ , between two collisions of particle 1 with another particle follows from Equation 2.7.9:

$$\tau = 1/\dot{N}_c = \frac{\pi}{8\dot{\gamma}\phi} \quad (2.7.11)$$

2.7.2 The collision frequency of a particle in 2D

In 2D the collision rate under a certain angle $d\dot{N}_c/d\vartheta$ is given by:

$$d\dot{N}_c = -n\mathbf{v}_{rel} \cdot 2ad\vartheta \mathbf{e}_r \quad (2.7.12)$$

$$\frac{d\dot{N}_c}{d\vartheta} = 4na^2\dot{\gamma} \sin \vartheta_o \cos \vartheta_o \quad (2.7.13)$$

and the total collision rate:

$$\begin{aligned} \dot{N}_c &= 2 \int_0^{\pi/2} \frac{d\dot{N}_c}{d\vartheta} d\vartheta = \frac{8}{\pi} \phi \dot{\gamma} \int_0^{\pi/2} \sin \vartheta_o \cos \vartheta_o d\vartheta_o \\ &= \frac{4}{\pi} \dot{\gamma} \phi \end{aligned} \quad (2.7.14)$$

hence, in 2D

$$\Phi(\vartheta_o) = 2 \cos \vartheta_o \sin \vartheta_o \quad (2.7.15)$$

and

$$\tau = 1/\dot{N}_c = \frac{\pi}{4\dot{\gamma}\phi} \quad (2.7.16)$$

2.7.3 The displacement of the particle in a collision

To describe the displacement of a particle (i) during a collision with particle (j) we describe the collision with respect to the center of resistance of the two colliding particles. The initial position of particle (i) is given by ϑ_o, φ_o (in 2D: $\varphi_o = 0$): $\mathbf{r}_{cm} = a(-\cos \vartheta_o \mathbf{e}_x + \sin \vartheta_o \mathbf{e}_s(\varphi))$. To obtain a simple collision rule we assume affine motion of the particles as not prohibited by excluded volume effects. When the particles become into contact they roll over each other in the xs -plane. Under this assumption the velocity during the collision, $\vartheta_o \leq \vartheta \leq \vartheta_1$, is:

$$\begin{aligned} \mathbf{v} &= \mathbf{v}_\infty \cdot (\mathbf{I} - \mathbf{e}_r \mathbf{e}_r) \\ &= a\dot{\gamma} \cos \varphi_o \sin^2 \vartheta (\sin \vartheta \mathbf{e}_x + \cos \vartheta \mathbf{e}_s) \end{aligned} \quad (2.7.17)$$

while the undisturbed velocity would be given by:

$$\mathbf{v}_\infty = a\dot{\gamma} \cos \varphi_o \sin \vartheta \mathbf{e}_x \quad (2.7.18)$$

The angular speed $\dot{\vartheta}$ is given by: $\dot{\vartheta} = \dot{\gamma} \cos \varphi_o \sin^2 \vartheta$ so the time a collision takes, is given by:

$$\Delta t = \frac{1}{\dot{\gamma} \cos \varphi_o} \int_{\vartheta_o}^{\vartheta_1} \frac{d\vartheta}{\sin^2 \vartheta} = \frac{(\cot \vartheta_o - \cot \vartheta_1)}{\dot{\gamma} \cos \varphi_o} \quad (2.7.19)$$

where ϑ_1 is the value of ϑ at which the collision stops, $\vartheta_1 = \pi - \vartheta_0$, or is taken over by the next collision:

$$\cot \vartheta_1 = \begin{cases} -\cot \vartheta_0 & \left(\frac{2 \cot \vartheta_0}{\dot{\gamma} \cos \varphi_o} \leq \tau \right) \\ \cot \vartheta_0 - \dot{\gamma} \tau \cos \varphi_o & \left(\frac{2 \cot \vartheta_0}{\dot{\gamma} \cos \varphi_o} > \tau \right) \end{cases} \quad (2.7.20)$$

Assuming a collision stops at a certain angle ϑ_1 irrespective of the initial values of ϑ_0 and φ_o , the average collision time in 3D is calculated as:

$$\begin{aligned} \langle \Delta t \rangle &= 3 \int_0^{\pi/2} \int_0^{\pi/2} \frac{(\cot \vartheta_0 - \cot \vartheta_1)}{\dot{\gamma} \cos \varphi_o} \cos \varphi_o \cos \vartheta_o \sin^2 \vartheta_o d\vartheta_o d\varphi_o \\ &= \frac{\pi}{2\dot{\gamma}} (1 - \cot \vartheta_1) \end{aligned} \quad (2.7.21)$$

and in 2D as:

$$\begin{aligned} \langle \Delta t \rangle &= 2 \int_0^{\pi/2} \frac{(\cot \vartheta_0 - \cot \vartheta_1)}{\dot{\gamma}} \cos \vartheta_o \sin \vartheta_o d\vartheta_o \\ &= \frac{1}{\dot{\gamma}} \left(\frac{\pi}{2} - \cot \vartheta_1 \right) \end{aligned} \quad (2.7.22)$$

The displacement $\Delta \mathbf{r}$ can be obtained from integration, from time 0 to τ , of the velocity (Equation 2.7.17):

$$\begin{aligned} \Delta \mathbf{r} &= \int_0^{\Delta t} \mathbf{v}(\vartheta, \varphi_o) dt + \int_{\Delta t}^{\tau} \mathbf{v}_{\infty}(\vartheta_1, \varphi_o) dt + \mathbf{v}_{cm} \tau \\ &= a \int_{\vartheta_0}^{\vartheta_1} (\sin \vartheta \mathbf{e}_x + \cos \vartheta \mathbf{e}_s(\varphi_o)) d\vartheta + \int_{\Delta t}^{\tau} a \dot{\gamma} \cos \varphi_o \sin \vartheta_1 \mathbf{e}_x dt + \mathbf{v}_{cm} \tau \end{aligned}$$

where \mathbf{v}_{cm} is given by:

$$\mathbf{v}_{cm} = \dot{\gamma} (y_0 - a \sin \vartheta_0 \cos \varphi_o) \mathbf{e}_x$$

The stochastic part of the displacement \mathbf{s} can be obtained by subtraction of the convective contribution to $\Delta \mathbf{r}$:

$$\Delta \mathbf{r}_c = \frac{1}{2} \dot{\gamma} \tau (y_0 + y_1) \mathbf{e}_x$$

which results in:

$$\begin{aligned} \mathbf{s} &= \int_0^{\Delta t} \mathbf{v}(\vartheta, \varphi_o) dt + \int_{\Delta t}^{\tau} \mathbf{v}_{\infty}(\vartheta_1, \varphi_o) dt + \dot{\gamma} \tau (y_0 - a \sin \vartheta_0 \cos \varphi_o) \mathbf{e}_x - \\ &\quad \frac{1}{2} \dot{\gamma} \tau (y_0 + y_1) \mathbf{e}_x \end{aligned}$$

In these expressions Δt is given by: $\Delta t = \min \{ \tau, (2 \cot \vartheta_0) / (\dot{\gamma} \cos \varphi_o) \}$. Hence, for $\left(\frac{2 \cot \vartheta_0}{\dot{\gamma} \cos \varphi_o} \leq \tau \right)$ one obtains:

$$\mathbf{s} = 0$$

and for ($\frac{2 \cot \vartheta_0}{\dot{\gamma} \cos \varphi_o} > \tau$):

$$\begin{aligned} \mathbf{s}/a = & [\sin \vartheta_1 - \sin \vartheta_0] \mathbf{e}_s + [\cos \vartheta_0 - \cos \vartheta_1 - \\ & \frac{1}{2} (\sin \vartheta_0 + \sin \vartheta_1) (\cot \vartheta_0 - \cot \vartheta_1) \mathbf{e}_x \end{aligned} \quad (2.7.23)$$

where we have used:

$$\dot{\gamma} \tau \cos \varphi_o = \cot \vartheta_0 - \cot \vartheta_1$$

(in 2D the obtained expressions for the displacements are valid if one substitutes $\varphi_o = 0$).

2.7.4 The self-diffusion tensor

The self-diffusion tensor \mathbf{D} for a particle can be calculated from:

$$\mathbf{D} = \frac{\langle \mathbf{s} \mathbf{s} \rangle}{2\tau} \quad (2.7.24)$$

The averaging has to be done with the weight function Φ (Equation 2.7.10) in the following way:

$$\langle \mathbf{s} \mathbf{s} \rangle = \int_{-\pi/2}^{\pi/2} \int_0^{\pi/2} (\mathbf{s} \mathbf{s}) \Phi(\vartheta_o, \varphi_o) \sin \vartheta_o d\vartheta_o d\varphi_o \quad (2.7.25)$$

$$= 3 \int_0^{\pi/2} \int_0^{\pi/2} (\mathbf{s} \mathbf{s}) \sin^2 \vartheta_o \cos \vartheta_o d\vartheta_o \cos \varphi_o d\varphi_o \quad (2.7.26)$$

The diad $(\mathbf{s} \mathbf{s})$ is for $\Delta t = (2 \cot \vartheta_0) / (\dot{\gamma} \cos \varphi_o) < \tau$ given by:

$$\begin{aligned} \langle \mathbf{s} \mathbf{s} \rangle &= a^2 \langle \tilde{\mathbf{s}} \tilde{\mathbf{s}} \rangle \\ \langle \tilde{\mathbf{s}} \tilde{\mathbf{s}} \rangle &= 3 \int_0^{\pi/2} \int_0^{\vartheta_m(\varphi_o)} (\tilde{\mathbf{s}} \tilde{\mathbf{s}}) \sin^2 \vartheta_o \cos \vartheta_o d\vartheta_o \cos \varphi_o d\varphi_o \end{aligned}$$

where $\vartheta_m(\varphi_o) = \arctan(16\phi / (\pi \cos \varphi_o))$. The dyad $(\tilde{\mathbf{s}} \tilde{\mathbf{s}})$ is given by:

$$\begin{aligned} \tilde{\mathbf{s}} = & [\sin \vartheta_1 - \sin \vartheta_0] \mathbf{e}_s + [\cos \vartheta_0 - \cos \vartheta_1 - \\ & \frac{1}{2} (\sin \vartheta_0 + \sin \vartheta_1) (\cot \vartheta_0 - \cot \vartheta_1) \mathbf{e}_x \end{aligned} \quad (2.7.27)$$

with

$$\cot \vartheta_1 = \cot \vartheta_0 - \frac{\pi \cos \varphi_o}{8\phi}$$

Finally one obtains an expression for the diffusion tensor:

$$\mathbf{D} = \dot{\gamma} a^2 \frac{4\phi}{\pi} \langle \tilde{\mathbf{s}} \tilde{\mathbf{s}} \rangle \quad (2.7.28)$$

Using Equations 2.7.27 and 2.7.28 all the components of the self-diffusion tensor can be calculated. In the 2D calculations no φ dependence exists and the weight function Φ is given by Equation 2.7.15, while in the expressions for the displacements one has to replace φ_o by 0.

**Shear-induced self-diffusion and
microstructure in non-Brownian
suspensions at non-zero Reynolds
numbers**

This paper addresses shear-induced self-diffusion in a monodisperse suspension of non-Brownian particles in Couette flow, by two-dimensional computer simulations following the Lattice Boltzmann method. This method is suited for the study of (many-particle) particulate suspensions and can not only be applied for Stokes flow, but also for flow with finite Reynolds number.

At relatively low shear particle Reynolds numbers ($Re_{\text{shear,p}}$) (up to 0.023), shear-induced diffusivity exhibited a linear dependence on the shear rate, as expected from theoretical considerations. Simulations at $Re_{\text{shear,p}}$ between 0.023 and 0.35, however, revealed that in this regime, shear-induced diffusivity did not show this linear dependence anymore. Instead, the diffusivity was found to increase more than linearly with the shear rate, an effect that was most pronounced at lower area fractions of 0.10 and 0.25.

In the same shear regime, major changes were found in the flow trajectories of two interacting particles in shear flow (longer and closer approach) and in the viscosity of the suspension (shear thickening). Moreover, the suspended particles exhibited particle clustering. The increase of shear-induced diffusivity is shown to be directly correlated with this particle clustering. As for shear-induced diffusivity, the effect of increasing shear rates on particle clustering was the most intensive at low area fractions of 0.10 and 0.25, where the radius of the clusters increased from about 4 to about 7 particle radii with an increase of the $Re_{\text{shear,p}}$ from 0.023 to 0.35. The importance of particle clustering to shear-induced diffusion might also indicate the importance of other factors that can induce particle clustering, such as, for example, colloidal instability.

3.1 Introduction

In concentrated non-Brownian suspensions, shear-induced diffusion affects the motion of the suspended particles and is consequently of major importance for the flow behaviour of these suspensions. A variety of interesting rheological phenomena in concentrated suspensions is invoked by shear-induced diffusion, such as viscous resuspension (during sedimentation and cross-flow filtration) and particle segregation in radial and pipe flow (see e.g. [51, 52]). Therefore, this subject has attracted considerable attention from researchers, starting with the first direct experimental study of Eckstein, Bailey and Shapiro in 1977 [14]. Later, theoretical as well as numerical work followed (see e.g. [26, 53]).

In contrast to the more familiar diffusion concepts of Brownian diffusion and turbulent diffusion, which are, respectively, caused by thermal fluctuations and inertial effects, shear-induced diffusion is caused by hydrodynamic particle-particle interactions. The diffusivity of the particles is the result of the spatial hindrance that they experience in a concentrated suspension which is macroscopically forced to flow. Although this process in principle is a deterministic process, it can be described as a diffusion process owing to the complex nature of the hydrodynamics.

A distinction can be made between shear-induced self-diffusion and shear-induced gradient diffusion (or migration). The first concept considers the motion of individual particles in a homogeneous suspension, whereas the latter considers collective particle migration in the presence of a gradient. This paper addresses the concept of shear-induced self-diffusion only.

To obtain information about shear-induced self-diffusion, the motion of individual particles in a suspension must be monitored. Experimental work is mostly carried out with the use of tracer particles in a suspension. An overview of experimental data on shear-induced self-diffusion is given in two articles of Breedveld and co-workers [17, 18]. Unfortunately, experimental techniques mostly impose severe limitations on the range of strain values during which the particles can be monitored, which complicates the work on shear-induced self-diffusion considerably. Theoretical analyses and numerical computations can therefore be helpful for comparison and for information that cannot be obtained with experiments.

A theoretical approach of shear-induced self-diffusion is complicated by the fact that a two-body system in the presence of only hydrodynamic interactions, either does not exhibit diffusive behaviour (for the motion parallel to the velocity gradient and vorticity directions) or exhibits singular behaviour (for the motion parallel to the fluid velocity). Approaches that have been applied to overcome this problem in the theoretical computation of shear-induced diffusion, are the introduction of an additional pair of particles [20], examination of three particle interactions [22], introduction of surface roughness on the particles [21] and introduction of residual Brownian motion and a hard-sphere inter-particle force [53]. The latter approach by Brady and Morris can be considered the most successful up to now. It predicts the correct level of anisotropy between the diffusion in the velocity gradient (D_{yy}) and vorticity (D_{zz}) direction. The calculated diffusivities are, however, a factor of about six higher than values from experimental studies. Moreover, the theory predicts a continuous increase of the diffusion coefficient with volume fraction, while experimental values level off at high volume fractions. We can therefore conclude that, in spite of the aforementioned rigorous attempts, up to now, no theory is available that satisfactorily predicts shear-induced diffusive behaviour.

Some numerical studies on shear-induced diffusion have been reported using Stokesian Dynamics (SD) simulations [25, 26, 54, 55]. Many-body hydrodynamic interactions are included in this simulation technique. The SD simulations provided self-diffusion coefficients that are of the same order of magnitude as experimental results. The computed anisotropy between D_{yy} and D_{zz} also compared well with experimental data. Although the SD simulations strongly contributed to the level of understanding of shear-induced diffusion, the results of the simulations are not uncontroversial. The dependence of the diffusion coefficient on the volume fraction, for example, is not clear. While earlier work shows a continuous increase of the diffusion coefficient with the volume fraction, recent work suggests the existence of a plateau at high volume fractions [25, 55]. This plateau was, however, only found for D_{yy} and not for D_{zz} . Another controversial aspect is the number of particles incorporated in the system. The computational costs for calculations on non-colloidal systems (dominated by hydrodynamics) are very high with SD and in most published work, systems were used with 27 particles only. Since this system size is small compared to any realistic system, the results have to be treated with care. The recent introduction of the Accelerated Stokesian Dynamics (ASD) simulation technique [56], based on a much faster computational algorithm, allows the study of large systems with typically 1000 suspension particles. Using ASD to study shear-induced self-diffusion, Sierou and Brady [27] indeed showed the relevance of high particle numbers and sufficiently high strains for reliable diffusion coefficients. Their results, covering the full diffusivity tensor, can probably be considered the most accurate up to now.

Besides the relatively high computational cost, SD, and also ASD, have other limi-

tations for the simulation of shear-induced diffusion. The suspending fluid is assumed to be Newtonian and to be flowing under conditions approximating Stokes flow (particle Reynolds number $Re_p \rightarrow 0$). Although ASD may have better possibilities, with SD, the application of non-spherical particle shapes and size distributions is complex. Moreover, it is difficult to make the method suitable for simulations in bounded regimes with container walls [33]. These aspects may be of importance to gain a better insight into shear-induced diffusion in practical systems. Therefore, although SD and ASD are robust methods that accurately resolve hydrodynamic interactions, they are not yet able to address all relevant aspects of shear-induced diffusion.

In this paper, a study on shear-induced diffusion is presented making use of a Lattice Boltzmann (LB) model for particulate suspensions [33]. This model combines Newtonian dynamics of solid particles with a discretised Boltzmann equation for the fluid phase. The many-body hydrodynamic interactions are fully accounted for (with inclusion of an explicit lubrication force for hydrodynamic interactions over very short distances). The LB model may have a number of advantages for the simulation of shear-induced diffusion over the SD model. Since the interactions between the fluid and the suspended solid particles can be calculated with simple local rules, the computational cost depends linearly on the amount of suspended particles, which makes many-particle simulations feasible. The LB model is also not restricted to the Stokes flow regime for fluid flow and can easily be applied for non-spherical particles, for particles with a size distribution and for systems bounded by container walls [33]. This may make the LB technique more suitable for the simulation of shear-induced diffusion in more complex systems, where the aforementioned aspects play a role.

The aim of this work is to examine shear-induced diffusion outside the Stokes flow regime, at finite Reynolds numbers, and investigate the effect of inertia. The fact that these conditions of finite Reynolds numbers are frequently applied in (industrial) processes of suspensions, such as milk and other foods, paints and river water, makes the relevance of this work evident. Although it is well-known that the rheological behaviour of concentrated suspensions can become non-Newtonian in this regime, as far as we know, the scaling of shear-induced diffusion with the shear rate has not been studied yet. In this study, we furthermore compare the shear-induced diffusive behaviour with the effects of shear on the flow trajectories of one particle and two interacting particles and on the viscosity of a multi-particle suspension, so as to be able to detect possible correlations. The study is carried out for two-dimensional (2D) systems in order to limit the computational costs. Although this might lead to differences in the scaling of the relations in comparison with three-dimensional systems, the trends will be similar as is presented in [78].

In section 3.2, we present an outline of our LB method for particulate suspensions. Subsequently, we show results of the shear-dependent behaviour of one (flow trajectory), two (flow trajectory) and multi-particle (viscosity) systems (section 3.3). In section 3.4, we present our results on shear-induced diffusion. As a relevant parameter, in section 3.5, an analysis is made of the suspension microstructure at different shear rates, whereafter we draw our conclusions.

3.2 Computer simulation method

We have applied the LB method in our simulations. Since this method has already been outlined extensively in literature (see e.g. [29, 33]), we will only recapitulate the most important points. The LB method models a compressible fluid (in which the speed of sound is finite) in the limit of low Mach number ($Ma = \text{flow velocity}/\text{speed of sound}$), by solving the discretised Boltzmann equation for fictitious fluid particles, that are constrained to move on a lattice. The state of the fluid is characterised by the single-particle distribution function $f_i(\mathbf{x}, t)$, describing the average number of particles at a particular node of the lattice \mathbf{x} , at a time t , with the discrete velocity \mathbf{c}_i , which brings the fluid particles in one time step to an adjacent lattice node. In the simulations described in this paper, the fluid dynamics were solved with a D2Q9 LB scheme, which is defined on a 2D square lattice with rest particles and 8 non-zero particle velocities. The velocity directions link lattice sites to its nearest and next-nearest neighbours. The velocity vectors on this 2D lattice are defined as:

$$\mathbf{c}_i = \begin{cases} (0, 0), & i = 0 \\ \left(\cos \frac{i-1}{2}\pi, \sin \frac{i-1}{2}\pi\right), & i = 1, 2, 3, 4 \\ \sqrt{2} \left(\cos \left(\frac{i-1}{2}\pi + \frac{\pi}{4}\right), \sin \left(\frac{i-1}{2}\pi + \frac{\pi}{4}\right)\right), & i = 5, 6, 7, 8 \end{cases} \quad (3.1)$$

The hydrodynamic fields mass density ρ , momentum density \mathbf{j} , and the momentum flux density Π are moments of this velocity distribution:

$$\rho = \sum_i f_i, \quad \mathbf{j} = \sum_i f_i \mathbf{c}_i, \quad \Pi = \sum_i f_i \mathbf{c}_i \mathbf{c}_i \quad (3.2)$$

The fictitious fluid particles evolve by collisions and subsequent propagation to neighbouring lattice sites. This two-step process is described by the following equations:

$$f'_i(\mathbf{x}, t) = f_i(\mathbf{x}, t) - \sum_j \Omega_{ij} f_j^{neq}(\mathbf{x}, t) \quad (3.3)$$

$$f_i(\mathbf{x} + \Delta \mathbf{x}_i, t + \Delta t) = f'_i(\mathbf{x}, t) \quad (3.4)$$

Here $f'_i(\mathbf{x}, t)$ is the post-collisional distribution function. The non-equilibrium part of the distribution function is defined as $f_i^{neq}(\mathbf{x}, t) = f_i(\mathbf{x}, t) - f_i^{eq}(\mathbf{x}, t)$. The lattice spacing is defined as $\Delta \mathbf{x}_i = \mathbf{c}_i \Delta t$. The collision operator Ω_{ij} controls the shear stress relaxation at every lattice site. In our simulations, we applied the collision operator of the Bhatnagar-Gross-Krook (BGK) model [37, 57], which is a simplification of the full LB model. The BGK collision operator is defined such that the distribution functions are simply relaxed at each time step towards the local equilibrium distribution with the relaxation time τ :

$$f_i(\mathbf{x} + \Delta \mathbf{x}_i, t + \Delta t) = f_i(\mathbf{x}, t) - \frac{f_i(\mathbf{x}, t) - f_i^{eq}(\mathbf{x}, t)}{\tau} \quad (3.5)$$

The relaxation time τ controls the relaxation of the viscous stress in the fluid and is linked to the kinematic viscosity ν via:

$$\nu = c_s^2 \left(\tau - \frac{1}{2} \right) \Delta t \quad (3.6)$$

where the speed of sound c_s is defined by $c_s^2 = c^2/3$. In our simulations we applied $\tau = 1.0$ (in lattice units), which corresponds to a kinematic viscosity ν of the fluid of $1/6$ (in lattice units). The equilibrium distribution $f_i^{eq}(\mathbf{x}, t)$ is chosen such that the Navier-Stokes equations for a weakly compressible system are obtained [36]. It can be expressed as a series expansion in powers of the flow velocity \mathbf{u} :

$$f_i^{eq} = \rho w_i \left(1 + \frac{1}{c_s^2} \mathbf{u} \cdot \mathbf{c}_i + \frac{1}{2c_s^4} \bar{\mathbf{u}}\bar{\mathbf{u}} : \bar{\mathbf{c}}_i\bar{\mathbf{c}}_i - \frac{1}{2c_s^2} \mathbf{u}^2 \right) \quad (3.7)$$

where $\bar{\mathbf{u}}\bar{\mathbf{u}}$ is the traceless part of $\mathbf{u}\mathbf{u}$, and the double dot product is defined as $A : B = \sum_{\alpha,\beta} A_{\alpha\beta} B_{\beta\alpha}$. The weight factors are given by $w_0 = 4/9$, $w_1 = w_3 = w_5 = w_7 = 1/9$ and $w_2 = w_4 = w_6 = w_8 = 1/36$.

In the LB scheme for particulate suspensions as developed by Ladd [29], the solid particles are defined by a boundary surface, which can be of any size or shape. The solid particles are placed on the lattice, where the boundary surface cuts some of the links between lattice nodes. Fluid particles moving along the boundary surface interact with the surface at boundary nodes that are located at the lattice nodes nearest to the boundary surface of the solid particles, following an alternative method to Ladd's, that was developed by Behrend [38]. In this method, called relaxed bounce back at the nodes, the LB collisions are carried out at every node, including the boundary nodes. The collision rules at the boundary surface enforce a stick boundary condition on the fluid, which means that the fluid velocity is matched to the local solid-body velocity \mathbf{u}_b . This local solid-body velocity \mathbf{u}_b (at position \mathbf{x}_b) is determined by the solid-particle velocity \mathbf{U} , its angular velocity Ω and the position of its center of mass \mathbf{R} :

$$\mathbf{u}_b = \mathbf{U} + \Omega \times (\mathbf{x}_b - \mathbf{R}) \quad (3.8)$$

After the collision phase, the boundary nodes are updated in the following way:

$$f_i(\mathbf{x} + \Delta\mathbf{x}_i, t + \Delta t) = f'_{-i}(\mathbf{x}, t) + \frac{2\rho w_i}{c_s^2} \mathbf{u}_b \cdot \mathbf{c}_i \quad (3.9)$$

$$f_i(\mathbf{x} - \Delta\mathbf{x}_i, t + \Delta t) = f'_i(\mathbf{x}, t) - \frac{2\rho w_i}{c_s^2} \mathbf{u}_b \cdot \mathbf{c}_i \quad (3.10)$$

For moving suspension particles, in this update, momentum is exchanged between the incoming particles from the fluid and the solid side (the combined momentum of the fluid and the solid phase is, however, conserved). From this momentum exchange, the force and torque exerted on a suspension particle is calculated. Hereinafter, the kinematic properties of the suspension particles are updated with a simple Euler forward integration of Newton's second law.

The choice of the location of the boundary nodes, the discretisation of the particle surface onto the lattice and the boundary update rules induce a certain hydrodynamic particle diameter that is larger than the diameter based on the number of occupied lattice nodes [30]. In dilute systems, in the Stokes flow regime and for sufficiently large particles, the difference between the input particle diameter and the hydrodynamic particle diameter can be considered constant (but dependent on the kinematic viscosity). In that situation, the hydrodynamic instead of the real particle diameter could be used for the calculation of the particle fraction or shear-induced diffusivity. In our simulations, we focus on rather concentrated suspensions outside the Stokes flow regime, where we not only expect the

deviation to be smaller than for dilute systems in the Stokes flow regime, but also to be dependent on the actual hydrodynamic conditions. Because determination of the actual hydrodynamic diameter in concentrated suspensions outside the Stokes flow regime would become very complex, we used the real particle diameter in our simulations, knowing that this gives a small, albeit probably negligible error. For the relatively large particle diameters of 16 lattice units applied in this study, this would give a deviation on the input particle diameter of at most 5%. The particle fraction and shear-induced diffusivity are the most important parameters that depend on the particle diameter. The quadratic dependence of these parameters on the particle diameter would, in its turn, give rise to a maximal deviation of 10% on the particle fraction and the shear-induced diffusivity. In general, this deviation lies within the standard deviation of our simulation results.

Since a suspended particle is essentially simulated by the introduction of a boundary surface, separating the interior of the particle from the exterior, the interior of the particle also consists of fluid. Ladd [30] examined the effects of the interior fluid on the behaviour of the particle. With a sufficiently high effective mass of the particle, the interior fluid only contributes an inertial force due to the extra mass of the particle. Our computations were carried out in this regime, with an effective mass density ρ_s/ρ of 10. By comparing simulation results at low Re_p with an effective mass of 3 and 10, we found that the relatively high effective particle mass did not contribute to the observed effects of Re_p on the viscosity and shear-induced diffusion in this paper. It can therefore be hypothesized that fluid inertia plays a larger role than particle inertia in our system; here, we do not take it into consideration any further.

Since shear-induced diffusion is mainly governed by hydrodynamic particle interactions, these interactions must be accurately resolved in the computations. When two suspension particles come into close contact with each other, the lubrication force becomes important. This force is caused by the attenuation of the fluid film in the gap between the two particles and is repulsive upon approach and attractive upon separation of the particles. When the gap width between two particles is of the order of one lattice spacing, the lubrication force is, however, not exactly resolved with the LB method. This is due to the discretisation of the particles and fluid on a grid and is a problem that is encountered by all numerical methods. To overcome this problem, we applied a lubrication correction as proposed by Ladd and Verberg [33] for a 3D system. It starts with an explicit calculation of the lubrication force when the gap width is smaller than two lattice units ($= 0.25a$). Since we considered a 2D system, we used the following equation for the lubrication force per unit length F , which is valid for the lubrication force between two cylinders (see Appendix 3.7):

$$F = \eta U \left(\left(\frac{h}{a} \right)^{-\frac{3}{2}} (F_0 + \frac{h}{a} F_1) - \left(\frac{h_c}{a} \right)^{-\frac{3}{2}} (F_0 + \frac{h_c}{a} F_1) \right),$$

$$h < h_c \tag{3.11}$$

$$F = 0, h > h_c \tag{3.12}$$

where two particles approach each other with a velocity U , $2h = |\mathbf{R}_{12}| - 2a$ is the gap (distance between the particle surfaces), F_0 and F_1 are numerical constants. In accordance with Ladd and Verberg [33], we applied a correction on the lubrication force to account for the lubrication force that is already resolved in the computations of the fluid dynamics. This was done by subtracting the lubrication force at a cut-off distance h_c from the total

lubrication force, as indicated in Equation 3.12. The cut-off distance h_c represents the cut-off distance between the particle surfaces for the added lubrication force and was chosen equal to one lattice unit ($= 0.125a$) in our study. For 3D systems, Nguyen and Ladd [40] showed that this correction leads to more accurate results for particle interactions at short interparticle distances, even with neutrally buoyant particles very near to contact and without causing instabilities in the particle dynamics. These improvements are also expected for a 2D system.

We have noticed, that in suspensions with particle fractions exceeding 0.40 and at relatively high shear rates, particle clustering and overlap can occur, which greatly affected the diffusive behaviour of the particles. This behaviour seems to be correlated with the lubrication breakdown of concentrated colloids, that was reported by Ball and Melrose [41]. As suggested by these authors, we applied a Hookean spring force between the particles for particle fractions exceeding 0.40 to avoid this clustering and overlap. This Hookean spring force was applied for gaps $2h$ smaller than a thickness δ and was applied in the direction of the line of particle centres, according to:

$$F_h = F_m - \left(\frac{F_m}{\delta} \right) 2h \quad (3.13)$$

with a maximal Hookean spring force F_m of 10.0 (in lattice units). The Hookean spring force is active in a layer around the particle with a thickness $\delta/2$ of 0.05 lattice units ($= 0.00625a$). When using the LB model as described above, we found a good agreement between our computer simulation results for the viscosity and model results of the Krieger-Dougherty model (particle fractions between 0.05 to 0.55), which is known to describe experimental data well. Especially at high particle fractions, the viscosity is known to be highly dependent on particle interactions. The good agreement with the Krieger-Dougherty model therefore indicates that our model captures the particle behaviour well.

3.3 Effects of hydrodynamics and inertia in particle suspensions

Our simulations on shear-induced diffusion are carried out in a 2D multi-particle suspension (actually cylinders) in a Couette system with solid moving walls. Before examining this rather complex system, we firstly studied the behaviour of a single cylinder and of two interacting cylinders in shear flow, in order to investigate some relevant effects in a simpler system. The case of the single cylinder studies wall effects and the effect of Re_p and is compared with data from literature concerning 3D systems. The case of two interacting cylinders is presented to show the effect of Re_p on the flow trajectory of two interacting cylinders in shear flow. For this specific case, neither analytical nor numerical (2D) solutions were available so the comparison with literature is only qualitative. Besides these one and two cylinder systems, we determined the effects of Re_p on the viscosity of a multi-particle suspension, which enabled us to examine the collective particle behaviour in a Couette system with solid moving walls and relate this behaviour to the results presented in section 3.4 and 3.5 of this paper. The results of the preliminary simulations are discussed in this section.

The computer simulations on a single and on two interacting cylinders were carried out in a Couette system, consisting of a box with solid walls at the upper and lower

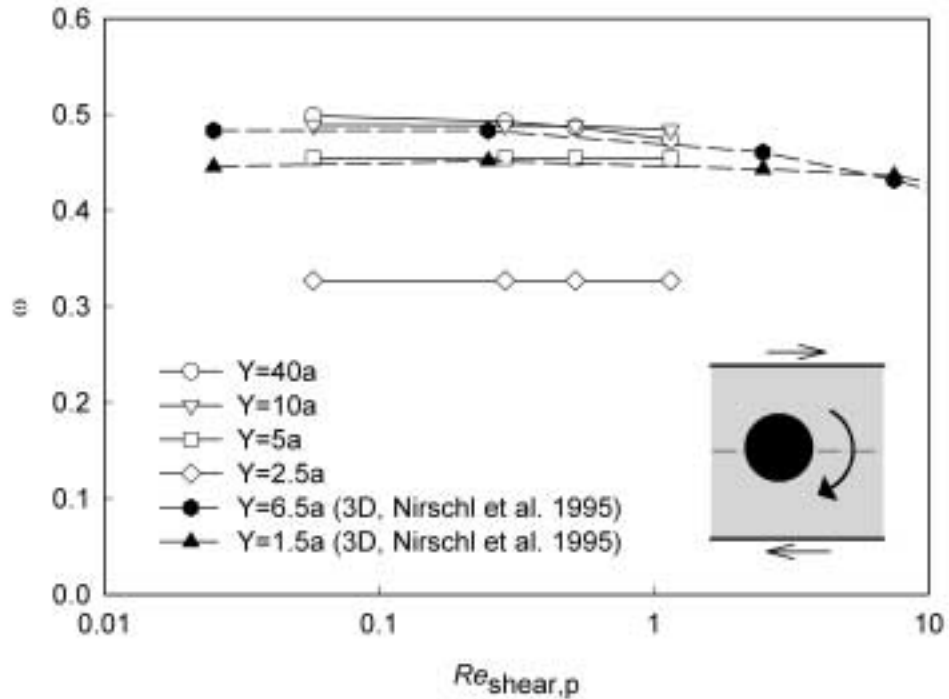


Figure 3.1: The angular velocity ω as a function of $Re_{\text{shear,p}}$ for a single cylinder with radius a in shear flow. The distance between the solid walls of the Couette system was varied between $2.5a$ and $40a$. The results are compared to results of Nirschl and co-workers [42] for a 3D system. The inset shows a scheme of the simulated situation.

side and periodic boundaries at the left- and right-hand side of the box. The walls move parallel to each other with a constant velocity, but in opposite directions. The width of the box between the periodic boundaries was equal to 640 lattice units ($=80a$). The height of the box between the two parallel walls was 320 lattice units ($=40a$) (in most cases) and the wall velocity was between 0.002 and 0.054 lattice units per time step, resulting in a shear rate between $1.25 \cdot 10^{-5}$ and $7.50 \cdot 10^{-4}$ per time-step. Therewith, the shear based particle Reynolds number $Re_{\text{shear,p}}$ ($= 4\dot{\gamma}a^2/\nu$, with ν the kinematic viscosity) was between 0.019 and 1.152 . For the case of a single cylinder, the height of the box and the wall velocity were varied, but in such a way that the shear rate and $Re_{\text{shear,p}}$ were in the range indicated above.

For a single cylinder placed at the horizontal centerline of the Couette system, the equilibrium angular velocity of the cylinder is determined as a function of the distance between the solid walls and as a function of $Re_{\text{shear,p}}$. In this paper, the angular velocity ω is normalised for the shear rate. We compare our results to results of Nirschl and others [42], who carried out comparable computations with a finite volume numerical scheme, but for a 3D system. Taylor [43] derived an analytical solution for low Reynolds number flow over a rotating sphere in simple shear, which predicts an angular velocity ω of a half. The computed angular velocity ω is presented as a function of $Re_{\text{shear,p}}$ in Figure 3.1.

For a distance between the walls $Y = 10a$ and $Y = 40a$ and $Re_{\text{shear,p}} < 0.5$, the angular velocity ω approached Taylor's solution to within a few percent. For $Re_{\text{shear,p}}$ up to 1.152 , no large influence of $Re_{\text{shear,p}}$ on the angular velocity ω is seen. The influence

was slightly larger for larger distances between the walls. This is in agreement with the findings of Nirschl and others [42] for a 3D system. The influence of $Re_{\text{shear,p}}$ can be attributed to the blockage of fluid near the particle axis. This blockage creates a recirculation of fluid, and the streamlines divert into the gap between the wall and the particle. Therewith the resistance to flow in the gap increases, and the flow losses are larger with increasing $Re_{\text{shear,p}}$, leading to a decrease of the angular velocity ω . When the distance between the walls is smaller, the recirculation is inhibited so that the effect of $Re_{\text{shear,p}}$ is less than for larger distances. When the distance between the walls decreased to $5a$ or smaller in our simulations, the walls had an increasing effect on the angular velocity ω . Compared to the 3D results of Nirschl and others, this effect is more pronounced in a 2D system. This can be understood because the intensity of the flow field around a cylinder is larger than around a spherical particle.

All together, these results lead us to the conclusion that in the shear regime of our study, $Re_{\text{shear,p}}$ does not have a significant effect on the rotation of a single cylinder. When the cylinder closely approaches a solid wall, the angular velocity decreases owing to the interaction with the wall. This effect is larger in a 2D than in a 3D system. These results also give an indication of wall effects in a Couette system where the cylinder is placed eccentrically in that system. It is known that cylinders tend to migrate to the centerline of a Couette system [58]. The migration velocity is, amongst others, dependent on the distance from the wall. We can expect that migration becomes important at particle distances from the wall where the angular velocity is significantly affected. Consequently, when wall effects on the total system need to be negligible, the distance between the walls in a multi-particle system needs to be sufficiently high. Therefore, the distance between the walls was minimally $56a$ in the simulations on multi-particle systems in the rest of this paper.

In another study, we determined the drag coefficient of a single cylinder settling along the centerline of a confined channel (results not shown). These results were found to be in good agreement with results of Feng and others [59] and Aidun and Lu [60], indicating that the drag of a transposing cylinder is accurately resolved with our LB method.

The interactions between two cylinders subjected to simple shear flow provide an important basis for analysing shear-induced diffusive behaviour of suspensions, because this behaviour can be considered the basis for shear-induced diffusion in the low concentration limit. Batchelor and Green [44] have derived analytical solutions for 3D systems of spheres without inertia. Trajectories can either extend to infinity (open trajectory) or not (closed trajectory). The interaction between equal-sized spheres is symmetric and such spheres can approach each other to exceedingly small separations. Factors such as surface roughness can disturb the symmetry of the process, because this can impose an additional force onto the spheres when in close contact. Therefore, closed trajectories will probably only occur for very smooth spheres. We have studied the effect of inertia on hydrodynamically interacting cylinders by varying $Re_{\text{shear,p}}$ in a system with two equal-sized cylinders in an open trajectory.

In our simulations, these two cylinders were placed in the box at heights symmetrical around the horizontal centerline, at a distance of $19.25a$ from the moving wall and $0.75a$ from the centerline. The initial horizontal distance between the cylinders was $10.0a$. Based on the simulations on one cylinder as presented in Figure 3.1, it can be expected that the walls did not affect the flow of the cylinders. The trajectories of the interacting cylinders were computed for various shear rates (Figure 3.2).

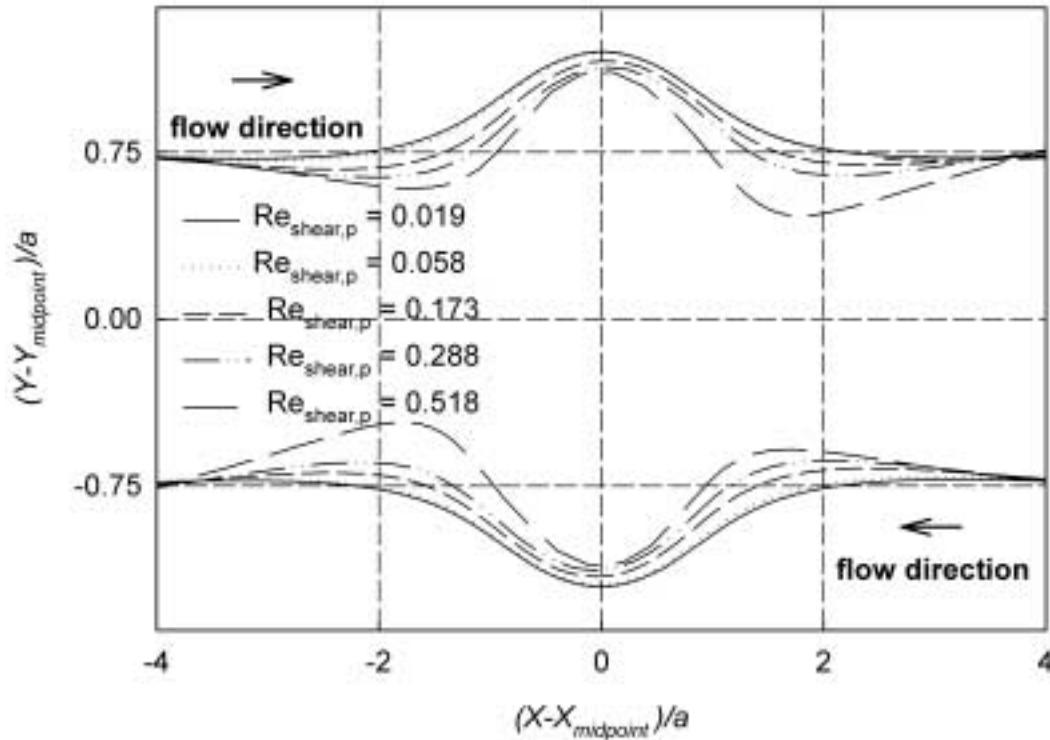


Figure 3.2: Flow trajectories for two interacting cylinders with radius a in shear flow. $Re_{\text{shear,p}}$ varied between 0.019 and 0.518. The positions are related to the initial midpoint of the two cylinders.

At $Re_{\text{shear,p}}$ 0.019 and 0.058, no clear effects of inertia can be seen in the flow trajectories. In their tumbling movement around each other, the cylinders reach a minimum separation of $0.20 * 2a$ (Figure 3.3). When compared to 3D systems, this minimum separation is large. This can be explained because the flow of fluid out of or into the gap during respectively approach or separation of two parallel cylinders is more hindered than for the case of spheres. The trajectories upon approach and upon separation are practically symmetric, which is in accordance with the relatively large separation distances in this system. At $Re_{\text{shear,p}} > 0.058$, inertial effects become visible in the trajectories. One effect is that the separation distance between the cylinders became smaller, both during approach and during separation. The minimum separation between the cylinders decreased to $0.11 * 2a$ for $Re_{\text{shear,p}}$ equal to 0.52 (Figure 3.3). This effect can be explained because inertia causes the cylinders to move to different streamlines, and is probably due to particle inertia rather than fluid inertia. A second effect is that at larger separation distances, the cylinders slowly moved towards the center axis of the system before they start tumbling over each other. Upon separation, a similar movement away from the center axis took place. Inertial effects in the fluid flow around the cylinders are the most probable cause for this effect. Finally, the trajectories upon approach and separation exhibited an increasing asymmetry with increasing $Re_{\text{shear,p}}$. This effect, although small, can be seen in Figure 3.3. The minimum separation was still too large to be able to explain the observed asymmetry with the action of the repulsive Hookean spring force F_h or with

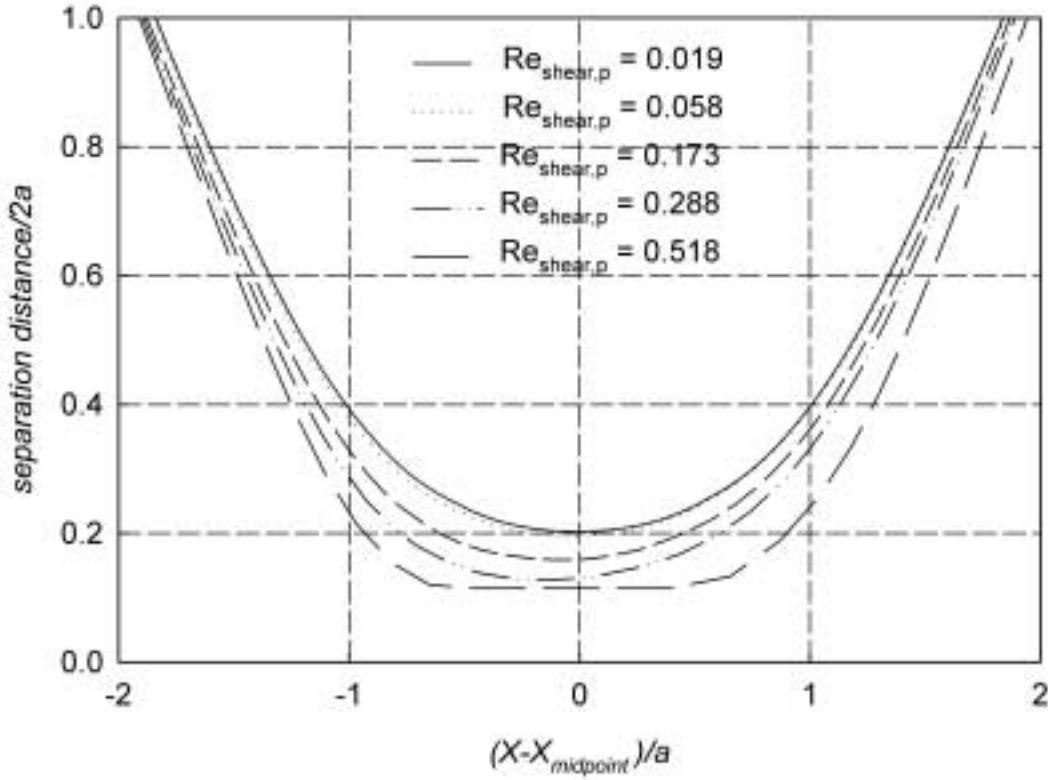


Figure 3.3: Separation distance as a function of the horizontal position of the upper cylinder, for two interacting cylinders with radius a in shear flow. $Re_{\text{shear,p}}$ varied between 0.019 and 0.518.

the effect of surface roughness (a different flow trajectory would then also be expected). Inertial effects seem, therefore, to be responsible for this asymmetry.

The inertial effects during the interaction between the cylinders lead to a dispersal of the cylinders at $Re_{\text{shear,p}}=0.52$, which proceeded with repeated encounters of the cylinders (Figure 3.4). Even when the separation distance between the cylinders has become larger than $7 * 2a$, the dispersal still proceeds. Because the vertical velocity decreases with increasing separation distance and does not exhibit a logarithmic trend in time, it is expected that the cylinders will have reached their equilibrium position at a separation distance of about $8 * 2a$. The distance from the walls was still about $12a$, so that it is not likely that this final separation distance is affected by the presence of the walls.

The viscosity is determined from a multi-cylinder suspension in a Couette system, with $Re_{\text{shear,p}}$ varying between 0.003 and 0.33. Our results for the viscosity are presented as relative values to results from the semi-empirical model of Krieger and Dougherty [46]. This model is known to give accurate predictions for the viscosity at low Re , for both 2D and 3D suspensions. The effective viscosity μ_s/μ_f is calculated as follows:

$$\mu_s/\mu_f = \left(1 - \frac{\langle\phi_s\rangle}{\phi_{\text{max}}}\right)^{-[\eta]\phi_{\text{max}}} \quad (3.14)$$

where $\langle\phi_s\rangle$ is the averaged solid volume or area fraction and ϕ_{max} is the maximum packing

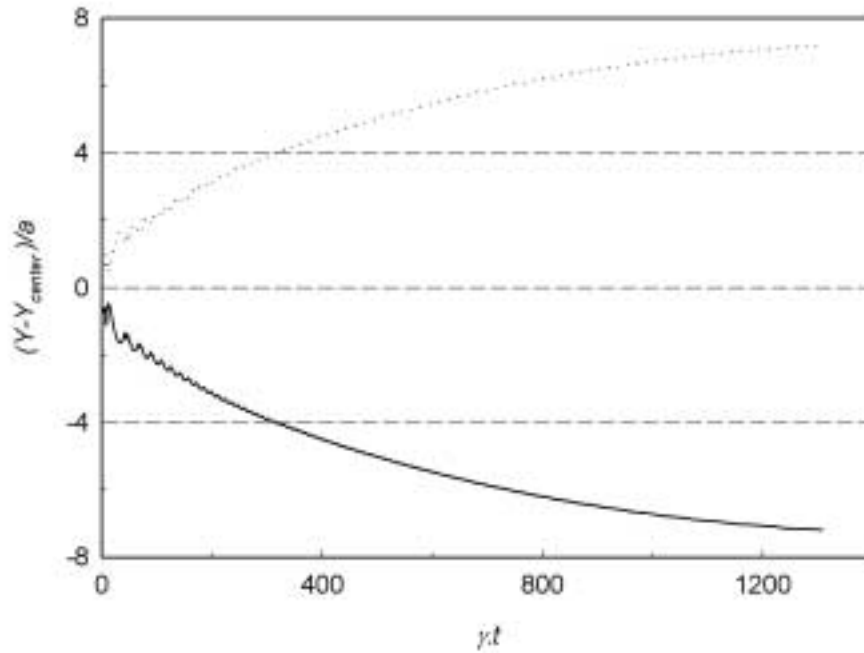


Figure 3.4: Vertical position $(Y - Y_{center})/a$ as a function of the strain $\dot{\gamma}t$ for two interacting cylinders with radius a in shear flow. $Re_{shear,p}$ was equal to 0.518. The initial position of the cylinders was symmetrical around the center axis, at a distance of $0.75a$ from the center axis and of $19.25a$ from the nearest wall. The oscillations in the trajectory are caused by the repeated encounters of the cylinders.

fraction, which has a value of 0.82 for a 2D suspension. The dimensionless factor $[\eta]$ is the intrinsic relative viscosity of the suspension and has a value of 2 for a 2D suspension.

In our computations, the system height and width were 518 ($= 64.75a$) and 259 ($= 32.38a$) lattice units, respectively, and the shear rate varied between $1.93 \cdot 10^{-6}$ and $2.16 \cdot 10^{-4}$ per time step. An amount of 66, 166 or 266 cylinders with radius a were randomly suspended in the domain, corresponding with area fractions ϕ of 0.10, 0.25 and 0.40, respectively. The viscosity was determined from the average stress at the walls over a strain range of at least 1.5 at a shear rate of $1.93 \cdot 10^{-6}$ per timestep, increasing to a strain range of 86 at a shear rate of $2.16 \cdot 10^{-4}$ per time-step. This increase of strain range was necessary to acquire sufficient accuracy at high shear rates, where the time-dependent fluctuations of the stress were higher.

Our viscosity data in the regime with low $Re_{shear,p}$ agree well with the Krieger-Dougherty model since the normalised viscosity is around 1.0 (Figure 3.5). At higher $Re_{shear,p}$, however, starting at $Re_{shear,p}=0.012$, shear thickening occurred in the suspensions with area fractions of 0.25 and 0.40. This shear thickening was most intense at an area fraction of 0.40, where the effective viscosity increased about 35% for an increase of $Re_{shear,p}$ to a value of 0.1. At these high values for $Re_{shear,p}$, the viscosity starts to level off. The velocity profile in the Couette system was found to be linear, except for $\phi = 0.40$ and $Re_{shear,p} > 0.2$, where slip started to occur near the wall. At $\phi = 0.40$ and $Re_{shear,p} = 0.33$, this lead to a decrease of the shear rate in the bulk phase of about 15% when compared to a situation with a linear profile. This might also have consequences

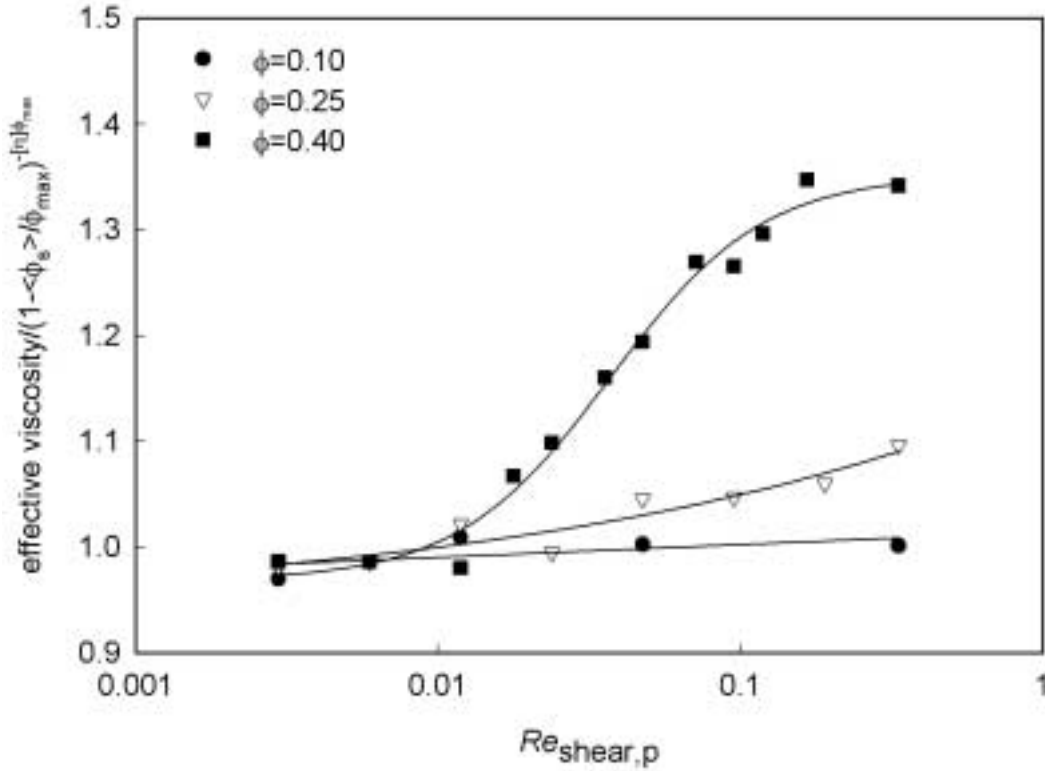


Figure 3.5: Viscosity of a 2D suspension as a function of $Re_{\text{shear},p}$ for suspensions with a cylinder area fraction ϕ of 0.10, 0.25 and 0.40. The viscosity is presented as the effective viscosity, normalised for model results of the Krieger-Dougherty model ($\phi_{\text{max}} = 0.82$, $[\eta] = 2$) at the respective area fractions. The lines are fits to the data points and are drawn as a guide to the eye.

for the accuracy of the viscosity calculations, since the viscosity is determined from the stress near the wall. For the great majority of the calculations, however, slip did not play a role and the viscosity calculations are expected to be accurate. For highly concentrated suspensions, the increase of viscosity with increasing particle fraction in the Stokes flow regime has been found to coincide with particle clustering [61]. It might be that in our case, where we found a viscosity increase with shear rate, particle clustering also plays a role. An analysis on particle clustering in our system is therefore presented in section 3.5.

Although limited results are available, shear thickening behaviour has also been observed by other authors, experimentally as well as in computer simulations (see e.g. [47, 62]). Shear thickening is found particularly in suspensions where hydrodynamic forces are dominant (at high Peclet number ($= \frac{8\mu_f a^3 \dot{\gamma}}{kT}$ where k is the Boltzmann constant and T the absolute temperature)). Similar to our results, Shakib-Manesh and others [47] observed shear thickening of 2D suspensions. In their study, for suspensions with a cylinder area fraction up to 0.52, the effect of shear thickening on the viscosity was only relevant when $Re_{\text{shear},p}$ was larger than about 0.5, so, in a quantitative sense, their results do not fully agree with ours. This may, however, be due to differences in the way the particle interactions are handled at short distances in the codes used. In contrast to our method, Shakib-Manesh and co-authors did not correct for the lubrication force at

short particle distances; this difference might be relevant for clustering behaviour of the suspension. This comparison shows that shear thickening can be delicately affected by interparticle forces, which hampers quantitative comparison of data.

3.4 Shear-induced diffusion at non-zero Reynolds numbers

In this section, we present results of LB simulations on shear-induced diffusion in 2D systems. In these 2D systems, we can distinguish components of the shear-induced self-diffusion tensor in the fluid velocity and in the velocity gradient direction, and their diagonal component. Whereas the displacements in the velocity gradient direction are purely determined by the hydrodynamic interactions between the cylinders, the displacements in the fluid velocity direction also consist of a convective term due to the shear flow of the fluid. The analysis of shear-induced self-diffusion in the velocity gradient direction is consequently more straightforward. Since the component in the velocity gradient direction is, in practice, the most relevant, we only describe our results for this direction.

The relevant time and length scales in the system are the shear rate $\dot{\gamma}$ and the cylinder radius a , respectively. On the basis of dimensional arguments, it can be shown that the self-diffusivity scales as $\dot{\gamma}a^2$ (in the Stokes flow regime). All diffusivities reported are therefore normalized on $\dot{\gamma}a^2$.

The shear-induced self-diffusion coefficients can be determined from the increase of the mean-square displacements with time after diffusive motion has been established, according to:

$$\langle y(t)y(t) \rangle \approx 2D_{yy}t \quad (3.15)$$

The angle brackets denote an average over all cylinders in the system, while y denotes the displacement of a single particle in the direction of the velocity gradient. D_{yy} denotes the self-diffusivity in the velocity gradient direction. This self-diffusivity is defined as the time rate of change of a half multiplied by the mean-square displacement:

$$D_{yy} \equiv \lim_{t \rightarrow \infty} \frac{1}{2} \frac{d}{dt} \langle y(t)y(t) \rangle \quad (3.16)$$

The motion of a non-Brownian cylinder is, in principle, purely deterministic and the displacement of a given cylinder depends only on the external velocity field and its interactions with all other cylinders in the system. To obtain the random displacements that are a characteristic of diffusive motion, the initial cylinder configuration must also be changed. As a consequence, the sampling time must be relatively long in order to determine the diffusion coefficients. Therefore, shear-induced diffusion can be characterised as a long-time diffusion process.

As for the aforementioned studies on one or two interacting cylinders in shear flow and on the viscosity in relation to the particle fraction, the system consisted of a Couette system with periodic boundaries in the flow direction of the fluid and two moving walls in the velocity gradient direction. A varying number of cylinders with a radius of 8 lattice units is randomly distributed in the system at the start of the simulation. The simulation runs were started with position-dependent fluid and cylinder velocities according to linear shear flow.

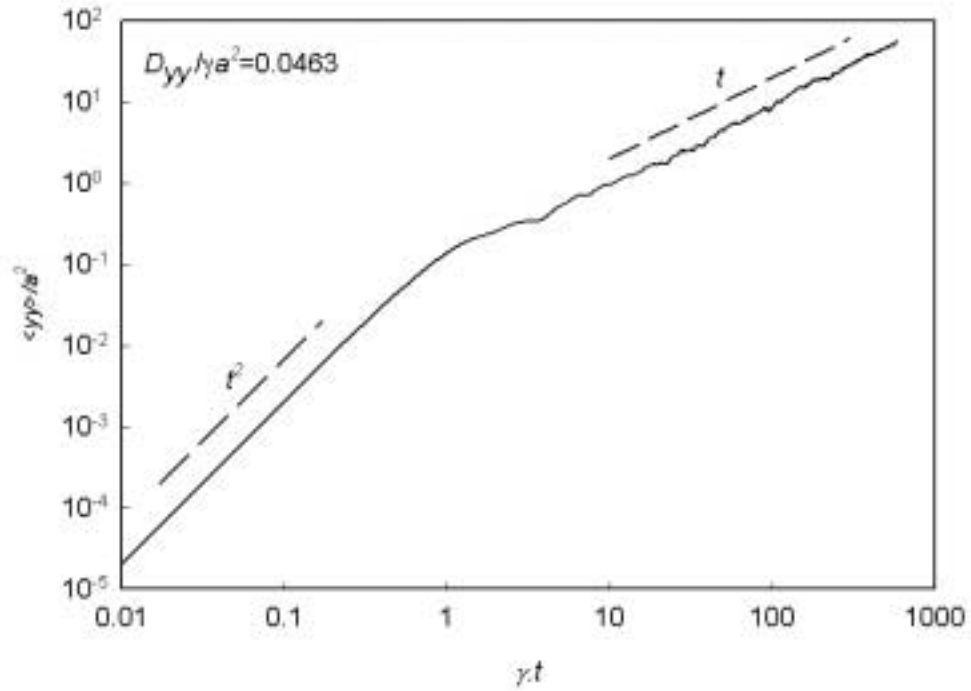


Figure 3.6: Mean-square displacement in the velocity gradient direction as a function of time, both presented as dimensionless values, for a 2D suspension ($N = 200$, $\phi = 0.25$) in shear flow at $Re_{\text{shear,p}} = 0.023$.

As an example of the typical time-dependent behaviour of the cylinder displacements, in Figure 3.6, a mean-square displacement curve is shown for a system with a cylinder number N of 200 and an area fraction ϕ of 0.25. From the double-logarithmic plot in Figure 3.6, it becomes clear that, at very short times, the mean-square displacement shows a quadratic temporal behaviour, which corresponds to the deterministic strongly correlated cylinder displacements in this regime. Only after a strain of about $\dot{\gamma}t = 8$ do the cylinder displacements become random, resulting in a linear behaviour of the mean-square displacement curves. The diffusion coefficient, which is evaluated from this simulation run, is also given in Figure 3.6. In order to evaluate the effect of the initial particle configuration on the diffusion coefficient, we split the displacement curve of one simulation run into several curves which start at different times of the simulation run (and consequently at different particle configurations). In each separate curve, the mean square displacement was monitored over a strain of 30. The final diffusion coefficient is the mean value of the diffusion coefficients that were determined from the individual mean square displacement curves.

From a strain $\dot{\gamma}t$ of about 1 to 8, a transitional regime exists, in which the temporal behaviour is neither quadratic nor linear. The time-dependent behaviour in our (2D) simulations seems to compare well with the findings of Sierou and Brady [27] from their (3D) ASD simulations. Our results confirm their statement that strains must be sufficiently long in order to obtain an accurate value for the shear-induced diffusion coefficient. Strains that are too small lead to an overestimation of the shear-induced diffusion coefficients. This probably explains the relatively high diffusion coefficients in some experimental studies,

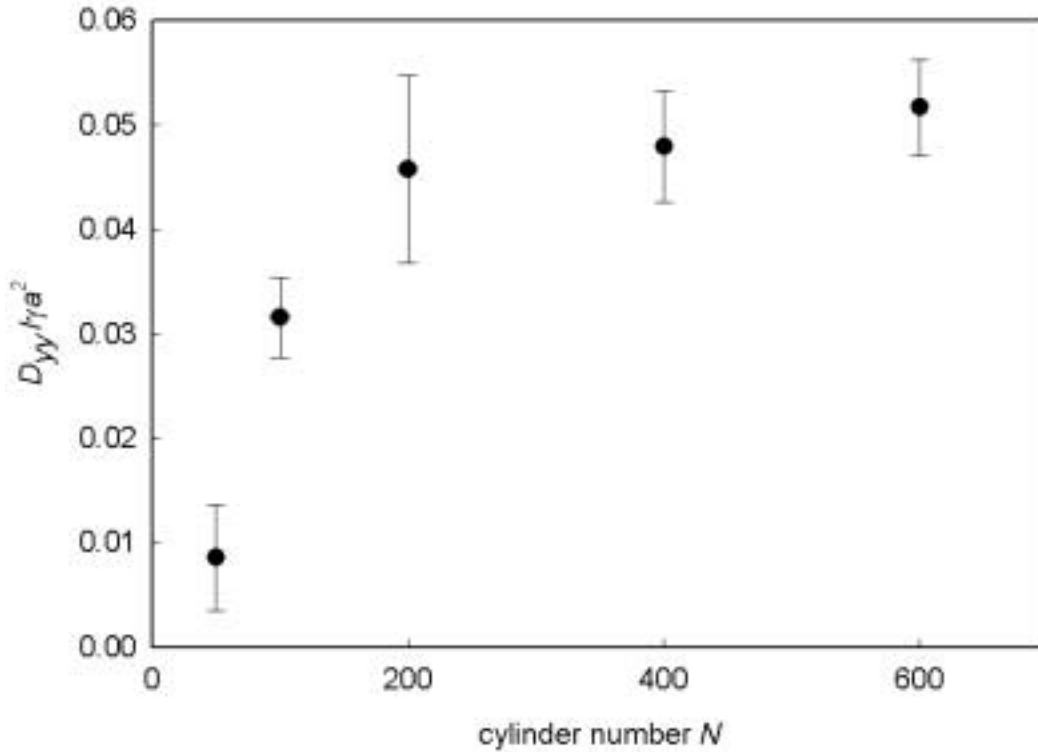


Figure 3.7: Component D_{yy} of the shear-induced self-diffusion coefficient as a function of the cylinder number N for a 2D suspension ($\phi = 0.25$) in shear flow at $Re_{\text{shear,p}} = 0.023$. The width of the simulation box between the periodic boundaries is varied, while the height between the confined walls is kept constant at $71a$. The error bars indicate the standard deviation of the mean shear-induced self-diffusion coefficient, which is determined from 6-12 individual mean-square displacement curves with different initial particle positions and over a strain of 30.

e.g. the study of Breedveld and co-workers [18].

The number of cylinders in the system is known to be an important factor in the determination of the diffusion coefficients [27]. The main reason for this is that for cylinder separations greater than the length of the system, the cylinders can interact with their periodic images, which affects the diffusivities. Smaller cylinder numbers correspond with a smaller system size, which might lead to a larger deviation in the calculated diffusivity. For concentrated suspensions, it can be expected that this deviation depends more on the cylinder number than on the system size (in other words, at higher concentrations, smaller system sizes would suffice). In our system, this idea is only relevant for the velocity direction, since we have no periodic boundaries in the velocity gradient direction. Because the number of cylinders that is sufficient for an accurate calculation of the diffusivity cannot be theoretically evaluated, it needs to be established in an empirical way. Therefore, in Figure 3.7, the calculated diffusion coefficients are presented as a function of the number of cylinders for an area fraction ϕ of 0.25. To investigate the effect of the number of cylinders, only the width X of the simulation box was varied, while the height Y between the confined walls was kept constant at $71a$.

For cylinder numbers smaller than $N = 100$, there is a rather sharp increase in diffu-

sivity with the number of cylinders. This is followed by a levelling off of the diffusivity with higher numbers of cylinders. The decrease of the standard deviation from $N = 200$ to $N = 600$ reflects the improved statistical accuracy by the increased cylinder number, since the same number of configurations is used for the calculation of shear-induced diffusivity. From the observed relationship, we draw the conclusion that a cylinder number of more than 100 is required for the determination of diffusivities with sufficient accuracy. Although not expected a priori, the relation between the diffusivity and the cylinder number is found to compare well with the one that was found in SD simulations for 3D systems [27]. Our results therewith confirm a statement of Sierou and Brady [27], namely that the results of Foss and Brady [55] are influenced by the fact that they only used a particle number N of 27 in their SD simulations. For the following simulations presented in this paper, we applied a cylinder number N of 200, unless otherwise stated. The size of the simulation box is chosen such that Y was always twice as large as X , as is the case in the simulations presented in Figure 3.7 with $N = 200$. The distance between the solid walls Y was such that the measured shear-induced diffusivity agrees with that of an infinitely large system (results not shown).

LB simulations are not limited to the Stokes flow regime. This makes it possible to determine the particle movements in systems with non-zero Reynolds numbers, which can be considered relevant for many practical systems. During pipeflow and microfiltration for example, the shear rate can, in general, easily exceed values of 1000 s^{-1} , which is already beyond the Stokes flow regime for suspensions with particles sizes in the micrometer range. On the basis of the consideration that particle interactions cause shear-induced diffusion and that the number of particle interactions scales linearly with the shear rate, it can be expected that the dimensionless diffusion coefficient $D_{yy}/\dot{\gamma}a^2$ is independent of $\dot{\gamma}$ in the regime where inertial or other shear-related effects do not (yet) play a role. To our knowledge, however, it is not known at which conditions inertial or other shear-related effects come into play and how they affect shear-induced diffusion. We therefore analysed the particle movements in the velocity gradient direction in relation to $Re_{\text{shear,p}}$.

For $Re_{\text{shear,p}}$ from 0.023 up to 0.346 and cylinder area fractions of 0.10, 0.25 and 0.40, the mean square displacement $\langle yy \rangle / a^2$ as a function of the strain $\dot{\gamma}t$ is presented in Figure 3.8. The relation was linear (after a strain $\dot{\gamma}t \approx 8$), as in accordance with shear-induced diffusive behaviour. We also observed that the average displacement in the velocity gradient direction remained (nearly) zero for particle area fractions of 0.10, 0.25 as well as 0.40. The particle distribution across the height between the two walls remained nearly constant in time as well, which also indicates that no net particle transport has taken place. At a cylinder area fraction of 0.10 and 0.25, a systematic increase of $\langle yy \rangle / a^2$ with $\dot{\gamma}t$ is observed when $Re_{\text{shear,p}}$ was increased. At a cylinder area fraction of 0.40, this increase with $Re_{\text{shear,p}}$ was also present, although not as evident as for an area fraction of 0.10 and 0.25. The diffusivity seems to reach a plateau value at this area fraction of 0.40. As mentioned in section 3.3, wall slip starts to occur at $\phi = 0.40$ and for $Re_{\text{shear,p}} > 0.2$. The effect of wall slip on the shear rate seems too small to explain the relatively small increase of the diffusivity at $\phi = 0.40$, but the behaviour might be related to microstructural features. This is investigated in the next section.

The results indicate that the dimensionless diffusion coefficient $D_{yy}/\dot{\gamma}a^2$, as determined from the slope of the curves in Figure 3.8, was not independent from the shear rate, as is shown in Figure 3.9. For $\phi = 0.10, 0.25$ and 0.40 , the increase started at about $Re_{\text{shear,p}} = 0.04$, which is comparable to where the shear thickening behaviour started.

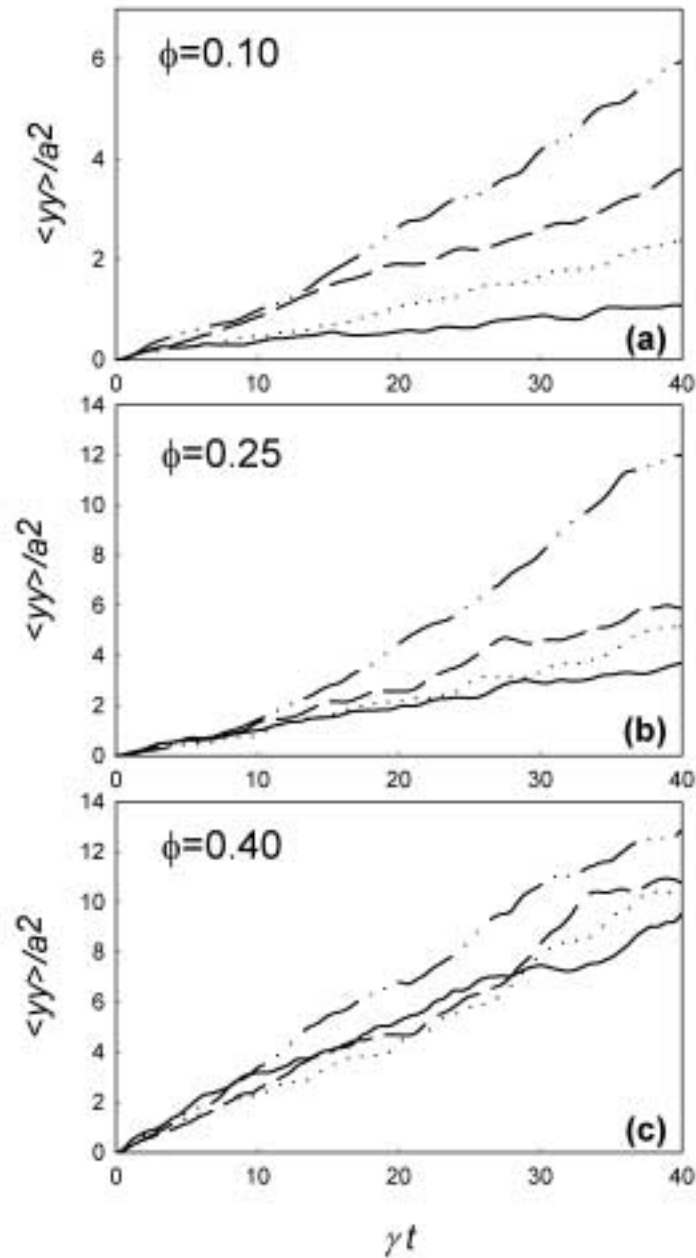


Figure 3.8: Mean-square displacement in the velocity gradient direction as a function of time, both presented as dimensionless values, for a 2D suspension ($N = 200$, $\phi = 0.10$ (a), 0.25 (b) and 0.40 (c)) in shear flow at $Re_{\text{shear,p}} = 0.023$ (solid line), 0.115 (dotted line), 0.161 (medium dashed line) and 0.346 (dash-dot-dotted line).

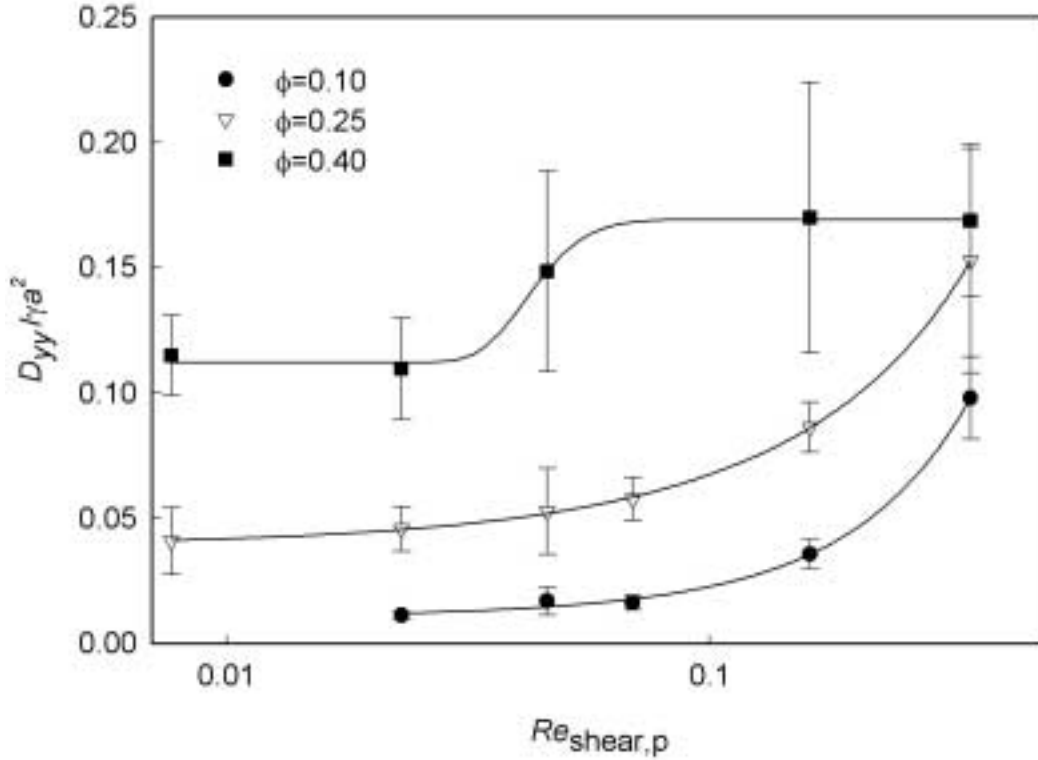


Figure 3.9: Component D_{yy} of the shear-induced self-diffusion coefficient as a function of $Re_{\text{shear,p}}$ for a 2D suspension ($N = 200$) in shear flow with a cylinder area fraction ϕ of 0.10 (filled circles), 0.25 (open triangles) and 0.40 (filled squares). The error bars indicate the standard deviation of the mean shear-induced self-diffusion coefficient, which is determined from 6-12 individual mean-square displacement curves with different initial particle positions and over a strain of 30. The lines are fits to the data points and are drawn as a guide to the eye.

The effect of the cylinder fraction was, however, opposite to the effect on the viscosity, because we observed the largest relative effects on shear-induced diffusion at the lower cylinder fractions.

In spite of the lower number of particle collisions, the standard deviation of the shear-induced diffusivity was relatively low at a particle area fraction $\phi = 0.10$. This indicates that, in principle, the averaging took place over sufficiently large strains and with sufficiently high cylinder numbers. The standard deviation, however, increased with increasing $Re_{\text{shear,p}}$ and when $D_{yy}/\dot{\gamma}a^2$ exceeded a value of about 0.10, the standard deviation was relatively large, indicating time-dependent fluctuations in the collective cylinder movements. This might be a combined effect of correlated movement of the cylinders, caused by particle clustering, and high stresses on the cylinders. Improving the accuracy of the shear-induced diffusion coefficients in this regime would require much larger systems, which was not deemed necessary in this study.

It may be expected that the dependence of the shear-induced diffusivity on $Re_{\text{shear,p}}$ is due to the correlated motion of cylinders, in other words, to the formation of a suspension microstructure. In the next section, this microstructure is analysed in order to have a

clearer picture of shear-induced changes in the suspensions.

3.5 Shear-induced changes in microstructure

In order to analyse the microstructure, we determined the 2D pair-distribution function, which represents the concentration distribution of cylinders around a cylinder. This pair-distribution function was assessed by averaging the pair-distribution function of two separate simulation runs. In each simulation run, the distribution function was determined by averaging the distribution at five different strains, namely at $\dot{\gamma}t = 30.0, 37.5, 45.0, 52.5$ and 60.0 . Cylinders at a position closer than a distance $0.2Y$ (Y =height between the walls) from the wall were excluded as reference particles from the distribution function, in order to avoid wall effects. The concentration distributions are only shown for ΔX and ΔY smaller than $3.5a$, because outside this region no cylinder preference positions could be observed. For a cylinder area fraction of 0.10, a clear effect of $Re_{\text{shear,p}}$ can be seen (Figure 3.10).

At $Re_{\text{shear,p}} = 0.023$, a concentration peak can be observed above and under the cylinder, at a distance of about $2a - 3a$. The concentration distribution was anisotropic as no peak can be observed left and right of the particle. At higher $Re_{\text{shear,p}}$, the concentration peak at a distance of about $2a - 3a$ becomes more circular (isotropic) as well as more pronounced. A maximum concentration peak with a value of about 1.4 a.u. is found at $Re_{\text{shear,p}} = 0.161$. These results clearly show that the cylinders tend to stay closer to each other at higher $Re_{\text{shear,p}}$. For a cylinder area fraction of 0.25, already at $Re_{\text{shear,p}} = 0.023$ a circular concentration peak was present at a distance of about $2a - 3a$ (Figure 3.10). Small peaks with a maximum concentration of about 2.8 a.u. were already present as well. With increasing $Re_{\text{shear,p}}$, the concentration peak was more pronounced, which again indicates an increased clustering of the particles. The concentration profile at a cylinder area fraction of 0.40 was already very pronounced at $Re_{\text{shear,p}} = 0.023$ with locally maximum concentrations of about 5.0 a.u. (Figure 3.10). In contrast to cylinder area fractions of 0.10 and 0.25, high $Re_{\text{shear,p}}$, however, did not invoke more clustering. This seems to be consistent with the effects on shear-induced diffusion, where we also found minor changes at a cylinder area fraction of 0.40.

In the pair-distribution function, the concentration peaks at short interparticle distances are generally very high, whereas they are less pronounced at longer interparticle distances, especially in the case of isotropic distributions. This makes the pair-distribution function less sensitive to concentration variations at longer interparticle distances and therefore not suited for the analysis of the size and density of the particle clusters. These parameters can, however, be determined from the scaling of the integrated pair correlation function, according to a version of the so-called sandbox method [63]. In this method, we consider the number of particles $n(r)$ in a sphere of radius r around any particle of the cluster. Simple linear regression on $\log(n)$ versus $\log(r)$ yields the parameters n_0 and d_f from the scaling relation for fractal clusters:

$$n(r) = n_0 \cdot \left(\frac{r}{a}\right)^{d_f} \quad (3.17)$$

where n_0 is a dimensionless proportionality constant (generally of order unity, the actual value of n_0 depends on the definition of r used) and d_f is the fractal dimensionality. In a

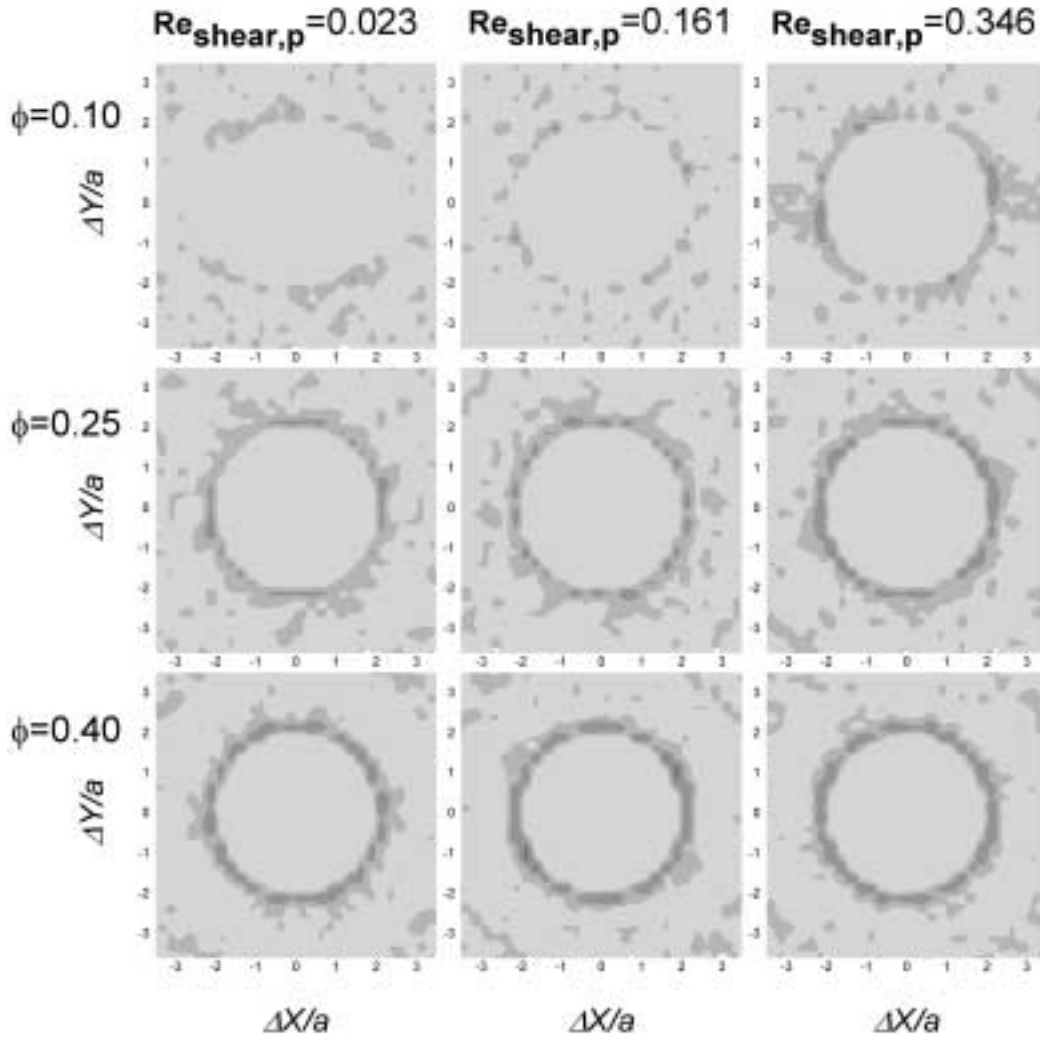


Figure 3.10: The 2D pair-distribution function, averaged over a strain $\dot{\gamma}t$ from 30 to 60, for a 2D suspension ($N = 200$) in shear flow with a cylinder area fraction ϕ of 0.10 (top), 0.25 (middle) and 0.40 (bottom) at $Re_{\text{shear},p} = 0.023$ (left), 0.161 (middle) and 0.346 (right). Dark regions represent high probability and light low.

plot of $\log(n)$ versus $\log(r)$, we would see a fractal regime for low values of r which ends at the size of the average cluster in the system (we have neglected effects of monomers, which have zero close neighbours and hence suppress n_0). At high values of r we have the homogeneous regime, where the number of neighbouring particles simply scales with the volume of the surrounding sphere. The prefactor then becomes the volume fraction:

$$n(r) = \phi \cdot \left(\frac{r}{a}\right)^3 \quad (3.18)$$

In our 2D system, the number of neighbouring cylinders scales with the area of the surrounding cylinder, which changes the power in this equation from 3 to 2. If the fractal regime extends all the way to the homogeneous regime, there is an intersection point between the two regimes. The radius which corresponds to this intersection point is called the correlation length ζ and is an indication of the average size of the aggregates. In many

systems, however, there will be a finite cross-over regime between the fractal and homogeneous regime, which can, for example, be due to the existence of clusters of various sizes and shapes. In this case, the correlation length can be defined by linear extrapolation of the fractal and homogeneous scaling regime to the intersection point.

In our results, from a distance of $5a - 10a$, the regime is indeed found to be homogeneous (Figure 3.11). The regime is clearly non-homogeneous for smaller distances, but the slope varies with the distance. This indicates that aggregates are present, but that the fractal dimensionality varies with the distance from the center of the aggregate. The averaged size of the aggregates can be obtained from the point where the non-homogeneous regime turns into the homogeneous regime; a constant fractal dimensionality is not required. Therefore, the correlation length was assessed by determining the distance r/a where the fit value, obtained by linear regression of the $\log(n(r))-\log(r/a)$ -plot at distances r/a larger than 10, deviated more than 5% from the actual value of $\log(n(r))$. These data are also given in figure 11. The correlation length is found to depend on the cylinder area fraction in the system as well as on $Re_{\text{shear,p}}$. The lowest correlation length of $2.3a$ is found for an area fraction of 0.40 and $Re_{\text{shear,p}} = 0.023$. For area fractions of 0.10 and 0.25, the correlation lengths were $4.0a$ and $3.9a$, respectively ($Re_{\text{shear,p}} = 0.023$). With increasing $Re_{\text{shear,p}}$, the correlation length tends to increase, to maximal $7.5a$, $6.9a$ and $5.3a$ for area fractions of 0.10, 0.25 and 0.40, respectively. The largest clusters are again found at the lowest area fraction.

Compared to the pair-distribution functions, these results provide additional information about the size of the clusters. The results agree well with each other; the largest effects of $Re_{\text{shear,p}}$ on the microstructure are found for the lowest area fractions. Moreover, the trends in the effects of $Re_{\text{shear,p}}$ on the microstructure agree well with the effects on shear-induced diffusion. It seems likely that the microstructure is the coupling factor for the effect of $Re_{\text{shear,p}}$ on shear-induced diffusion. The development of particle clustering might, moreover, be related to the longer and closer approach of two interacting particles at higher shear rates. This direct relationship with microstructure does, however, not exist for the viscosity of the suspension, where not only the microstructure seems to be important but also the averaged solid volume fraction, resulting in a more pronounced effect of $Re_{\text{shear,p}}$ at high area fractions [47]. Because of the direct coupling between microstructure and shear-induced diffusion, it can be expected that other factors that can affect the microstructure, such as attractive colloidal forces between the particles, will also affect shear-induced diffusion.

In our results, $Re_{\text{shear,p}}$ starts to have a significant effect on the shear-induced diffusivity at a value of about 0.1. In practical systems, for a suspension with particles with a radius a of $3 \mu\text{m}$, for example, a shear rate of about 2800 s^{-1} would be required in order to obtain this significant effect. For larger particles, this value quickly drops to even lower values. The shear rate in this example is well within the range of commonly applied shear rates, which indicates the relevance of this study to practical systems.

3.6 Conclusions

In this study, the LB method was applied in order to examine the effects of shear rate on the flow behaviour and microstructure of non-Brownian suspensions in a Couette system. In the shear regime studied, inertial effects on a single cylinder were negligibly small.

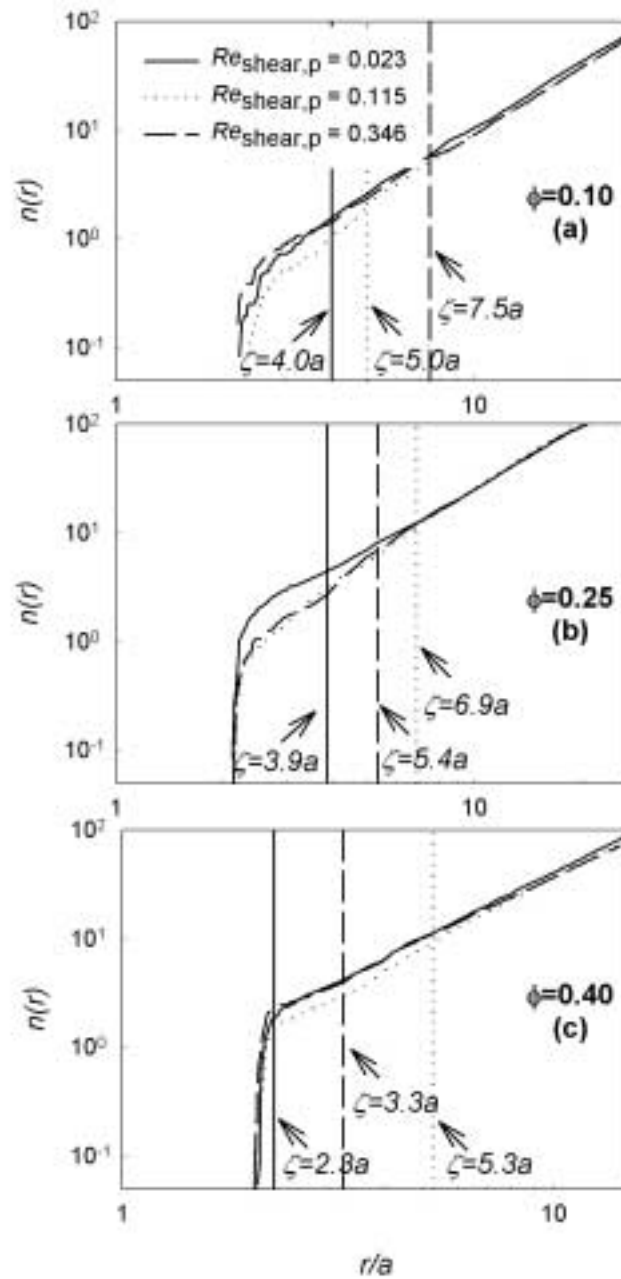


Figure 3.11: The number of cylinders $n(r)$ contained in a circle of radius r for a 2D suspension in shear flow with a cylinder area fraction of 0.10 (a), 0.25 (b) and 0.40 (c) at $Re_{\text{shear,p}} = 0.023-0.346$. The values are time-averaged over a strain $\dot{\gamma}t$ from 30 to 60. The correlation length ζ represents the distance where the cylinder distribution changes from non-homogeneous into homogeneous.

In a system with two interacting cylinders, however, some effects of the shear rate were present. First, the cylinders approached each other more closely and during a longer time with increasing shear rate, which is in accordance with expectations when inertia causes them to move to other streamlines. Secondly, at $Re_{\text{shear,p}}$ higher than 0.06, the particle trajectory started to become asymmetric, finally leading to a dispersal of the two particles. The viscosity was also dependent on the shear rate in the shear regime studied: the suspension namely exhibited shear thickening behaviour.

In order to know how we could reliably evaluate shear-induced self-diffusion in our system, first, the displacements of the particles were monitored as a function of strain. The simulations clearly showed that shear-induced self-diffusion is a long-time diffusive behaviour, which typically only established itself after a strain of about 5-10. Furthermore, it is shown that at least a few hundred suspended particles are needed in the simulations to resolve shear-induced diffusion coefficients reliably. For systems with fewer than 100 particles, the suspended particles interact with their periodic images over the periodic boundaries in the system, leading to an underestimation of the diffusion coefficients.

Following the developed method, the effect of $Re_{\text{shear,p}}$ up to 0.35 on shear-induced self-diffusion was investigated for particle fractions of 0.10, 0.25 and 0.40. In contrast to theory for the Stokes flow regime, which predicts a linear increase of the diffusivity with shear rate, the mean square particle displacements were found to increase faster at increasing $Re_{\text{shear,p}}$, leading to a similar increase of the dimensionless shear-induced diffusion coefficient $D_{yy}/\dot{\gamma}a^2$. This increase was most pronounced at particle fractions of 0.10 and 0.25 and started already at $Re_{\text{shear,p}}$ equal to 0.05-0.07, which is comparable to the shear regime where effects on two interacting particles and the viscosity arose.

Analysis of the microstructure of the suspensions revealed that an increase of $Re_{\text{shear,p}}$ leads to an increase of particle clustering, especially at particle fractions of 0.10 and 0.25. The effects of $Re_{\text{shear,p}}$ on particle clustering relate well to the effects on shear-induced diffusion, indicating that the microstructure of suspensions is a key factor for shear-induced diffusivity. This will be very relevant for suspensions with attractive inter-particle forces.

Acknowledgements

Friesland Foods is greatly acknowledged for supporting this research. Prof Dr Mike Cates and Dr Kevin Stratford from Edinburgh University as well as Dr Joost van Opheusden from Wageningen University are greatly thanked for fruitful discussions. The authors would like to acknowledge the support of the Dutch Ministries of Economic Affairs, Education, Culture and Sciences and of Housing, Spatial Planning and the Environment through a grant of the Dutch Program Economy, Ecology and Technology and the support of the European Commission through grant number HPRI-CT-1999-00026 (the TRACS Programme at EPCC).

3.7 Lubrication force in a 2D suspension

We apply lubrication theory to calculate the hydrodynamic force between two cylinders in a 2D suspension. For small gaps (i.e. rim to rim distances) $2h$ the force between two adjacent cylinders can be calculated, solving the flow field in the gap upto first order in

$\epsilon = h/a$. In the calculation two cylinders are considered, approaching each other with a velocity $2U$. A Cartesian coordinate system ($\mathbf{e}_x, \mathbf{e}_z$) was used with the origin at the center of the gap. The z -coordinate, taken along the line of centers, was scaled on h and the x -coordinate was scaled on \sqrt{ah} ; the z -component of the velocity was scaled on U , the x -component on $\sqrt{a/h}U$. The pressure was scaled on $a\eta U/h^2$. Under these conditions, the differential equation for the dimensionless streamfunction ψ becomes:

$$\frac{\partial^4 \psi}{\partial z^4} + 2\epsilon \frac{\partial^4 \psi}{\partial x^2 \partial z^2} + \epsilon^2 \frac{\partial^4 \psi}{\partial x^4} = 0 \quad (3.7.1)$$

The rim of both disks is described by $z = \pm b(x)$ with

$$b(x) = 1 + \frac{1}{2}x^2 + \epsilon \frac{1}{8}x^4 + \epsilon^2 \frac{1}{16}x^6 + \dots \quad (3.7.2)$$

and the boundary conditions on these rims read:

$$v_z = - \frac{\partial \psi}{\partial x} = \mp 1, \quad (3.7.3)$$

$$v_x = \frac{\partial \psi}{\partial z} = 0, \quad (3.7.4)$$

For convenience, $\psi = 0$ is chosen at $z = 0$, so ψ is odd in z . This equation can be solved assuming

$$\psi = \psi_0 + \epsilon \psi_1 + \dots \quad (3.7.5)$$

where ψ_0 fulfils the boundary conditions (3.7.3) and (3.7.4) and $\partial \psi_1 / \partial x = \partial \psi_1 / \partial z = 0$ on the rim of the particle. The solution is given by:

$$\psi_0 = \frac{1}{2}x \left(3 \left(\frac{z}{b} \right) - \left(\frac{z}{b} \right)^3 \right) \quad (3.7.6)$$

$$\psi_1 = \frac{3}{20}g(x) \left(\frac{z}{b} \right) \left(1 - \left(\frac{z}{b} \right)^2 \right)^2 \quad (3.7.7)$$

where $g(x) = 4x(b')^2 - 2bb' - xbb''$ and b', b'' are the first and second derivatives of $b = b(x)$, respectively. The pressure along the line $z = 0$ can be calculated by integrating:

$$\left(\frac{\partial p}{\partial x} \right)_{z=0} = -3b^{-3} \left(x + \epsilon \left(\frac{3}{5}g(x) - \frac{1}{2}f(x) \right) \right) \quad (3.7.8)$$

where $f(x) = 2x(b')^2 - 2bb' - xbb''$. The zz -component of the total stress tensor (the superfix $^{[D]}$ indicates the dimensional form)

$$T_{zz}^{[D]} = -p^{[D]} + 2\eta \frac{\partial v_z^{[D]}}{\partial z^{[D]}}$$

reads in dimensionless form

$$T_{zz} = -p + 2\epsilon \frac{\partial v_z}{\partial z} = -p - 2\epsilon \frac{\partial^2 \Psi}{\partial x \partial z}$$

where also T_{zz} has been scaled on $p_0 = a\eta U/h^2$. The (dimensionless) force per unit length, F , on the particle is calculated by integrating T_{zz} along the line $z = 0$ (swopping the order of integration of the $\partial p/\partial x$ term):

$$\begin{aligned} F(\epsilon) &= 2 \int_0^\infty (T_{zz})_{z=0} dx \\ &= 2 \int_0^\infty x \left(\frac{\partial p}{\partial x} \right)_{z=0} dx - 4\epsilon \int_0^\infty \left(\frac{\partial^2 \Psi}{\partial x \partial z} \right)_{z=0} dx \\ &= \int_0^\infty \frac{3x}{b^3(x)} \left(2x + \epsilon \left(\frac{6}{5}g(x) - f(x) \right) \right) dx - 4\epsilon \int_0^\infty \frac{3}{2b^2}(b - xb')dx \end{aligned} \quad (3.7.9)$$

This expression can be rewritten as:

$$F(\epsilon) = F_0 + \epsilon(F_1 - F_2)$$

where

$$\begin{aligned} F_0 &= \int_0^\infty \frac{6x^2}{(1 + \frac{1}{2}x^2)^3} dx = \frac{3}{4}\pi\sqrt{2} = 3.3322 \\ F_1 &= \int_0^\infty \frac{3x}{(1 + \frac{1}{2}x^2)^3} \left(\left(\frac{25}{10}x^3 - \frac{3}{5}x - \frac{6x^5}{(8 + 4x^2)} \right) \right) dx = \frac{207}{80}\pi\sqrt{2} = 11.496 \\ F_2 &= \int_0^\infty 6 \frac{(1 - \frac{1}{2}x^2)}{(1 + \frac{1}{2}x^2)^2} dx = 0.0 \end{aligned}$$

are numerical constants. In our simulations, we have erroneously used a value of $F_1 = 12.829$, which lead to about 1% overestimation of the lubrication force. The lubrication force per unit length in dimensional form, $F^{[D]} = p_0\sqrt{ah}F$, follows from Equation 3.7.9 as:

$$F^{[D]} = \left(\frac{h}{a} \right)^{-3/2} \eta U F(h/a) = \left(\frac{h}{a} \right)^{-3/2} \eta U \left(F_0 + \frac{h}{a} F_1 \right) \quad (3.7.10)$$

which expression is correct in first order of ϵ .

Shear-induced self-diffusion in bidisperse suspensions

Shear-induced diffusion is an important transport mechanism in concentrated suspensions in shear flow, and is relatively well understood, but only for monodisperse suspensions. Presently, not much attention is paid to shear-induced diffusion in polydisperse suspensions, in spite of the widespread incidence of these suspensions. This paper addresses shear-induced diffusion in bidisperse suspensions. Our study is carried out by means of computer simulations on two-dimensional suspensions in a Couette system, following the Lattice Boltzmann method. Two aspects were found to be of particular importance, namely particle clustering and the dominance of large particles. From the shear thickening behaviour of the suspensions at non-zero Reynolds numbers, which is known to be highly correlated with particle clustering, it became clear that particle clustering increased with increasing relative fraction of large particles and with increasing size of the large particles. This effect is explained with the fact that larger particles experience more inertia. This is opposite to what happens in the Newtonian regime, where the viscosity of bidisperse suspensions is always lower than that of corresponding monodisperse suspensions. Because particle clustering also induces an increase of shear-induced diffusivity, the presence of large particles can amplify this increase.

The second aspect is the dominance of large particles over small particles. It is found that when the relative area fraction of large particles exceeds 0.3, the shear-induced diffusivity is totally determined by these large particles, in other words the small particles behave as 'slave particles'. In this situation, their shear-induced diffusivity could be strongly increased by the presence of the large particles. Below this relative fraction of 0.3, the large particles did not have a specific effect on the small particles. The shear-induced diffusivity of the large particles was much lower than expected for a monodisperse suspension. When the relative fraction of large particles exceeded 0.3, the shear-induced diffusivity of the large particles increased to a level that would be expected for the suspension without the small particles. The results presented in this paper are relevant for prediction of rheology and shear-induced mass transport in polydisperse suspensions.

4.1 Introduction

Shear-induced diffusion is a transport phenomenon that occurs in concentrated suspensions under shear flow. It is important for various processes, such as sedimentation and filtration, and for transport of suspensions, such as in pipes and channels. In a previous paper [39], we addressed the topic of shear-induced self-diffusion in non-Brownian suspensions at non-zero Reynolds numbers. These suspensions were monodisperse, as in most other studies on shear-induced self-diffusion (see e.g. [27, 50]). Because in general, industrially relevant suspensions are not monodisperse, but have a relatively broad particle size distribution, it is important to understand the effects of polydispersity. In this paper we address shear-induced self-diffusion in suspensions containing particles with a bimodal size distribution, hereafter shortly called bidisperse suspensions.

In concentrated suspensions undergoing shear flow, hydrodynamic particle interactions are responsible for the shear-induced diffusion process. This leads to particle displacements in the fluid velocity direction, as well as in the velocity gradient and in the vorticity direction, but in an anisotropic way. Because the mechanism is different from

that of Brownian diffusion (thermal fluctuations) and turbulent diffusion (inertial effects), shear-induced diffusion becomes important at conditions of high Péclet numbers, where it dominates Brownian diffusion, and of low Reynolds numbers, where turbulent diffusion is not yet strong. The Péclet number is defined as $Pe = 8\mu_f a^3 \dot{\gamma} / kT$, where μ_f is the dynamic viscosity of the fluid phase, a is the particle radius, $\dot{\gamma}$ is the shear rate, k is the Boltzmann constant and T the absolute temperature. The relevant Reynolds number is the shear based particle Reynolds number, which is defined as $Re_{\text{shear,p}} = 4\dot{\gamma}a^2/\nu$, where ν is the kinematic viscosity.

When addressing the topic of shear-induced diffusion, two types of behaviour need to be distinguished. The first is shear-induced self-diffusion, which concerns the behaviour of suspended particles in a homogeneous suspension and reflects the mobility of individual particles in such a suspension. The second is shear-induced migration, which concerns collective particle migration processes and leads to macroscopically observable effects such as viscous resuspension [64], particle size segregation [65] and net migration of particles within inhomogeneous shear flows [15].

Only a few studies address the topic of shear-induced diffusion in non-monodisperse suspensions. Moreover, the majority of these studies considers the effects of polydispersity in systems with non-homogeneous particle concentrations, where shear-induced migration plays a role, like e.g. in pipe flow, systems with curvature (parallel-plate geometry, wide-gap Couette device) and systems with particle sedimentation (see e.g. [65–68]). As far as we know, up to now, the subject of shear-induced self-diffusion in bi- or polydisperse suspensions has not been addressed at all. Therefore, we first review the work on shear-induced migration in non-monodisperse suspensions and afterwards consider the effects of particle polydispersity in a wider perspective. The rheological behaviour of particulate suspensions is put forward to reveal some relevant aspects of flow of non-monodisperse suspensions.

Experimental studies on shear-induced migration in bidisperse suspensions mostly report an overall suspension behaviour that is similar to monodisperse suspensions. In pipe flow for example, as for monodisperse suspensions, high overall particle concentrations were found in the centre of the channel, where the shear rate is lowest, in the presence of blunted velocity profiles [68, 69]. Overall shear-induced diffusivities for bidisperse suspensions are sometimes reported to be somewhat less than for the monodisperse suspensions with the respective small and large particles [67]. While aforementioned studies focused on well-mixed bidisperse suspensions, some other studies reported on the phenomenon of shear-induced size segregation in bidisperse suspensions [68, 70]. In systems with a spatially varying strain rate, as for example in pipe flow, particle size segregation as well as non-uniform overall particle distributions can occur. When size segregation occurs, the larger particles are mostly enriched in regions with lower shear rates. The distribution of the smaller particles can also be non-uniform, but this only seems to occur at higher concentrations than for large particles. A notable exception on this behaviour is reported by Krishnan and others [65], who measured particle segregation in a parallel plate device. Tracer particles that were larger than the bulk particles, were found to migrate to regions of higher stress instead of lower stress. This behaviour was explained in terms of a curvature-induced migration flux.

Numerical work on shear-induced migration in polydisperse suspensions is scarce. In the field of analytical models however, some progress has been achieved. A phenomenological model for shear-induced migration, based on particle migration mechanisms pro-

posed by Leighton and Acrivos [15], Phillips and others [16] and Krishnan and others [65], was extended to a model for polydisperse suspensions by Shauly and others [71]. This model was found to predict experimental data on shear-induced migration well, both size segregation and migration of large and small traces were recovered. Because the model is based on dimensional and phenomenological considerations, while the explicit forms of the effective properties are, as yet, unknown, successful application of this model depends on the available knowledge of these effective properties. As an example, the effective viscosity of the suspensions under consideration should be known.

Numerous experimental as well as numerical work reports on the viscosity of bidisperse suspensions (see e.g. [72–75]). They all consider the viscosity in the region of low shear rates ($Re_{\text{shear,p}} \ll 1$), where the viscosity is independent of the shear rate (Newtonian regime). Differences with the viscosity of monodisperse suspensions are found when the total volume fraction exceeds a value of about 0.40. At these high fractions, the viscosity of bidisperse suspensions is lower than of monodisperse suspensions. The minimum viscosity is reached when the relative volume fraction of small particles is about 0.25 to 0.35 [74, 76]. Probstein and co-workers [75] proposed an approach for the viscosity of bidisperse suspensions, in which the maximum packing concentration for a bidisperse suspension ϕ_{max} is calculated in relation to the maximum packing fraction for a monodisperse suspension $\phi_{\text{max}0}$:

$$\frac{\phi_{\text{max}}}{\phi_{\text{max}0}} = \left[1 + \frac{3}{2} |b|^{3/2} \left(\frac{\phi_1}{\phi} \right)^{3/2} \left(\frac{\phi_2}{\phi} \right) \right] \quad (4.1)$$

where $b = (a_1 - a_2) / (a_1 + a_2)$, a_1 and ϕ_1 are the radius and the local concentration of species 1 and a_2 and ϕ_2 are the radius and the local concentration of species 2 ($a_1 > a_2$). Chang and Powell [72] found that when the relative viscosity of bidisperse suspensions is related to the volume fraction after normalisation with the maximum packing fraction, one mastercurve is obtained, that accurately describes experimental as well as numerical viscosities for three-dimensional (3D) as well as two-dimensional (2D) suspensions. The reduction of viscosity compared to monodisperse suspensions is explained by the authors with differences in microstructure of the suspensions. As already put forward by Bossis and Brady [77] for monodisperse suspensions, high viscosities have been related to the formation of particle clusters in the suspensions. Bidisperse suspensions are thought to have smaller average clusters at a fixed total volume fraction, due to the presence of smaller particles. This effect of bidispersity on particle clustering might be relevant for shear-induced diffusion as well, because we already noticed before that particle clustering strongly affects shear-induced diffusion for monodisperse suspensions [39].

The aim of the present work was to study shear-induced self-diffusion in bidisperse suspensions. In order to do this, we applied the same numerical technique as in our previous study [39], namely the Lattice Boltzmann (LB) method for particulate suspensions, originally developed by Ladd [29, 30]. In another study [78], we have noticed that 3D LB simulations on shear-induced self-diffusion are computationally very intensive. Since it is also shown that simple scaling relations suffice for the transposal of 2D simulation results into data for 3D real systems [78], this study comprises a 2D study. In contrast to the often applied Stokesian dynamics method, the LB method is not only suited for the Stokes flow regime, but also for higher Reynolds number flows. Because of the practical interest of higher Reynolds number flows and the lack of knowledge on the rheological

behaviour of bidisperse suspensions at these higher Reynolds numbers, the first part of our work is devoted to these effects. The second part focuses on shear-induced self-diffusion of bidisperse suspensions and the observed behaviour is related to the rheological behaviour. Finally, we draw conclusions about the effect of Reynolds number and particle interactions on shear-induced self-diffusion in bidisperse suspensions.

4.2 Computer simulation method

The LB method has already extensively been explained in literature (see e.g. [34]). Here, we will only briefly recapitulate some general information about the LB method so that the emphasis is more on specific aspects of our own model.

The LB method models a compressible fluid (in which the speed of sound is finite) in the limit of low Mach number (Ma =flow velocity/speed of sound), by solving the discretised Boltzmann equation for fictitious fluid particles, that are constrained to move on a lattice. The state of the fluid is characterised by the single-particle distribution function $f_i(\mathbf{x}, t)$, describing the average number of particles at a particular node of the lattice \mathbf{x} , at a time t , with the discrete velocity \mathbf{c}_i , which brings the fluid particles in one time step to an adjacent lattice node. In the simulations described in this paper, the fluid dynamics were solved with a D2Q9 LB scheme, which is defined on a 2D square lattice with rest particles and 8 non-zero particle velocities. The velocity directions link lattice sites to its nearest and next-nearest neighbours. The hydrodynamic field's mass density ρ , momentum density \mathbf{j} , and the momentum flux density Π are moments of this velocity distribution:

$$\rho = \sum_i f_i, \mathbf{j} = \sum_i f_i \mathbf{c}_i, \Pi = \sum_i f_i \mathbf{c}_i \mathbf{c}_i \quad (4.2)$$

The fictitious fluid particles evolve by collisions and subsequent propagation to neighbouring lattice sites. In a collision step, the distribution function is relaxed towards the local equilibrium distribution according to:

$$f_i(\mathbf{x} + \Delta \mathbf{x}_i, t + \Delta t) = f_i(\mathbf{x}, t) - \frac{f_i(\mathbf{x}, t) - f_i^{eq}(\mathbf{x}, t)}{\tau} \quad (4.3)$$

The relaxation time τ controls the relaxation of the viscous stress in the fluid and is linked to the kinematic viscosity ν via:

$$\nu = c_s^2 \left(\tau - \frac{1}{2} \right) \Delta t \quad (4.4)$$

where the speed of sound c_s is defined by $c_s^2 = c^2/3$. In our simulations we applied $\tau = 1.0$ (in lattice units), which corresponds to a kinematic viscosity ν of the fluid of $1/6$ (in lattice units). The equilibrium distribution $f_i^{eq}(\mathbf{x}, t)$ is chosen such that the Navier-Stokes equations for a weakly compressible system are obtained [37].

In the LB scheme for particulate suspensions as developed by Ladd [29], the solid particles are defined by a boundary surface, which can be of any size or shape. The spherical (3D) or circular (2D) particles are projected on the lattice, where the boundary surface cuts some of the links between lattice nodes. Fluid particles moving along the boundary surface interact with the surface at boundary nodes that are located at the lattice nodes

nearest to the boundary surface of the solid particles, following an alternative method to Ladd's, that was developed by Behrend [38]. In this method, called relaxed bounce back conditions at the nodes, the LB collisions are carried out at every node, including the boundary nodes. The collision rules at the boundary surface enforce a stick boundary condition on the fluid, which means that the fluid velocity is matched to the local solid-body velocity \mathbf{u}_b . This local solid-body velocity \mathbf{u}_b (at position \mathbf{x}_b) is determined by the solid-particle velocity \mathbf{U} , its angular velocity Ω and the position of its center of mass \mathbf{R} :

$$\mathbf{u}_b = \mathbf{U} + \Omega \times (\mathbf{x}_b - \mathbf{R}) \quad (4.5)$$

After the collision phase, the boundary nodes are updated in the following way:

$$f_i(\mathbf{x} + \Delta\mathbf{x}_i, t + \Delta t) = f'_{-i}(\mathbf{x}, t) + \frac{2\rho w_i}{c_s^2} \mathbf{u}_b \cdot \mathbf{c}_i \quad (4.6)$$

$$f_i(\mathbf{x} - \Delta\mathbf{x}_i, t + \Delta t) = f'_i(\mathbf{x}, t) - \frac{2\rho w_i}{c_s^2} \mathbf{u}_b \cdot \mathbf{c}_i \quad (4.7)$$

For moving suspension particles, in this update, momentum is exchanged between the incoming particles from the fluid and the solid side (the combined momentum of the fluid and the solid phase is however conserved). From this momentum exchange the force and torque exerted on a suspension particle is calculated. Hereafter the kinematic properties of the suspension particles themselves are updated with a simple Euler forward integration of Newton's second law.

By the projection of the suspended particles on the lattice, a discrete representation of the surface is obtained, which becomes more and more precise as the surface curvature gets smaller and which is exact for surfaces parallel to lattice planes. Together with the choice of the location of the boundary nodes and the boundary update rules, the discretisation of the particle surface onto the lattice induces a hydrodynamic particle diameter that is slightly larger than the diameter based on the number of occupied lattice nodes [29]. It is therefore often proposed that the particle diameter should be corrected for this hydrodynamic effect. The magnitude of the correction is mostly based on the particle behaviour in the Stokes flow regime and at low particle concentrations. As also presented in an earlier paper [39], we have seen that in suspensions in shear flow, particles can approach each other very close, such that particles would largely overlap when the hydrodynamic particle size would be taken into account. The closest approach distance is moreover found to be dependent on conditions such as the particle concentration and the shear rate. Since assessment of the hydrodynamic particle diameter in these systems is virtually impossible, while the corrections would probably be very small, we did not apply this correction but used the input particle diameter in our calculations.

Since a suspended particle is essentially simulated by the introduction of a boundary surface, separating the interior of the particle from the exterior, the interior of the particle also consists of fluid. Ladd [30] examined the effects of the interior fluid on the behaviour of the particle. With a sufficiently high effective mass of the particle, the interior fluid only contributes an inertial force due to the extra mass of the particle. Our computations were carried out in this regime, with an effective mass ρ_s/ρ of 10. The magnitude of the inertial effects in our computations was limited because $Re_{\text{shear,p}}$ was relatively small. Moreover, by comparing simulation results with an effective mass of 3 and 10, we found that the relatively high effective particle mass did not contribute to the observed effects on the

viscosity and shear-induced diffusion in this paper. The observed effects of changing Re therefore seem to be caused by fluid inertial effects and not by the inertia of the particles.

Since shear-induced diffusion is mainly governed by hydrodynamic particle interactions, these interactions need to be accurately resolved in the computations. When two suspension particles come into close contact with each other, the lubrication force becomes important. This force is caused by the attenuation of the fluid film in the gap between the two particles and is repulsive upon approach and attractive upon separation of the particles. When the gap width between two particles is in the order of one lattice spacing, the lubrication force is however not exactly resolved with the LB method. This is due to the discretisation of the particles and fluid on a grid and is a problem that is encountered by all numerical methods. To overcome this problem we applied an explicit calculation of the lubrication force when the gap width was smaller than two lattice units ($= 0.25a$). Since we considered a 2D system, we used the following equation for the lubrication force per unit length F , which is valid for the lubrication force between two cylinders [39]:

$$F = \frac{1}{2}\eta\mathbf{U}_{12}\cdot\hat{\mathbf{R}}_{12} \left(\left(\frac{a_1 + a_2}{h} \right)^{\frac{3}{2}} \left(F_0 + \frac{h}{a_1 + a_2} F_1 \right) - \left(\frac{a_1 + a_2}{h_c} \right)^{\frac{3}{2}} \left(F_0 + \frac{h_c}{a_1 + a_2} F_1 \right), h < h_c \right) \quad (4.8)$$

$$F = 0, h > h_c$$

where $\mathbf{U}_{12} = \mathbf{U}_1 - \mathbf{U}_2$, $h = |\mathbf{R}_{12}| - (a_1 + a_2)$ is the gap (distance between the particle surfaces), F_0 is the numerical constant $\frac{3}{4}\pi\sqrt{2} = 3.3322$ and F_1 is the first order correction for the lubrication limit $h/2a \ll 1$ with a value of $\frac{231}{80} \cdot \pi \cdot \sqrt{2} = 12.829$. The unit vector $\hat{\mathbf{R}}_{12} = \mathbf{R}_{12}/|\mathbf{R}_{12}|$. In accordance with Ladd and Verberg [33], we applied a correction on the lubrication force to account for the lubrication force that is already resolved in the computations of the fluid dynamics. This was done by subtracting the lubrication force at a cut-off distance h_c from the total lubrication force, as indicated in Eq. 4.8. The cut-off distance h_c represents the cut-off distance between the particle surfaces for the added lubrication force and was chosen equal to two lattice units ($= 0.25a$) in our study. For 3D systems, Nguyen and Ladd [40] showed that this correction leads to more accurate results for particle interactions at short interparticle distances, even with neutrally buoyant particles very near to contact and without causing instabilities in the particle dynamics.

We have noticed, that in suspensions with relatively high particle fractions or at high particle Reynolds number, particle clustering and overlap can occur, which greatly affects the diffusive behaviour of the particles. This behaviour seems to be correlated with the lubrication breakdown of concentrated colloids, that was reported by Ball and Melrose [41]. As suggested by these authors, we applied a Hookean spring force between the particles to avoid this clustering and overlap. This Hookean spring force was applied for gaps h smaller than a thickness δ and was applied in the direction of the line of particle centres, according to:

$$F_h = F_0 - \left(\frac{F_0}{\delta} \right) h \quad (4.9)$$

with a maximal Hookean spring force F_0 of 10.0 (in lattice units). The Hookean spring force is active in a layer around the particle with a thickness $\delta/2$ of 0.05 lattice units

(= 0.00625 a). When using the LB model as described above, we found a good agreement between our computer simulation results for the viscosity and model results of the Krieger-Dougherty model (particle fractions between 0.05 to 0.55), which is known to describe experimental data well. Especially at high particle fractions, the viscosity is known to be highly dependent on particle interactions. The good agreement with the Krieger-Dougherty model therefore indicates that our model captures the particle behaviour well.

For reasons of clarity, we chose to denote the suspended cylinders as particles, although our system actually consists of a 2D suspension. The simulation results are presented in dimensionless parameters to make interpretation easier. Unless otherwise stated, length scales are normalised with respect to the particle radius of the smallest particle in the system (=8.0 lattice units).

4.3 Rheology and microstructure of bidisperse particle suspensions at non-zero Reynolds numbers

In our previous paper [39], we showed that the shear-induced diffusive behaviour of the suspended particles is affected by particle clustering, which was found to be increasingly relevant with increasing $Re_{\text{shear,p}}$. The viscosity of hydrodynamically interacting hard sphere suspensions is known to be affected by particle clustering, which coincides with a shear thickening behaviour of the suspension [68]. This was confirmed in our previous paper as well. To obtain a better understanding of shear-induced diffusion in bidisperse suspensions, it is therefore relevant to analyse rheology and microstructuring phenomena in these suspensions. In addition to particle clustering, bidisperse suspensions can also exhibit particle size segregation, which may also affect shear-induced diffusion. Although the velocity profile is in principle linear in our Couette system, we have noticed that the presence of the walls can induce nonlinearity, especially at high particle fractions. Herewith, the shear rate can spatially vary and this might invoke particle size segregation, in a similar way as for pressure-driven flow [68, 70].

In order to analyse the rheology and microstructure of bidisperse suspensions, we carried out computer simulations on 2D suspensions in Couette flow. The distance between the two moving walls was 64.75 a and the distance between the two periodic boundaries 32.375 a . The simulation box was filled with a varying number of suspension particles, up to a maximum of 375. The radius of the smallest particle a in the bidisperse suspension was always equal to 8.0 lattice units, while the radius of the largest particle depended on the size ratio. Shear flow was created by moving the walls with constant velocity in opposite directions. This resulted in $Re_{\text{shear,p}}$ varying between 0.003 and 0.66. In this paper, the viscosity is normalised for the viscosity according to the Krieger-Dougherty model [46], which holds for a monodisperse suspension in the Newtonian regime:

$$\eta_r = \left(1 - \frac{\langle\phi_s\rangle}{\phi_{\text{max}}}\right)^{-[\eta]\phi_{\text{max}}} \quad (4.10)$$

where $\langle\phi_s\rangle$ is the averaged particle fraction and ϕ_{max} , the maximum packing fraction, has a value of 0.82 for a 2D suspension. The dimensionless factor $[\eta]$ is the intrinsic relative viscosity of the suspension and has a value of 2 for a 2D suspension. By means of this normalisation procedure, it can easily be seen when the actual viscosity deviates from

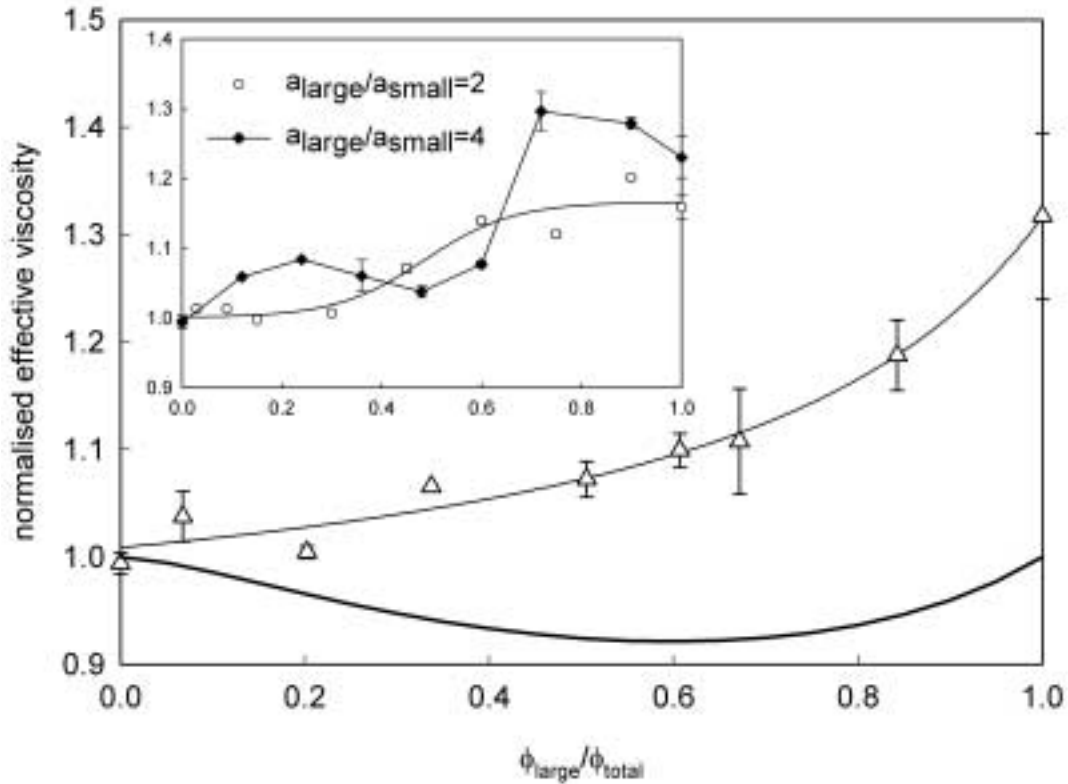


Figure 4.1: Simulation results for the viscosity of a 2D bidisperse suspension ($\phi_{\text{total}}=0.40$, $a_{\text{large}}/a_{\text{small}}=3$) as a function of the relative fraction of large particles $\phi_{\text{large}}/\phi_{\text{total}}$ at a $Re_{\text{shear,p}}$ (calculated for the smallest particles) of 0.012. The viscosity is normalised for the viscosity according to the Krieger-Dougherty model. The error bars indicate the standard deviation. The line without symbols represents model calculations for the viscosity in the Newtonian regime, according to Eq. 4.1 [75]. The inset presents similar results but for $a_{\text{large}}/a_{\text{small}}=2$ and 4. The lines connecting the data points are drawn to guide the eye.

the viscosity that is predicted for a monodisperse suspension in the Newtonian regime ($\eta \neq 1$).

The viscosity of a bidisperse suspension was determined as a function of the relative fraction of large particles for a diameter ratio of large to small particles of 2, 3 and 4 (Figure 4.1). In contrast to the results of Chang and Powell [72, 73], the viscosity was not always lower than that of the respective monodisperse suspensions. This can be explained with the shear thickening behaviour of the suspension. For the large particles in the suspension, $Re_{\text{shear,p}}$ is respectively 4, 9 or 16 times higher than for the small particles at a certain shear rate, because of the proportionality of $Re_{\text{shear,p}}$ to a^2 . It can therefore be expected that the large particles exhibit more intense shear thickening and this probably causes the increase of viscosity with increasing fraction of large particles. In spite of this effect however, at first the viscosity remains relatively stable at low fractions of large particles, whereas it increases faster at relative fractions exceeding 0.5 – 0.6. This behaviour might be related to microstructuring phenomena in the bidisperse systems, as also occurs in the Newtonian flow regime. No clear minimum is observed in the viscosity

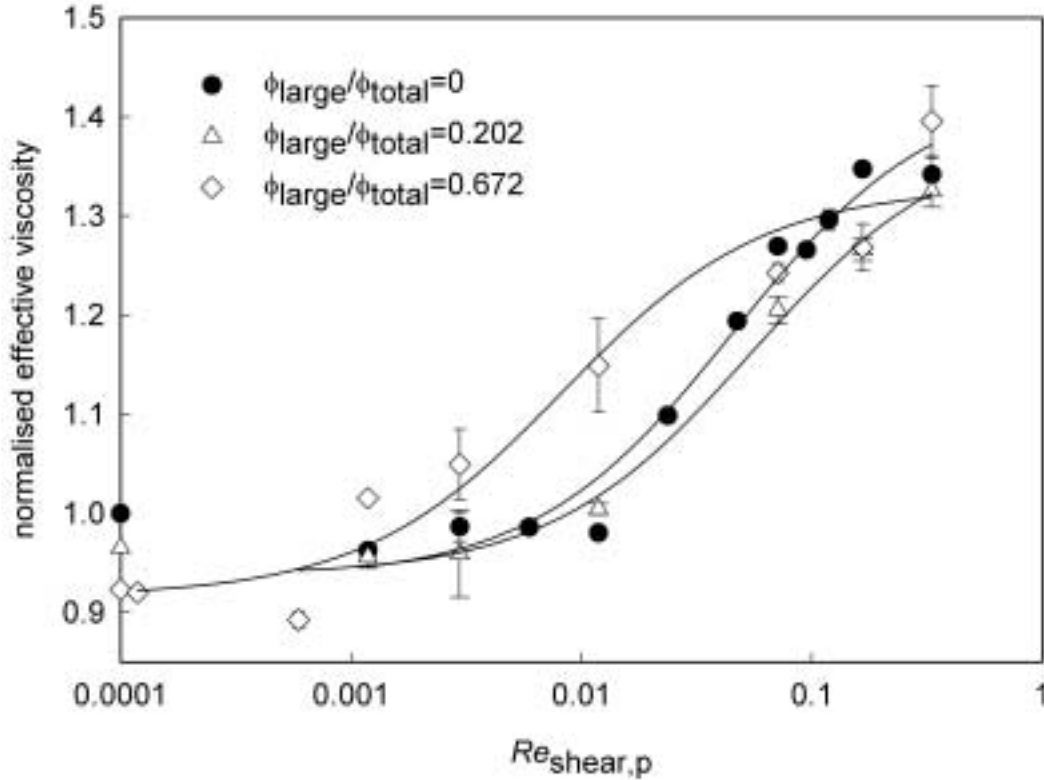


Figure 4.2: Viscosity dependence of 2D bidisperse suspensions ($\phi_{\text{total}}=0.40$, $a_{\text{large}}/a_{\text{small}}=3$) on $Re_{\text{shear},p}$ (calculated for the smallest particles) as compared to a monodisperse suspension. The viscosity is normalised for the viscosity according to the Krieger-Dougherty model. The symbols on the Y-axis represent model calculations for the viscosity in the Newtonian regime, according to Eq. 4.1 [75]. The error bars indicate the standard deviation and lines are drawn as a guide to the eye.

for diameter ratios of 2 and 3, which might be due to the dominance of the shear thickening behaviour of the large particles. The total area fraction of particles of 0.40 is still quite low as well, so that the decrease of viscosity compared to monodisperse suspensions (in the Newtonian regime) is small, less than 10%, as becomes clear from the model calculations in Figure 4.1. This is different for the suspension with a diameter ratio of 4. Although the effective viscosity does not become smaller than 1.0, a clear minimum is present at a relative fraction of 0.5 – 0.6. This seems to be a combined effect of 1) an intense shear thickening due to the large size of the largest particles and 2) intense microstructuring phenomena leading to a pronounced viscosity minimum, as predicted by Eq. 4.1 [75]. These results show that the viscosity of bidisperse suspensions can be affected by shear thickening, leading to higher viscosities with increasing fractions of large particles, which is in contrast to the Newtonian regime where the viscosity of bidisperse suspensions is lower than for monodisperse suspensions. The $Re_{\text{shear},p}$ for the largest particles in the suspension probably determines whether an effect of shear thickening will be present.

The shear thickening behaviour of bidisperse suspensions is investigated in more detail by examining the effect of $Re_{\text{shear},p}$ on the viscosity (Figure 4.2). The increase of

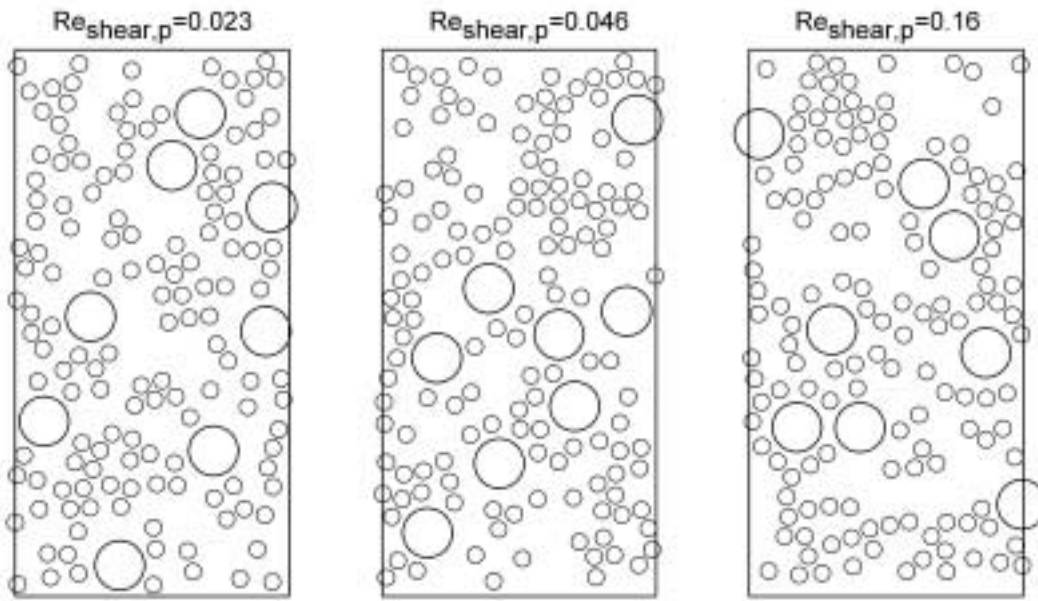


Figure 4.3: Snapshots of the particle configuration (2D bidisperse suspensions, $\phi_{\text{total}}=0.40$, $a_{\text{large}}/a_{\text{small}}=3$, $\phi_{\text{large}}/\phi_{\text{total}}=0.34$) at a $Re_{\text{shear,p}}$ (calculated for the smallest particles) of 0.023 (left), 0.046 (middle) and 0.16 (right).

viscosity with the $Re_{\text{shear,p}}$ was slightly dependent on the relative fraction of large particles. At a relative fraction of large particles of 0.672, the onset of shear thickening was at a lower $Re_{\text{shear,p}}$, which resulted in a higher viscosity. From a $Re_{\text{shear,p}}$ of about 0.1 upward, the viscosities were of the same order of magnitude again, due to the faster increase of viscosity of the other two suspensions with less large particles. The effects of shear on bidisperse suspensions do not differ fundamentally from the effects on monodisperse suspensions as presented in [39]. This can also be seen in Figure 4.3, where snapshots of the particle configurations are shown. At higher $Re_{\text{shear,p}}$, the particle clustering was more intense, in a comparable way as has been seen in monodisperse suspensions [39]. This figure also demonstrates that there was no important particle segregation of large and small particles in the system. In that respect, this figure can be considered illustrative for the other simulation results, where no particle segregation is found as well.

4.4 Shear-induced self-diffusion in bidisperse suspensions

Shear-induced self-diffusivity reflects the mobility of individual particles in a suspension under shear flow and can be determined from the individual diffusive particle displacements. Shear-induced diffusion is a so-called long-time diffusive behaviour, which shows stochastic behaviour after a longer time. The reason for this behaviour is that the motion of a given particle is in principle purely deterministic and dependent on the external velocity field and its interactions with all other particles in the system. Only when the initial particle configuration has drastically changed, do the particle displacements become random, due to the complex nature of the hydrodynamics. This long-time diffusive effect is

reflected in the definition of shear-induced self-diffusivity:

$$\mathbf{D}_s \equiv \lim_{t \rightarrow \infty} \frac{1}{2} \frac{d}{dt} \langle \mathbf{x}(t) \mathbf{x}(t) \rangle \quad (4.11)$$

\mathbf{D}_s denotes the shear-induced self-diffusivity tensor. The angle brackets denote an average over all particles in the system, while \mathbf{x} denotes the displacement of a single particle. The long-time diffusive character of shear-induced self-diffusion is also clear from the relation between mean square displacement of particles in a monodisperse suspension and the strain $\dot{\gamma}t$, as presented in our previous paper [39]. This relation exhibited a linear dependence, indicating that the behaviour has become stochastic, only after a strain $\dot{\gamma}t$ of about 8.

As is usual, we normalised all reported shear-induced diffusivities on $\dot{\gamma}a^2$. The shear rate $\dot{\gamma}$ and the particle radius a are relevant time and length scales in the system, so that after normalising, a dimensionless parameter is obtained that is independent from the actual velocities. In a 2D system, we distinguish components of the shear-induced self-diffusion tensor in the fluid velocity and in the velocity gradient direction and their diagonal component. The displacements in the velocity gradient direction are purely determined by the hydrodynamic interactions between the particles, whereas the displacements in the fluid velocity direction are mainly determined by the convective flow. In our system, the convective particle displacements are hard to assess with sufficient accuracy because of the time-dependent velocity fluctuations in the system and the characteristic shear flow pattern, which slightly deviates from perfectly linear. Because the component in the velocity gradient direction is most relevant for many practical situations, we have limited ourselves to the analysis of this latter component of the shear-induced diffusion tensor. Our system consists of a Couette system, with periodic boundaries in the flow direction and two moving walls in the velocity gradient direction. The distance between the boundaries was chosen such, that the obtained diffusion coefficients correspond with diffusion in an infinitely large system [39]. The distance between the two moving walls was twice as large as between the periodic boundaries. The simulation box contained a number of 200 or 150 particles, respectively with one size (monodisperse) or two different sizes (bidisperse). The simulation runs were started with a random particle distribution and position-dependent fluid and particle velocities according to linear shear flow.

The diffusion coefficient was determined from the regression coefficient in the linear part of the simulation curve of the mean square displacement versus the strain. In order to evaluate the effect of the initial particle configuration on the diffusion coefficient, we split the simulation curve of one simulation run into several curves with a strain span of 30, which start at different times and consequently at different initial positions. The final diffusion coefficient is the mean value of the diffusion coefficients that are obtained from these individual curves, mostly from two different simulation runs.

In Figure 4.4, we present the dependence of the shear-induced diffusivity on $Re_{\text{shear,p}}$ for the smallest particles in a bidisperse suspension with a relative fraction large particles of 0.34. The increase of shear-induced diffusivity with increased $Re_{\text{shear,p}}$ is probably caused by a stronger particle clustering, as can be observed visually in Figure 4.3. This effect of particle clustering may be the underlying cause of the effect on viscosity as well (see previous section). When comparing the bidisperse suspension with the monodisperse, it becomes evident that the shear-induced diffusivity is not only higher for a bidisperse suspension than for a monodisperse suspension, but also that the bidis-

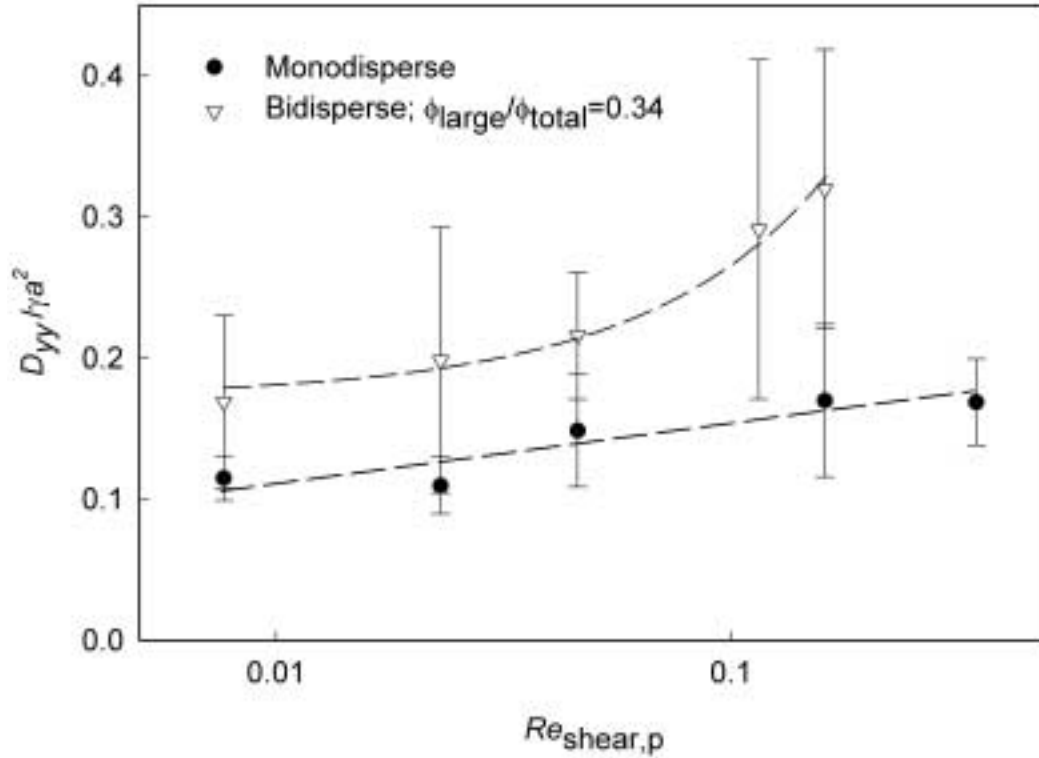


Figure 4.4: Component D_{yy} of the shear-induced self-diffusion coefficient of the small particles in a 2D bidisperse suspension ($a_{\text{large}}/a_{\text{small}}=3$, $N_{\text{total}}=150$) as compared to monodisperse suspensions ($N_{\text{total}}=200$) in shear flow as a function of $Re_{\text{shear},p}$ (calculated for the small particles) at a total particle area fraction $\phi_{\text{total}} = 0.40$. Error bars indicate the standard deviation. Lines are drawn to guide the eye.

perse suspension shows a larger increase with increasing $Re_{\text{shear},p}$. Both results indicate a more intense particle clustering and are probably due to the higher susceptibility of large particles to particle clustering.

We continue with results on shear-induced diffusivity at $Re_{\text{shear},p}=0.023$. It is clear from Figure 4.4 that the difference in shear-induced diffusivity between the monodisperse suspension and the bidisperse suspension at this $Re_{\text{shear},p}$ is relatively small, while the intensity of particle clustering is relatively low. This regime was therefore considered to be suitable for the analysis of interactions between large and small particles.

In order to investigate the volume fraction dependence of the shear-induced diffusivity for bidisperse suspensions, simulations were carried out with bidisperse suspensions with a diameter ratio of large to small particles of 3. In Figure 4.5, D_{yy} is presented for the smallest particles in the system. From this figure, it is clear that the diffusivity of particles in a bidisperse suspension is dependent on the composition. At a relative area fraction of large particles of 0.34, the diffusion coefficients were already slightly higher than for a monodisperse suspension with the same total area fraction of particles. At higher relative area fractions, the increase was even larger.

In Figure 4.6, the data for the large particles in the bidisperse suspension are shown. The results clearly show that in this case, the diffusivity was much lower than expected

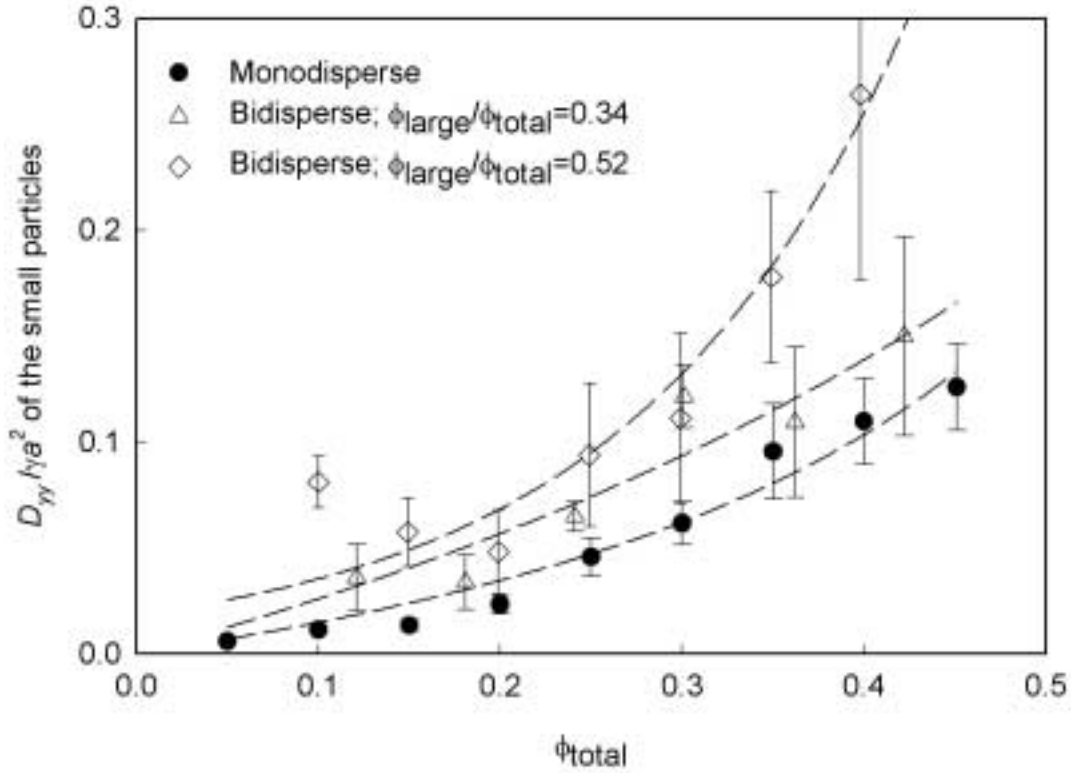


Figure 4.5: Component D_{yy} of the shear-induced self-diffusion coefficient of the small particles in a 2D bidisperse suspension ($a_{large}/a_{small}=3$, $N_{total}=150$ (bidisperse suspensions) or 200 (monodisperse suspensions)) as a function of the total particle area fraction ϕ_{total} in shear flow at a $Re_{shear,p}$ of 0.023 (calculated for the small particles). Error bars indicate the standard deviation. Lines are drawn to guide the eye.

for a monodisperse suspension. It is evident that the diffusivity of the small as well as the large particles is not only the result of the total particle fraction in the system, but also of the particle size distribution. The presence of large particles is found to have a positive effect on the diffusivity of small particles, whereas small particles have a reverse effect on large particles.

We compared the (non-normalised) diffusivity of the small particles to the expected diffusivity of the large particles when these large particles are present in a monodisperse suspension with the same area fraction as that of large particles in the bidisperse suspension. Figure 4.7 shows that the diffusivity of the small particles in the bidisperse suspensions is practically the same as the expected diffusivity of the large particles. This strongly suggests that the small particles behave as 'slave particles' in the suspension, whose mobility is completely determined by the presence of the large particles in the system. For the large particles, this would mean that their diffusivity is unaffected by the presence of the small particles and that their diffusivity is the same as for a monodisperse suspension with the large particles solely. From Figure 4.8, it can be seen that this was indeed the case in the bidisperse suspensions. Also when $\phi_{large} > 0.2$, the small and the large particles are expected to behave as 'slave' and 'master particles' respectively, thus following the curves of the monodisperse large particles in 4.7 and 4.8.

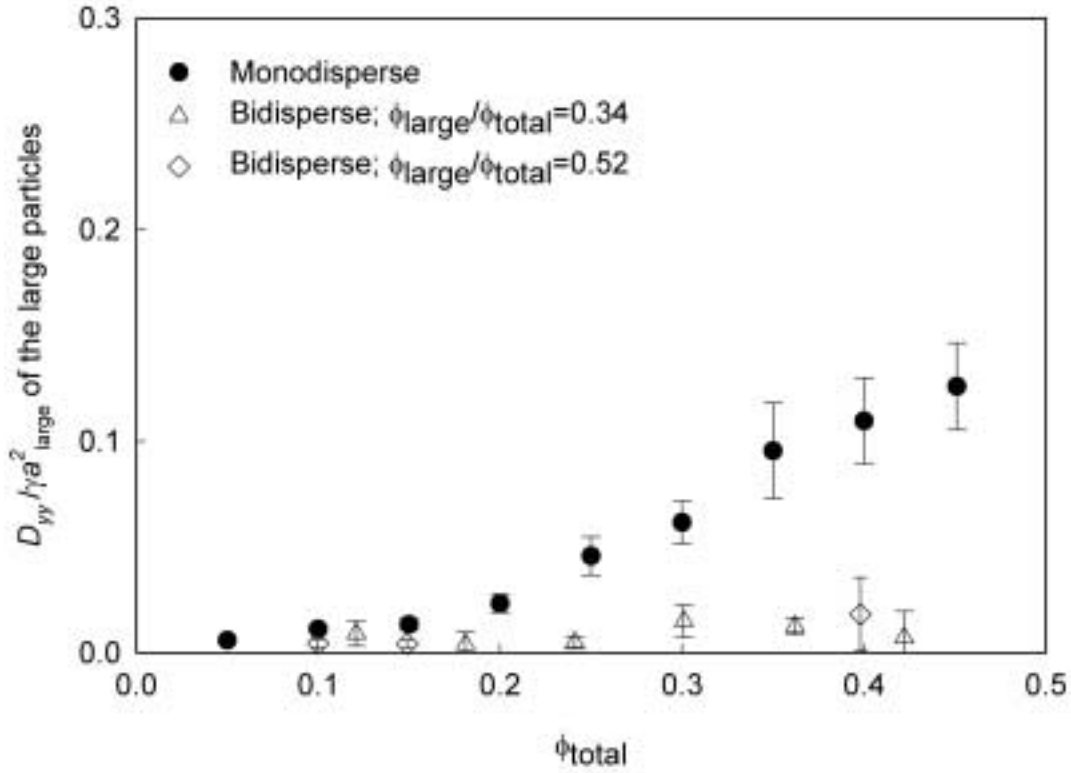


Figure 4.6: Component D_{yy} of the shear-induced self-diffusion coefficient of the large particles in a 2D bidisperse suspension ($a_{\text{large}}/a_{\text{small}}=3$, $N_{\text{total}}=150$ (bidisperse suspensions) or 200 (monodisperse suspensions)) as a function of the total particle area fraction ϕ_{total} in shear flow at a $Re_{\text{shear,p}}$ of 0.023 (calculated for the small particles). Error bars indicate the standard deviation.

In Figure 4.5, the shear-induced diffusion coefficients of the small particles in the bidisperse suspensions were all higher than for the monodisperse case. We can however expect that there will only be an increase when the large particles in the bidisperse suspensions are present in a sufficient amount and/or with a sufficient diameter ratio. We investigated this for bidisperse suspensions with a total particle area fraction of 0.40, but with varying diameter ratio and relative area fraction of large particles. The results in Figure 4.9 show that the diffusivity of the small particles is indeed related to the diameter ratio. At a fixed relative amount of large particles, the diffusivity increases with the diameter ratio. This increase with the diameter ratio was steeper when the relative amount of large particles was higher. The increase starts at a certain onset point, indicating that when the diameter ratio and the relative amount of large particles are not sufficiently high, the diffusivity of the small particles is not affected compared to the monodisperse case. This onset value is mostly determined by the relative fraction of large particles and to a much lower extent to the diameter ratio. After putting the relative fraction of large particles on the X-axis (Figure 4.10), for $\phi_{\text{large}}/\phi_{\text{total}} < 0.6$ a mastercurve is obtained from which can be seen that the diffusivity starts to increase at a relative area fraction of large particles of about 0.3. At relatively high amounts of large particles, e.g. with 26.7 number% of large particles (Figure 4.10), the diffusivities seem to level off, so that the diffusivity of

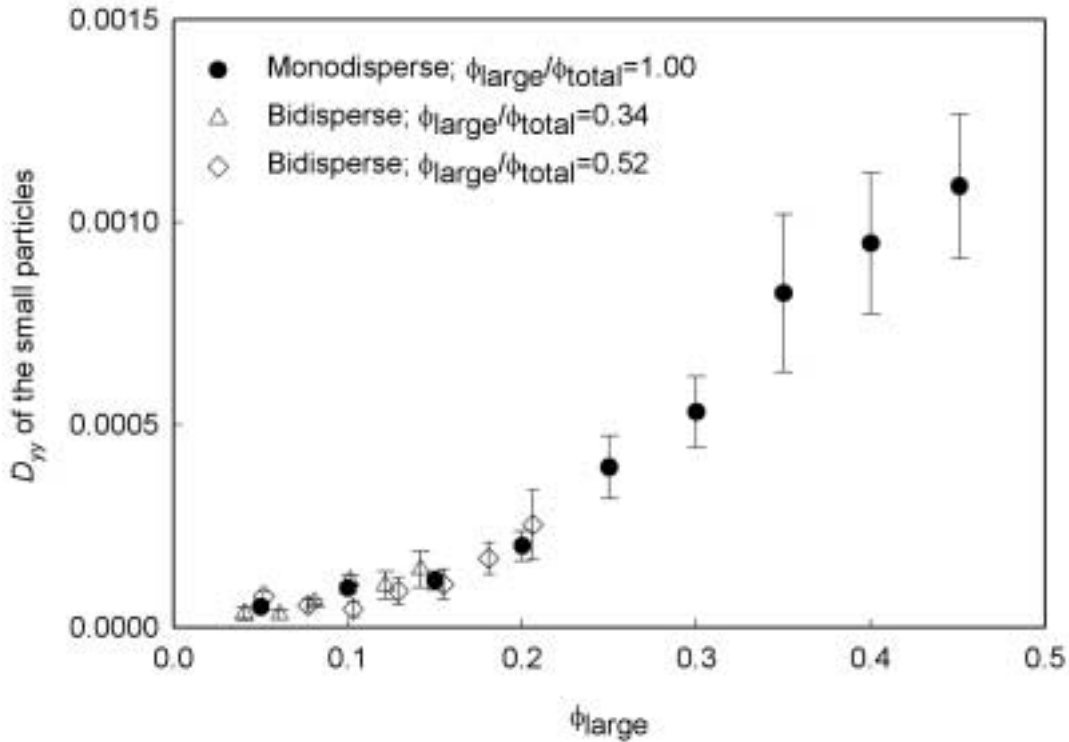


Figure 4.7: The non-normalised diffusivity (in lattice dimensions) of the small particles in a bidisperse suspension ($a_{\text{large}}/a_{\text{small}}=3$, $N_{\text{total}}=150$) in relation to the fraction of large particles ϕ_{large} at a $Re_{\text{shear,p}}$ of 0.023 (calculated for the small particles), as compared to the non-normalised diffusivity of large particles in a monodisperse suspension. Error bars indicate the standard deviation.

the small particles is smaller than expected. Although we did not explore this regime in more detail, we think that this might be due to the effect of the relatively limited box size for the large particles. Sierou and Brady [27] have shown earlier that a limited box size can lead to a decrease of the diffusivity.

It is of importance to interpret the reason why the onset value is at a fraction of large particles of 0.3. For a monodisperse suspension, $D_{yy}/\dot{\gamma}a^2$ is dependent on ϕ . It can be debated that the onset point is determined by the situation in which the diffusivity of the larger particles starts to become larger than the diffusivity of a monodisperse suspension with $\phi_{\text{total}} = 0.4$. In Figure 4.5, it can be seen that the latter diffusivity is equal to 0.11, corresponding with a non-normalised diffusivity of 0.00011 (in lattice dimensions, at $Re_{\text{shear,p}}=0.023$). For particle size ratios of 2, 3 and 4, the larger particles obtain this non-normalised diffusivity at a fraction ϕ of respectively 0.21, 0.12 and 0.06. These values are smaller than found for the onset point, which indicates that the contribution of the small particles themselves to the diffusivity cannot be neglected at this onset point. Therefore, this phenomenon does not seem to completely explain the value of the onset-point. Another related phenomenon is the area surrounding a large particle that is significantly influenced by the presence of this large particle. At a relative fraction of large particles of 0.3, the fraction ϕ_{large} was 0.12. From 2D simulations on the rotation of a single particle in the vicinity of a wall and on the interaction between two particles in shear flow [39], it

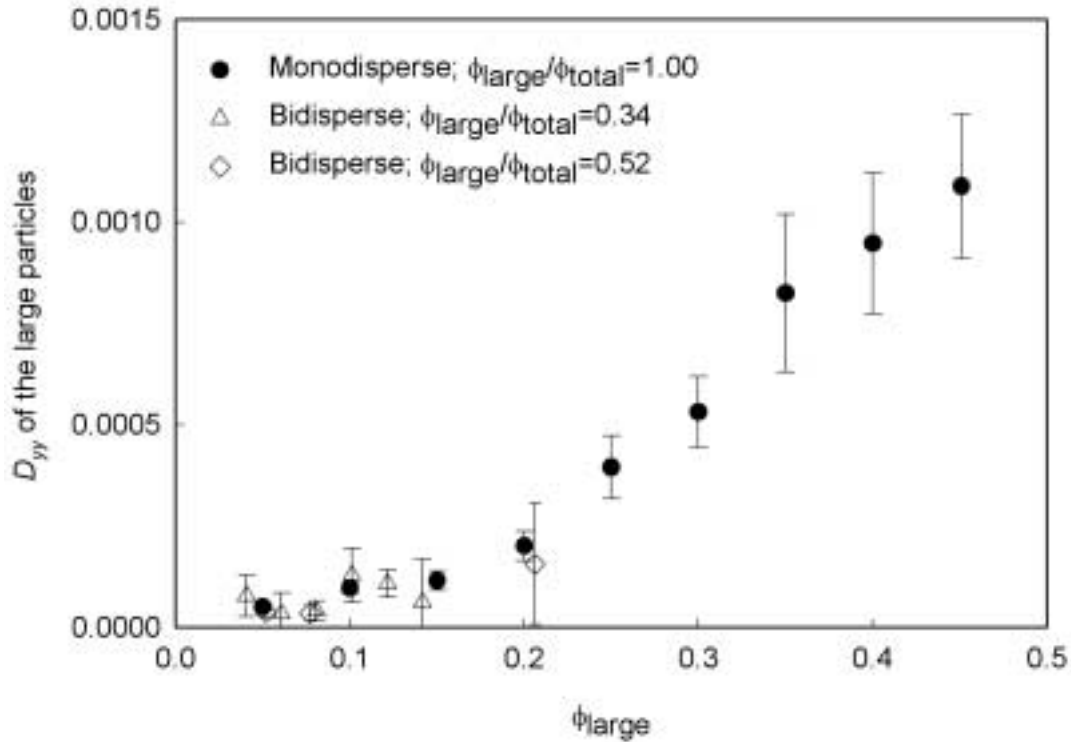


Figure 4.8: The non-normalised diffusivity (in lattice dimensions) of the large particles in a bidisperse suspension ($a_{\text{large}}/a_{\text{small}}=3$, $N_{\text{total}}=150$) in relation to the fraction of large particles ϕ_{large} at a $Re_{\text{shear,p}}$ of 0.023 (calculated for the small particles), as compared to the non-normalised diffusivity of large particles in a monodisperse suspension. Error bars indicate the standard deviation.

can be estimated that such a particle affects the fluid flow in an influence area, which we assume to be of circular shape, with a radius of about $3a$. This indicates that the influence area measures a fraction of $3^2 * 0.12 = 1.08$, in other words, at this point the influence of the large particles can be felt in the whole box. This estimation agrees well with the actual onset point. Since it is known that Re only has a minor effect on the size of this influence area, it can be anticipated that the onset value of 0.3 is not dependent on Re .

It would also be of interest to investigate the shear-induced diffusivity of the larger particles in a bidisperse suspension with a relative area fraction of large particles smaller than 0.3. It can be hypothesized that the large particles then would have a diffusivity that is about $(a_{\text{large}}/a_{\text{small}})^2$ times as small as for a monodisperse suspension with the same total particle fraction. At these conditions however, the amount of large particles in our simulations was too low to be able to determine this diffusivity with sufficient statistical reliability.

These results lead us to the conclusion that the shear-induced diffusivity of the small particles in bidisperse suspensions with a total area fraction of 0.40 can be roughly divided into two regimes: (1) when the relative area fraction of large particles is less than 0.3, the small particles move as in a monodisperse suspension with the same total particle area fraction and no particular effect of the large particles can be seen, (2) when the relative area fraction of large particles however exceeds the value of 0.3, the small particles

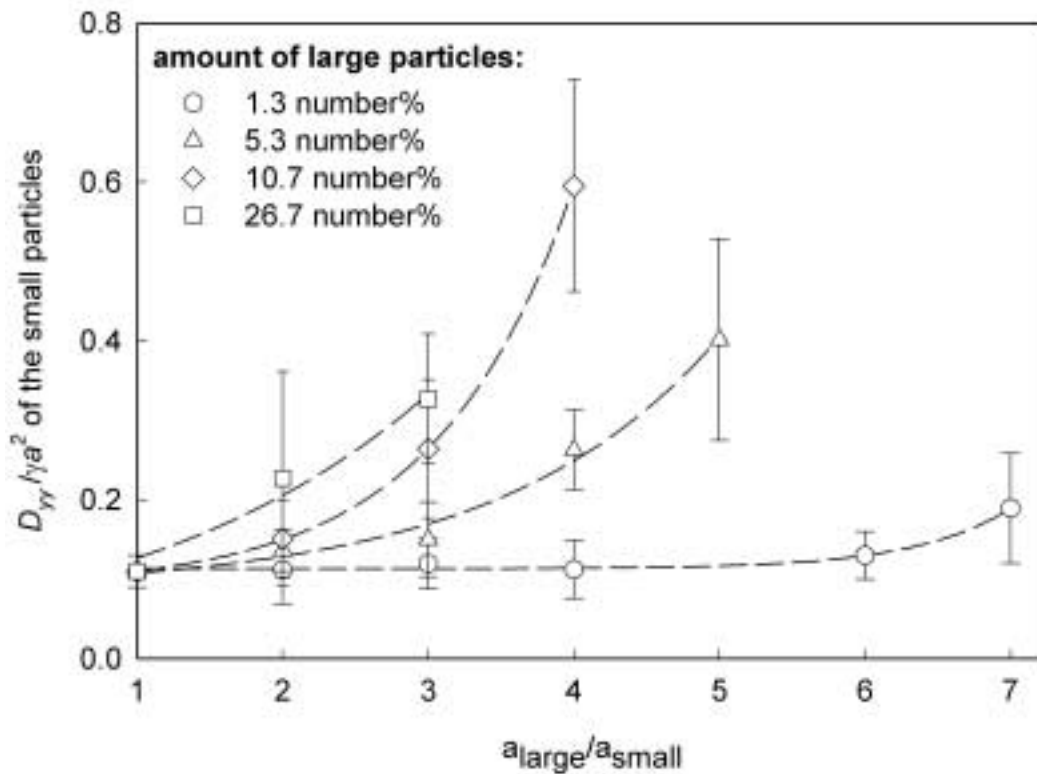


Figure 4.9: Component D_{yy} of the shear-induced self-diffusion coefficient of the small particles in a 2D bidisperse suspension ($\phi_{\text{total}}=0.40, N_{\text{total}}=150$ (bidisperse suspensions) or 200 (monodisperse suspensions)) as a function of the ratio of the particle radii $a_{\text{large}}/a_{\text{small}}$ in shear flow at a $Re_{\text{shear,p}}$ of 0.023 (calculated for the small particles) and for different number frequencies of large particles. The number frequencies correspond with relative fractions of large particles $\phi_{\text{large}}/\phi_{\text{total}}$ ranging between 0.05-0.40 (1.3 number%), 0.18-0.58 (5.3 number%), 0.32-0.66 (10.7 number%) and 0.59-0.77 (26.7 number%). Error bars indicate the standard deviation. Lines are drawn to guide the eye.

behave as 'slave particles' and obtain a higher diffusivity, which is totally governed by the diffusivity of the large particles in the system. Shear-induced diffusivity is affected by the particle size distribution, which is of importance for the relation between shear-induced diffusivity in polydisperse suspensions and in monodisperse suspensions.

4.5 Conclusions

It is shown that bidisperse suspensions, in analogy with monodisperse suspensions, exhibit shear thickening behaviour. The size and relative fraction of large particles highly determine the degree of shear thickening at a certain shear rate. This can be explained because the shear based particle Reynolds number $Re_{\text{shear,p}}$, which is a relevant parameter for shear thickening, has a quadratic dependence on the particle radius. Moreover, the viscosity of the bidisperse suspensions was not always lower than for monodisperse suspensions, as is the case in the Newtonian regime, but increased with increasing relative

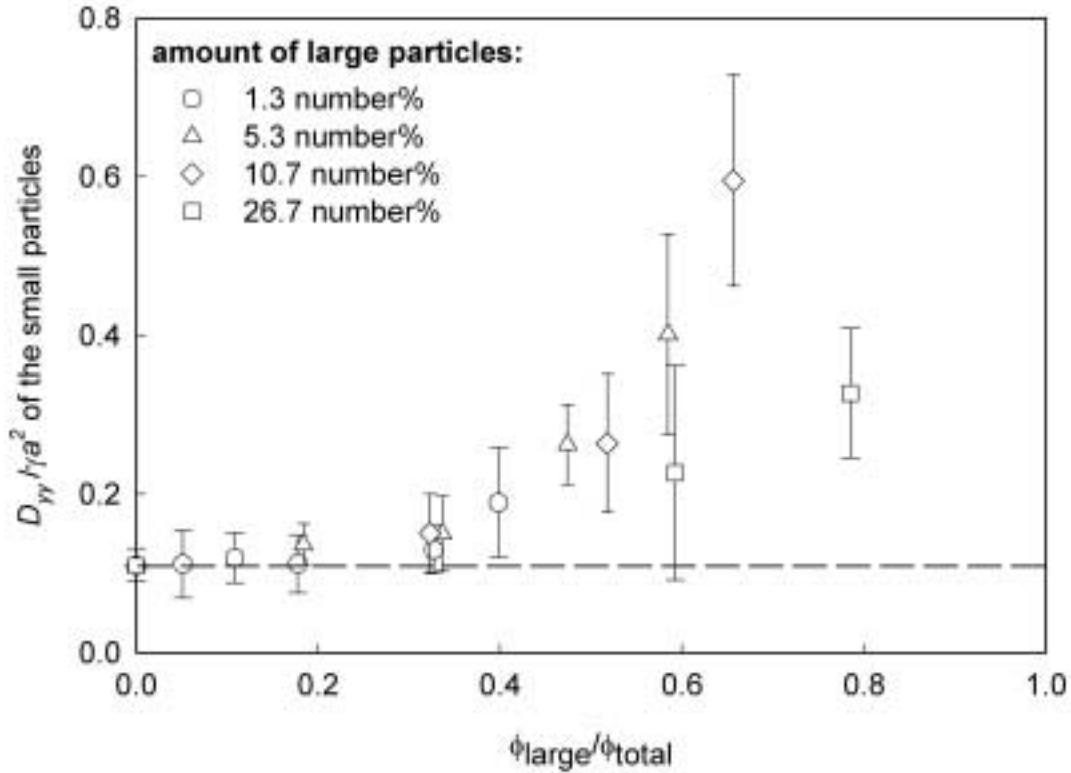


Figure 4.10: Component D_{yy} of the shear-induced self-diffusion coefficient of the small particles in a 2D bidisperse suspension ($\phi_{total}=0.40, N_{total}=150$ (bidisperse suspensions) or 200 (monodisperse suspensions), $a_{large}/a_{small}=2, 3, 4$ or 5) as a function of the fraction of large particles ϕ_{large} in shear flow at a $Re_{shear,p}$ of 0.023 (calculated for the small particles) and for different number frequencies of large particles. The number frequencies correspond with relative fractions of large particles $\phi_{large}/\phi_{total}$ ranging between 0.05-0.40 (1.3 number%), 0.18-0.58 (5.3 number%), 0.32-0.66 (10.7 number%) and 0.59-0.77 (26.7 number%). Error bars indicate the standard deviation. The dashed line indicates the value of D_{yy} in a monodisperse suspension.

fraction of large particles. This increase was not gradual, which can be caused by particle structuring phenomena in the bidisperse suspensions.

Shear thickening behaviour in monodisperse suspensions is known to coincide with particle clustering and an increase of shear-induced diffusivity. In bidisperse suspensions, we have also found an increase of shear-induced diffusivity with increasing $Re_{shear,p}$. The rheology as well as the shear-induced diffusivity of bidisperse suspensions is largely determined by the larger particles in the suspension. The influence of the larger particle on the fluid flow field can not only lead to increased particle clustering and shear thickening, but also to an increased diffusivity of the smaller particles.

In bidisperse suspensions, the small and large particles exhibited a different (normalised) shear-induced diffusivity $D_{yy}/\dot{\gamma}a^2$. Whereas the diffusivity of the small particles increased compared to the monodisperse situation, the diffusivity of the large particles declined. The non-normalised shear-induced diffusivity D_{yy} was however similar for the small and large particles, indicating an equal absolute mobility, which was predominantly

determined by the relative fraction of large particles in the system. The predominance of the large particles became evident when the relative fraction of large particles exceeded a value of about 0.3, independent of the size ratio of the particles. In that case, the shear-induced diffusivity of both the small and the large particles are dependent on ϕ_{large} solely. Or in other words, the small particles can be seen as 'slave particles' that are totally ruled by the large 'master particles'. Below the onset value of 0.3, the shear-induced diffusivity $D_{yy}/\dot{\gamma}a^2$ of the small particles was similar to that of equal-sized particles in a monodisperse suspension with the same total particle fraction.

In this study, it is shown how shear-induced diffusivity is affected by the particle size distribution, leading to a better understanding of the relation between shear-induced diffusivity in polydisperse suspensions and in monodisperse suspensions.

Acknowledgements

Friesland Foods is greatly acknowledged for supporting this research. The authors would like to acknowledge the support of the Dutch Ministries of Economic Affairs, Education, Culture and Sciences and of Housing, Spatial Planning and the Environment through a grant of the Dutch Program Economy, Ecology and Technology.

**Shear-induced diffusion model for
microfiltration of polydisperse
suspensions**

A detailed study on concentration polarisation during microfiltration (MF) was carried out in order to improve control on cake layer formation. Concentration polarisation is reduced by several back-transport mechanisms, however, for particles in the size range 0.5-30 μm shear-induced diffusion is the predominant one. Shear-induced diffusion is caused by the hydrodynamic interactions between particles in shear flow, which are strongly dependent on the particle size. Because of this, the polydispersity of suspensions is expected to have a large effect on cake layer formation. Although this aspect will be of considerable practical relevance, it has only received minor attention in literature. In this work, the effect of particle size distribution on MF was investigated by studying the steady-state flux of bidisperse suspensions with a ratio of particle radii of 3. The flux appeared to be completely determined by the smaller particles; it remained almost constant between a volume fraction of 0.2 and 1 of small particles. This trend in the steady-state flux was in good agreement with calculations based on a shear-induced particle migration model for polydisperse suspensions. Since polydispersity is a common property of suspensions, the present work may contribute to optimisation of flux and selectivity in MF processes, which depend largely on adequate control of cake layer formation. This can be achieved by implementation of the developed model in process control routines.

5.1 Introduction

Crossflow microfiltration (MF) is a well-known technique for the separation of microparticles, emulsion droplets and micro-organisms from fluids, with many (potential) industrial applications in food and bioprocess engineering [79]. In these processes, concentration polarisation mostly leads to the formation of a cake layer at the membrane surface, which has a large negative effect on flux and selectivity. Therefore, concentration polarisation can be considered a key factor in the control of MF processes. Concentration polarisation is governed by two simultaneous processes: (1) convective transport of particles towards the membrane along with the permeate flow and (2) back-transport of particles from the concentrated layer into the bulk phase. In case of an excess particle flux towards the membrane, a cake layer builds up. When convective transport balances back-transport, the situation can be considered a steady-state. In this situation only minor variations in cake layer resistance and flux are expected. Shear-induced diffusion can be considered the predominant back-transport mechanism during MF of suspensions with particles in the range of 0.5-30 μm [10]. This mechanism comprises the diffusive movements of particles in a shear field that are caused by hydrodynamic interactions. In the presence of a concentration or shear rate gradient, shear-induced diffusion leads to a net migration of particles in the direction of a lower concentration or shear rate, therewith effectively reducing concentration polarisation. Using the fundamental knowledge about shear-induced diffusion, the MF behaviour of monodisperse suspensions can, in general be predicted well. However, practically relevant suspensions are seldom monodisperse. Polydispersity, that is known to influence permeate flux and flow resistance of cake layers, seems to be the rule. Incorporation of effects of polydispersity in shear-induced diffusion models for MF would therefore be an important step toward a better control of concentration polarisation during MF of practically relevant suspensions. In this article, we

present our research conducted on the effects of polydispersity on concentration polarisation during MF. We investigated the effect of the particle size distribution of a bidisperse suspension on the steady-state flux and compared our results with predictions obtained with a particle migration model for polydisperse suspensions [71].

5.2 Shear-induced migration model for polydisperse suspensions

For the quantitative description of shear-induced diffusion, most MF models use the research of Eckstein and co-workers [14] and Leighton and Acrivos [15, 80]. The research of these authors was directed at self-diffusion of monodisperse particles in a suspension under shear. A frequently applied equation for shear-induced diffusion, reported by Leighton and Acrivos, is

$$D_s = 0.33\dot{\gamma}a^2\phi^2 (1 + 0.5e^{8.8\phi}) \quad (5.1)$$

All symbols are explained in the nomenclature list. For the steady-state permeate flux, Davis and Sherwood [81] derived the following equation, using an exact similarity solution with shear-induced diffusion as the dominant mechanism for particle back-transport

$$\langle J \rangle = 0.072\dot{\gamma}_0 \left(\frac{\phi_w a^4}{\phi_b L} \right)^{1/3} \quad (5.2)$$

Shear-induced self-diffusion of particles in polydisperse suspensions has to our knowledge not been reported. Phillips and co-workers [16] proposed a phenomenological model for shear-induced particle migration. The model is based on particle migration potentials. Migration is induced by two mechanisms, a nonuniform frequency of particle interactions in a shear field and a nonuniform viscosity field. Shauly and co-workers [71] extended this model to polydisperse suspensions with various particle sizes. For the system investigated here, the total flux of particles of species i can be described with

$$j_i = -k\dot{\gamma}\bar{a}a_i\phi\phi_i \left[\nabla \ln(\dot{\gamma}\phi_i) + \frac{\bar{a}}{a_i} \nabla \ln \mu^\lambda \right] \quad (5.3)$$

The term outside the brackets equals the shear-induced diffusion coefficient for the i th particle. The migration potential in the shear-induced particle migration model consists of an interaction and a viscosity term. For the viscosity of monodisperse suspensions, Krieger [46] found:

$$\mu = \left(1 - \frac{\phi}{\phi_m} \right)^{-m} \quad (5.4)$$

where $m = 1.82$ and the maximum packing density for a monodisperse suspension (ϕ_{m0}) is assumed to be 0.68. This expression was extended by Probstein and co-workers [75] to describe the effective viscosity of a bidisperse suspension. In the approach of Probstein and co-workers the maximum packing density is not taken as a constant but is calculated as a function of the species local concentrations ϕ_1 and ϕ_2 , as is shown in Equation 5.5:

$$\frac{\phi_m}{\phi_{m0}} = \left[1 + \frac{3}{2} |b|^{3/2} \left(\frac{\phi_1}{\phi} \right)^{3/2} \left(\frac{\phi_2}{\phi} \right) \right] \quad (5.5)$$

with $b = (a_1 - a_2)/(a_1 + a_2)$.

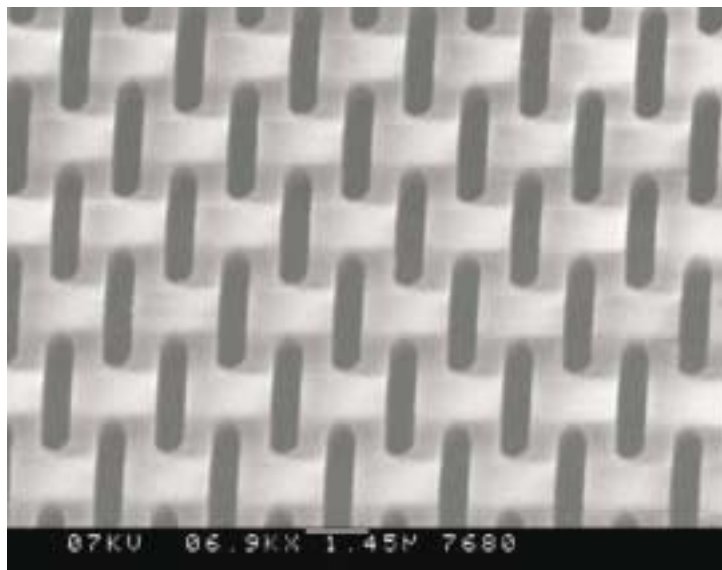


Figure 5.1: *Electron microscope photo of a microsieve.*

5.3 Materials and methods

Microfiltration (MF) experiments were performed with microsieves, MF membranes that are fabricated with silicon micromachining technology. This technology allows the construction of smooth, thin membranes with very well defined pores. The membrane resistance of microsieves is typically 100 to 1000-fold smaller than for conventional membranes. The microsieves we used had a membrane surface area of 30.2 mm^2 and slit-shaped pores with a length and width of 3 and $0.7 \mu\text{m}$ respectively. The thickness of the membrane was only $1 \mu\text{m}$. A SEM-photo is given in Figure 5.1. The feed for MF consisted of suspensions of polystyrene spherical particles (surfactant-free, sulfate polystyrene, Interfacial Dynamics Corporation, USA) in a neutrally buoyant mixture of demineralized water and glycerol (density 1.055 g/ml at 293 K). The experiments were carried out in a parallel plate device with a channel height of 0.25 mm . The temperature of the feed was kept constant at 298 K . The pressure was monitored with two pressure sensors in the parallel plate device, one before and one after the microsieve. The pressure at the permeate side of the microsieve was atmospheric. The feed flow rate was monitored with a rotameter and the permeate flux was measured with an analytical balance. Since the microsieve was divided into porous and non-porous fields, the permeate flux was calculated based on the surface area of the porous fields only.

5.4 Results and discussion

5.4.1 Predicted steady-state fluxes

Using Equation 5.3, we first calculated the diffusion coefficients for the separate particles in a bidisperse suspension as a function of the suspension composition and related these values to the diffusion coefficients in case of a monodisperse suspension (Figure 5.2). The ratio of the particle radii a_2/a_1 was 3 (equal to that in the experiments). In the calculations, the total volume fraction of particles ϕ in the concentration polarisation layer

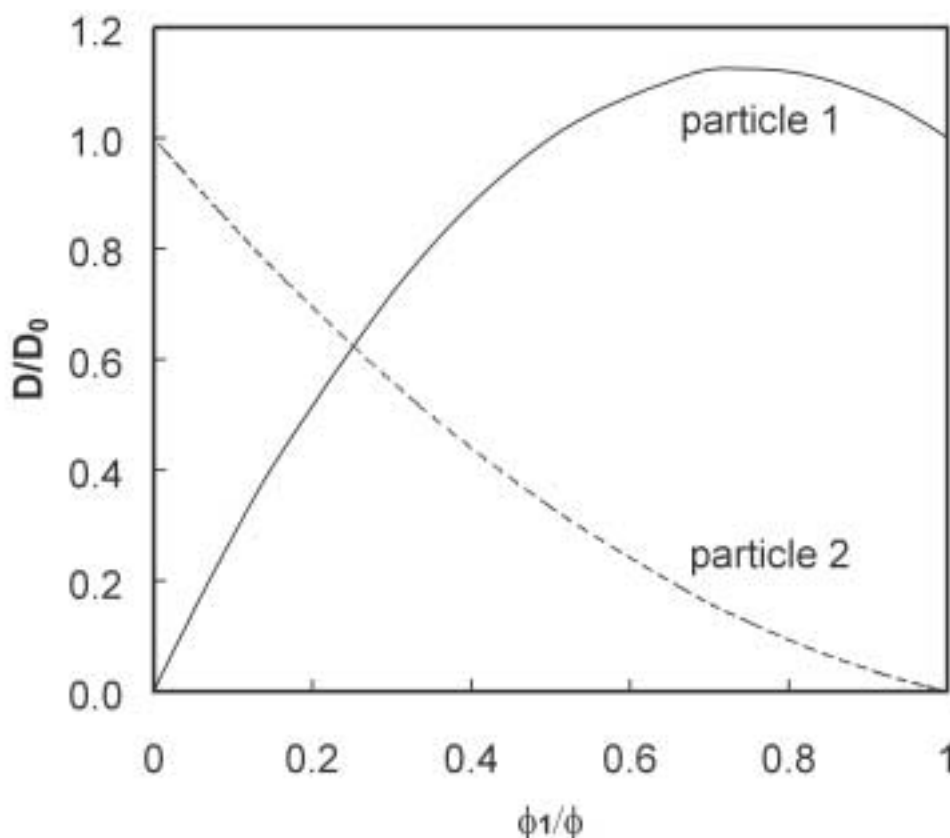


Figure 5.2: Relative diffusion coefficient for the separate particles in a bidisperse suspension as a function of suspension composition for a total volume fraction of 0.6 and $a_2/a_1=3$, as calculated on basis of the particle migration model.

was always assumed 0.6. Starting from a monodisperse suspension of particle 1 ($\phi_1/\phi=1$), the diffusion coefficient first increases with increasing amount of particle 2. This is due to the increase of the mean particle radius (Equation 5.3: \bar{a}) in the suspension. From a volume ratio ϕ_1/ϕ of 0 up to 0.75, the increasing volume fraction of particle 1 (ϕ_1) in the suspension causes the diffusion coefficient to increase. In contrast to particle 1, particle 2 shows a monotonous decrease of the diffusion coefficient with increasing volume ratio of the small particle. This is because the mean particle radius and the concentration of particle 2 both decrease. Apparently, the diffusion coefficient of the smaller particle in the bidisperse suspension has a different dependence on suspension composition as compared to that of the larger particle. But what does this imply for the steady-state flux during MF? To analyse this effect, we calculated the steady-state flux using Equation 5.2, but adjusted for the relative change of the diffusion coefficients of both particles 1 and 2, as compared to the monodisperse case. With these model calculations we get two relations for the steady-state flux as a function of suspension composition (Figure 5.3).

We can expect that the lowest value for the steady-state flux will actually be measured during MF, because this represents the situation in which neither for particle 1 nor for particle 2 an excess particle flux exists. According to Figure 5.3, this would imply that for a volume ratio ϕ_1/ϕ lower than 0.75, the back-transport flux of particle 1 determines the

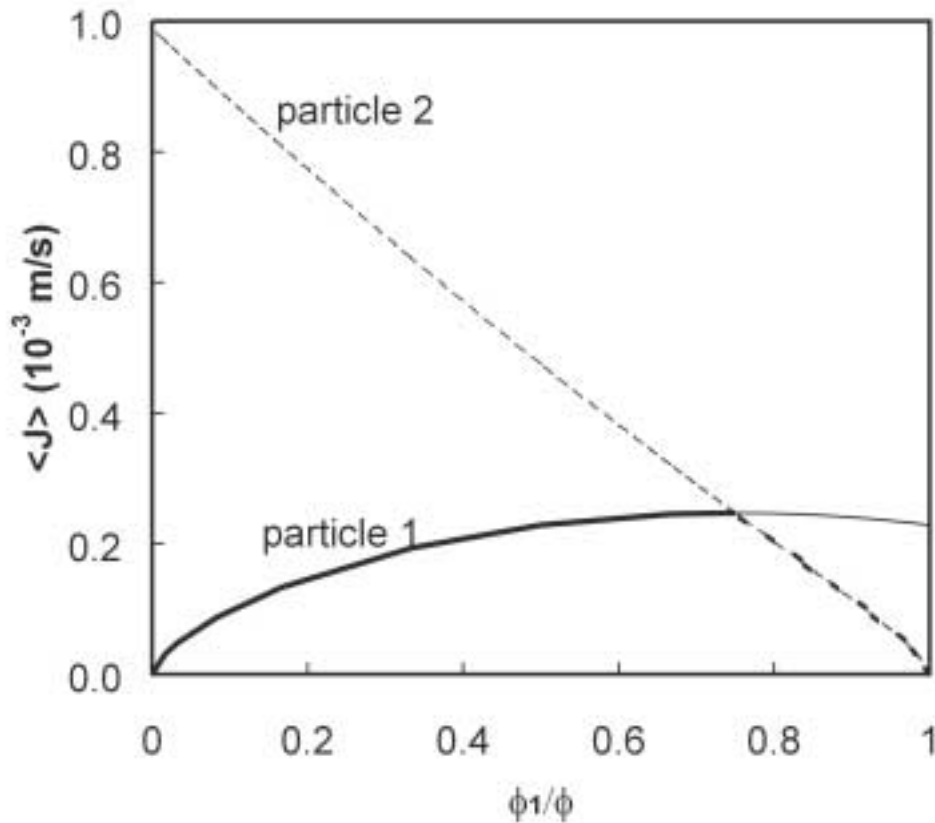


Figure 5.3: Length-averaged steady-state permeate flux for cross-flow MF, calculated for the separate particles ($a_1=0.8 \mu\text{m}$; $a_2=2.4 \mu\text{m}$) in a bidisperse suspension based on the particle migration model. The bold lines indicate the predicted actual steady-state flux. Microfiltration conditions: $\dot{\gamma}_0 = 2.0 \cdot 10^3 \text{ s}^{-1}$; $\phi_w = 0.6$; $\phi_b = 1.5 \cdot 10^{-5}$; $T = 298 \text{ K}$; $L = 4.1 \cdot 10^{-3} \text{ m}$.

steady-state flux, while for a volume ratio ϕ_1/ϕ higher than 0.75 particle 2 does (except for a volume ratio ϕ_1/ϕ of exactly 0 or 1). From this, it follows that the flux is comparable to the flux of the monodisperse suspension of the smaller particle for a volume ratio from 0.25 up to 0.75. For volume ratios ϕ_1/ϕ near 0 or 1, the experimentally determined flux values should be considered with care, because measured fluxes may easily be influenced by particle depletion in the concentration polarisation layer or by very slow cake layer formation. Please note, in the calculations we only consider the concentration difference between concentration polarisation layer and bulk phase for the migration potential. We assume that the shear rate and the viscosity do not change the migration potential significantly from that of the monodisperse case. This seems a reasonable assumption. We calculated, using the model of Probst and co-workers (Equation 5.5), that for the bidisperse suspension, the volume fraction in the concentration polarisation layer would need to rise from $\phi=0.60$ to 0.66 (in the most extreme case) in order to achieve the same viscosity as for the monodisperse suspension. This increase in volume fraction gives an increase in steady-state flux of only 3%.

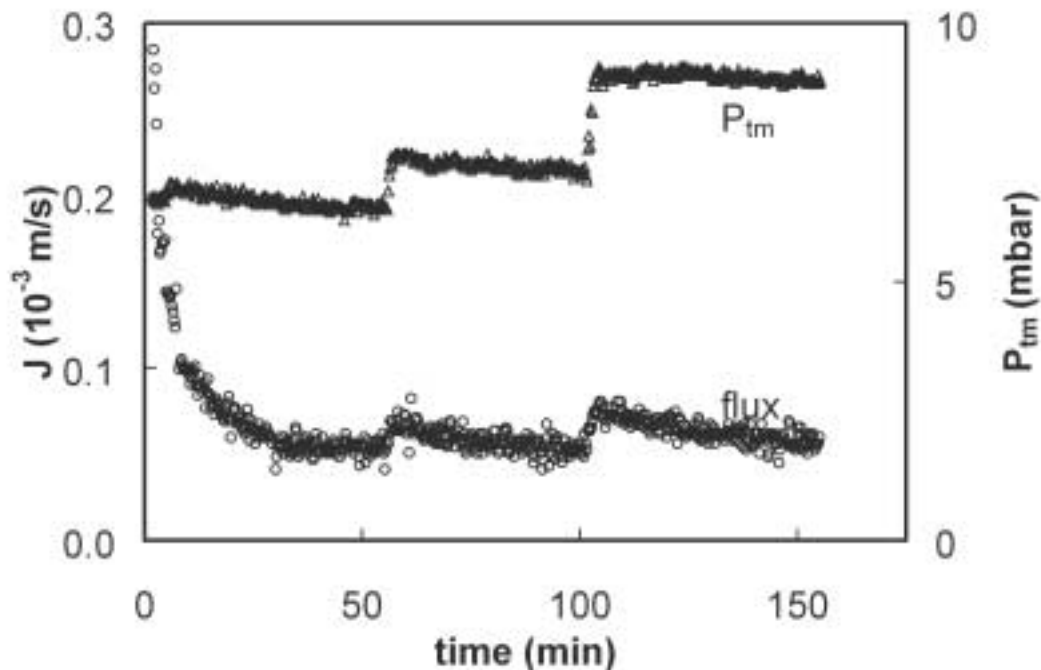


Figure 5.4: Flux and transmembrane pressure during microfiltration of a bidisperse suspension of polystyrene particles ($a_1 = 0.8 \mu\text{m}$, $\phi_1/\phi = 0.8$ and $a_2 = 2.4 \mu\text{m}$, $\phi_2/\phi = 0.2$). The transmembrane pressure was step-wise increased during the run. Microfiltration conditions: $\dot{\gamma}_0 = 2.0 \cdot 10^3 \text{ s}^{-1}$; $\phi_b = 1.5 \cdot 10^{-5}$; $T = 298 \text{ K}$.

5.4.2 Experimental results

Steady-state flux levels were determined for monodisperse suspensions with particle radii of 0.8 and 2.4 μm and for bidisperse suspensions, consisting of mixtures of these two particles. This was done by step-wise increasing the transmembrane pressure during a filtration run and measuring the steady-state flux (an example is shown in Figure 5.4).

Due to the low membrane resistance of microsieves, already at an extremely low transmembrane pressure a cake layer is formed and a steady-state flux level is achieved. In a steady-state situation, an increase of the transmembrane pressure only resulted in a temporary increase of the permeate flux. The subsequent decrease of the flux can be explained with extra accumulation of particles on the membrane surface, resulting in a thicker cake layer. From our calculations on bidisperse suspensions, we expected that the particle with the largest excess particle flux would determine the steady-state flux level.

As can be seen from Figure 5.5, for all bidisperse mixtures the steady-state flux was comparable to the flux of the monodisperse suspension with the smaller particles. The variation in flux between the mixtures was relatively small. Apparently, in the bidisperse mixtures, the smaller particle had a larger excess particle flux and determined the steady-state flux level. This is in agreement with our model predictions. Comparison of the measured steady-state flux levels with values that are predicted by the shear-induced diffusion model reveals that the measured fluxes are about 5 times lower. This might be due to an overestimation of the predicted steady-state flux for short filter lengths (L).

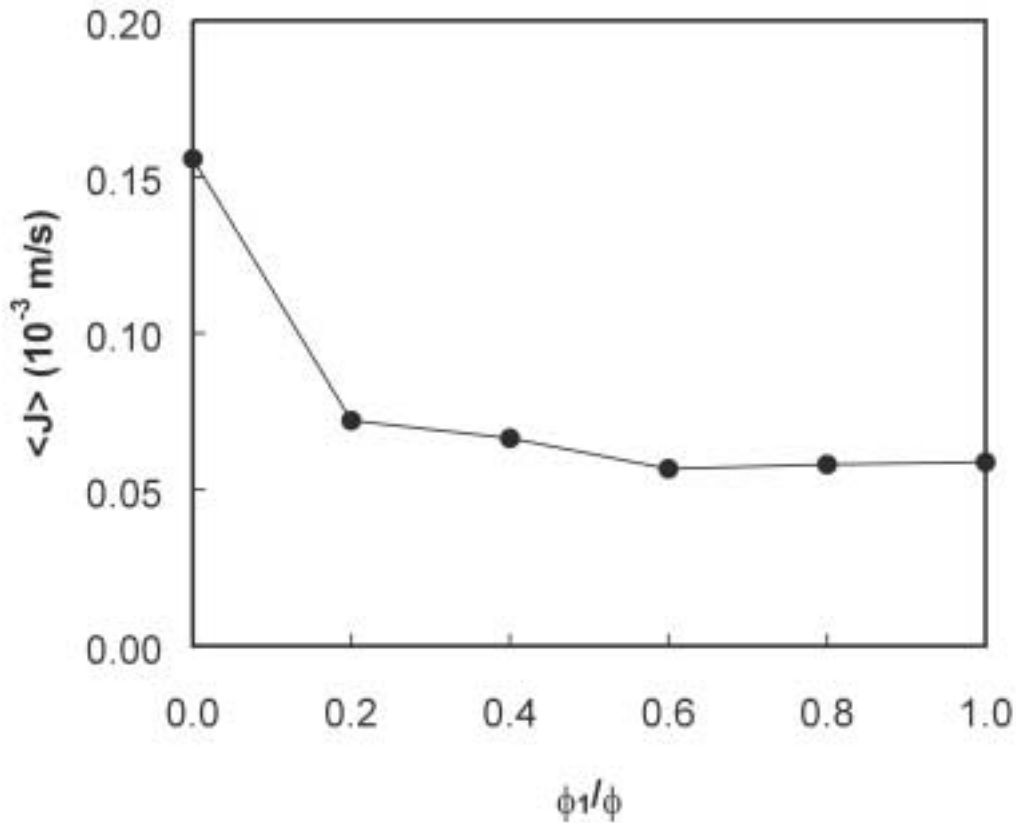


Figure 5.5: Measured steady-state flux for microfiltration of a bidisperse suspension of polystyrene particles ($a_1 = 0.8 \mu\text{m}$; $a_2 = 2.4 \mu\text{m}$) as a function of suspension composition. Microfiltration conditions: $\dot{\gamma}_0 = 2.0 \cdot 10^3 \text{ s}^{-1}$; $\phi_b = 1.5 \cdot 10^{-5}$; $T = 298 \text{ K}$.

According to Equation 5.2, the flux of monodisperse suspensions increases with the diameter of the particles with a power-dependence of 1.33. For the particles investigated here ($a_2/a_1 = 3$), a flux ratio (J_2/J_1) of 4.3 is expected, while we measured a flux ratio of 2.7. This effect is currently investigated further.

5.5 Conclusions

In this study, we found that the steady-state flux for MF of a bidisperse suspension with a ratio of particle radii of 3 has a level that is comparable to that of a monodisperse suspension of the smallest particle (in the bidisperse suspension). The trend in the observed behaviour could be described accurately with a particle migration model for polydisperse suspensions. This model takes the effect of the particle size distribution on the shear-induced migration of individual particles into account.

List of symbols

a particle radius, m

\bar{a}	average particle radius, m
b	dimensionless function in Eq. 5.5
D_s	shear-induced diffusivity, m ² /s
$\langle J \rangle$	length-averaged permeate flux, m/s
j_i	migratory flux of particle i , m ² /s
k	dimensionless particle migration parameter in Eq. 5.3
L	filter length, m
P_{tm}	transmembrane pressure, bar

Greek symbols:

ϕ	particle volume fraction
ϕ_b	particle volume fraction in the bulk suspension
ϕ_m	maximum packing density
ϕ_{m0}	maximum packing density for a monodisperse suspension
ϕ_w	particle volume fraction at the channel wall
$\dot{\gamma}$	shear rate, s ⁻¹
$\dot{\gamma}_0$	nominal shear rate at the membrane surface, s ⁻¹
λ	dimensionless particle migration coefficient in Eq. 5.3
μ	viscosity, kg/m.s

Acknowledgements

We would like to thank Aquamarijn Microfiltration BV (Zutphen, the Netherlands) for supplying the microsieves. Friesland Foods is greatly acknowledged for supporting this research. The authors would like to acknowledge the support of the Dutch Ministries of Economic Affairs, Education, Culture and Sciences and of Housing, Spatial Planning and the Environment through a grant of the Dutch Program Economy, Ecology and Technology.

Effects of particle size segregation on crossflow microfiltration performance: control mechanism for concentration polarisation and particle fractionation

Although the principal mechanisms of crossflow microfiltration (MF) are well-known, the practical applicability of the resulting microfiltration models is still limited. This can be largely attributed to the lack of understanding of effects of polydispersity in the particulate suspensions, as relevant to concentration polarisation in MF. This paper describes an investigation of concentration polarisation behaviour of bidisperse suspensions, in the regime where shear-induced diffusion is the dominant back-transport mechanism. In the transient flux regime, the particle deposition onto the membrane was monitored by means of Confocal Scanning Laser Microscopy. As in accordance with the linear dependence of the shear-induced diffusivity on a^2 , only the small particles in the bidisperse suspensions were found to deposit onto the membrane. The back-transport flux that was calculated from the deposition rate and the actual permeate flux, was found to be independent of the composition of the suspension, whereas it was equal to the back-transport flux of a monodisperse suspension of the small particles only, with a similar total particle fraction. These results can be explained with the occurrence of particle size segregation in the feed flow, which leads to an enrichment with small particles of the suspension near the membrane. The findings are also shown to be relevant to particle fractionation processes by MF. In such fractionation processes, particle size segregation is found to have a strong effect on the separation characteristics such as particle size and fat content of the permeate. A polydisperse suspension could be fractionated using a membrane having a pore size larger than the largest particles present. The fractionation thus results not from size exclusion in the membrane, but from segregation effects in the feed channel.

6.1 Introduction

It is already known for a century that the yield of microfiltration (MF) processes can be improved by means of a crossflow parallel to the membrane [82]. The shear flow that is induced in this way, reduces the deposition of suspended particles onto the membrane and enables operation at a (quasi-)stationary filtration rate for a long time.

In spite of the success of MF, the process of particle deposition and its effects on MF are only marginally understood, because of the great number of parameters that is involved. Just to name a few, particle size distribution, shape and deformability of the suspended particles, flow resistance of the deposited layer, and membrane morphology. It is obvious that for process design and improvement, a better understanding of crossflow MF is of major importance; preferably based on (model) predictions. The two key aspects for this are: 1) the kinetics of particle deposition and 2) the properties of the deposited layer. This paper will focus solely on the kinetics of particle deposition.

The last twenty years, significant progress has been made in the understanding of crossflow effects on suspensions with hard spherical particles of one size. The models that are available for such systems, distinguish different mechanisms for the reduced particle deposition onto the membrane such as Brownian diffusion, shear-induced diffusion, inertial lift and surface transport [10]. The relevance of these particle back-transport mechanisms for an actual MF system is determined by mainly the shear rate and the particle radius. When colloidal interactions play a role, normally for particle sizes between 10 nm and 1 μm , the potential barrier between particles is also relevant [83].

For particle sizes between 0.5 and 30 μm , shear-induced diffusion is the most relevant back-transport mechanism [10]. Since particle-particle interactions determine shear-induced diffusion, modelling of the MF process of polydisperse suspensions in the shear-induced diffusive regime requires knowledge of the ensemble behaviour of the suspended particles. Kramadhathi and co-workers [84] evaluated the shear-induced diffusion model of Romero and Davis [8] for MF of a polydisperse feed suspension. Their calculations showed amongst others that the average particle size in the deposited layer was in general smaller than in the bulk phase, due to the lower deposition rate of the larger particles. Although their calculations may be illustrative for the effects of polydispersity, the predictions of Kramadhathi and co-workers have not been validated yet. In earlier work [85], we adapted a shear-induced migration model of Shauly and co-workers [71] for MF of bidisperse suspensions and found that this model gave a good description of the stationary filtration rate for relative volume fractions of large particles between 20 and 80%. The paper is one of the few that include the effects of particle polydispersity on the kinetics of particle deposition, albeit directed at stationary situations.

Experimental work of several authors revealed that the average particle size in the deposited layer is smaller than in the bulk phase of the suspension [86–88]. Kim and co-workers [89] found a good correlation between experimental results on the cake resistance and a newly defined effective particle diameter, which was related to shear-induced diffusivity. In our earlier work [85], we analysed the stationary filtration rate for a bidisperse particle suspension, in the regime of shear-induced diffusion. We found that the smallest particle in the suspension determined the filtration rate. For the particle size ratio of 3 used in this study, the stationary filtration rates for the bidisperse suspensions were similar to that of monodisperse suspensions of the smallest particle.

This paper presents an experimental study on the behaviour of bidisperse suspensions in the shear-induced diffusive back-transport regime of MF. The particle deposition onto the membrane is monitored in the transient flux regime by means of Confocal Laser Scanning Microscopy. In this way, the back-transport of the separate particles in the bidisperse suspension is quantified as a function of the suspension composition (ratio of particle radii, relative volume fraction of large and small particles). The observed behaviour is related to different shear-induced diffusion phenomena described in literature. The practical relevance of our findings is demonstrated in a study on fractionation of milk fat globules. In the next paragraph, we give an overview of those shear-induced diffusion phenomena in bi- or polydisperse suspensions that are relevant to MF.

6.2 Shear-induced diffusion in polydisperse suspensions

6.2.1 Particle back-transport as determined by shear-induced migration

Shear-induced migration comprises the phenomenon of collective particle behaviour as a result of shear-induced diffusion. In a suspension that is subjected to a shear flow, hydrodynamic particle-particle interactions can give rise to this diffusive behaviour, which is the main cause for back-transport of particles between 0.5 and 30 μm [10]. Romero and Davis used a model of Leighton and Acrivos [15] for the description of the shear-induced

diffusivity D_s of a monodisperse suspension with hard, spherical particles:

$$D_s = 0.33\dot{\gamma}a^2\phi^2 (1 + 0.5e^{8.8\phi}) \quad (6.1)$$

From this equation, it becomes clear that the particle radius strongly affects the shear-induced diffusivity. It can therefore be anticipated that the particle size distribution will be of considerable influence as well.

Romero and Davis [8] have developed a MF model, describing the particle deposition onto the membrane and the permeate flux, with shear-induced migration as the back-transport mechanism for monodisperse suspensions. According to an exact similarity solution of this model [81], the stationary permeate flux J_{ss} is given by:

$$\langle J_{ss} \rangle = 0.072 \cdot \dot{\gamma}_{\text{wall},0} \cdot \left(\frac{\phi_c \cdot a^4}{\phi_b \cdot L_m} \right)^{1/3} \quad (6.2)$$

where $\dot{\gamma}_{\text{wall},0}$ is the nominal shear rate at the wall, ϕ_c and ϕ_b are respectively the particle volume fraction in the particle layer and in the bulk phase, a is the particle radius, and L_m is the total membrane length. The angle brackets denote that the flux is averaged over the membrane length. This solution is valid for a bulk particle volume fraction $\phi_b < 0.1$, for a situation where the permeate flux is determined by the flow resistance of the particle layer at the membrane, and for a membrane length that is much longer than the length of the particle layer-free zone at the beginning of the membrane.

Shauly and co-workers [71] took the particle size distribution into account in a shear-induced migration model, which was originally developed by Phillips and co-workers [16]. This phenomenological model describes shear-induced diffusive particle fluxes resulting from a gradient in particle interactions and a gradient in shear stress [71]:

$$j_i = -k\dot{\gamma}\bar{a}a_i\phi\phi_i \left[\nabla \ln(\dot{\gamma}\phi_i) + \frac{\bar{a}}{a_i} \nabla \ln \mu^\lambda \right] \quad (6.3)$$

where j_i is the migratory flux of particle i , k and λ are dimensionless constants, \bar{a} is the average particle radius and μ is the viscosity. The term outside the brackets denotes the shear-induced diffusivity $D_{s,i}$ for the i th particle.

In previous work [85], we carried out calculations on the stationary flux by introducing the shear-induced diffusivity of the small particles (in bidisperse suspensions: Equation 6.3) in the model for the stationary permeate flux J_{ss} (Equation 6.2). Therewith, the particle volume fraction remains as a driving force for shear-induced migration.

6.2.2 Shear-induced particle segregation in channel flow

It is known from literature that shear-induced migration can also lead to size segregation of particles in a suspension subjected to channel flow. The center region of the channel is found to be enriched with large particles, whereas the zone near the channel wall was almost depleted of large particles [68]. This size segregation could be important for microfiltration systems, because the crossflow is usually much larger than the flow through the membrane. In that way, only the composition of the suspension that flows closely along the membrane wall may be relevant to concentration polarisation and cake layer formation. Whether this is also the case in this study, is discussed in the results section.

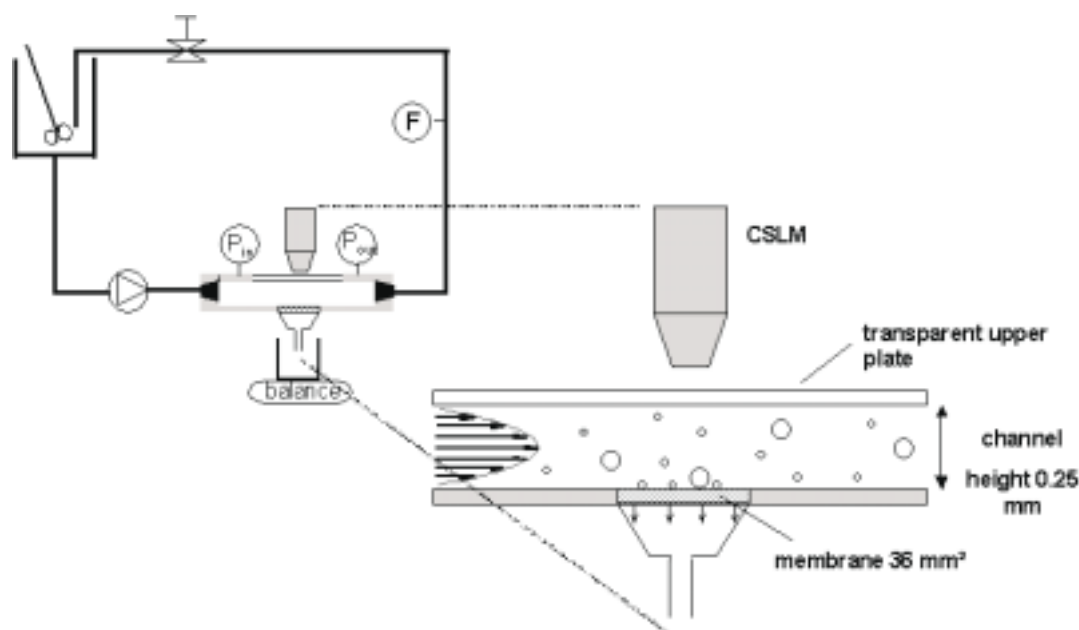


Figure 6.1: Schematic drawing of the microfiltration set-up with on-line monitoring of particle deposition onto the membrane by means of CSLM. A detailed description is given in the text.

6.3 Materials and methods

6.3.1 CSLM experiments

Microfiltration set-up

A crossflow MF system was used, consisting of a parallel plate device with a channel height of 0.25 mm and a channel width of 26 mm (Figure 6.1). The feed was continuously recirculated over the parallel plate device with a crossflow velocity of 0.04 m/s. This yields a shear rate $\dot{\gamma}$ at the membrane surface of 1000 s^{-1} . The volume in the recirculation loop was such that no significant concentration took place during an experiment. The pressure was monitored with two pressure sensors in the parallel plate device, at equal distance up- and downstream of the membrane. At the permeate side the pressure was atmospheric. The experiments were performed at ambient temperature.

A polyethersulfon MF membrane (Omega, low-protein binding modified, Filtron, USA) with a Molecular Weight Cut-Off (MWCO) of 100 kDa and a membrane area of 36 mm^2 was used. The feed consisted of a suspension of dyed polystyrene spherical particles (surfactant-free, sulfate polystyrene, density 1.06 g/ml, Interfacial Dynamics Corporation, USA) in demineralised water. The particles were dyed with fluorescent coloring agents in order to make them visible with the Confocal Scanning Laser Microscope (CSLM). Particles with a diameter of 1.6 and 4.0 or of 1.6 and 9.8 μm were mixed to obtain a bidisperse suspension. With these particle diameters, together with the relatively low shear rate of 1000 s^{-1} , we are well within the shear-induced diffusive regime [10]. The total volume fraction ϕ_{total} of particles was always $1.8 \cdot 10^{-5}$. Because it is known that the smaller particles mainly deposit onto the membrane and it is expected that these smaller particles will be influenced most at relatively high concentrations of large parti-

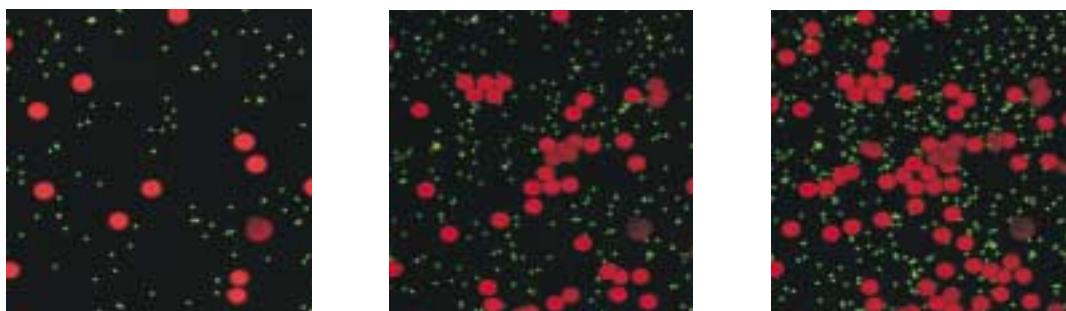


Figure 6.2: Example of the particle deposition onto the membrane during MF of a bidisperse suspension, as monitored with CSLM. The images represent a time sequence, where time proceeds from left to right, and consist of an overlay of images that were taken separately of the different-sized particles (particle diameter 1.6 and 9.8 μm).

cles, bidisperse suspensions with more than 70% v/v large particles were chosen for the experiments.

Analysis of the particle deposition and the permeate flux

The permeate flux through the membrane was monitored with an analytical balance. The particle deposition onto the membrane was monitored with CSLM (Leica TCS SP2, Leica Microsystems, Heidelberg, Germany). Hereto, a lens was used with a magnification of 20 and a working distance of 3.2 mm. The CSLM images encompassed 0.036 mm² membrane surface. The excitation wave length of the laser was 488 nm. The different-sized particles had different colors, so they were viewed separately at an emission wave length of 500-536 nm and 568-621 nm respectively. The CSLM generates x-y images of the focal plane. Because the depth z at which the particles deposit was not exactly known beforehand, the 2-D images were scanned at different depths. The acquisition time for one x-y image was about 1 s, while the total scan took about 30 s.

Figure 6.2 shows an example of CSLM images, taken during MF of a bidisperse suspension at three points in time. The figure shows an overlay of the images that were taken separately for each particle-size. These separate images were analysed with the image processing software Qwin (Leica Microsystems, Heidelberg, Germany), which first converts the image into a binary file. The amount of particles deposited onto the membrane was assessed by counting the pixels with an intensity above a certain threshold value. For each experiment, a calibration was carried out first in order to relate the amount of pixels to the number of particles. The assessment of the amount of particles was only possible when less than one layer of particles was deposited onto the membrane. Therefore, only data for a total surface occupation of less than 60-65%, as derived from the counting of the pixels, were taken into account. The amount of particles on the membrane is presented as the surface load Γ , which corresponds to the volume of particles per surface area of membrane (unit: ml/m²). The theoretical maximum surface load Γ corresponds to the surface load of one layer of particles with a volume fraction of 1.0 and is dependent on the particle size: 1.1 ml/m² (1.6 μm), 2.7 ml/m² (4.0 μm) and 6.5 ml/m² (9.8 μm). Since we are only interested in concentration polarisation-controlled particle deposition, we have corrected the surface load for the amount of particles that deposited otherwise (physico-chemical adsorption). This amount of adsorbed particles is determined from calibration curves,

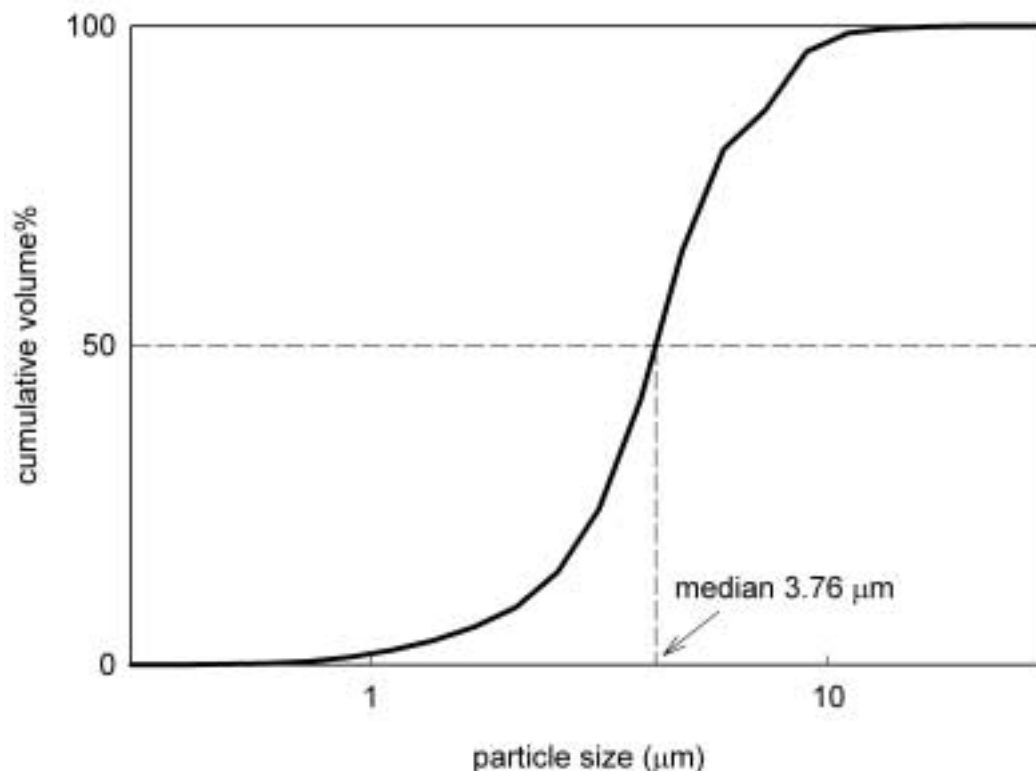


Figure 6.3: Cumulative particle size distribution of milk, as analysed by laser diffraction.

which were measured for the respective monodisperse suspensions at $\phi_{\text{total}} = 1.8 \times 10^{-5}$. It is assumed that the adsorption rate is linearly dependent on the concentration of the respective particle in the bulk phase.

6.3.2 Fractionation of milk fat globules

Raw milk (fat content 4.40%) was used in the experiments. The particle size distribution (psd), which is primarily determined by the milk fat globules present in milk, is shown in Figure 6.3.

The MF set-up consisted of the Alfa Laval MFS-1 system, equipped with a $5.0 \mu\text{m}$ ceramic MF membrane (SCT Membralox P19-40, tubular $\alpha\text{-Al}_2\text{O}_3$ membrane, tube diameter 4.0 mm, membrane area 0.20 m^2). The filtration temperature was 50°C and the crossflow rate was set at 2.2 or $6.6 \text{ m}^3/\text{h}$, corresponding to a crossflow velocity (CFV) of 2.6 and 7.7 m/s respectively. The wall shear rate $\dot{\gamma}_{\text{wall},0}$, which is given by $8v/d_t$ (v =velocity, d_t =tube diameter), was equal to 5.1×10^3 and $15.4 \times 10^3 \text{ s}^{-1}$ respectively. At a CFV of 7.7 m/s, not only shear-induced diffusion, but also inertial lift may play a role as back-transport mechanism, especially for the largest milk fat globules [10]. The experiments were carried out following the so-called Uniform Transmembrane Pressure concept [90] by circulating permeate co-current to the retentate. The permeate circulation capacity was adjusted to the actual crossflow rate in order to create a permeate pressure drop equal to the retentate pressure drop. The experiments were carried out in continuous mode at a concentration factor $\text{CF} (=Q_{\text{feed}}/Q_{\text{retentate}})$ of 2.5. The transmembrane pressure

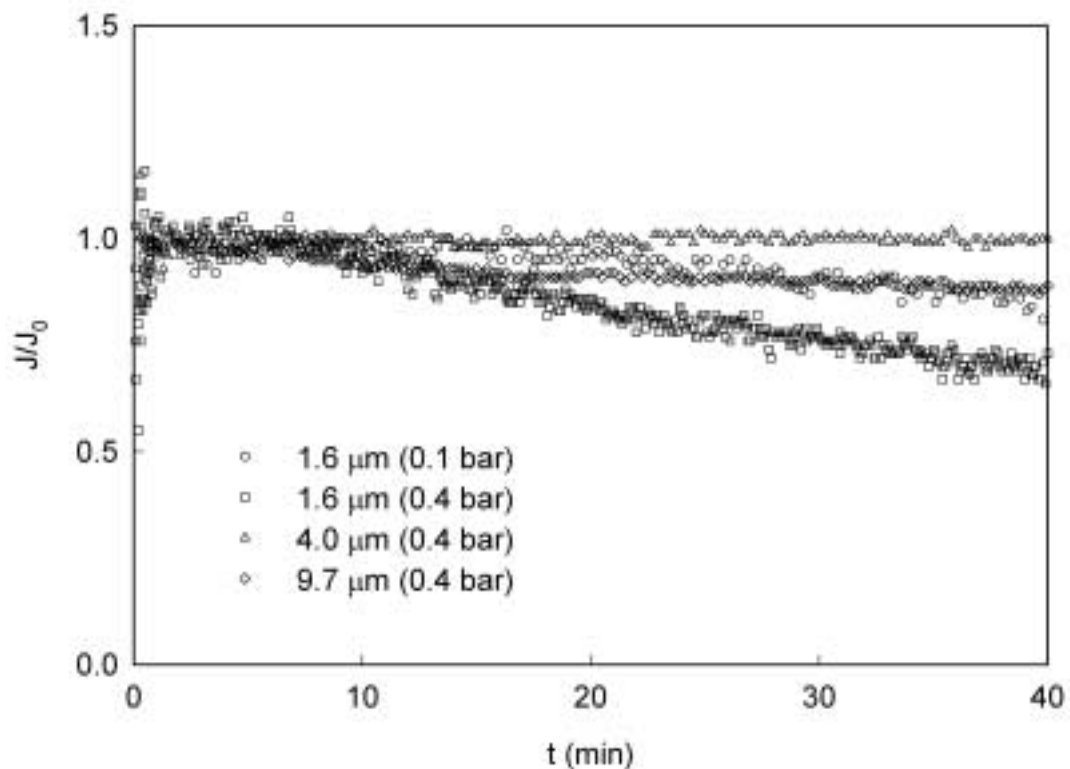


Figure 6.4: The relative flux J/J_0 as a function of time for a suspension with $1.6 \mu\text{m}$ particles at a TMP of 0.1 and 0.4 bar and for suspensions with 4.0 and $9.7 \mu\text{m}$ particles at a TMP of 0.4 bar.

was adjusted in such a way that the permeate flux was between 0.069 and 0.56 mm/s. Each experiment was started at a low permeate flux of 0.069 mm/s, allowed to settle for 0.5 h, and followed by a run of 0.5 h at a similar permeate flux. Then the permeate flux was increased stepwise to 0.139, 0.278 and 0.417 or 0.556 mm/s, in three more runs of 0.5 h each. At the end of each run, samples were taken of the retentate and permeate, and analysed for fat content (Röse Gottlieb method) and particle size distribution (laser diffraction, Mastersizer X (Malvern Instruments, Malvern, UK)).

6.4 Results

6.4.1 Kinetics of particle deposition

The CSLM experiments are carried out at a transmembrane pressure (TMP) of 0.4 bar, which goes together with a clean water flux (CWF) of 0.3 mm/s. From Figure 6.4, it becomes clear that at a TMP of 0.4 bar the flux decrease is strongest for the $1.6 \mu\text{m}$ particle suspension. The fluxes for the other particles are fairly constant. This is in agreement with Equation 6.2, which predicts that only monodisperse suspensions with a particle diameter of $1.6 \mu\text{m}$ will exhibit flux decline and particle deposition. At a TMP of 0.1 bar, the flux was also fairly constant for $1.6 \mu\text{m}$ particles, as was expected from Equation 6.2.

For particle diameters of 4.0 and $9.8 \mu\text{m}$, some particle deposition has been monitored

with CSLM (Figure 6.5). The surface load Γ was found to increase almost linearly in time. Since the initial flux J_0 was lower than the flux predicted by Equation 6.2 for the respective particles, it is unlikely that this particle deposition is caused by an unbalance in the concentration polarisation-controlled transport of particles towards the membrane. We therefore hypothesize that this particle deposition is due to physico-chemical adsorption, which is not related to the phenomena that are currently under investigation. For the particle size of $1.6 \mu\text{m}$, the total particle deposition was much faster at a TMP of 0.4 bar than at 0.1 bar, therewith indicating that it is still well-possible to distinguish between the concentration polarisation-controlled kinetics in which we are interested and adsorption effects. In the following results, we have therefore corrected the surface load for the amount of adsorbed particles, as described in section 6.3. The corrections that we have applied this way are in the order of 17% of the original surface load Γ .

The flux and surface load during filtration of bidisperse suspensions (particle sizes 1.6 and $4.0 \mu\text{m}$) were investigated. The flux decline was very slow and depended on the concentration of small particles: the fastest flux decline is found for the suspension with the highest concentration of small particles (Figure 6.6). In the first few minutes of filtration, for concentrations of small particles of 10, 15 and 20%, the flux was relatively low and unstable, due to start-up effects. Therefore, the following analysis of our results is based on the momentaneous flux. The surface load Γ for the small particles increases to 0.07 - 0.16 ml/m^2 in the first 10 min of the filtration run (Figure 6.6). After the start-up period, the increase was practically linear in time and was faster with increasing concentration of small particles. The surface load for the large particles was found to be negligibly small (results not shown). Apparently, the back-transport velocity of the large particles in the bidisperse suspensions does not decrease drastically compared to a monodisperse suspension. The linear increase of the surface load can be understood as follows: the transport of particles towards the membrane only decreased very slowly, as is reflected in the observation that the flux is almost constant, and the back-transport of particles is also expected to be constant in time since bulk volume fractions and CFV remain constant. Therefore, the deposition rate of particles, which is the difference between the two transport velocities, is constant as well.

For bidisperse suspensions with particle sizes of 1.6 and $9.8 \mu\text{m}$, similar trends were found as with particle sizes of 1.6 and $4.0 \mu\text{m}$ (Figure 6.7). The higher the amount of small particles, the more small particles are deposited. Moreover, both experiments carried out with 10% small particles show similar numerical values for the surface load. The surface load Γ of the large particles was negligibly small again (results not shown). The flux decline was very gradual, albeit that the suspension with 2.5% small particles showed some start-up problems.

6.4.2 Shear-induced diffusive particle behaviour

In order to analyse the shear-induced diffusive behaviour of the small particles in the bidisperse suspensions, we calculated the back-transport fluxes in our experiments and compared these to the back-transport fluxes as predicted by Equation 6.2. The back-transport flux in the experiments is calculated in three steps: 1) determine the particle deposition rate as a function of time by progressive regression of Γ over t over a time interval of 4 min, moving along the time axis, 2) determine the maximum value for the deposition rate as to exclude possible start-up effects, 3) determine the back-transport

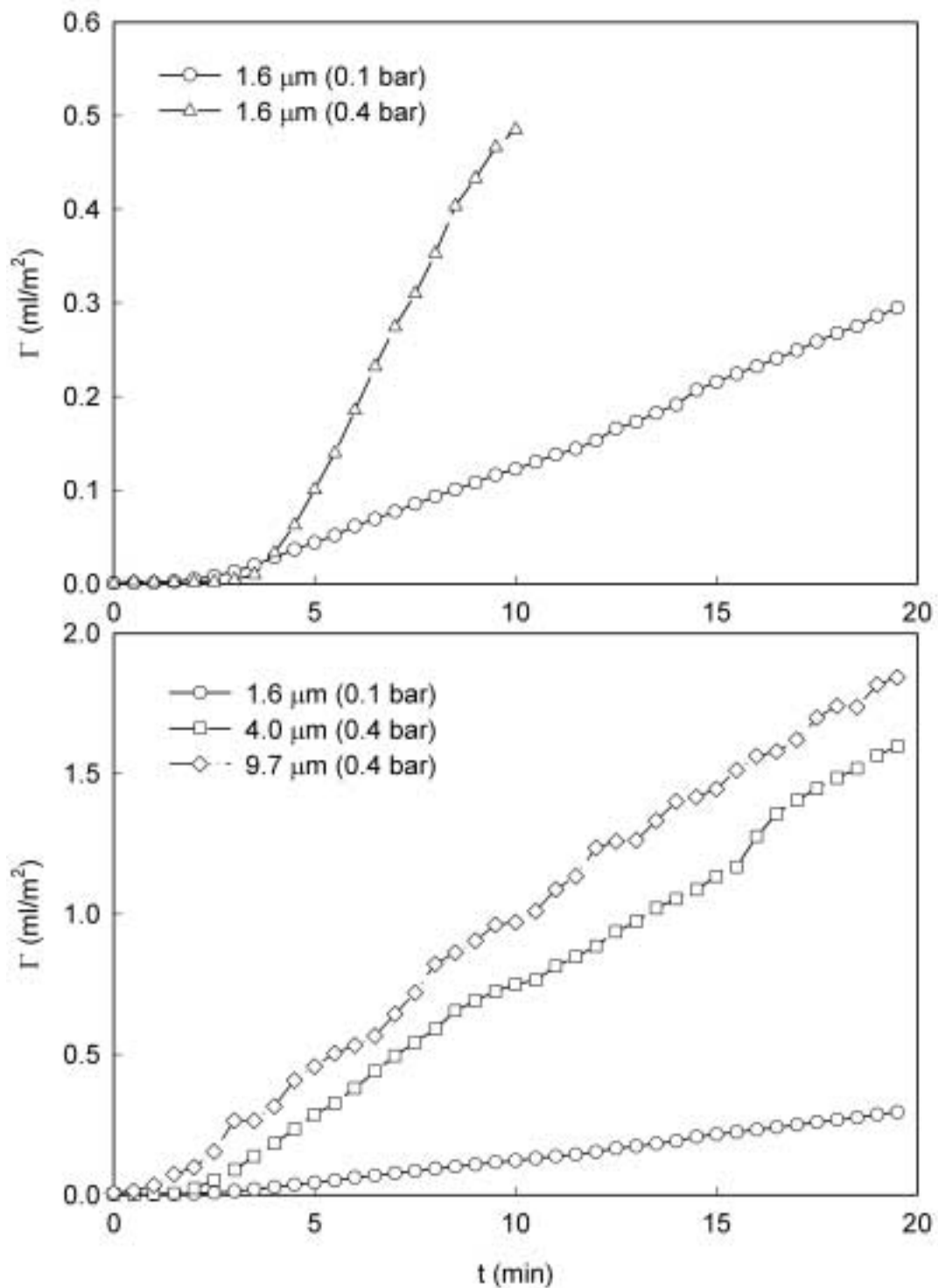


Figure 6.5: The surface load Γ as a function of time for a monodisperse suspension with 1.6 μm particles at a TMP of 0.1 and 0.4 bar (top) and for suspensions with 1.6 (TMP 0.1 bar), 4.0 (TMP 0.4 bar) and 9.7 (TMP 0.4 bar) μm particles (bottom).

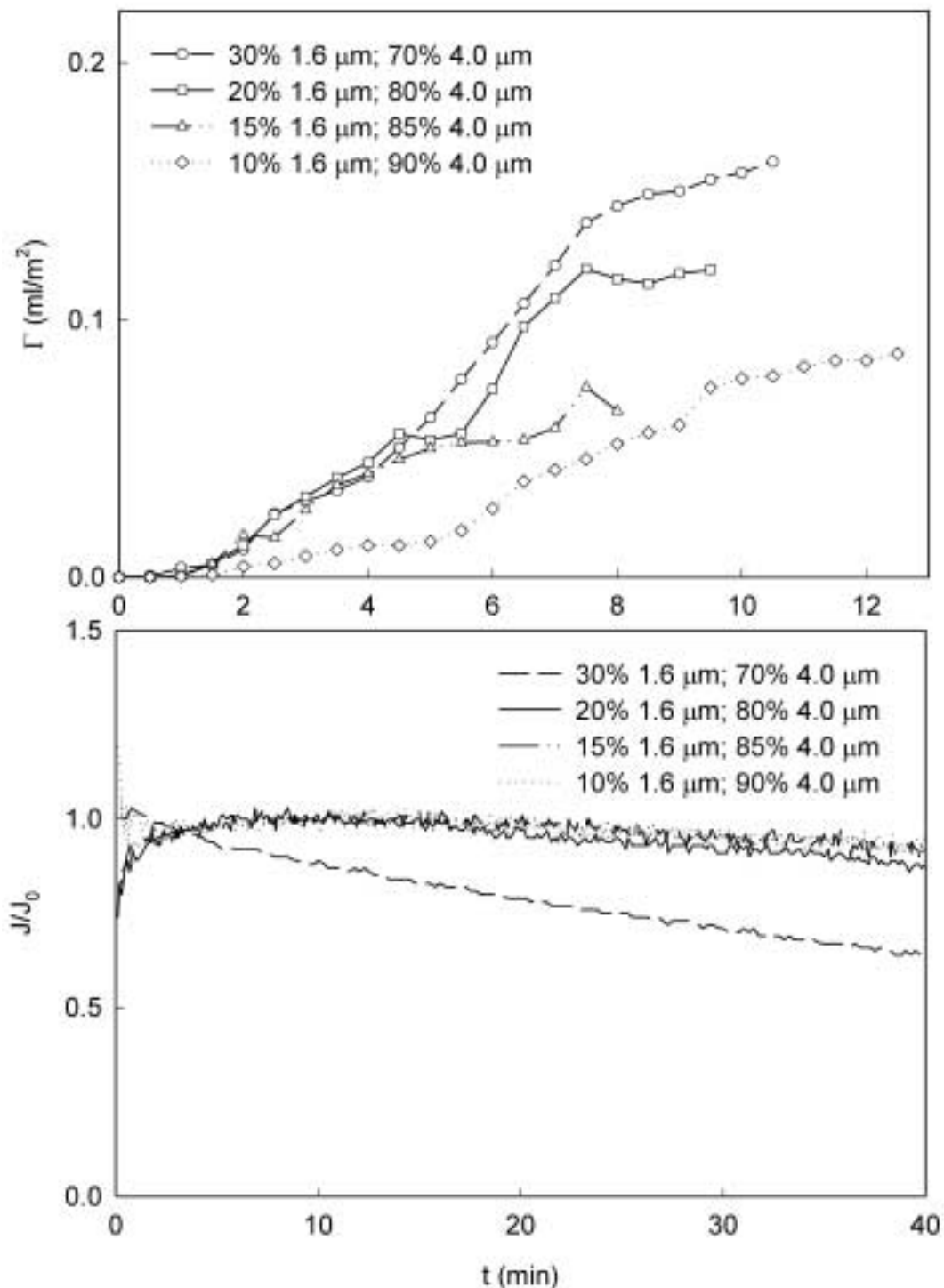


Figure 6.6: The surface load Γ (top) and the relative flux J/J_0 (bottom) as a function of time for bidisperse suspensions with 1.6 and 4.0 μm particles (TMP 0.4 bar).

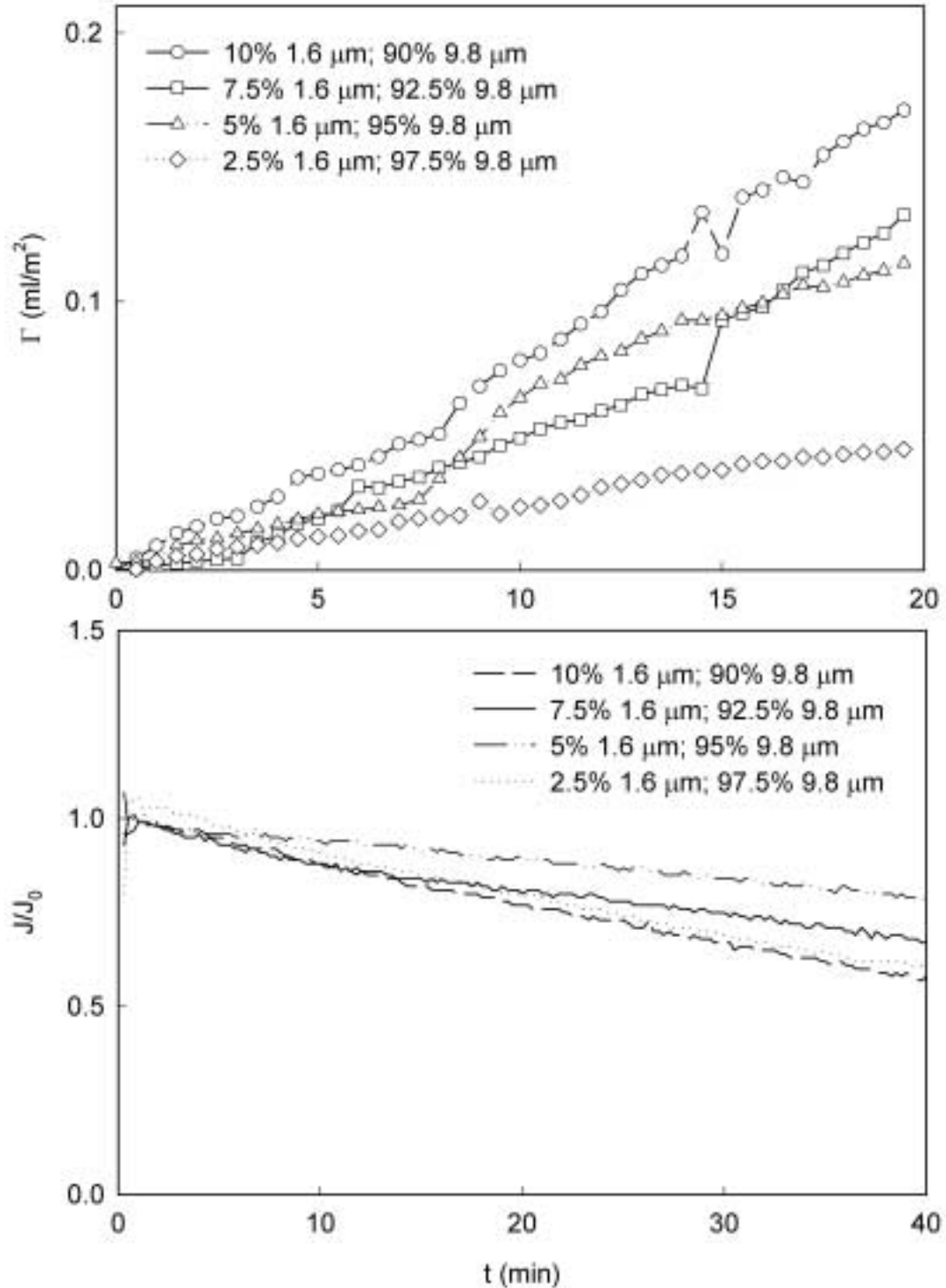


Figure 6.7: The surface load Γ (top) and the relative flux J/J_0 (bottom) as a function of time for bidisperse suspensions with 1.6 and 9.8 μm particles (TMP 0.4 bar).

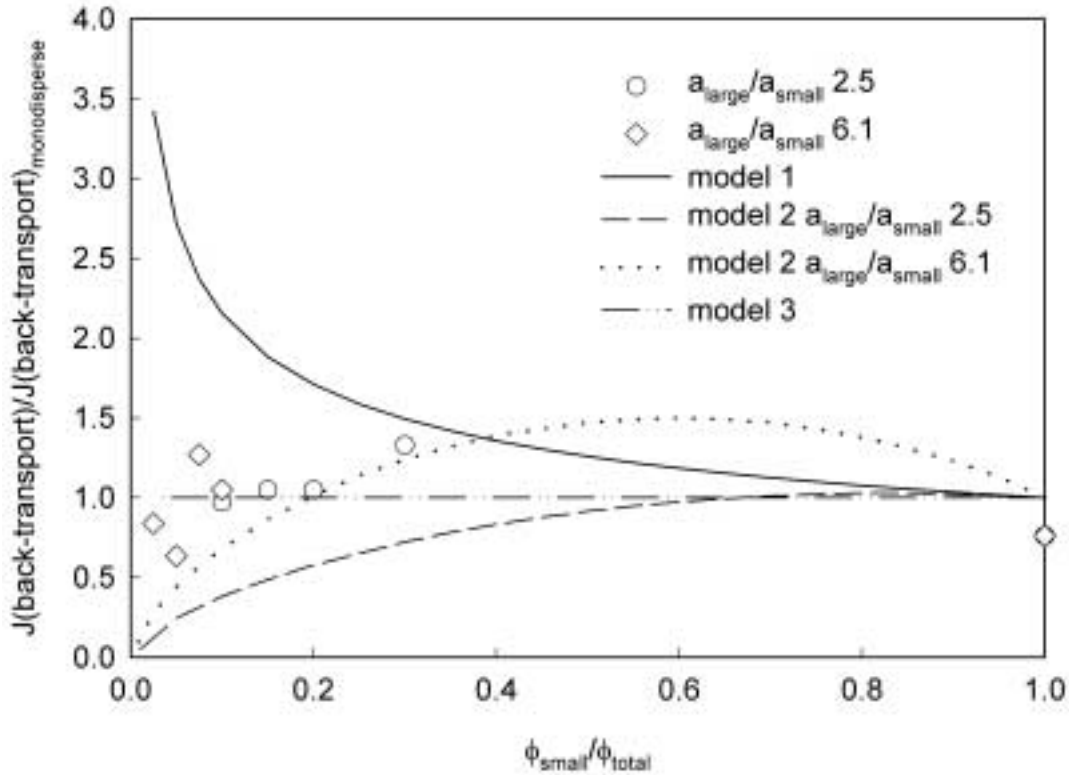


Figure 6.8: The back-transport flux as measured for bidisperse suspensions and compared to model predictions of three different models, as explained in the text.

flux by subtracting the deposition flux from the actual flux at the corresponding time. The results are shown in Figure 6.8. The experimental data are compared with the predictions for three different cases, each with other assumptions for the interaction between the two different-sized particles.

The first case is based on the assumption that the shear-induced diffusivity of the small particles is not influenced by the presence of the large particles at all. Most likely, this will only occur when the concentration polarisation layer is free of large particles, because otherwise interactions between the small and large particles in this layer are expected to change the shear-induced diffusivity (Equation 6.1 and 6.3). The back-transport flux for this first case is consequently calculated with Equation 6.2, with the actual concentration of small particles in the bulk ϕ_b and a fraction of small particles at the membrane $\phi_c = 0.6$ (as mostly assumed in shear-induced diffusion models for monodisperse suspensions [8, 10, 81]). Because the concentration difference between bulk phase and concentration polarisation layer is highest, the maximal back-transport flux is calculated in this way. In the second case, we assume that the shear-induced diffusivity of the small particles in the concentration polarisation layer is affected by the presence of large particles. This implies that the ratio of small to large particles is the same in the bulk phase and in the concentration polarisation layer (but only the small particles deposit). The shear-induced diffusivity is calculated according to $D_{s,i}$ in Equation 6.3, which depends on the actual ratio of particle sizes. Next, Equation 6.2 is corrected for this change of the shear-induced

diffusivity by correction of the value of a . Hereafter the back-transport flux is calculated (Equation 6.2). In the third case, we assume that particle size segregation as measured in bidisperse suspensions by Lyon and Leal [68] occurs in the feed flow. These authors found that the region close to the wall was totally depleted of large particles, whereas the fraction of small particles was equal to that of a monodisperse suspension with the same total volume fraction of particles. We have therefore taken the total particle fraction ($=\phi_{\text{large}} + \phi_{\text{small}}$) as the bulk fraction ϕ_b in our calculations ($\phi_c = 0.6$) and subsequently calculated the back-transport flux with Equation 6.2.

The three cases described earlier are used to calculate the back-transport flux as a function of the fraction of small particles. In Figure 6.8, the normalised back-transport flux (relative to back-transport in a monodisperse suspension) is shown. In the first case, the normalised back-transport flux is a function of the concentration of small particles and will decrease with increasing concentration of small particles (Equation 6.3). For the second case, the normalised back-transport flux is a function of the concentration of both particles and their size aspect ratio. The curves show an optimal ratio of small to large particles for back-transport. The third case shows back-transport behaviour which is independent of the fraction of small particles. The measured back-transport fluxes are all between 0.64 and 1.33 of the back-transport flux for a monodisperse suspension. The experimental data are best described by model 3 that takes particle size segregation into account. The back-transport flux of the small particles in the bidisperse suspension does not seem to be affected by the particle composition and is equal to that of a monodisperse suspension with the same total volume fraction of particles. Based on these results, it can be expected that the steady-state flux $\langle J_{\text{ss}} \rangle$ of these bidisperse suspensions will also be equal to that of monodisperse suspensions, which is in accordance with our previous findings [85]. Measuring the steady-state flux $\langle J_{\text{ss}} \rangle$ for the suspensions used in this paper is very difficult, since the flux decline is very slow. Therefore, these measurements were not carried through till steady-state was reached.

Our CSLM method has given us important clues on the kinetics of particle deposition during MF and shows that particle size segregation is a factor that can be of importance while designing MF processes. Whether this is the case is tested in a milk filtration set-up.

6.4.3 Fractionation of milk fat globules

The fractionation of milk fat globules is carried out partly following a patented process [91], but at much lower flux levels and with a membrane with a relatively large pore size. The measured TMP is shown as a function of J in Figure 6.9. The TMP increases nearly linear with J , with an identical slope for the different CFV's. Moreover, the slope was identical to the slope for clean water. This indicates that no deposition of fat globules has taken place and that J is controlled by the membrane resistance solely. Apparently, the membrane pore size is larger than the fat globule size of the permeating fat globules, such that they can pass the membrane. The absolute values of the TMP are higher at a CFV of 7.7 m/s. As can also be concluded from the measurements of the cleanwaterflux, these higher values are due to the presence of an offset pressure in the system, probably caused by the placement of the pressure sensors near a pipe constriction, just outside the membrane module.

At a CFV of 2.6 m/s, the relative fat content of the permeate increased from 0.43 ($J=0.069$ mm/s) to 0.79 ($J=0.42$ mm/s) with increasing J (Figure 6.10). The mean par-

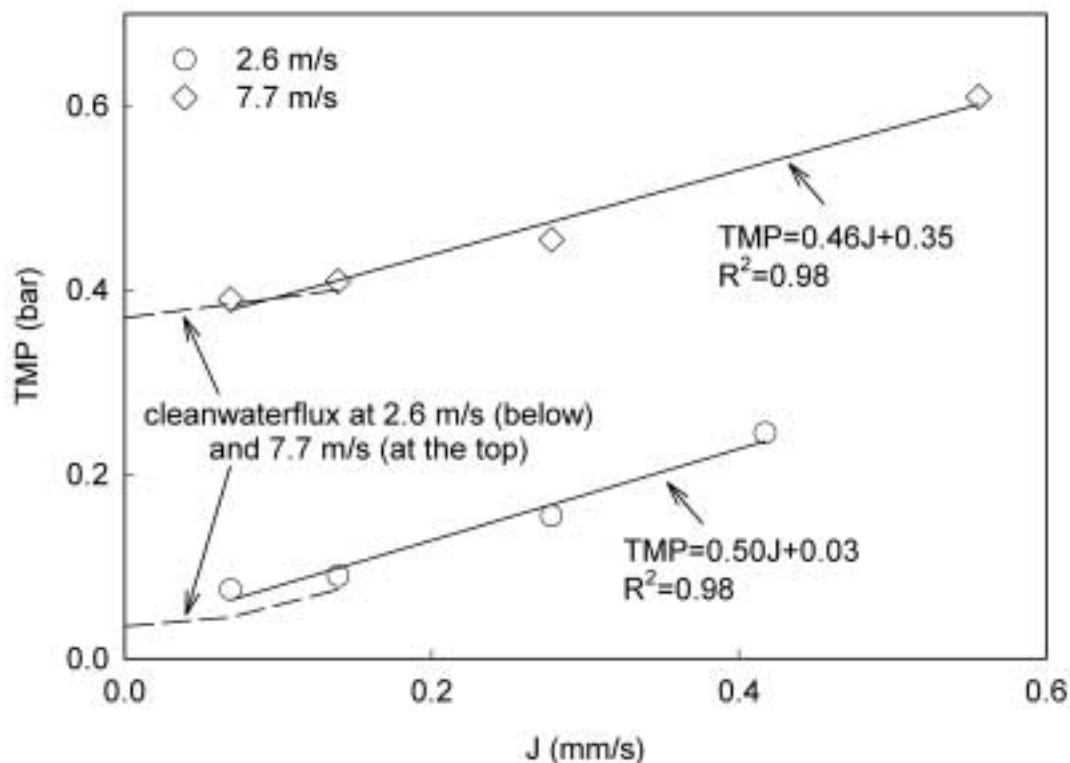


Figure 6.9: Transmembrane pressure TMP as a function of the permeate flux J (crossflow velocity CFV 2.6 and 7.7 m/s) during MF ($5.0 \mu m$, $50^\circ C$, CF 2.5) of milk. The solid lines represent fit results of linear regression, whereas the dashed lines show the relation between TMP and J for clean water.

ticle size showed a similar trend and increased from 3.0 to $3.6 \mu m$. At a CFV of 7.7 m/s, the relative fat content was always lower and the particle size was always smaller. The increase with J was less pronounced as well. The average values were 0.29 (relative fat content) and $2.9 \mu m$ (median psd).

It is clear that the fat globules are separated on size. As stated above, deposition of fat globules onto the membrane can be excluded as the cause for this separation. It could be debated whether the membrane itself could act as a screen, without resulting in particle deposition. It can be seen in Figure 6.10 that at $CFV=2.6$ m/s and $J=0.42$ mm/s, the fat globule size and the fat content of the permeate approaches that of the feed very near. At different conditions, but with the same membrane however, the fat globule size and the fat content of the permeate shifted to totally different values. This effect cannot be explained with the screening action of the membrane.

The results in Figure 6.10 indicate that particle size segregation takes place. In contrast to the bidisperse suspensions, for the largest fat globules and $CFV=7.7$ m/s, the particle size segregation may not be solely induced by shear-induced diffusion. Because of the relatively large particle size and high wall shear rate, inertial lift can also play a role. As can be seen in Figure 6.10, also in this regime, particle size segregation was still evident. In general, particle size segregation increases with increasing shear rate. This will result in smaller particle sizes in the region near the wall and consequently in smaller particle

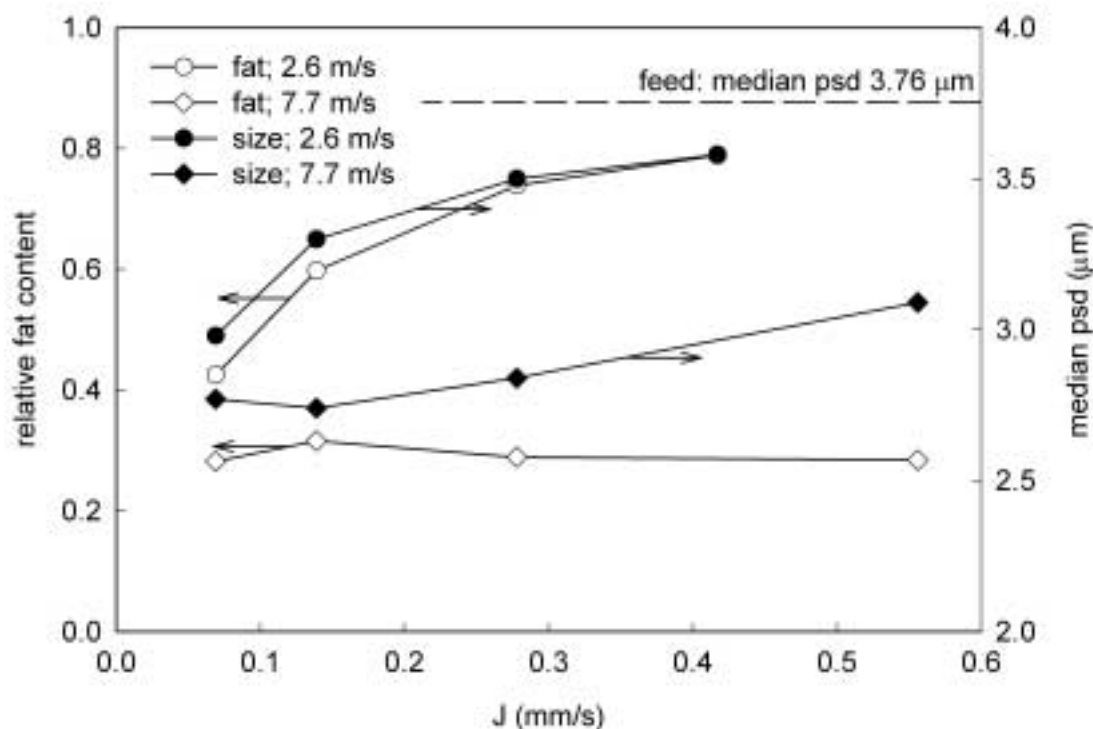


Figure 6.10: The fat content, relative to the fat content of milk, and the median of the particle size distribution in MF-permeate as a function of the permeate flux J (crossflow velocity CFV 2.6 and 7.7 m/s) during MF ($5.0 \mu\text{m}$, 50°C , CF 2.5) of milk.

sizes in the permeate. In Figure 6.10, the median indeed decreases with increasing CFV indicating that particle size segregation was more severe at a CFV of 7.7 m/s. Moreover, an increase of particle size in the permeate can be expected with increasing J (no retention by membrane), a trend that is expected to be more pronounced at lower shear rates. This is because a larger part of the crossflow, with larger particle sizes, permeates through the membrane. Again, this was measured. We can therefore conclude that particle size segregation is not only significant for bidisperse suspensions, but also for polydisperse particle fractionation by MF. In such particle fractionation processes, the composition of the permeate can be controlled with the CFV and J , while the only limitation for the pore size of the membrane is that it is larger than the largest particles in the feed suspension.

6.5 Conclusions

In order to investigate the shear-induced diffusive behaviour of particles in bidisperse suspensions, as relevant to concentration polarisation in MF processes, we have analysed the flux and particle deposition onto the membrane. The particle deposition was monitored by means of on-line CSLM. From the measured deposition rate of the small particles and the flux, it could be concluded that the back-transport flux of the small particles did not depend on the composition of the bidisperse suspension and was equal to the back-transport flux of the monodisperse suspension with the same total particle volume fraction. These

results can be explained with the occurrence of particle size segregation in the feed flow, leading to an enrichment with small particles of the suspension in the vicinity of the membrane wall. This conclusion is not only relevant to concentration polarisation in MF processes, but also to particle fractionation by MF as is shown in a study on the fractionation of milk fat globules. Here, particle size segregation leads to a distinct effect on the separation characteristics of the process such as particle size and fat content of the permeate, leading to fractionation of a polydisperse suspension with a membrane having a pore size that is larger than the largest particle present.

List of symbols

a	particle radius, m
CF	concentration factor
CFV	crossflow velocity, m/s
CWF	clean waterflux, m/s
d	diameter, m
D	diffusivity, m^2/s
j	migratory particle flux, m^2/s
J	transmembrane flux, m/s
k	dimensionless particle migration parameter in Eq. 6.3
L	length, m
Q	mass flow rate, m^3/s
t	time, s
TMP	transmembrane pressure, bar
v	velocity, m/s

Greek symbols:

$\dot{\gamma}$	shear rate, s^{-1}
Γ	surface load, ml/m^2
λ	dimensionless particle migration coefficient in Eq. 6.3
μ	viscosity, $\text{kg}/\text{m}\cdot\text{s}$
ϕ	particle volume fraction

Subscripts:

b	bulk
c	cake
m	membrane
s	shear-induced
ss	steady-state
t	tube
0	nominal

Acknowledgements

Friesland Foods is greatly acknowledged for supporting this research. Anno Koning (Friesland Foods) is thanked for the skilful application of the CSLM-technique. Henk Streppel (Friesland Foods) is gratefully thanked for carrying out the pilot-plant fractionation experiments. The authors would like to acknowledge the support of the Dutch Ministries of Economic Affairs, Education, Culture and Sciences and of Housing, Spatial Planning and the Environment through a grant of the Dutch Program Economy, Ecology and Technology.

**Differential analysis of particle
deposition layers from micellar casein
and milk fat globule suspensions**

Particle deposition behaviour on membrane filters is of the utmost importance for the flux and selectivity. For milk filtration not only the particle behaviour as such but also the behaviour in time is a factor to take into account. Therefore we applied a differential analysis to the flux decline during dead-end filtration of latex, casein micelles and milk fat globules.

Based on our analysis for latex we distinguished two regions, one best described by pore blocking and one by cake filtration. Besides these two regions, no other time dependent behaviour was observed, as was expected for latex. However, for casein micelles and milk fat globules various other time dependent effects were observed and quantified.

Pore blocking of an UF membrane by micellar casein was relatively inefficient, as concluded from the values of the pore blocking parameter of 0.1-0.2. In contrast, the cake resistance was relatively high, 35 times higher than expected from the Carman-Kozeny theory. This may be attributed to a decrease of the size of the casein micelles, leading to the formation of very compact layers. The specific cake resistance of micellar casein was lower for a MF membrane where depth filtration played a role.

Milk fat globules generate layers with a very high cake resistance, both for liquid and for partly crystallised fat. For liquid fat, spreading of milk fat globules onto the membrane and deformation of milk fat globules seem to be the main cause for the high cake resistance. When a large part of the milk fat was crystallised ($T=5^{\circ}\text{C}$), partial coalescence of milk fat globules in the cake layer seems to play a role.

Differential cake analysis proved to be a valuable method for the evaluation of concentrated particle layers, resulting in better knowledge about the specific (time dependent) particle behaviour in these layers. In this way, parameters are identified that are essential for the design of microfiltration or ultrafiltration processes.

7.1 Introduction

Microfiltration is a widely applied technique in the food and bioprocess industry for the separation and fractionation of particles in suspensions, such as present in milk. Milk contains about 15% v/v colloidal particles, mainly casein micelles (proteins) and (emulsified) fat globules. The development of the Uniform Transmembrane Pressure (UTP) concept in the 70's and 80's of the last century [90] enabled succesful microfiltration of this concentrated suspension on an industrial scale. This opened the way for the application of microfiltration for e.g. the reduction of bacteria and spores [92], fractionation of fat globules [91] and the separation of casein micelles and serum proteins in milk [92].

The performance of microfiltration processes is governed by particle deposition onto the membrane. Therefore, prediction of flux (decline) and separation performance requires a good understanding of this particle deposition process. Not only the deposition rate, but also the properties of the deposited layer play an important role.

Studies on the properties of deposition layers of (other) proteins [93–97] and emulsion droplets [98] are mostly carried out by modelling of dead-end filtration processes with a constant pressure drop. Two different modelling approaches can be distinguished: 1) based on the filtration equations of Hermia [99], and 2) based on the sieve mechanism of Flippov [100]. Both approaches recognise two different mechanisms: pore blocking

and cake filtration. The first mechanism is usually relevant in the beginning of the deposition process, and the second one after the deposition process has progressed for some time. Both approaches as well as both mechanisms can be expressed in one characteristic filtration law, describing how the change in resistance ($\frac{d^2t}{dV^2}$) is related to the resistance (inverse flux, $\frac{dt}{dV}$):

$$\frac{d^2t}{dV^2} = k \cdot \left(\frac{dt}{dV} \right)^n \quad (7.1)$$

The values of the constant k and the exponent n depend on the filtration mechanism. For pore blocking, n can vary between 1 and 2, and for cake filtration $n=0$. The two approaches of Hermia and Flippov are only different in the formulation of pore blocking. Hermia distinguishes three blocking mechanisms, complete, standard and intermediate blocking, each with a fixed value for n of 2, 1.5 and 1 respectively. Flippov uses a single parameter β (see section 7.2.4) to describe pore blocking for a given filter and suspension. This parameter has physical meaning: it is the ratio of the area of influence of a particle above a pore and the pore area itself. In other words, the value of the single parameter is a measure for the relative flux decline caused by the deposition of a single particle onto the membrane as related to the relative projection area of this particle on the membrane. The exponent n does not have a specific value in this approach.

The abovementioned models are valid for non-compacting and non-compressive particle layers. For soft and polydisperse colloids such as casein micelles and fat globules, these models may be lacking sufficient detail. Models that do take compaction and compression during a filtration run into account are also available (see e.g. [101–103]), but these models require detailed data on the concentration distribution in the particle layers. Since in general, the layers formed during milk microfiltration are very thin, analysis of the concentration distribution is technically complex. This may be the reason that presently, no systematic study on the properties of milk deposition layers has been published.

In this paper, we present a new differential approach for the analysis of the properties of deposition layers, based on simple flux measurements in dead-end filtration experiments. In this method, one single flux curve is separated into a series of curves, such that a time-sequence of flux curves is obtained, each representing a different stage of the filtration process. The time interval of each stage is taken such that the constant k and the exponent n can be considered constant. In this way, pore blocking and cake filtration can be evaluated separately in each stage of the process, but one can also discern the effects of compaction and compression of the particles on the flux decline in time.

We applied this approach to dead-end filtration of colloidal suspensions of casein micelles and milk fat globules. In this way we focus on the properties of these industrially relevant components, that, surprisingly enough, have not been studied systematically. With our differential flux analysis approach we were able to quantify the particle behaviour and found very large differences between the various particles under study.

7.2 Materials and methods

7.2.1 Preparation of colloidal suspensions

Latex particles

Three different suspensions were used; suspensions of latex particles, casein micelles and of milk fat globules. The latex particles (surfactant-free, sulfate polystyrene, density 1.06 g/ml, Interfacial Dynamics Corporation, USA) had mean diameters of 0.42 and 0.60 μm and were suspended in a mixture of demineralised water with 23.1 % w/w glycerol, which has the same density as the latex particles. The viscosity of the water-glycerol mixture is 2 mPa·s (25°C).

Casein micelles

The suspension of casein micelles was prepared from pasteurised skim milk. The skim milk contained 3.6% w/w protein (Kjeldahl method), consisting of 2.7% w/w casein and 0.7% w/w serum protein. The skim milk was microfiltered (Alfa Laval MFS-1 system, filtration temperature 50°C) with a 0.2 μm ceramic MF membrane (SCT Membralox P19-40, tubular $\alpha\text{Al}_2\text{O}_3$ membrane, tube diameter 4.0 mm, membrane area 0.20 m²) up to a concentration factor ($=Q_{\text{feed}}/Q_{\text{retentate}}$) of 7 (viscosity measurements) or of 4 and subsequently diafiltered (100%) and diluted (100%) with protein-free milk serum (dead-end filtration measurements), in order to increase the protein purity of the casein micelle fraction. After MF to a concentration factor of 4 and subsequent diafiltration, a micellar casein suspension was obtained with 6.1% w/w casein and 1.4% w/w serum protein. Since the voluminosity of casein micelles is about 4 ml/g and of serum proteins about 1.5 ml/g (room temperature) [104], the volumetric protein purity was about 92%. By means of ultrafiltration (filtration temperature 50°C) with a membrane with a Molecular Weight Cut Off (MWCO) of 5 kDa, a protein-free milk serum was obtained from milk, which was used to suspend the casein micelle fraction. After preparation of both the casein micelle fraction and the milk serum, a preservative was added after which the liquids were kept at a temperature of 2°C. The mean diameter of the casein micelles was 104 nm, as according to Walstra and others [104]. For viscosity measurements at 50°C, the voluminosity was taken equal to 3 ml/g [104]. The viscosity of the milk serum was assumed to be equal to that of water.

Milk fat globules

Pasteurised cream, prepared by centrifugation of milk, was used as raw material for the fat globule suspension. To remove protein from the cream, it was diafiltered with protein-free milk serum (prepared following the aforementioned method). Diafiltration was carried out batch-wise, with an intensity of four times 100%, using a microfiltration set-up (Alfa Laval MFS-1 system, filtration temperature 50°C) with a 0.8 instead of a 0.2 μm ceramic MF membrane. The ratio of protein to fat (Röse Gottlieb method) decreased from about 0.87 in milk (4% w/w fat) to about 0.02 in the cream after diafiltration. The fat globule fraction was suspended in the same medium and kept in the same way as the casein micelle fraction. The size distribution of the fat globules was assessed by laser diffraction

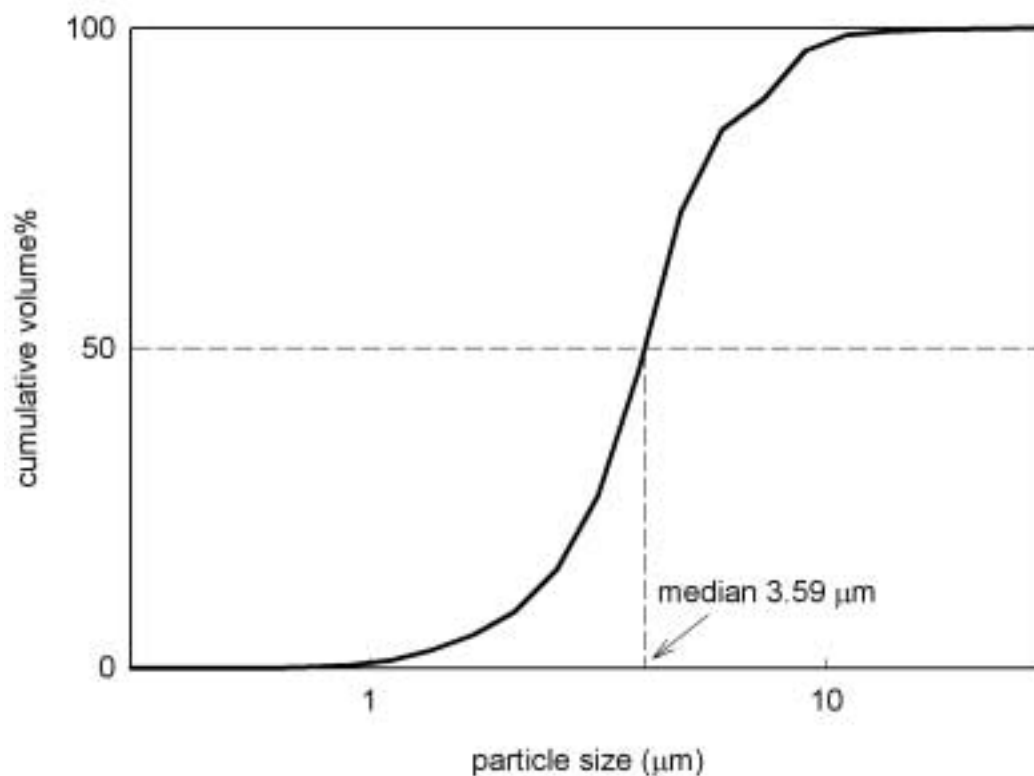


Figure 7.1: Cumulative particle size distribution of milk fat globule suspension, as analysed by laser diffraction.

(Mastersizer X, Malvern Instruments, Malvern, UK). The median of the distribution was $3.59 \mu\text{m}$ (batch I, Figure 7.1) and $3.50 \mu\text{m}$ (batch II).

Milk fat consists of a heterogeneous mixture of lipids with a melting range between -30 and $+40^\circ\text{C}$ [104]. At low temperatures, the amount and the morphology of the fat crystals can vary strongly depending on the (temperature) history of the product. To exclude temperature history effects in the filtration experiments at 5°C , the fat globules were molten and subsequently recrystallised in the following standardised way. The fat globule suspension was prepared 16 h before the start of the experiment, heated to 40 – 45°C and cooled down and kept at 5°C .

The concentrations of particles in the suspensions are given in this paper as volumetric concentrations, unless indicated otherwise.

7.2.2 Viscosity of micellar casein suspensions

Viscosity measurements were carried out at 50°C with a Physica MCR300 rheometer. For casein micelle concentrations lower than 0.5, the double gap cylinder geometry DG 26.7 with gap diameters of 0.42 and 0.47 mm was used; for higher concentrations the gap diameter was 1.13 mm (type CC 27). The measurements were carried out by starting at a shear rate of 0.01 1/s, increasing the shear rate logarithmically to 1000 1/s and subsequently decreasing it again to 0.01 1/s. The casein micelle concentrate was measured after storage at 4°C . The viscosity in relation to the casein micelle concentration was determined from

the viscosity in the descending series of shear rates.

7.2.3 Dead-end filtration

For dead-end filtration we made use of a device (type Omegacell, Pall Life Sciences) that was thermostatted by means of a jacket which was connected to a waterbath. The latex and micellar casein suspensions were filtered at a temperature of 25°C, the milk fat globule suspensions at 5°C and 45°C. Compressed air was used to control the transmembrane pressure. The weight of the permeate was continuously monitored with an analytical balance connected to a computer. The volume of the membrane cell was 150 ml. The membrane was placed at the bottom of the cell and had a membrane area of 23.2 cm². The membrane material was polyethersulfon (Omega, Pall Life Sciences). Two different pore sizes were used, a pore size of 0.3 μm and a MWCO of 10 kDa.

7.2.4 Analysis of cake properties

Filtration properties

We distinguish two different mechanisms for flux decline, pore blocking and cake filtration. For pore blocking, we follow the approach of Flippov and others [100], who derived the following filtration equation:

$$V^* = \frac{1}{\beta} \ln(1 + \beta t^*) \quad (7.2)$$

The dimensionless variables V^* and t^* are defined as follows:

$$V^* = \gamma n V \quad \text{and} \quad t^* = \gamma n \left. \frac{dV}{dt} \right|_{t=0} t \quad (7.3)$$

where n is the number of particles per unit volume, V is the permeate volume, t is the filtration time and γ represents the area ratio of the pore to the filter area:

$$\gamma = \frac{\pi \bar{d}^2}{4S} \quad (7.4)$$

where \bar{d} is the mean pore diameter and S is the filter area. The parameter γ is a single dimensionless constant for all suspension concentrations and operating pressures. In this pore blocking model, β is the only parameter that must be identified from experimental measurement. It represents the ratio of the area of influence of a particle above a pore and the pore area itself and relates the relative flux decline caused by the deposition of a single particle onto the membrane to the relative projection area of this particle on the membrane. For a membrane with distinct circular pores, such as track-etched membranes and microsieves, β should have a value of slightly larger than unity. For tortuous path membranes as used in this study, the value of β can also lie between zero and unity because the fluid has the possibility to flow laterally within the membrane structure.

The value of β was evaluated by regression analysis, minimising the residual sum of squares between the (smoothed) measured and model fluxes. Smoothing of the measurements was found to be necessary, since the resolution of the weight measurements

introduced too much noise in relation to the relative short time interval that was used in the fit. The measurements were smoothed by fitting the measured permeate volume versus time with a cubic polynomial. Because the value of β is expected to be dependent on the amount of particles deposited onto the membrane, we have split the initial flux curve into various stages and assessed β in every stage. The length of the stage matches with the deposition of a fixed amount of particles. This fixed amount corresponds to one deposited layer of average-sized particles with a volume fraction of 0.6. In this way, values for β are obtained for each “separate layer”. For the latex and micellar casein suspensions, β was analysed for the first up to the tenth layer, and for the milk fat globule suspensions for the first, second and third layer. The value for the initial flux $\left. \frac{dV}{dt} \right|_{t=0}$ was reset at each stage.

For cake filtration a comparable approach is used. The equation for the flux during dead-end microfiltration with a constant pressure drop is [105]:

$$J(t) = J_0 \left(1 + \frac{2\hat{R}_c \phi_s \Delta p t}{(\phi_c - \phi_s) \eta_0 R_m^2} \right)^{-1/2} \quad (7.5)$$

where J is the permeate flux, \hat{R}_c is the specific cake resistance, ϕ_s and ϕ_c are the particle fraction in the bulk and in the cake respectively, Δp is the transmembrane pressure, η_0 is the viscosity of the particle-free medium and R_m is the membrane resistance. The initial flux J_0 is given by:

$$J_0 = \frac{\Delta p}{\eta_0 R_m} \quad (7.6)$$

When the cake resistance is the dominating resistance, the equation for $J(t)$ as well as the corresponding equation for $V(t)$ reduce to power law functions of t , with slopes of -0.5 and 0.5, respectively, in a log-log plot. Here, the values of \hat{R}_c and ϕ_c need to be determined from measurements. Since we cannot determine them independently, we consider them as coupled parameters. A least squares fit on the fluxes (no smoothing) was carried out to assess \hat{R}_c and ϕ_c . The flux curve was again split into various stages. For the latex and micellar casein suspensions, the stages comprise five particle layers from 2.5-7.5, 7.5-12.5, 12.5-17.5, etcetera up to 42.5-47.5 particle layers thick. For the fat globule suspensions, the stages comprise a one-particle thick layer, from layer 1 up to 12. During cake filtration of monodisperse suspensions of rigid spherical particles, the values for \hat{R}_c and ϕ_c are constant and pressure-independent. The specific cake resistance \hat{R}_c can be estimated with the Carman-Kozeny equation, which is given by:

$$\hat{R}_c = \frac{K(1 - \epsilon_c)^2 S_c^2}{\epsilon_c^3} \quad (7.7)$$

where ϵ_c is the void fraction of the cake, and S_c is the solids surface area per unit volume of solids in the cake. For rigid spherical particles of radius r , the specific surface area is $S_c = 3/r$, the void fraction of a randomly packed cake is $\epsilon_c \approx 0.4$ (so $\phi_c \approx 0.6$), and the constant K is reported to have a value of 5.0. For polydisperse suspensions, Thies-Weesie and Philipse [106] developed the following equation:

$$\hat{R}_c = \frac{C(1 - \epsilon_c)^2}{\epsilon_c^3} \frac{1}{[1 + 4\sigma^2] \langle r \rangle^2} \quad (7.8)$$

where C is a constant with a value of 45, $\langle r \rangle$ is the number-averaged radius, and the standard deviation σ is equal to:

$$\sigma = \frac{\langle r^2 \rangle - \langle r \rangle^2}{\langle r \rangle^2} \quad (7.9)$$

In case of compaction or compression, \hat{R}_c and ϕ_c are not constant during filtration, but increase with the amount of deposited particles. The increase of \hat{R}_c and ϕ_c reflect both the properties of the newly deposited layer(s) and the changes in the existing layer(s).

Both for pore blocking and for cake filtration, and for every fit procedure, the 95% confidence interval of the fit parameter was determined. Sometimes, this 95% confidence interval was relatively large, for instance due to start-up effects or pressure fluctuations. Therefore, it was decided to exclude values if the confidence interval was larger than $\pm 50\%$ of the fit parameter itself.

Fat content milk fat globule layer

For the analysis of the fat content of the milk fat globule layer, a filtration run was carried out at a temperature of 5°C and a TMP of 2.2 bar. After the total suspension was filtered and only a cake layer of fat globules was left on the membrane, this cake layer is collected and analysed with NMR. $^1\text{H-NMR}$ experiments were carried out on a Bruker DRX500 spectrometer operating at 500.13 MHz. Spectra were taken at 21°C , using 90° pulses and a relaxation delay of 30 s. Samples were prepared by dissolving 45 mg of the milk fat sample in 1.5 g CDCl_3 and separation of the chloroform layer by centrifugation at 14000 g for 5 min. The signal of residual CHCl_3 was used as an internal reference. The fat content was determined by comparing the intensity of the glycerol- $\text{C}_\alpha\text{H}_2$ resonance of the milk fat sample with that of a butter sample with a known fat content.

7.3 Results

7.3.1 Latex suspensions

Figure 7.2 shows the collected permeate volume as a function of time for latex suspensions with $0.42 \mu\text{m}$ particles. The order of the relation varied from 0.8 at the start, to 1.0 a short time later and to 0.7 at the end of filtration. This indicates that the volume increase is relatively fast at the start, accelerates slightly and then slows down gradually during filtration. Because both pore blocking and cake filtration do not necessarily give constant orders, it cannot be assessed where either mechanism prevails. Therefore, we applied our differential cake analysis method to these data in order to determine the respective model parameters.

For pore blocking as well as cake filtration, different stages of the flux curve are fitted. Figure 7.3 shows the measured values together with the fitted model lines. Fits with the pore blocking model are used for the first ten particle layers. These layers were formed within 0.5 h. Due to start-up instabilities, the fit line for the first particle layer could not be assessed, but for the others (up to particle layer 10) β has a value between 0.016 and 0.021 (Figure 7.4), and shows a tendency to increase slightly with increasing number of particle layers. The values are much lower than 1.0, indicating that the particles block

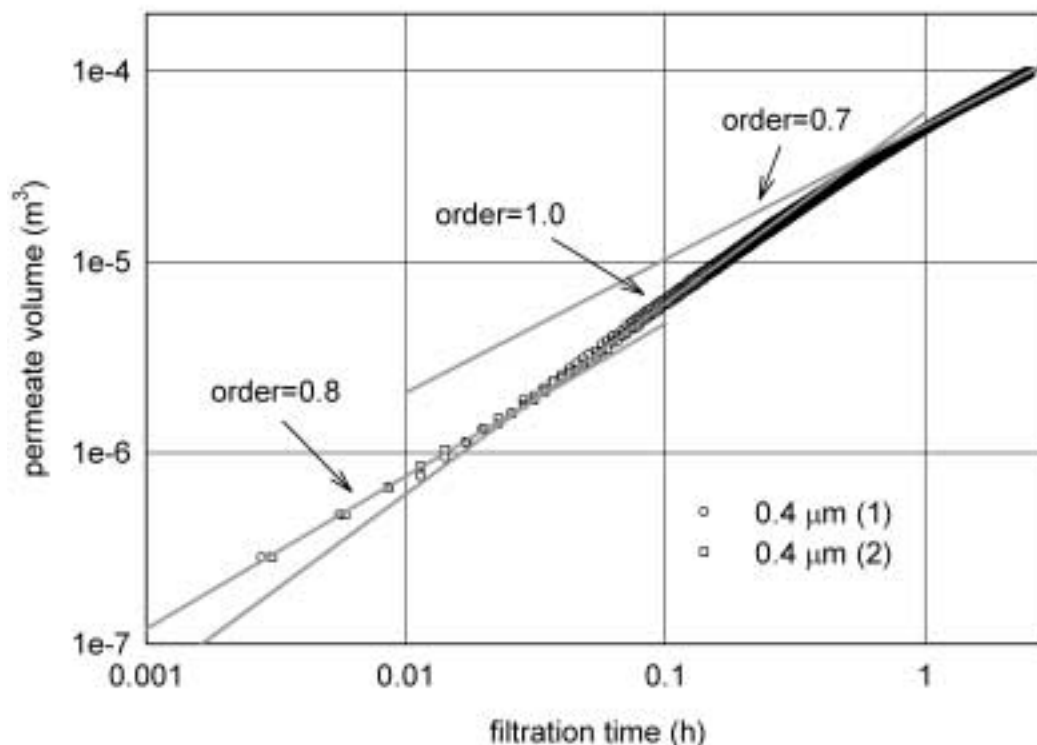


Figure 7.2: Permeate volume versus time during MF (TMP 16 mbar) of a latex suspension ($0.42 \mu\text{m}$, $3 \cdot 10^{-6} \%$).

the membrane rather inefficiently. This is probably related to the tortuous membrane structure, which allows lateral flow of the fluid in the membrane structure. The flux decline per formed layer is fairly equal.

The cake filtration model is fitted over a trajectory corresponding with 2.5 up to 47.5 particle layers. For the cake filtration model, \hat{R}_c is shown in Figure 7.4, which is calculated for $\phi_c = 0.6$. The values of \hat{R}_c are slightly scattered. Except for the first 10 particle layers of the $0.42 \mu\text{m}$ particle, \hat{R}_c is found to be independent of the number of particle layers. The mean values for \hat{R}_c are $8.2 \cdot 10^{15}$ ($0.42 \mu\text{m}$ particles) and $5.5 \cdot 10^{15}$ ($0.60 \mu\text{m}$ particles) $1/\text{m}^2$. This is comparable to the values predicted by the Carman-Kozeny model: $5.7 \cdot 10^{15}$ ($0.42 \mu\text{m}$) and $2.8 \cdot 10^{15}$ ($0.60 \mu\text{m}$). The fact that the measured \hat{R}_c is slightly higher than the predicted values can be attributed to particle polydispersity.

The differential cake analysis method thus enables us to analyse the evolution of the cake properties during a filtration run. The constant value of \hat{R}_c indicates that no compression or compaction occurred, which is in accordance with expectations. The slightly lower values of \hat{R}_c for the first 10 particle layers could indicate that the (pure) cake filtration regime had not started yet, but that pore blocking is the prevailing mechanism. This agrees with the constant values found for β , and with the findings of Kosvintsev and others [107], who found cake filtration for 12 and more particle layers.

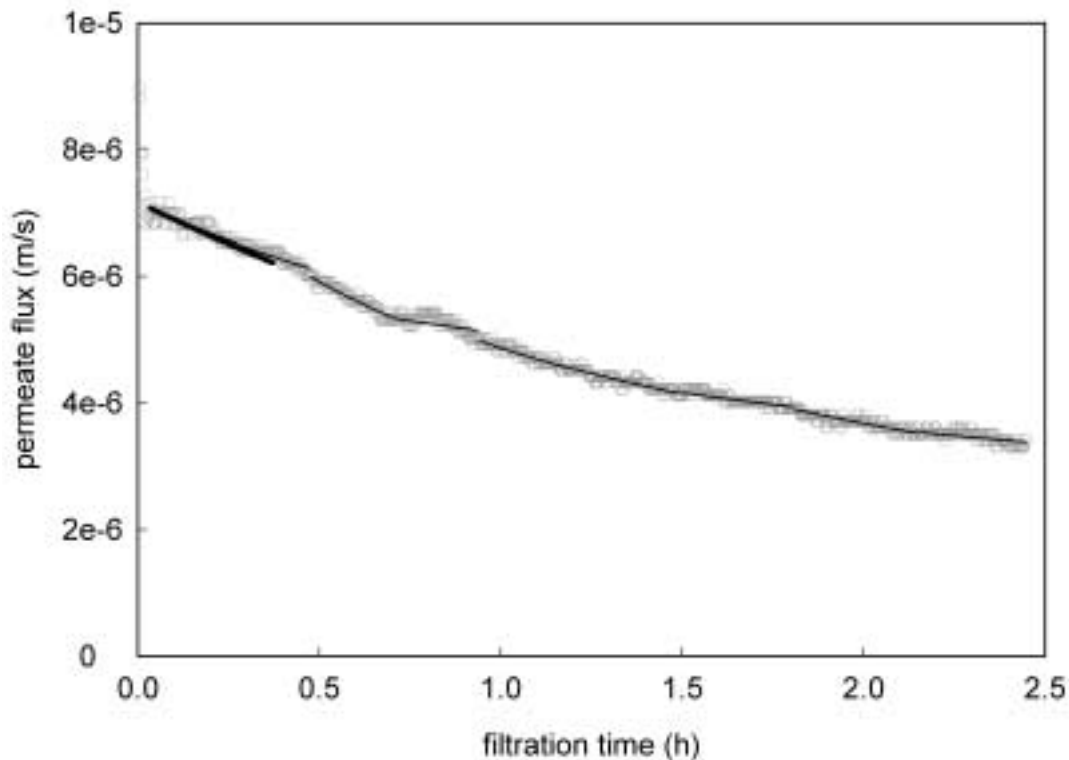


Figure 7.3: Comparison of measured flux and model lines according to the differential cake analysis method. The symbols represent the measured flux (MF, TMP 16 mbar, latex $0.42 \mu\text{m}$, $3 \cdot 10^{-6} \%$), the bold lines the fits of the pore blocking model and the normal lines represent the fits of the cake filtration model.

7.3.2 Micellar casein suspensions

Pore blocking and cake filtration

Compared to MF of a $0.42 \mu\text{m}$ latex suspension, the order at the start of filtration of a micellar casein suspension is similar (0.8), whereas at the end a much larger part of the curve follows an order of 0.7 (results not shown). This latter point indicates that the ratio of cake resistance to membrane resistance was higher for filtration of micellar casein than of $0.42 \mu\text{m}$ particles, since the order is 0.5 for a negligible membrane resistance. It is however not yet clear whether this is an effect of the first particle deposition layers or of later formed layers.

From the permeate flux decline (Figure 7.5), it is found that the flux decline was less gradual than for latex particles. At the start, the flux decline was very fast, but slowing down strongly after about 0.15 h. This indicates that the specific resistance of the deposit is relatively high. In order to investigate whether compaction or compression occurs, the influence of TMP was determined as well by differential flux analysis.

The values for β are higher than for the latex particles (Figure 7.6), indicating that the casein micelles block the membrane more effectively than the latex particles. No clear effect of TMP on β is observed. The more effective blocking may be due to: 1) the relatively large size of the micelles as compared to the pores, so that they do not enter

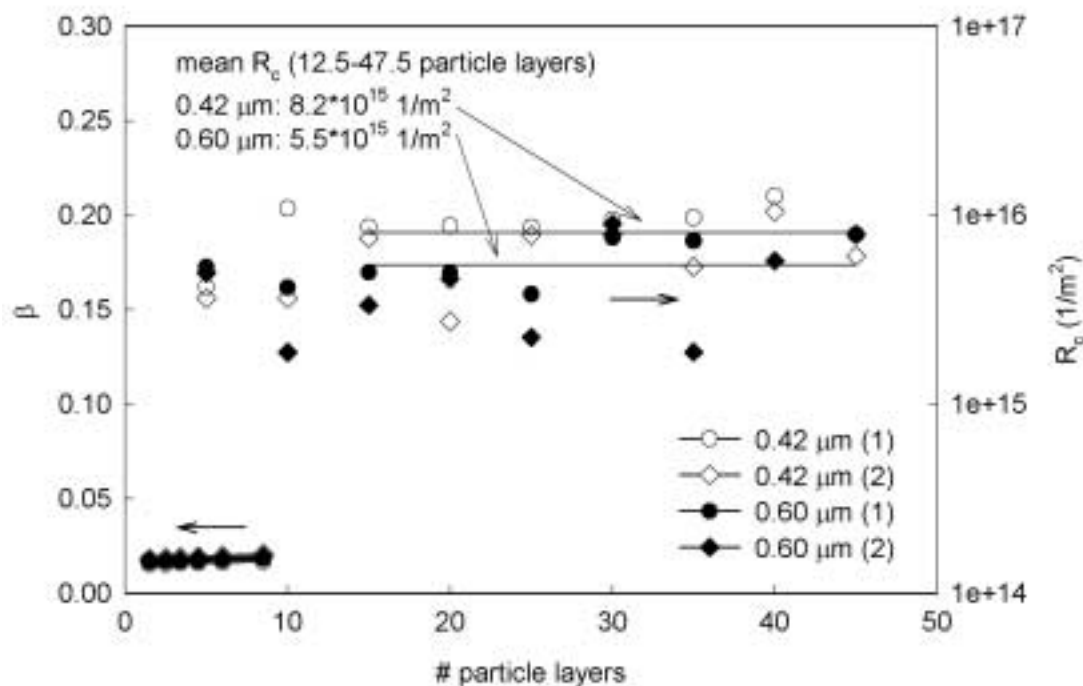


Figure 7.4: Overview of the fit parameters β and \hat{R}_c (calculated under the assumption that $\phi_c = 0.6$) as a function of the amount of latex (0.42 and 0.60 μm) deposited onto the membrane during MF at a TMP of 16 mbar.

the membrane and occupy a maximum area on the membrane and 2) the high packing density of the micellar casein layers. During the formation of the first seven particle layers, β seems to increase slightly, while β decreases when 7-10 particle layers have formed (TMP higher than 0.5 bar). The reason for this change is not totally clear, but it may indicate a flux-dependent cake morphology.

The mean \hat{R}_c (12.5-47.5 particle layers) was $3.3 \cdot 10^{18}$ $1/\text{m}^2$, which is 400-600 times higher than that of the latex particles (Figure 7.6). The Carman-Kozeny equation gives $9.4 \cdot 10^{16}$ $1/\text{m}^2$, so the measured value is approximately 35 times higher. No clear trend is observed for \hat{R}_c as a function of number of particle layers or TMP, which indicates that compaction or compression does not play a major role. The relatively high value for \hat{R}_c may be caused by particle polydispersity but also by a change of the specific micelle volume. Casein micelles are highly swollen particles which contain around 75% water. The outer layer exists of a “hairy” layer of hydrophilic κ -casein tails, which is relatively even more voluminous. Mechanical interparticle forces and hydrodynamic forces may therefore lead to shrinkage and/or deformation of the micelles when present in a concentrated suspension, and thus result in very dense layers. The shrinkage and/or deformation may occur so quickly that no dependency of TMP or the layer thickness is observed in the experimental parameter regime. Such a behaviour can be evident from the viscosity at higher concentrations.

Therefore, the viscosity of micellar casein suspensions was measured as a function of the concentration of casein at different shear rates (Figure 7.7). The casein volume

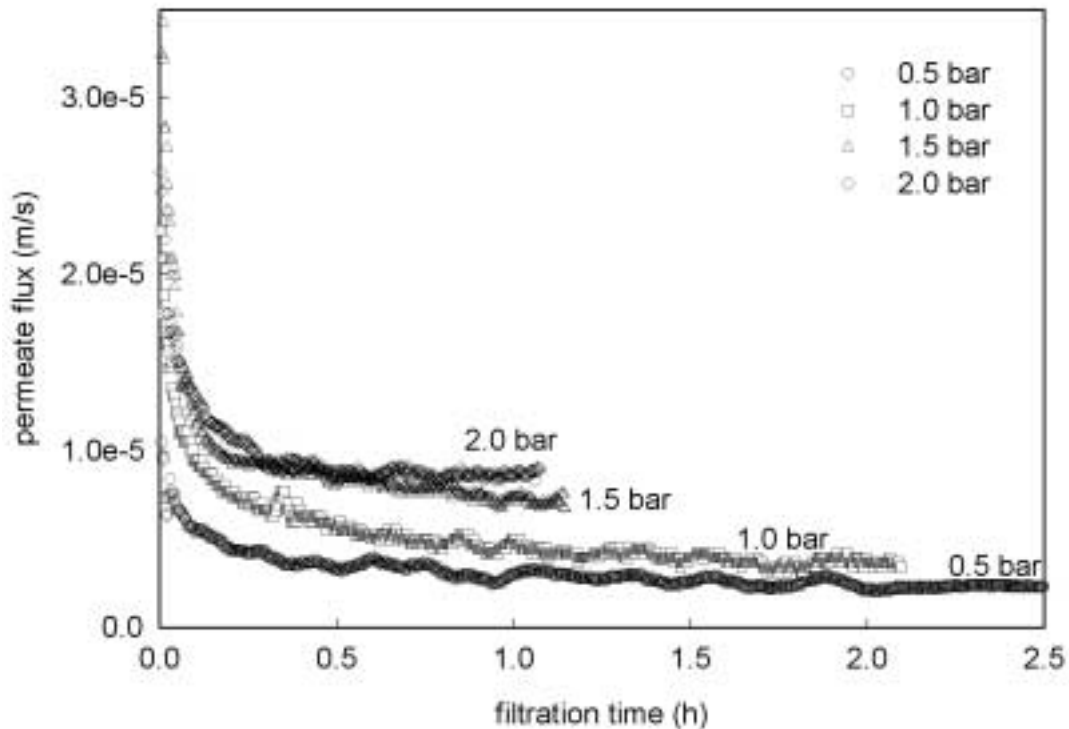


Figure 7.5: Permeate flux as a function of time for UF of a micellar casein suspension (0.0024%) at a TMP of 0.5, 1.0, 1.5 and 2.0 bar.

fraction was calculated with a voluminosity of 3 ml/g and ranged between 0 and 0.76. The micellar casein suspensions were shear thinning; at a shear rate of 10 1/s, the relative viscosity increased to about 17 and 13000 at casein volume fractions of 0.37 and 0.76 respectively, but at a shear rate of 1000 1/s, the relative viscosity was about 6 and 560 at similar concentrations. In theory, at a concentration of 0.74, the viscosity as described by the Eilers model has an asymptote, whereas the measured values increase more gradually. These results indicate that micellar casein suspensions can be highly concentrated, but that they also are very shear-sensitive. This can be due to a stress-dependent voluminosity of the casein micelles, possibly in combination with attractive interactions between the micelles. The viscosity measurements thus confirm our hypothesis that the specific micellar volume may have decreased in a cake layer.

When micellar casein suspensions are filtered over the MF membrane, the flux decline differs from that of the UF membrane (Figure 7.8). At the start of filtration, the flux decline was less steep. This is also clear from the values of β (Figure 7.9), which are smaller for MF, especially for the first particle layer. \hat{R}_c was about 10-35 times smaller than for UF. Since the mean pore size of the MF membrane was about 3 times larger than the size of the casein micelles, while the retention of casein micelles was verified to be equal to 1.0, it is most likely that depth filtration was an important filtration mechanism here. During depth filtration, casein micelles deposit in the internal pore structure of the membrane, which apparently leads to relatively small specific cake resistances, depending on the filtration velocity. The low TMPs seem to correspond to low \hat{R}_c 's while the high

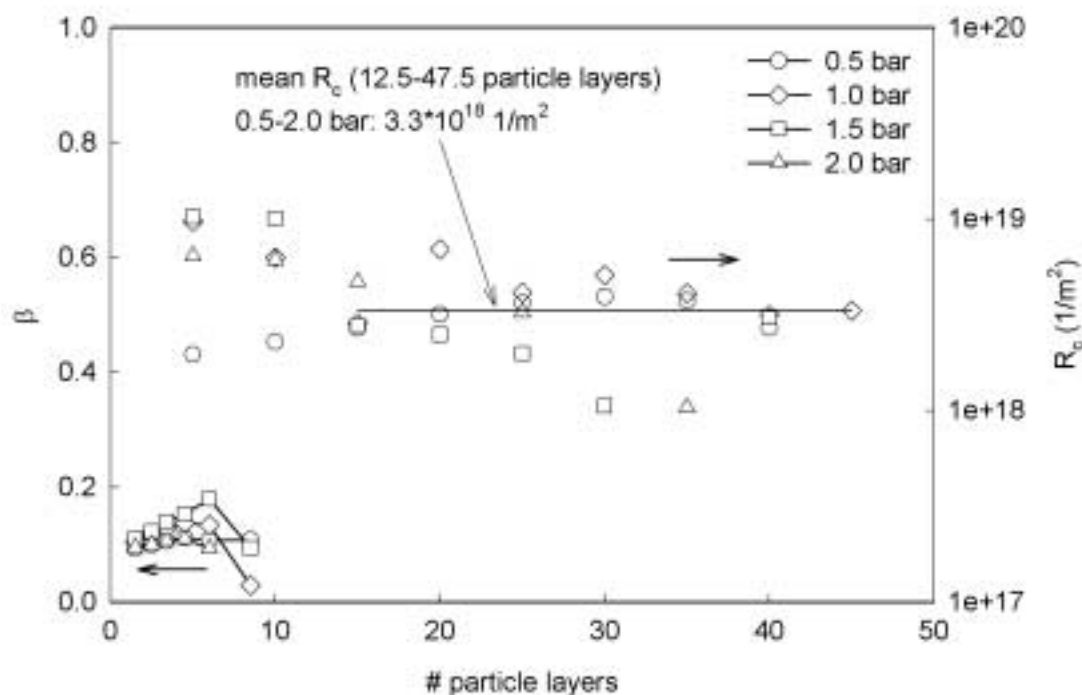


Figure 7.6: Overview of the fit parameters β and \hat{R}_c (calculated under the assumption that $\phi_c = 0.6$) as a function of the amount of casein deposited onto the membrane during UF at a TMP of 0.5, 1.0, 1.5 and 2.0 bar.

TMPs correspond to high \hat{R}_c 's. The results thus show that different membrane structures can lead to large differences in flux decline, even for permeate fluxes of the same order of magnitude, and that the membrane used has a big influence on the behaviour of the cake layer formed.

7.3.3 Milk fat globule suspensions

During UF of milk fat globule suspensions, the order of the increase of permeate volume versus time was again 0.8 at the start of filtration, comparable to that of latex and the micellar casein suspension (results not shown). After about 0.2 h filtration, the order decreased to 0.5, indicating cake filtration with negligibly small membrane resistance. The initial flux decline was very fast for the milk fat globule suspension (Figure 7.10), as is also reflected in the values for \hat{R}_c (Figure 7.11). In spite of the relatively large mean particle size of $3.6 \mu\text{m}$, \hat{R}_c has a value of $1.7 \cdot 10^{18} \text{ 1/m}^2$, which is of the same order as for UF of the micellar casein suspension. The Carman-Kozeny model for polydisperse suspensions (Equation 7.8) predicts a \hat{R}_c of $1.4 \cdot 10^{14} \text{ 1/m}^2$, so the experimentally found \hat{R}_c is $9.0\text{-}47 \cdot 10^3$ times larger for the fat globules. On top of that, \hat{R}_c increased with a factor 7 when the TMP was increased from 0.4 to 2.2 bar. The high values for \hat{R}_c , together with the pressure dependency, point to compression of the cake layer, which can be expected since milk fat is liquid at 45°C so the droplets can deform easily. Based on the Laplace pressure, which is given by $2\gamma/a$ (γ =interfacial tension), it can be expected that fat droplets start to deform at a pressure of 0.01-0.1 bar (γ estimated at 1-10 mN/m).

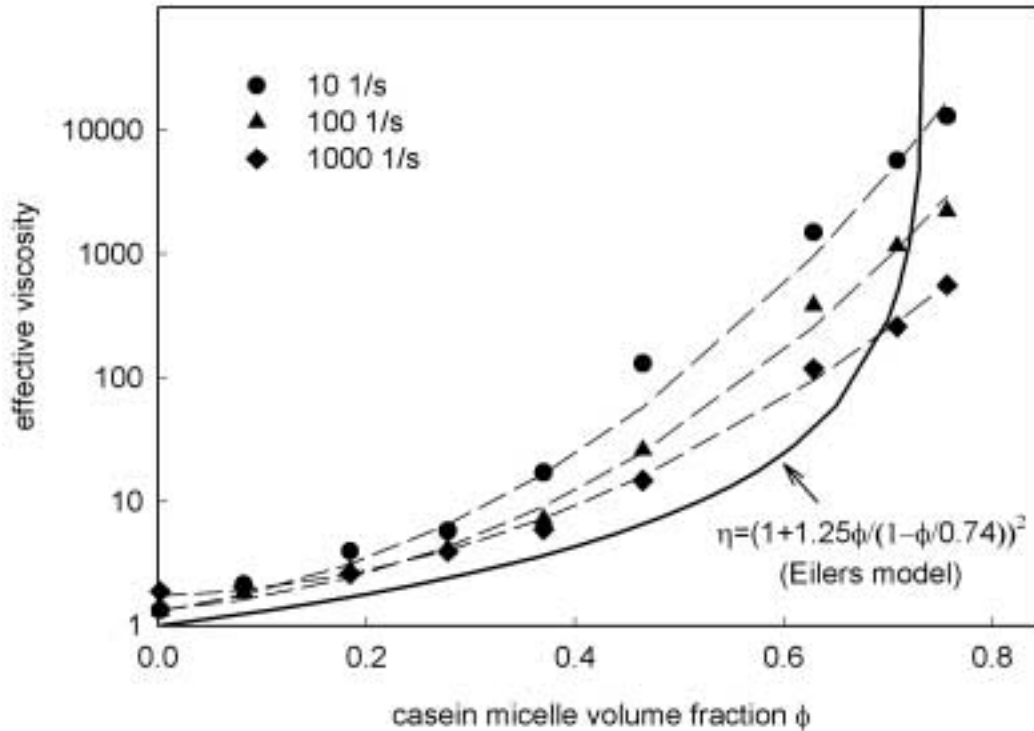


Figure 7.7: The effective viscosity ($=\eta_{\text{suspension}}/\eta_{\text{water}}$) of micellar casein suspensions as a function of the volume fraction of casein micelles, at shear rates of 10, 100 and 1000 1/s (temperature 50°C). Each data point represents the average of two or three different measurements. The lines connecting the data points are drawn as a guide to the eye. The solid line indicates the viscosity as predicted by the Eilers model, with $\phi_{\text{max}} = 0.74$.

Although part of the TMP is present over the membrane itself, a TMP between 0.4 to 2.2 bar is expected to be sufficient for deformation of fat droplets. During filtration at constant TMP, \hat{R}_c remained constant between 3 and 12 particle layers formed onto the membrane, indicating that the deformation of the milk fat droplets did not vary with cake height.

The values for the pore blocking parameter β are substantially higher than for casein micelles. For the first particle layer, β has a value of about 1.3, which indicates that the fat globules spread on the membrane surface. The value of β for the second layer is 0.4. For the third layer, the value of β seems to exhibit a pressure dependency. These results show a similar tendency as for \hat{R}_c , i.e. that milk fat globules form very compact and compressible particle layers at a temperature of 45°C.

The flux curves for UF of milk fat globule suspensions at a temperature of 5°C are presented in Figure 7.12. Due to the 2.6-fold higher viscosity, the permeate fluxes are lower than at 45°C. The flux decline is again very fast, and \hat{R}_c was found to be even higher than at 45°C (Figure 7.13). Due to its dependency on TMP, \hat{R}_c varied between $4 \cdot 10^{18}$ 1/m² at a TMP of 0.8 bar and $8 \cdot 10^{18}$ 1/m² at a TMP of 2.2 bar. The dependency of \hat{R}_c on TMP is however much less than at 45°C. Especially at the lowest TMP values, \hat{R}_c is higher than at 45°C. The fat content of the milk fat globule layer, as analysed with NMR, was 76%. When both the particle polydispersity and the fat content of 76% are taken into

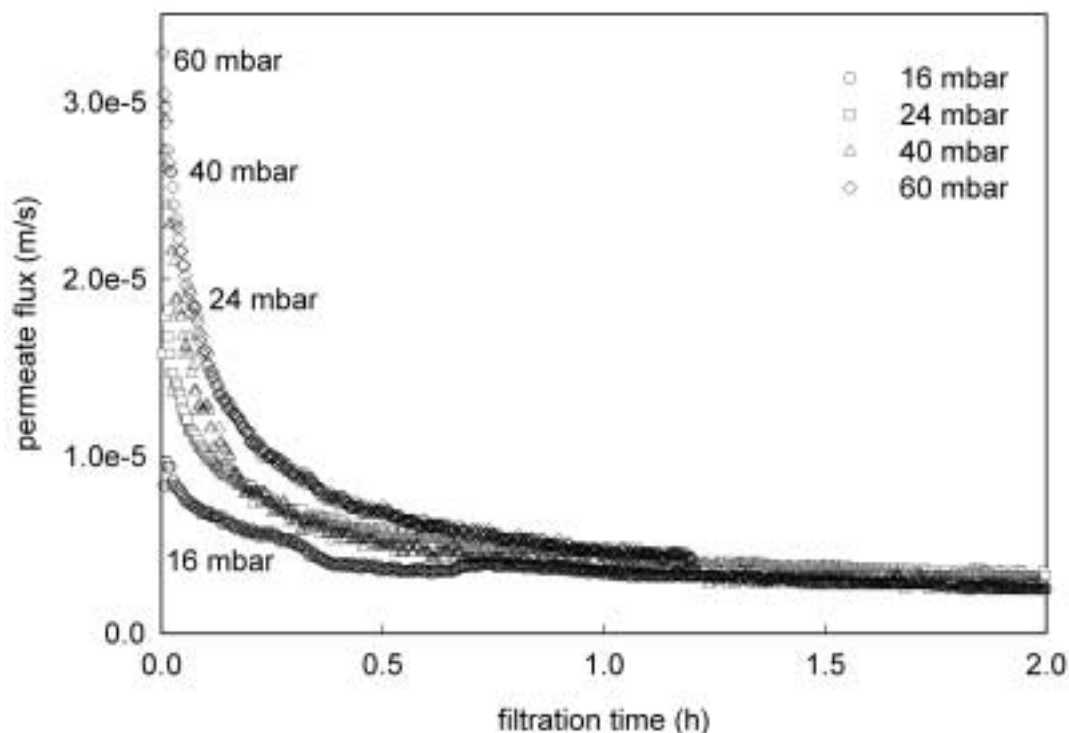


Figure 7.8: Permeate flux as a function of time for MF of a micellar casein suspension (0.0024%) at a TMP of 16, 24, 40 and 60 mbar.

account, according to Equation 7.8, the calculated value of \hat{R}_c is $1.1 \cdot 10^{15} \text{ 1/m}^2$, which is about 7 times higher than when the fat content is 0.6. This can however still not explain the difference with measured values.

The values for β are slightly higher as well and exhibit a similar trend as for 45°C . Based on the fact that about 50-60% of the milk fat is crystallised at 5°C [108], one would expect that the milk fat globules are less deformable and form less compressible particle layers. This does not appear to be true. On the other hand, it is known that partly crystallised fat globules can easily coalesce when they are brought together. This phenomenon is often referred to as partial coalescence [109], and leads to the formation of a network of fat crystals, “glued” together by liquid fat. Partial coalescence is known to occur for instance during the whipping of cream and the churning of butter. Our hypothesis is that partial coalescence occurs in the cake layers at 5°C , and that this has a negative effect on the permeate flux.

The differential flux analysis method proved to be a valuable method for the evaluation of time-dependent behaviour of particle deposition layers from micellar casein and milk fat globule suspensions, which are relevant input parameters for process design.

7.4 Conclusions

In order to analyse the properties of particle deposition layers on membrane filters, a differential method is applied, which gives an estimate of the properties per layer of particles

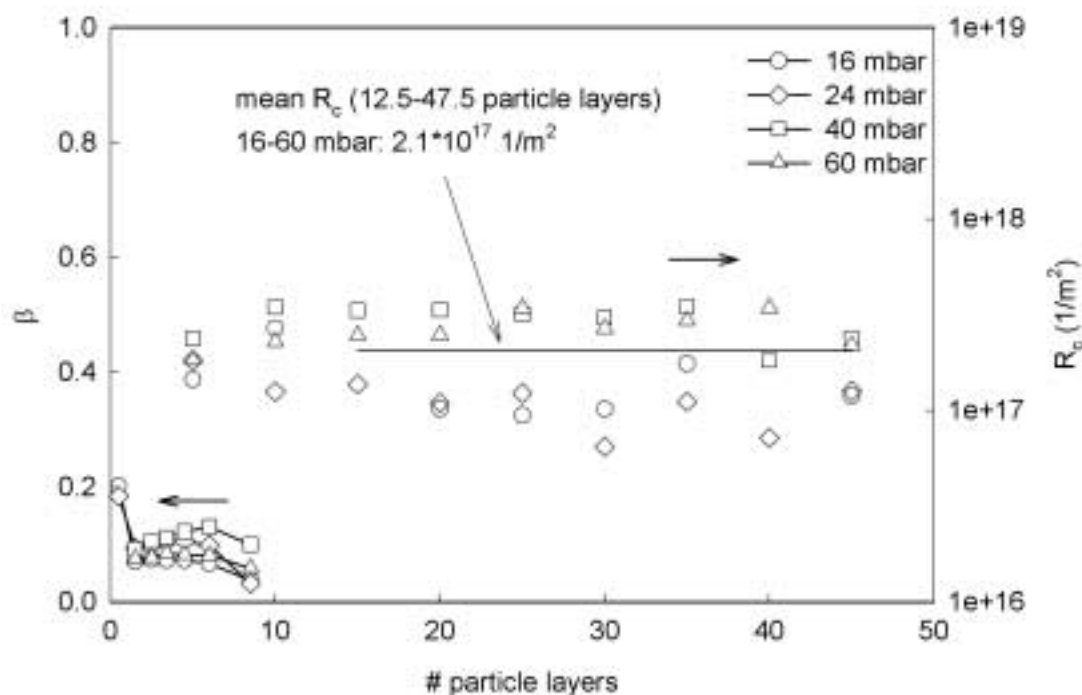


Figure 7.9: Overview of the fit parameters β and \hat{R}_c (calculated under the assumption that $\phi_c = 0.6$) as a function of the amount of casein deposited onto the membrane during MF at a TMP of 16, 24, 40 and 60 mbar.

deposited onto the membrane. This enabled the independent assessment of model parameters of the pore blocking and the cake formation mechanism and allowed for the detection of compaction or compression during the filtration run. Differential analysis of deposition layers of latex particles revealed that these did not exhibit compaction or compression and that the specific cake resistance agreed fairly well with that predicted by the Carman-Kozeny equation.

The behaviour of casein micelles and milk fat globules was found to differ strongly from that of ideal hard spheres. This can for example be concluded from the specific cake resistance, which was in general much higher than predicted by the Carman-Kozeny equation. For UF of micellar casein, no compaction or compression is observed in the pressure range studied, but high specific cake resistances are found. This is probably due to the formation of very compact layers. For a membrane with a much larger pore size ($0.3 \mu\text{m}$), the specific cake resistance was about 10-35 times lower than for UF, which can be ascribed to the formation of particle layers into the membrane rather than on the membrane. Virtually all casein micelles were retained by the membrane.

The behaviour of milk fat globules differed substantially from the micellar casein. For temperatures of 45°C (at which milk fat is liquid) as well as 5°C (at which 50-60% of milk fat is crystallised), the value of β for the first particle layer was higher than one, which probably indicates that the fat globules spread on the membrane surface. The values of β for the second and third layer were again higher than for micellar casein. At 45°C , compression was found, such that the specific resistance increased 5 times upon an increase of TMP from 0.4 to 2.2 bar. At 5°C , compression was less intense, but the specific

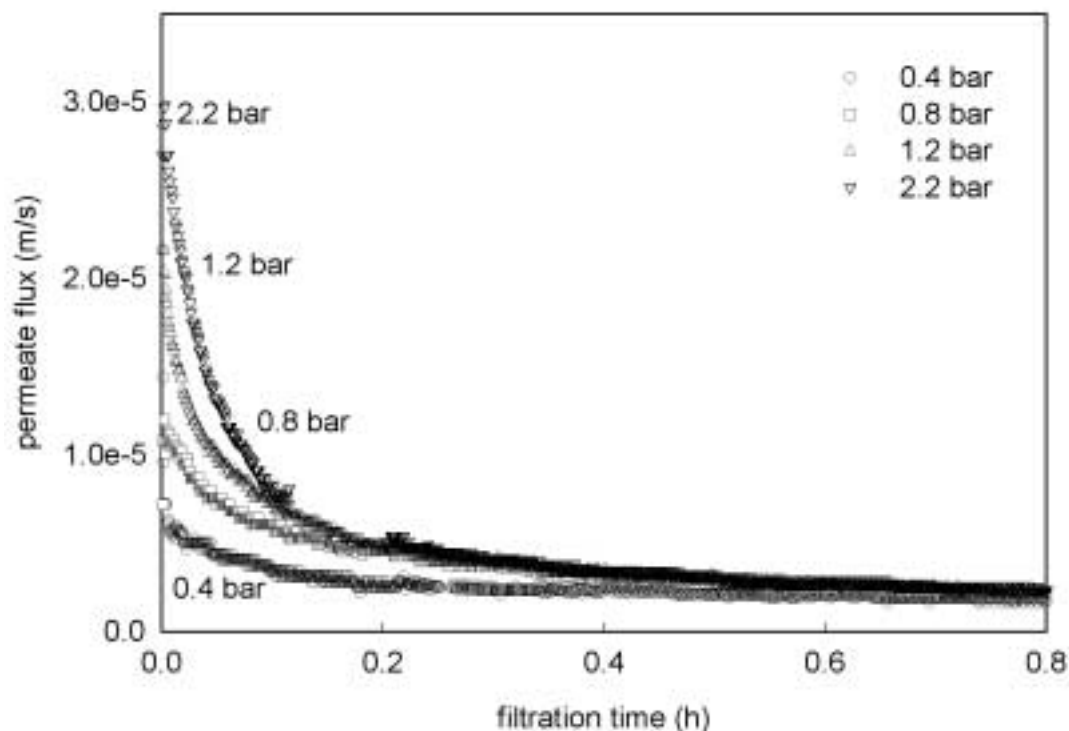


Figure 7.10: Permeate flux as a function of time for UF (T 45°C) of a milk fat globule suspension (0.12%) at a TMP of 0.4, 0.8, 1.2 and 2.2 bar.

resistance was similar to that found at the highest pressures for 45°C. This, together with the very high values of β , points to partial coalescence, leading to a network of fat crystals, “glued” together by liquid fat, comparable to what is also seen during the whipping of cream and the churning of butter.

A general conclusion is that the properties of the cake layer depend not only on the properties of the feed suspension and the operating conditions, but on the type of membrane as well.

Differential cake analysis proved to be a valuable method for the evaluation of concentrated particle layers and can be used as a method to identify characteristic parameters of these particle layers. The generated knowledge is not only relevant for the design of membrane filtration processes but also of other systems where concentrated suspensions are used.

Acknowledgements

Friesland Foods is greatly acknowledged for supporting this research. Henk Streppel (Friesland Foods, preparation micellar casein and milk fat globule suspensions from milk), Miriam Krijgsman (Friesland Foods, viscosity measurements) and Harry Rollema (NIZO, NMR measurements) are thanked for their valuable contribution to the research. The authors would like to acknowledge the support of the Dutch Ministries of Economic Affairs, Education, Culture and Sciences and of Housing, Spatial Planning and the Environment

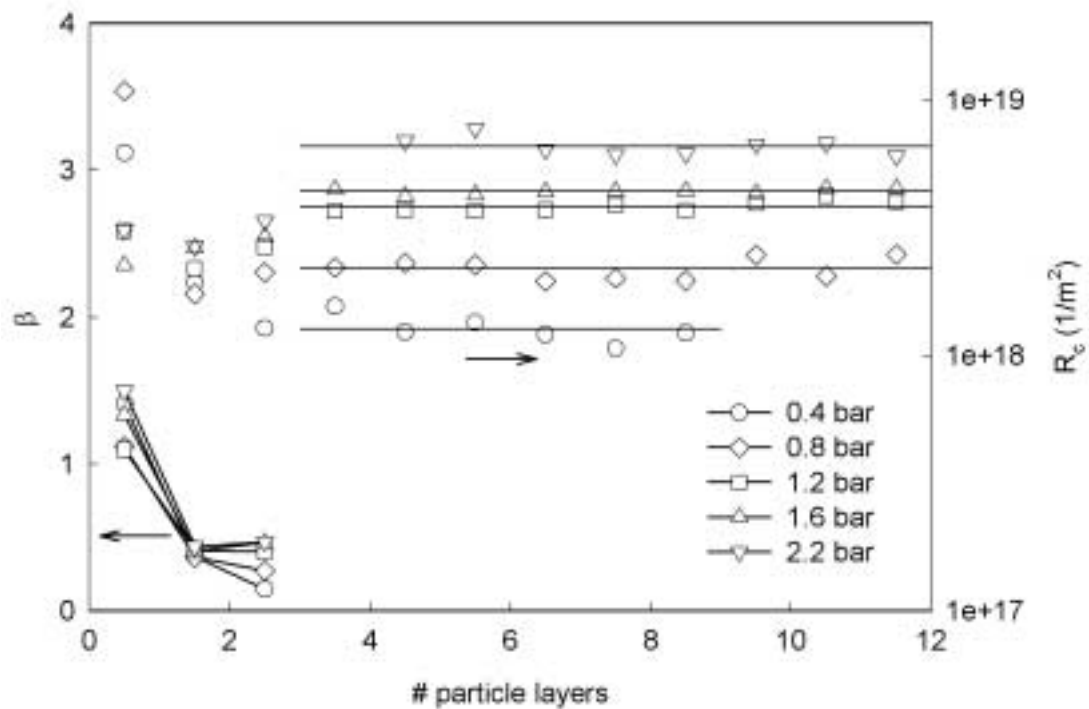


Figure 7.11: Overview of the fit parameters β and \hat{R}_c (calculated under the assumption that $\phi_c = 0.6$) as a function of the amount of milk fat deposited onto the membrane during UF ($T = 45^\circ\text{C}$) at a TMP of 0.4, 0.8, 1.2, 1.6 and 2.2 bar. For the determination of β of the first particle layer, J_0 is not fitted, but calculated according to a value for R_m of $8.4 \cdot 10^{12}$ 1/m.

through a grant of the Dutch Program Economy, Ecology and Technology.

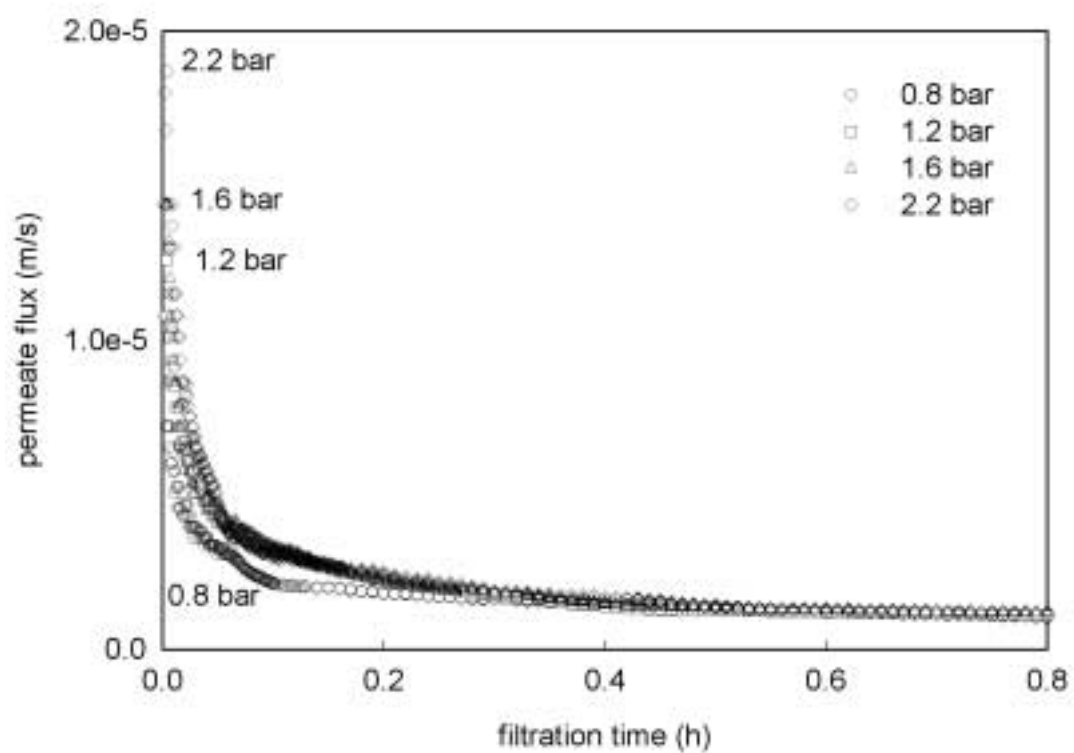


Figure 7.12: Permeate flux as a function of time for UF ($T 5^{\circ}\text{C}$) of a milk fat globule suspension (0.12%) at a TMP of 0.8, 1.2, 1.6 and 2.2 bar.

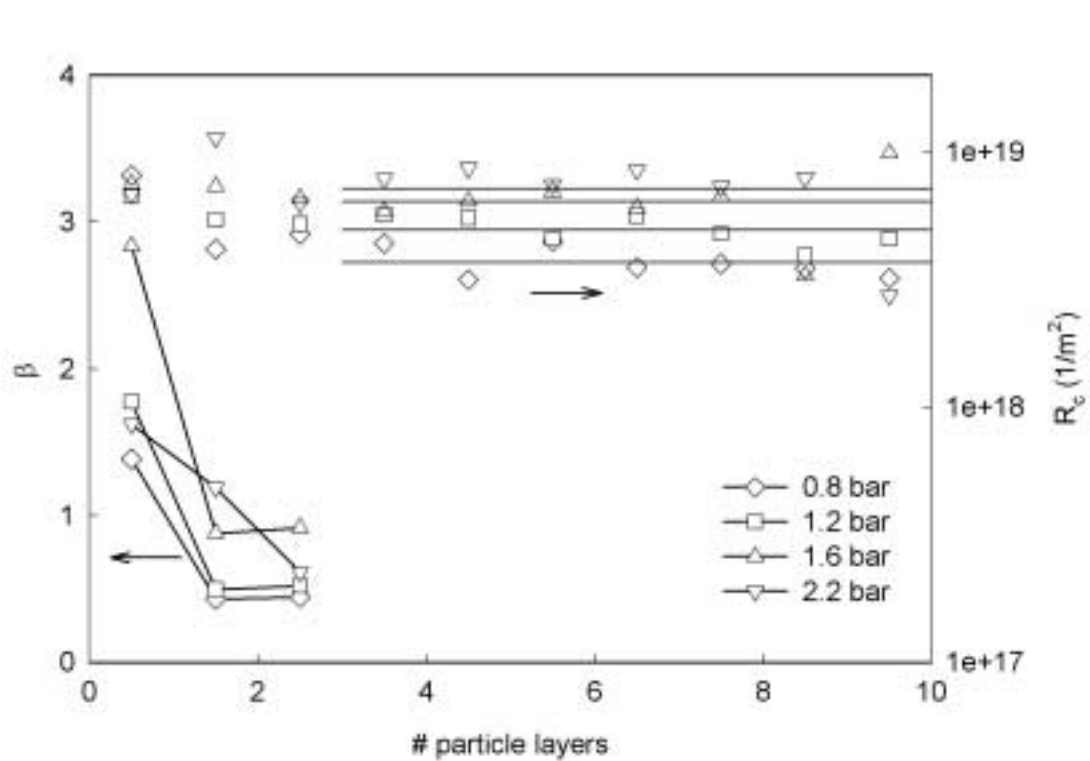


Figure 7.13: Overview of the fit parameters β and \hat{R}_c (calculated under the assumption that $\phi_c = 0.6$) as a function of the amount of milk fat deposited onto the membrane during UF ($T = 5^\circ\text{C}$) at a TMP of 0.8, 1.2, 1.6 and 2.2 bar.

**A suspension flow model for
hydrodynamics and concentration
polarisation in crossflow
microfiltration**

A new computer simulation model is proposed for suspension flow in microfiltration systems. In this model, the diffusion of the suspended microparticles is governed by the mechanism of shear-induced migration. Using an Euler-Euler approach, hydrodynamics and convection-diffusion are simultaneously resolved according to the Lattice Boltzmann method. The new suspension flow model allows the complete solution of the flow field (including calculation of the actual local shear rate) in systems with complex geometries and the application of a pressure gradient over the feed flow channel as well as over the membrane. The cake layer dimensions and permeability are explicitly taken into account. For a simple cross-flow system, a comparison is made between the new suspension flow model and existing models. The more realistic approach of the suspension flow model is found to be especially significant for the calculation of the cake layer profile at the beginning and the end of the membrane. Also the effect of narrowing of the flow channel by cake formation on the suspension flow pattern (at a constant pressure gradient over the flow channel) is more realistically predicted. Finally, some examples are presented of the concentration polarisation and cake layer formation in microfiltration systems with more complex geometries. The newly developed suspension flow model has generic applicability as a design tool for microfiltration membranes, systems and processes. Extensions of the model to three-dimensional systems (including parallel computations), as well as adaptations of the diffusion model to anisotropic diffusivity can be relatively easily achieved.

8.1 Introduction

The performance of microfiltration processes is in general mainly determined by concentration polarisation, which arises from the simultaneous transport of non-permeable species towards and back from the membrane surface. Modelling of flow and concentration polarisation in microfiltration systems is already often put forward as an important tool to help understand and optimise these systems. Although numerous filtration models of varying degrees of complexity and simplification have appeared in literature, most of them do not apply for microfiltration, due to the different diffusion mechanism in particulate suspensions as compared to molecular solutions.

As has been identified by Belfort and others [10], for particulate suspensions with particle sizes between 0.5 and 30 μm , shear-induced diffusion can often be considered the relevant back-transport mechanism in the concentration polarisation process. Other back-transport mechanisms are Brownian diffusion and inertial lift, which are respectively dominant for particle sizes smaller than 0.5 μm and larger than 30 μm . This paper addresses modelling of flow and concentration polarisation in the shear-induced diffusive regime. Shear-induced diffusion, also called hydrodynamic diffusion, is a transport mechanism that is caused by hydrodynamic particle interactions in a suspension in shear flow. Excluded volume effects can then lead to particle displacements. In contrast to inertial lift, which is only relevant in the regime where the Reynolds number based on the particle size is not negligible, shear-induced diffusion occurs in the slow laminar flow regime as well. A general property of shear-induced diffusion is that it increases proportionally with the shear rate.

About two decades ago, shear-induced diffusion was first introduced in relation to microfiltration theory by Zydney and Colton [110]. Their concentration polarisation model is based upon the classical L ev eque solution for mass transfer in which they replaced the Stokes-Einstein diffusivity with the shear-induced diffusivity, as determined from experimental data of Eckstein and others [14]. In the same year as Zydney and Colton, Davis and Leighton presented a model that describes the transport of a concentrated layer of particles along a porous wall under laminar flow conditions [7]. In this model, shear-induced diffusion accounts for the lateral migration of particles away from the porous wall. Instead of the approximate fit to the data of Eckstein and others, Davis and Leighton applied data of Leighton and Acrivos [64] for shear-induced diffusion, which were about 25 times greater and were shown to better describe the viscous resuspension of a settled layer of rigid particles in shear flow.

Romero and Davis [8] extended the model of Davis and Leighton from a local treatment of the particle layer to a global model of crossflow microfiltration. This global model is able to predict the axial dependence of the permeate flux and the thickness of the concentrated particle layer under steady or quasi-steady operation. The model also describes under which conditions a stagnant layer of packed particles exists beneath the flowing layer. In a following step, the global model was converted into a transient model, which not only describes the steady-state behaviour but also the time-dependent decline of the permeate flux due to particle layer buildup [9].

In the aforementioned models, particle convection parallel to the membrane walls was ignored. As a consequence, the models are only valid for very small particle volume fractions in the bulk of the suspension ϕ_b . Davis and Sherwood overcame this limitation in their similarity solution for crossflow microfiltration under conditions where the stagnant particle layer provides the controlling resistance to flow [81]. In their solution, the stagnant particle layer grows like $x^{1/3}$, where x denotes the dimensionless distance from the filter entrance. Their solution is however only valid in the situation that the critical length needed for the stagnant layer to form is much smaller than the filter length. Pelekasis developed a model which does not have this limitation [111], although his solution is only valid in situations where the permeate flux can be considered constant over the membrane length. This model is valid over a wide range of bulk particle concentrations. It is shown that in the limit where the particle volume fraction in the bulk suspension $\phi_b \rightarrow 0$, the model of Davis and Leighton is recovered.

All the abovementioned models have in common that they assume the bulk flow to be fully developed Poiseuille flow with a time-independent flow rate. This is valid for a straight flow channel, when the permeate velocity is much smaller than the average downchannel velocity of the suspension and when the stagnant layer is much thinner than half the channel width. These conditions are often not met in reality. First of all, the flow channel may deviate from perfectly circular or rectangular, e.g. when turbulence promoters are present. Secondly, when suspensions are filtered with particles that have a relatively low cake resistance, the cake layer height can become significant compared to the channel half width. Poiseuille flow can still be considered present when the cake layer height does not vary much along the filter length (and the actual flow velocity profile can be adapted to the actual channel height). The flow pattern can however easily deviate from Poiseuille flow when the cake layer height strongly varies along the filter length, like e.g. at the beginning and at the end of the filter. Thirdly, the flow pattern can also be time-dependent, such as when oscillating cross-flow or backpulsing is applied. One

should moreover realise that, in contrast to Brownian diffusion, shear-induced diffusion depends linearly on the shear rate. Local deviations of the flow field from Poiseuille flow will therefore have a large influence on the local morphology of the flowing and stagnant particle layer.

This indicates that a more generic model with broad applicability to membrane systems requires an accurate, more detailed solution of the fluid flow field. This is possible with computational fluid dynamics (CFD). So far, this technique is not often applied to membrane systems. Recently, Wiley and Fletcher [112] successfully developed a generic CFD model that incorporates the flow across the membrane wall. In their article, they also reviewed earlier attempts in this field, which in general lead to less generic solutions than their model. Another recent approach is that of Richardson and Nassehi [113]. These authors developed a finite element model for the solution of concentration profiles in flow domains with curved porous boundaries. Although both models may be extensible to modelling of concentration polarisation in microfiltration processes, with shear-induced diffusion as back-transport mechanism and with cake layer formation, up to now no results on this subject have been published.

The present work is directed at the development of a CFD model for flow and concentration polarisation in microfiltration systems with shear-induced diffusion as back-transport mechanism. We apply the Lattice Boltzmann (LB) method for this aim, which is based on kinetic theory, the physical theory describing the dynamics of large systems of particles. The LB method, being a discrete version of the Boltzmann equation, is in special cases identical to the finite volume scheme as used by Wiley and Fletcher [112]. Both methods can be applied for laminar as well as turbulent flows. The LB method may however have some advantages when compared to other finite difference schemes. Complex geometries can be quickly set-up and easily used in the LB method, while in other methods, the use of complex geometries is a major issue. The LB method is also very convenient for systems with moving boundaries and multiphase systems such as fluid flow with suspended particles. In the present work, this may be relevant for the simulation of rapidly growing, flowing and stagnant layers. Finally, LB schemes can be very easily implemented on a parallel computer, which facilitates computations of large systems.

Although the LB simulations can be easily carried out in three dimensions, as a first step, the present work presents results on two-dimensional (2D) systems. In order to validate the model, the simulation results are compared with results of approximate models when appropriate. Hereafter, the effects of some variations in the geometry on the flowing and stagnant particle layers and the resulting flux will be shown.

8.2 Computer simulation method

8.2.1 Suspension flow model

The suspension flow model is based on an Euler-Euler description of the system, in which both the hydrodynamics and the suspension flow are completely resolved. The hydrodynamics are calculated according to the continuity and Navier-Stokes (NS) equations:

$$\begin{aligned} \frac{\partial \rho}{\partial t} &= \nabla \cdot \rho \mathbf{u} \\ \frac{\partial \rho \mathbf{u}}{\partial t} + \mathbf{u} \cdot \nabla \rho \mathbf{u} &= -\nabla p + \nu \nabla^2 \rho \mathbf{u} + F \end{aligned} \quad (8.1)$$

where $-\nabla p$ is the pressure gradient and F is the body force. The LB method solves the NS equation for weakly compressible conditions, therewith behaving as a pseudo-compressible scheme [114]. An advantage of this approach is that the Poisson equation does not need to be solved for the pressure. For the calculation of the NS equation, the kinematic viscosity ν ($= \eta/\rho$, with η representing the dynamic viscosity) of the fluid needs to be known. In our suspension flow model, we took into account that the viscosity η depends on the local concentration of suspended microparticles. Hereto, a model is used that is also applied by Romero and Davis [8]:

$$\eta(\phi) = \eta_0 \left[1 + 1.5 \frac{\phi}{\left(1 - \frac{\phi}{0.6}\right)} \right]^2 \quad (8.2)$$

where ϕ represents the particle volume fraction and η_0 the viscosity of the particle free medium. In our suspension flow model, the feed for the microfiltration process consists of a particulate suspension with particles of a size between 0.5 and 30 μm . These suspended particles are described as a component that is continuously distributed in the fluid. Their distribution over the system is calculated according to the convection-diffusion equation:

$$\frac{\partial \phi}{\partial t} + \mathbf{u} \cdot \nabla \phi = D \nabla^2 \phi \quad (8.3)$$

The velocity field \mathbf{u} is calculated according to the NS equation. In our simulations, the diffusion coefficient D represents the shear-induced diffusion coefficient, following the shear-induced migration model of Leighton and Acrivos [8, 64]:

$$D = 0.33 \dot{\gamma} a^2 \phi^2 (1 + 0.5 e^{8.8\phi}) \quad (8.4)$$

where $\dot{\gamma}$ is the shear rate and a is the radius of the suspended particles. Both the viscosity η and the shear-induced diffusivity D are treated as time and location dependent variables in our suspension flow model. In order to resolve the NS equation as well as the convection-diffusion equation the LB method is followed, which is explained in the next two paragraphs.

8.2.2 Lattice Boltzmann method for hydrodynamics and convection-diffusion

For a general introduction to the LB method, we refer to Succi [34]. In this article, we will explain relevant aspects of our method, without going into much detail. Hydrodynamics and convection-diffusion were solved with two separate LB schemes. Here, we will first introduce the LB method for the case of hydrodynamics.

The LB method discretises kinetic theory by collecting fluid mass in discrete lattice gas particles, locating these particles on points of a regular lattice and moving the particles according to a finite, discrete set of velocities, taking them to adjacent lattice points. As a consequence of this discretisation procedure space, time and particle velocity are discrete variables. Physical quantities are represented by moments of a particle distribution function, in contrast to finite volume schemes, where physical quantities are represented by continuous fields. The lattice gas particles behave like real particles: they move and collide on the lattice. Collision occurs when particles encounter each other at a lattice point.

After collision they move to adjacent lattice points. If this is done within the constraints of physical conservation laws and with a lattice with sufficient symmetry, real physical phenomena can be modelled this way.

In analogy with the Boltzmann equation of the classical kinetic theory, the state of the particles on a lattice point is characterised by the particle distribution function $f_i(\mathbf{x}, t)$, describing the average number of particles at a particular node of the lattice \mathbf{x} , at a time t , with the discrete velocity \mathbf{c}_i , which brings the particles in one time step to an adjacent lattice node. In the simulations described in this paper, the hydrodynamics were solved with a D2Q9 LB scheme, which is defined on a 2D square lattice with rest particles and 8 non-zero particle velocities. The velocity directions link lattice sites to its nearest and next-nearest neighbours. The velocity vectors on this 2D lattice are defined as:

$$\mathbf{c}_i = \begin{cases} (0, 0), & i = 0 \\ (\cos \frac{i-1}{2}\pi, \sin \frac{i-1}{2}\pi), & i = 1, 2, 3, 4 \\ \sqrt{2} (\cos (\frac{i-1}{2}\pi + \frac{\pi}{4}), \sin (\frac{i-1}{2}\pi + \frac{\pi}{4})), & i = 5, 6, 7, 8 \end{cases} \quad (8.5)$$

The particle distribution function contains information on physical properties of the fluid. The hydrodynamic field's mass density ρ , momentum density \mathbf{j} , and the momentum flux density Π , being identical to the field's in the NS equation, are moments of this velocity distribution:

$$\rho = \sum_i f_i, \quad \mathbf{j} = \sum_i f_i \mathbf{c}_i, \quad \Pi = \sum_i f_i \mathbf{c}_i \mathbf{c}_i = \rho c_{s,f}^2 I + \rho \mathbf{u} \mathbf{u} = pI + \rho \mathbf{u} \mathbf{u} \quad (8.6)$$

The lattice gas particles evolve by collisions and subsequent propagation to neighbouring lattice sites. This two-step process is described by the following equations:

$$f'_i(\mathbf{x}, t) = f_i(\mathbf{x}, t) - \frac{f_i(\mathbf{x}, t) - f_i^{eq}(\mathbf{x}, t)}{\tau_f} + \frac{c_{i\alpha} F_\alpha}{c_{s,f}^2} \quad (8.7)$$

$$f_i(\mathbf{x} + \Delta \mathbf{x}_i, t + \Delta t) = f'_i(\mathbf{x}, t) \quad (8.8)$$

Here $f'_i(\mathbf{x}, t)$ is the post-collisional distribution function. The lattice spacing is defined as $\Delta \mathbf{x}_i = \mathbf{c}_i \Delta t$. F is the body force and the speed of sound $c_{s,f}$ is defined by $c_{s,f}^2 = c^2/3$. In our simulations, we applied the BGK model [37, 57], which is a simplification of the full LB model. In this BGK model, the distribution functions are simply relaxed at each time step towards the local equilibrium distribution $f_i^{eq}(\mathbf{x}, t)$ with the relaxation time τ_f . This relaxation time τ_f controls the relaxation of the viscous stress in the fluid and is linked to the kinematic viscosity ν via:

$$\nu = c_{s,f}^2 \left(\tau_f - \frac{1}{2} \right) \Delta t \quad (8.9)$$

In our simulations τ_f , and therewith the kinematic viscosity $\nu (= \eta/\rho)$ of the fluid on each lattice point was dependent on the local particle concentration, according to Equation (8.2). The equilibrium distribution $f_i^{eq}(\mathbf{x}, t)$ is chosen such that the weakly compressible NS equations (8.1) are obtained [36]. It can be expressed as a series expansion in powers of the flow velocity \mathbf{u} :

$$f_i^{eq} = \rho w_i \left(1 + \frac{1}{c_{s,f}^2} \mathbf{u} \cdot \mathbf{c}_i + \frac{1}{2c_{s,f}^4} \bar{\mathbf{u}} \bar{\mathbf{u}} : \mathbf{c}_i \mathbf{c}_i - \frac{1}{2c_{s,f}^2} \mathbf{u}^2 \right) \quad (8.10)$$

where $\bar{\mathbf{u}}\bar{\mathbf{u}}$ is the traceless part of $\mathbf{u}\mathbf{u}$, and the double dot product is defined as $A : B = \sum_{\alpha,\beta} A_{\alpha\beta}B_{\beta\alpha}$. The weight factors are given by $w_0 = 4/9$, $w_1 = w_3 = w_5 = w_7 = 1/9$ and $w_2 = w_4 = w_6 = w_8 = 1/36$.

The computation scheme for convection-diffusion has a strong analogy with the scheme for hydrodynamics. The particle distribution function $g_i(\mathbf{x}, t)$ now contains information on physical properties of the diffusive component, in our case the suspended particles. For reasons of clarity, we will refer to fluid particles for the lattice gas particles in the hydrodynamics scheme and to suspended particles for the lattice gas particles in the convection-diffusion scheme. The relevant continuum field derived from the latter scheme represents the concentration of suspended particles ϕ :

$$\phi = \sum_i g_i \quad (8.11)$$

The relaxation parameter in the collision operator of the convection-diffusion scheme is not related to the kinematic viscosity ν but to the diffusion coefficient D :

$$D = c_{s,g}^2 \left(\tau_g - \frac{1}{2} \right) \Delta t \quad (8.12)$$

Here, the speed of sound $c_{s,g}$ is also defined by $c_{s,g}^2 = c^2/3$. In our simulations, this diffusion coefficient D represents the shear-induced diffusion coefficient, according to the shear-induced migration model of Leighton and Acrivos [64], which is given by Equation (8.4). Since the diffusion coefficient is dependent on the time and location dependent variables $\dot{\gamma}$ and ϕ , it is recalculated every timestep at every lattice point. The shear rate $\dot{\gamma}$ is calculated from the diagonal vectors of the non-equilibrium part of the distribution function according to [115]:

$$-\frac{c_{s,f}^2}{\omega} \rho \dot{\gamma} = \sum_{i=0}^{i=8} c_{i,x} c_{i,y} (f_i - f_i^{eq}) \quad (8.13)$$

Because we considered the diffusion to be isotropic, the absolute value for $\dot{\gamma}$ was used for the calculation of the shear-induced diffusivity D . More recent investigations have shown that shear-induced diffusion is not an isotropic process, but that the diffusivity depends on the direction relative to the shear field (see e.g. [19, 27]). Moreover, improved models have become available for shear-induced migration (see e.g. [16]). Our model can be easily adapted to implement such modifications of the shear-induced diffusivity models. We do however not expect that taking into account anisotropy will have a large effect, since convection is strongly dominant along the flowlines.

Typical for the LB scheme is that the resulting finite difference equation for the evolution of ϕ is identical to the Lax-Wendroff (LW) finite volume scheme in case of $\tau_g=1$ [116]. Both the LW and the LB scheme automatically correct for numerical diffusion, for the LB scheme as a consequence of the constraints for the equilibrium distribution. If $\tau_g \neq 1$, spurious oscillations, which are present in the LW scheme, are damped in the LB scheme. The LB scheme therewith behaves like a third order accurate scheme (for $\tau_g \neq 1$) [116].

In order to have stable calculations, stability criteria have to be met. In the hydrodynamics scheme, the grid Courant number Cr , which is a measure for the relative flow

velocity on the grid, should meet the following condition:

$$\text{Cr} = \frac{\mathbf{u} \Delta t}{\Delta x} < 1 \quad (8.14)$$

Also the compression of the medium should be sufficiently small, such that the Mach number Ma :

$$\text{Ma} = \frac{\mathbf{u}}{c_{s,f}} \ll 1 \quad (8.15)$$

The abovementioned conditions are met by a proper choice of the model parameters in our system. For the convection-diffusion scheme, the criteria for the diffusivity need some more attention because of the variation of the diffusivity with the shear rate and the concentration of suspended particles. The Fourier number Fo^* is a measure for the diffusion velocity on the grid:

$$\text{Fo}^* = \frac{D \Delta t}{\Delta x^2} \leq 0.5 \quad (8.16)$$

We have chosen our model parameters such that even when D is maximal in our system, this condition is met. Also the ratio between convection and diffusion is subjected to a stability condition. The timescale of diffusivity needs to be sufficiently fast compared to convection, which is reflected in the grid Peclet number Pe^* :

$$\text{Pe}^* = \frac{\mathbf{u} \Delta x}{D} \leq 25 \quad (8.17)$$

Because the LB method behaves as a third order accurate scheme, the limiting value can be higher than the common value of 2. We have estimated the value of 25 ourselves by carrying out simulations with different maximal values for Pe^* . When $\text{Pe}^* > 25$, spurious oscillations were sometimes found, leading to anomalous results. Because of its dependency on the shear rate and the concentration of suspended particles, the shear-induced diffusivity D can strongly vary in our system. In order to meet the condition for Pe^* , the value of Pe^* was calculated at every time-step and at every node of the lattice. When the condition $\text{Pe}^* < 25$ was not met, the diffusivity was locally adjusted such that $\text{Pe}^* = 25$. The consequence is that D cannot become zero (as e.g. in the center of the flow channel, where the shear rate is equal to zero), but has a certain minimum limit, depending on the actual flow velocity \mathbf{u} . When \mathbf{u} is relatively high, such as in the center of the flow channel, the minimum limit for D is also high. In our system, the maximal flow velocity in the channel and therewith the shear rate at the wall was so high, that D did not need to be adjusted in the largest part of the concentration polarisation layer. Only in the center area of the flow channel with relatively high flow velocity and where the concentration of suspended particles ϕ was lower than about 0.10, might the diffusivity be set slightly higher than according to the shear-induced migration model. The effect of this correction on the simulation results was however found to be negligibly small.

8.2.3 Initial and boundary conditions

In figure 8.1, the geometry of the microfiltration system is depicted. Its geometry and dimensions are inspired on the newly emerging class of micro-engineered membranes,

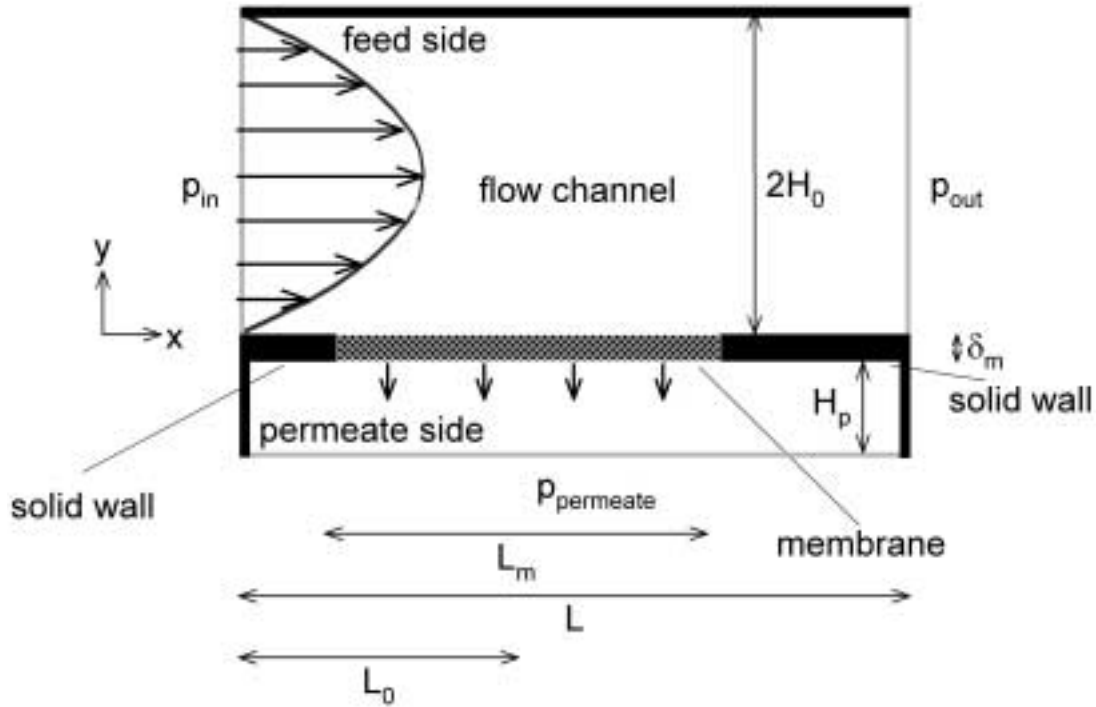


Figure 8.1: Lay-out of the 2D microfiltration system. Black lines indicate solid walls, whereas grey lines indicate pressure boundaries. A detailed description is given in the text.

called microsieves [31]. The feed side consists of a rectangular flow channel with a length L of $90 \mu\text{m}$ and a height $2H_0$ of $36 \mu\text{m}$.

A cross-flow is induced by a pressure gradient $(p_{\text{in}} - p_{\text{out}})/L$ over the channel of $3.0 \text{ Pa}/\mu\text{m}$, which results in $U_0=0.32 \text{ m/s}$ and $\dot{\gamma}_{\text{wall},0}=54000 \text{ s}^{-1}$. The permeate side consists of a rectangular box with a width L of $90 \mu\text{m}$ and a height H_p of $2.4 \mu\text{m}$. At the wall underneath the membrane, a constant pressure is applied, such that the average TMP was 1780 Pa . The feed and the permeate side are separated from each other by a wall with a thickness δ_m of $1.2 \mu\text{m}$. From the flow inlet side (left) up to the flow outlet side (right), this wall consecutively consists of $15 \mu\text{m}$ solid wall, $45 \mu\text{m}$ membrane and $30 \mu\text{m}$ solid wall. The membrane resistance R_m was $1.62 \cdot 10^8 \text{ m}^{-1}$. The feed suspension contained particles with a radius a of $2.5 \mu\text{m}$ in a volume fraction ϕ of 0.05 . The viscosity μ and specific cake resistance R'_c were calculated according to Equation (8.2) and (8.23). At the inlet and the outlet of the flow channel as well as at the permeate side, pressure boundary conditions are applied. This is done following the method proposed by Zou and He [117]. The pressure is kept constant at these boundaries:

$$p(x=0) = p_{\text{in}}; \quad p(x=L) = p_{\text{out}}; \quad p(y=0) = p_{\text{permeate}} \quad (8.18)$$

The transmembrane pressure (TMP) is defined as the pressure difference between the flow channel and the permeate side at a position halfway the membrane ($x = L_0$) and, when assuming a linear pressure gradient, is given by:

$$\text{TMP} = p_{\text{in}} - \frac{L_0}{L} (p_{\text{in}} - p_{\text{out}}) - p_{\text{permeate}} \quad (8.19)$$

For the suspended particles, boundary conditions with a fixed inlet concentration and a free outflow are applied at these boundaries, according to:

$$\phi(x=0) = \phi_b; \quad \frac{\partial \phi(x=L)}{\partial x} = 0 \quad (8.20)$$

There is no need for a boundary condition for suspended particles at the permeate side ($y=0$), since a no-flux condition is applied at the membrane. At the solid walls at the top side of the feed side and at the left and right side of the permeate side no-slip conditions are applied to the fluid. The suspended particles are subjected to a no-flux condition at these boundaries.

The geometry is divided into a feed and a permeate side by the presence of a horizontally placed membrane. The membrane is placed between two solid walls at the beginning and the end of the flow channel. The suspended particles are fully retained by the membrane, by application of no-flux conditions. For the fluid, the membrane is described as a porous medium. The fluid experiences a hydraulic resistance when passing the membrane, because part of the fluid is retained. Hereto, a body force F is applied on the fluid when passing the membrane, following Darcy's law:

$$F = -\frac{\rho \mathbf{u}}{K_{\text{membrane}}} \quad (8.21)$$

The coefficient K_{membrane} is dependent on the membrane resistance R_m , the membrane thickness δ_m and the viscosity of the fluid phase, according to:

$$\frac{1}{K_{\text{membrane}}} = \eta \frac{R_m}{\delta_m} \quad (8.22)$$

During filtration, a high concentration of suspended particles may be reached at the membrane surface, which may subsequently lead to the formation of a stagnant cake layer. Suspensions with monodisperse, hard spherical particles form a cake layer when the concentration reaches a value of 0.60. This cake layer behaves as a porous medium; suspended particles are fully retained by the cake, while the fluid experiences a flow resistance. In our simulations, this process of cake layer formation is simulated in a similar way. When the concentration of suspended particles locally exceeds a value of 0.60, the respective lattice point is described as a porous medium, in a similar way as the membrane. No-flux conditions are applied for the suspended particles, while the fluid experiences a body force as given by Equation (8.21) with the coefficient K_{cake} . This coefficient is chosen such that the Carman-Kozeny relation is obeyed:

$$\frac{1}{K_{\text{cake}}} = \eta R'_c = \eta \frac{C(1 - \varepsilon_c)^2 S_c^2}{\varepsilon_c^3} \quad (8.23)$$

The Carman-Kozeny relation describes the specific cake resistance of a monodisperse, non-compressible cake with porosity ε_c , specific surface $S_c = 3/a$ and constant C . Randomly packed cake layers normally have a porosity $\varepsilon_c \approx 0.4$, while the constant $C \approx 5$. Not only the stagnant cake layer, but also the flowing concentrated layer can be considered a porous medium. In general, the flow resistance of this layer is negligibly small. Therefore, we have neglected this effect, as is usual in MF modelling [10].

The initial conditions of the simulations are consistent with a fully developed parabolic velocity profile for the fluid particles in the flow channel, following Poiseuille type flow by a downchannel pressure gradient:

$$-\frac{dp}{dx} = 3 \frac{\eta_b U_0}{H_0^2} \quad (8.24)$$

where η_b is the viscosity in the bulk of the suspension, U_0 is the average flow velocity, H_0 is the channel half width. The concentration of suspended particles in the flow channel was initially equal to the bulk concentration. At the permeate side of the membrane, the initial velocity of the fluid particles as well as the concentration of suspended particles was equal to zero.

8.3 Results

8.3.1 Simulation of microfiltration with the suspension flow model

In this section of the paper, we will first present results of the suspension flow model on the effect of transmembrane pressure. In this way, the development of the permeate flux in time is analysed at conditions with and without the presence of a cake layer. It is also investigated whether a steady-state situation occurs. The suspension flow model is compared with the existing model of Romero and Davis [8] and Davis and Sherwood [81], in order to validate our model. This comparison is made on basis of the position-dependence of the flux and cake layer thickness in the steady-state regime so as to analyse the differences in cake layer profile along the membrane between the different models. To make comparison with the similarity solution of Davis and Sherwood possible, the simulations were carried out in the regime where the cake layer is thin compared to the channel height. Finally, we will step from a simple cross-flow system to systems with a more complex geometry, in order to illustrate the advanced possibilities of the suspension flow model compared to existing models. As examples of systems with a more complex geometry, simulation results of the steady-state flux will be presented of a system with a discontinuous membrane, a system with flow barriers and a system with a corrugated membrane. The permeate flux J in the simulation results is equal to the fluid velocity u underneath the membrane. The length-averaged flux $\langle J \rangle$ is the average permeate flux over the length of the membrane.

8.3.2 Effect of transmembrane pressure on flux and cake layer formation

In figure 8.2, the development of the length-averaged flux $\langle J \rangle$ in time is shown for different transmembrane pressures (TMP). The initial flux increases proportional to the TMP. At a TMP of 1180 Pa, the flux $\langle J \rangle$ remains constant in time. Here, the transport of suspended particles towards the membrane is too low to cause cake layer formation. At a TMP of 1780 Pa and higher however, the flux $\langle J \rangle$ declines in the initial phase, but reaches a steady-state at about 0.01 s. Figure 8.2 also shows the flux at $t=0$ as calculated from the membrane resistance and TMP (=flux particle-free medium J_0). This makes clear that the cake formation process does not start immediately at $t=0$, but about 1 ms later. This is due

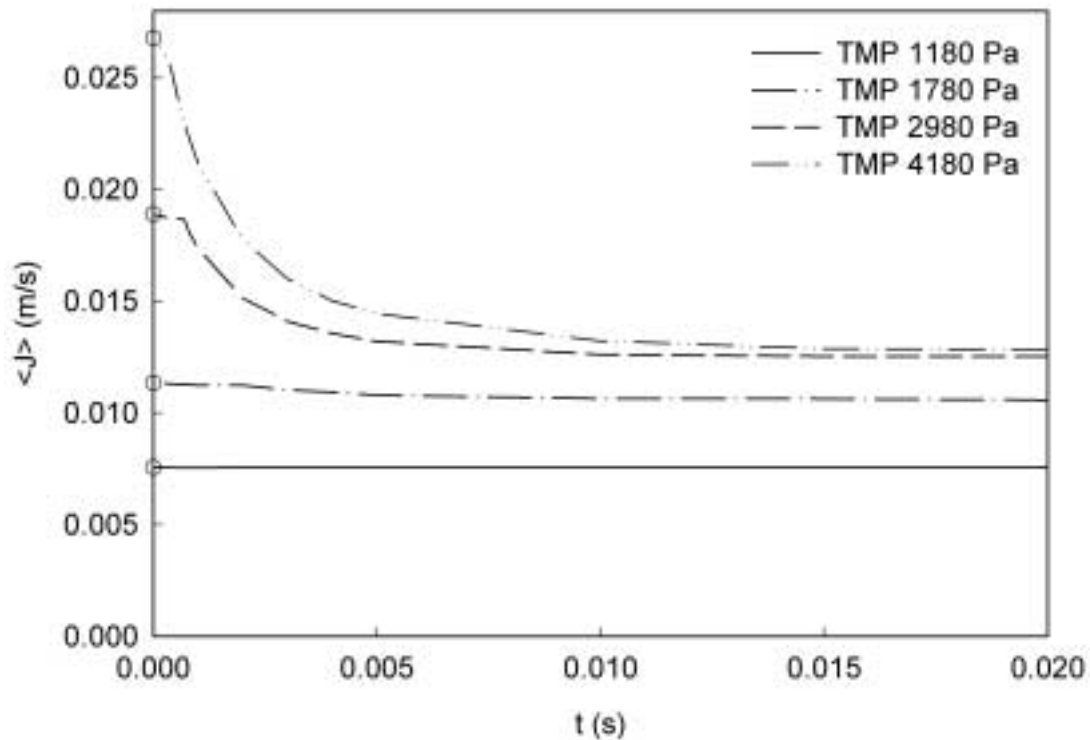


Figure 8.2: The length-averaged flux as a function of time for a transmembrane pressure of 1180, 1780, 2980 and 4180 Pa. Other system parameters as in figure 8.1. The calculated values for J_0 are depicted as circles on the Y-axis.

to the time required to develop the concentration polarisation profile. The steady-state concentration distribution near the membrane is presented in figure 8.6.

In accordance with the fluxes in figure 8.2, it can be seen that the cake is thickest at the highest TMP (4180 Pa), namely $5.7 \mu\text{m}$, while no cake is formed at a TMP of 1180 Pa. The cake gradually increases in thickness along the membrane, reaches a maximum thickness at about $2/3$ of the membrane length and then decreases to a thickness of zero at the end of the membrane. The cake at the end of the membrane is steep. The concentration polarisation layer follows more or less the shape of the cake layer. It has a thickness of about $5 \mu\text{m}$, which is equal to 1 suspended particle diameter in this case. It can be seen that the concentration change is relatively fast at low particle concentrations, which results in a sharp transition from concentration polarisation layer into bulk phase. This effect is due to the dependence of the shear-induced diffusivity on ϕ , and is different from Brownian diffusion-dominated concentration polarisation. Behind the membrane, the concentration polarisation layer disappears only very gradually. The difference between the length-averaged steady-state flux $\langle J_{ss} \rangle$ at 1780 and 4180 Pa (see also figure 8.3) can mainly be explained with the relative length of the cake-free zone at the beginning of the membrane, but differences in the cake-morphology at the end of the membrane and the narrowing of the flow channel by the cake formation may also have some effect.

At lower TMP, the length of the cake-free zone is relatively long so that in a large part of the membrane the maximum particle concentration at the membrane wall has not

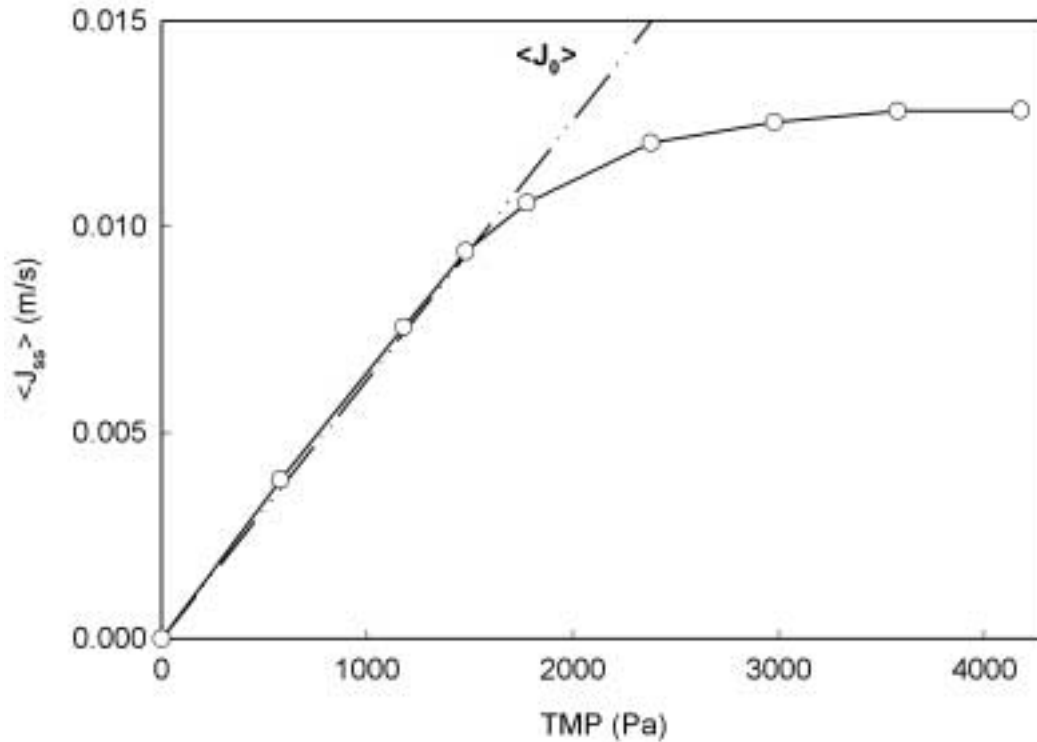


Figure 8.3: Length-averaged steady-state flux as a function of transmembrane pressure. Also indicated is the calculated line for the nominal flux $\langle J_0 \rangle$. System parameters as in figure 8.2.

reached the value of 0.6, which leads to less back-transport of suspended particles and therewith to a lower steady-state flux. At higher TMP, the cake-free zone disappears completely (which is contrary to the model of Romero and Davis). In this regime, the difference in cake height can also contribute to the difference in steady-state flux $\langle J_{ss} \rangle$. We can take the situation at a TMP of 2980 Pa as an example. Here the maximal thickness of the cake is $3.0 \mu\text{m}$, which is about 8% of the total channel height. The pressure gradient Δp over the channel is kept constant, so if we assume that the channel height has decreased with 8% over the total channel length, the crossflow velocity U will decrease according to:

$$\Delta p = f \cdot \frac{L}{D_h} \cdot \frac{1}{2} \rho U^2 \quad (8.25)$$

where f is the friction factor, L the length of the flow channel, D_h the hydraulic diameter and ρ is the fluid density. Since it follows that the velocity only decreases with a factor $\sqrt{0.92} = 0.96$, it becomes clear that according to:

$$\dot{\gamma}_{\text{wall}} = \frac{2U_{\text{max}}}{H_0} \quad (8.26)$$

the shear rate at the wall $\dot{\gamma}_{\text{wall}}$ will be raised locally with about 4% by the presence of the cake layer (compared to the situation without a cake layer). This higher shear rate can cause a thinner concentration polarisation layer and faster particle back-transport (a

higher shear-induced diffusivity), therewith resulting in a higher steady-state flux $\langle J_{ss} \rangle$. This behaviour results in a steady-state flux $\langle J_{ss} \rangle$ as a function of TMP as presented in figure 8.3. At low TMP, no cake layer is formed so that the flux follows the linear trend for the particle-free medium. At a TMP of 1780 Pa, a cake layer starts to be formed, so that the flux $\langle J_{ss} \rangle$ levels off and becomes almost constant at a TMP of 3600 Pa.

These results show that the suspension flow model is not only able to simulate the flux and cake layer formation in time, but also the dependence on TMP. This is not only possible in the limits of infinitely thin cake layers or infinitely small flux decline, but also in transient regimes, as described in the model of Romero and Davis [8, 9].

8.3.3 Position-dependence of flux and cake layer thickness

The suspension flow model incorporates a number of factors that are neglected in the model of Romero and Davis [8], such as 1) the variation of TMP over the length of the membrane, 2) the fully resolved velocity field following NS and 3) the axial migration of suspended particles between the bulk phase and the concentration polarisation layer (which e.g. enables the calculation of the dispersion of the concentration polarisation layer at the end of the membrane). In this paragraph, we will analyse which differences this brings about for the cake layer thickness and the flux. In the situation of an infinitely thin cake layer, and for a distance along the membrane $x \gg x_{cr}$, where x_{cr} is the length of the cake-free zone at the beginning of the membrane, Romero and Davis predict that the steady-state flux decreases along the membrane with the distance x , as given by:

$$J_{ss}(x) = J_0 \cdot \left[\frac{3}{2} \cdot \frac{(x - x_{cr})}{x_{cr}} + 1 \right]^{-1/3} \quad (8.27)$$

where J_0 is the nominal transmembrane flux (=flux of particle-free medium). According to the similarity solution of Davis and Sherwood [81], under the conditions of $\phi_b < 0.1$, cake-dominated resistance and $L \gg x_{cr}$, the length-averaged flux $\langle J_{ss} \rangle$ is given by:

$$\langle J_{ss} \rangle = 0.072 \cdot \dot{\gamma}_{wall,0} \cdot \left(\frac{\phi_c \cdot a^4}{\phi_b \cdot L_m} \right)^{1/3} \quad (8.28)$$

where $\dot{\gamma}_{wall,0}$ is the nominal shear rate at the wall, ϕ_b the bulk particle volume fraction and L_m is the total membrane length. For the particle volume fraction in the cake $\phi_c (=1 - \varepsilon_c)$ a value of 0.6 was taken in our calculations.

First, the flux J_{ss} of the suspension flow model is compared with the model of Romero and Davis (figure 8.4). The latter model does not take the pressure drop over the flow channel into account, so that the flux J_{ss} is equal to the flux of the particle-free medium (at the average TMP) from the beginning of the membrane until the critical distance x_{cr} . Behind this point, the flux declines as predicted by Equation (8.27). In the computer simulations, conditions are chosen such that the cake layer did not become thicker than 10% of the channel height, so that $\dot{\gamma}_{wall}$ can be considered constant in time. In the suspension flow model, the critical distance x_{cr} and the flux at the beginning of the membrane are dependent on the total membrane length. This can mainly be ascribed to the variation of TMP over the length of the membrane; since the average TMP is similar, the TMP at the beginning of the membrane is higher with longer membrane lengths. Due to these differences in TMP, the flux J_{ss} also drops off more quickly for longer membrane

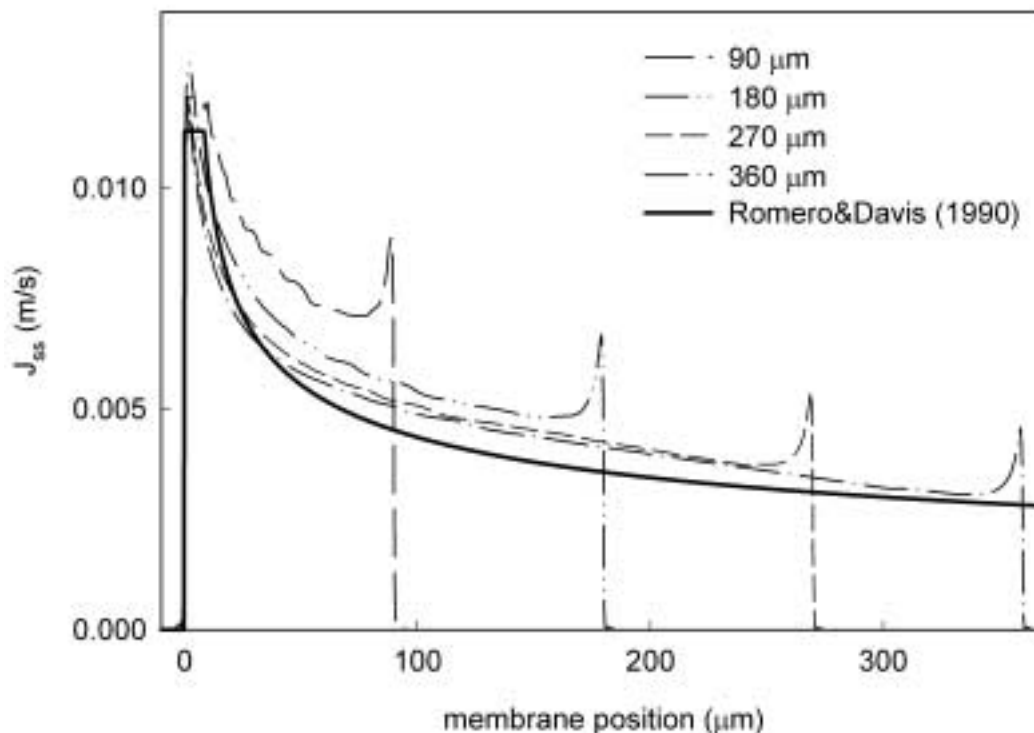


Figure 8.4: Steady-state flux as a function of position along the membrane for total membrane lengths between 90 and 360 μm . Also indicated is the calculated line for the steady-state flux as predicted by the model of Romero and Davis (Equation (8.27)). Other system parameters as in figure 8.1.

lengths. At the end of the membrane, the flux exhibits a peak due to the dispersion of the concentration polarisation layer.

In figure 8.5, it is shown how the length-averaged steady-state flux $\langle J_{ss} \rangle$ depends on the membrane length. For short membrane lengths, the difference between the suspension flow model and the model of Romero and Davis is relatively large. At a membrane length of 90 μm , the flux was almost 30% higher for the suspension flow model. The fluxes are however practically the same at longer membrane lengths, indicating that differences in cake layer formation between the models mainly occur at the beginning and the end of the membrane. This is in accordance with our expectations, since axial convective transport can be expected to be most relevant in these regions. With increasing membrane length, there is an increasing difference between the fluxes at different TMP. An increase of TMP can apparently lead to a more than proportional growth of the cake layer with eventually a lower flux. This may be due to the decrease of the mass flow rate $Q (= 2U \cdot H_0)$ through the flow channel at higher TMP. The decrease of flux with increasing TMP does not agree with the expected effect of narrowing of the channel as explained in paragraph 8.3.2, since we then would expect an increase of $\dot{\gamma}_{\text{wall}}$ and therewith an increase of the flux as well. As explained before, the effect of narrowing of the channel by cake formation will lead to a lower cross-flow velocity but a higher shear rate at the place where the cake layer is at its highest point. At other places along the membrane however, where the cake layer is thinner, the cross-flow velocity U will even be lower, which, in combination with the

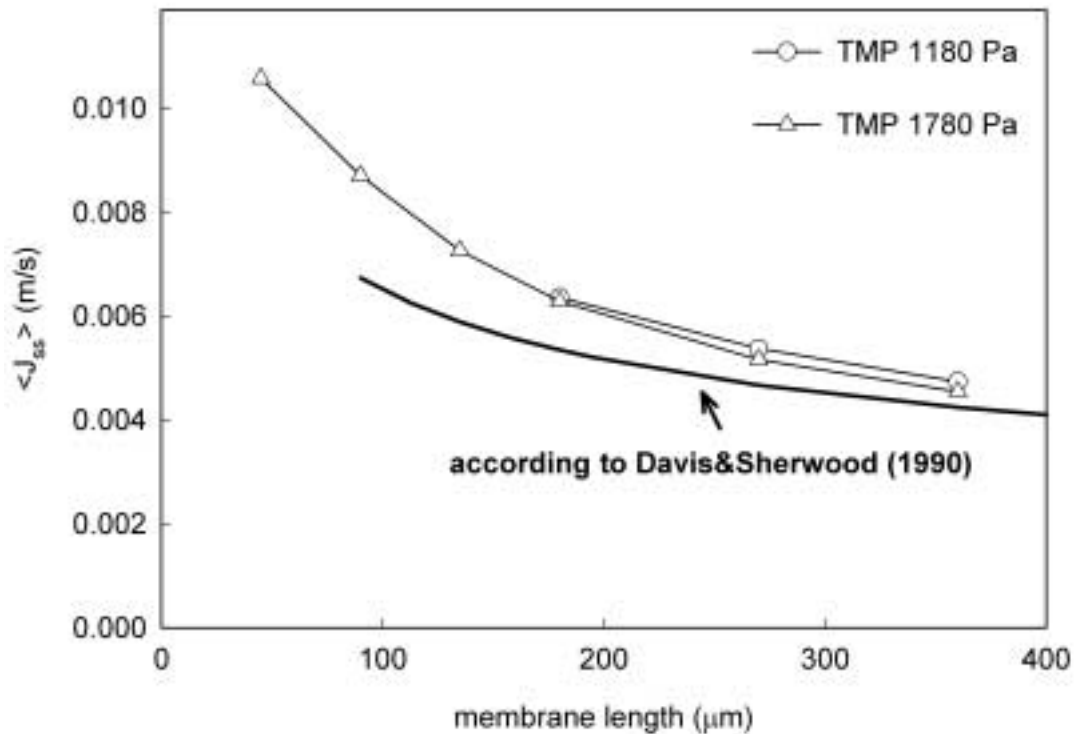


Figure 8.5: Length-averaged steady-state flux as a function of membrane length. Also indicated is the steady-state flux as predicted by the model of Davis and Sherwood (Equation (8.28)). Other system parameters as in figure 8.1.

higher channel height, can now lead to a drop of the shear rate. Thus, at places along the membrane where the cake layer height is less than maximal, the drop of the shear rate can lead to a decrease of the flux J_{ss} . This latter effect seems to prevail in the simulations in figure 8.5.

The results in this paragraph show that for simple cross-flow systems with relatively long membranes, our suspension flow model predicts cake layer profiles that converge to the profiles that are predicted by the model of Romero and Davis. Differences between the predicted cake layer profiles mainly occur at the beginning and the end of the membrane, resulting in a higher $\langle J_{ss} \rangle$ for short membrane lengths with the suspension flow model. Since the suspension flow model incorporates extra features as compared to the model of Romero and Davis, the results of this model can be considered to be more accurate, which is particularly relevant to systems with short membrane lengths and large variation of TMP over the length of the membrane.

8.3.4 Microfiltration in systems with different geometries

The solution of the flow field in the suspension flow model enables the calculation of concentration polarisation in more complex flow geometries. In this paragraph we will demonstrate some possibilities of the model by showing some examples. First, the effect of the presence of separate pore fields will be demonstrated. In such a situation, pore fields and solid walls alternate along the length of the membrane channel. This will result

in extra membrane beginnings and ends, where the flux is relatively high. The passage of the concentration polarisation layer over a piece of solid wall will namely lead to a (partial) dispersion, so that the flux at the start of the next membrane field will be higher than without the presence of the solid wall. The division of a homogeneous membrane into pore fields and fields with solid walls might be used as a means to optimise the flux. The benefit of dispersion of the concentration polarisation layer and the presence of repetitive membrane ends should then compensate for the diminished back-transport due to the reduced wall concentration at the solid walls. The suspension flow model enables an accurate flux prediction for these types of membranes. The presence of separate pore fields can also be an intrinsic property of some membrane types, such as the so-called microsieves [31], membranes prepared by micro-engineering which usually feature these distinct pore fields. The mechanical strength of these ultrathin microsieves is dependent on the size and division of the pore fields over the membrane surface. Here, the suspension flow model can be used to find the optimal lay-out of the pore fields as determined by both flux and mechanical strength.

In figure 8.7, the steady-state flux J_{ss} is presented for a homogeneous membrane with a total length of $135 \mu\text{m}$ and for a membrane with the same total length, which is divided into three evenly distributed membrane fields with a length of $33 \mu\text{m}$ and two solid walls with a length of $18 \mu\text{m}$. It can be seen that the flux at the pore fields is clearly higher for the subdivided membrane. The length-averaged flux $\langle J_{ss} \rangle$ (membrane length similar to homogeneous membrane) is however about 5% lower. In this situation, the diminished back-transport is the dominant effect, which is unfavourable for the flux. In case of microsieves, the mechanical strength will however improve much by this subdivision [118].

The dispersion of the concentration polarisation layer might improve with the presence of flow barriers at the solid walls. Whether or not this will render a positive flux effect is dependent on the trade-off between this improved dispersion on the one hand and the decreased wall shear rate on the other hand. With the suspension flow model, we are able to compute the effect of flow barriers. An example is given in figure 8.8.

Here, triangles with a height of $2.7 \mu\text{m}$ were placed centrally on the solid walls. It can be seen in figure 8.8 that the flux is hardly influenced by the presence of these barriers, although their height exceeds the height of the cake layer. This might be related to the microscale of the flow barriers. Because the Reynolds number is linearly dependent on the square height of the flow barrier, it will hardly be affected by the presence of these small flow barriers. In figure 8.8, it can accordingly be seen that the flow barriers do not induce flow disturbances such as vortices. On the other hand, because of the mechanism of shear-induced diffusion, the wall shear rate has a large effect on the flux. The decrease of the wall shear rate, due to an increased flow resistance of the flow channel, is the dominant effect in this example, such that the length-averaged steady-state flux $\langle J_{ss} \rangle$ was about 3% lower. Although more research is needed, this example might indicate that microscale flow barriers are not effective for flux improvement.

Another possibility for a higher flux would be the use of corrugated membranes. These corrugations are expected to lead to a better dispersion of the concentration polarisation layer and increased flow resistance, as for the system with triangles, but would also affect the shear rate profile at the membrane wall for the total membrane length. More information on the application of corrugated membranes can e.g. be found in [119]. In our example, the membrane corrugations consist of triangles of membrane material, which

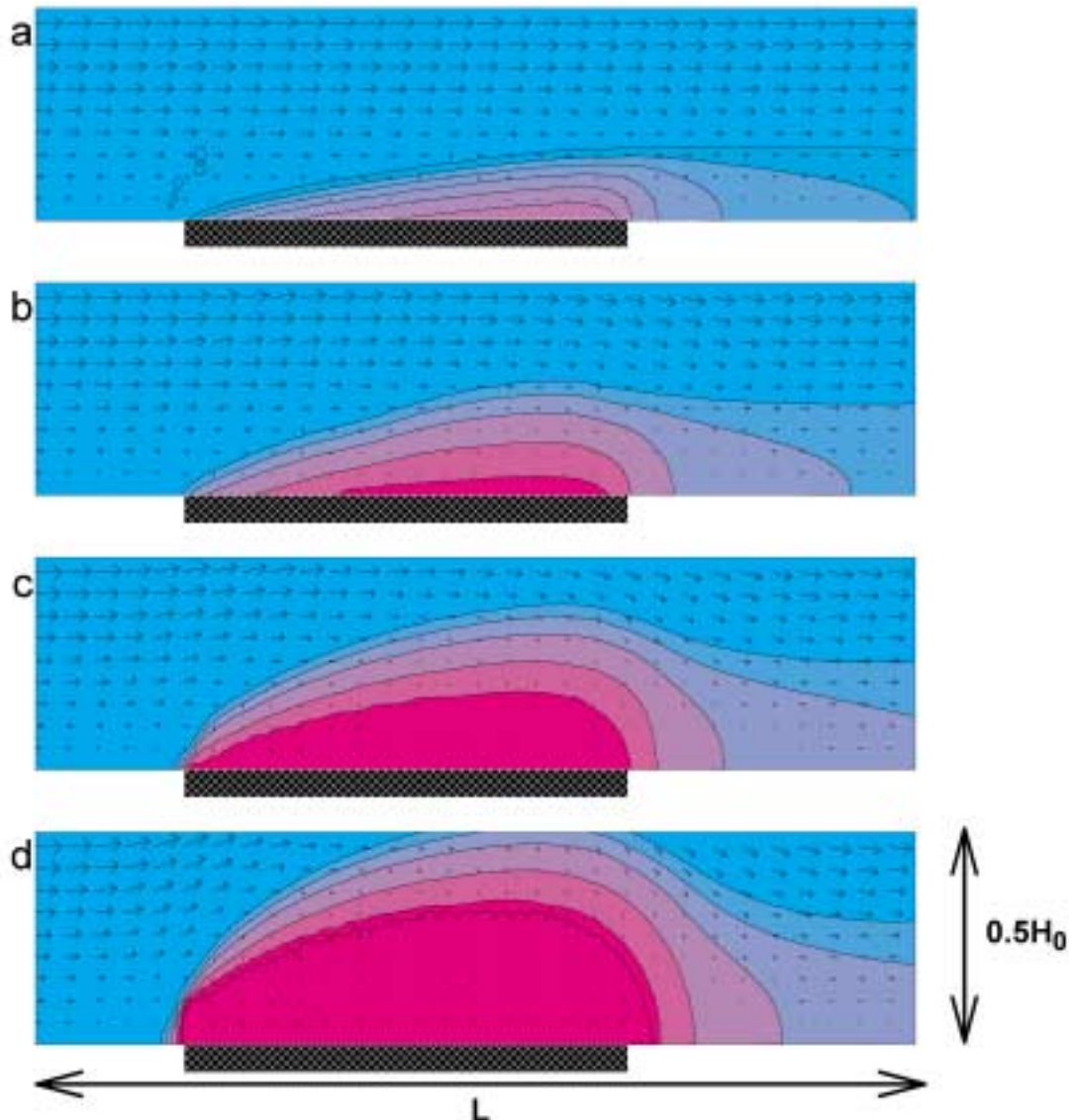


Figure 8.6: Concentration distribution and flow field near the membrane in the steady-state situation for a transmembrane pressure of 1180 (a), 1780 (b), 2980 (c) and 4180 (d) Pa. Only the part just above the membrane, with a height of $9.0 \mu\text{m}$ is presented. The colors indicate the particle volume fraction, ranging from 0.0-0.1 (turquoise) to 0.5-0.6 (pink). The concentration polarisation layer already develops before the beginning of the membrane. Other system parameters as in figure 8.1.

are placed centrally on the membranes. The size was such that the membrane surface area was increased with 1.8 %. Because the membrane has become much thicker at the position of the triangles, application of a similar TMP as for the aforementioned computations would lead to a suboptimal flux. Therefore TMP was increased to 5340 Pa.

Figure 8.9 shows the flux along the membrane in steady-state situation. At the beginning and the end of the membrane, the steady-state flux J_{ss} is about 1.5 times higher than without the membrane corrugations. Because of the reduced cake formation in these regions, the relatively high TMP results in this high steady-state flux J_{ss} . This result also indicates that the membrane corrugations are particularly favourable in a system with

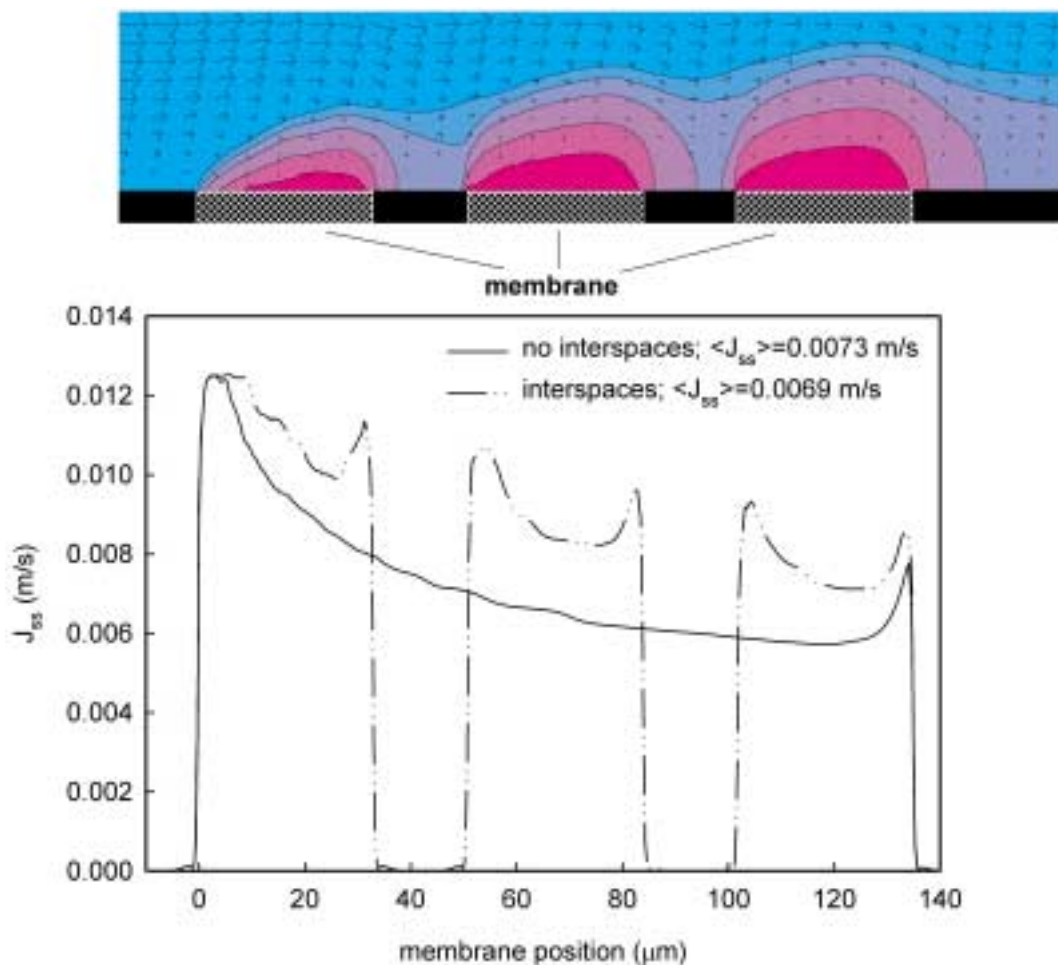


Figure 8.7: Steady-state flux as a function of position along the membrane for a homogeneous membrane with a total membrane length of 135 μm and for a membrane with the same total length, which is divided into three evenly distributed pore fields with a length of 33 μm and two solid walls with a length of 18 μm (see figure above graph). Also indicated is the length-averaged steady-state flux for both situations. The figure on top shows the concentration distribution and the flow field for the membrane with interspaces (settings as in 8.6). Other system parameters as in figure 8.1.

membrane interspaces, where we have an increased number of membrane beginnings and ends. In the center region of the membrane pieces, the flux is lower than without corrugations. The presence of the corrugations apparently results in a lower mean wall shear rate $\dot{\gamma}_{\text{wall}}$, which leads to a lower steady-state flux J_{ss} . The length-averaged flux $\langle J_{ss} \rangle$ is however higher in the system with membrane corrugations, suggesting that further research in this direction would be worthwhile. Clearly, the suspension flow model presented in this article can be a very helpful tool for these types of optimisations.

8.4 Conclusions

In this article, a new computer simulation model is proposed which enables the study of concentration polarisation behaviour and cake layer formation in crossflow microfiltra-

tion systems. The new model solves the NS equations for the suspension flow together with the convection-diffusion equation for the suspended particles and follows the Lattice Boltzmann method. Diffusion of the suspended particles takes place according to the mechanism of shear-induced migration, which describes the migration of particles in a suspension in shear flow. The shear-induced migration velocity increases linearly with the shear rate and is strongly concentration-dependent.

Upon application for simple crossflow systems, the new suspension flow model yields more realistic results for the flux and cake layer profile than existing models. This is due to the fact that the suspension flow model totally resolves the suspension flow and the shear-induced diffusion behaviour of the suspended particles, including a time- and location-dependent shear rate, whereas the existing models normally assume a Poiseuille flow profile and neglect axial transport between the bulk phase and the concentration polarisation layer. In contrast to existing models, the new suspension flow model moreover accounts for pressure loss in the flow channel.

From comparison with results of the model of Romero and Davis [8], it became clear that the more realistic approach of the suspension flow model is especially significant for the calculation of the cake layer profile at the beginning and the end of the membrane. Also the effect of narrowing of the flow channel by cake formation on the suspension flow pattern (at a constant pressure gradient over the flow channel) leads to a substantial improvement of the predictions. In the situation of long membrane lengths and thin cake layers, the solution of the suspension flow model converges to that of the model of Romero and Davis.

The suspension flow model has a wider applicability than the existing models. Besides the use for simple crossflow systems, the suspension flow model allows for application in microfiltration systems with complex geometries and moving boundaries. In order to exemplify these possibilities, calculations are presented on systems with a discontinuous membrane, with flow barriers and with corrugated membranes. From these examples, it became clear that this model can be a valuable tool for the design of microfiltration membranes, systems and processes.

List of symbols

Symbols Lattice Boltzmann method (in lattice units):

a	particle radius
\mathbf{c}_i	discrete velocity fluid particles
$c_{s,f}$	speed of sound fluid particles
$c_{s,g}$	speed of sound suspended particles
D	diffusion coefficient
F	body force
$f_i(\mathbf{x}, t)$	particle distribution function fluid particles
$f'_i(\mathbf{x}, t)$	post-collisional distribution function
$g_i(\mathbf{x}, t)$	particle distribution function suspended particles
\mathbf{j}	momentum density
p	pressure
t	time
\mathbf{u}	flow velocity

\mathbf{x}	a particular node of the lattice
w_i	weight factor

Greek symbols:

$\dot{\gamma}$	shear rate
η	dynamic viscosity
ν	kinematic viscosity
Π	momentum flux density
ρ	mass density
τ_f	relaxation time fluid particles
τ_g	relaxation time suspended particles
ϕ	suspended particle volume fraction

Symbols system parameters:

a	radius of the suspended particles, m
C	constant in Eq. (8.23)
D	diffusion coefficient, m/s
D_h	hydraulic diameter, m
f	friction factor
H_0	half-height of the channel, m
H_p	height permeate side, m
J	transmembrane flux, m/s
$\langle J \rangle$	length-averaged flux, m/s
J_0	nominal transmembrane flux, m/s
J_{ss}	steady-state flux, m/s
K	coefficient in Eq. (8.21)
L	length of the flow channel, m
L_0	length from flow inlet until halfway membrane, m
L_m	total membrane length, m
p	pressure, Pa
Q	mass flow rate, m ² /s
R_m	membrane resistance, m ⁻¹
R'_c	specific cake resistance, m ⁻²
S_c	specific surface, m ⁻¹
TMP	transmembrane pressure, Pa
u	velocity, m/s
U	crossflow velocity, m/s
U_0	average nominal flow velocity, m/s
U_{\max}	maximal flow velocity, m/s
x	dimensional distance along the filter, m
x_{cr}	critical distance, m

Greek symbols:

$\dot{\gamma}$	shear rate, s ⁻¹
$\dot{\gamma}_{\text{wall}}$	shear rate at the wall, s ⁻¹
$\dot{\gamma}_{\text{wall},0}$	nominal shear rate at the wall, s ⁻¹
δ_c	thickness of the cake layer, m

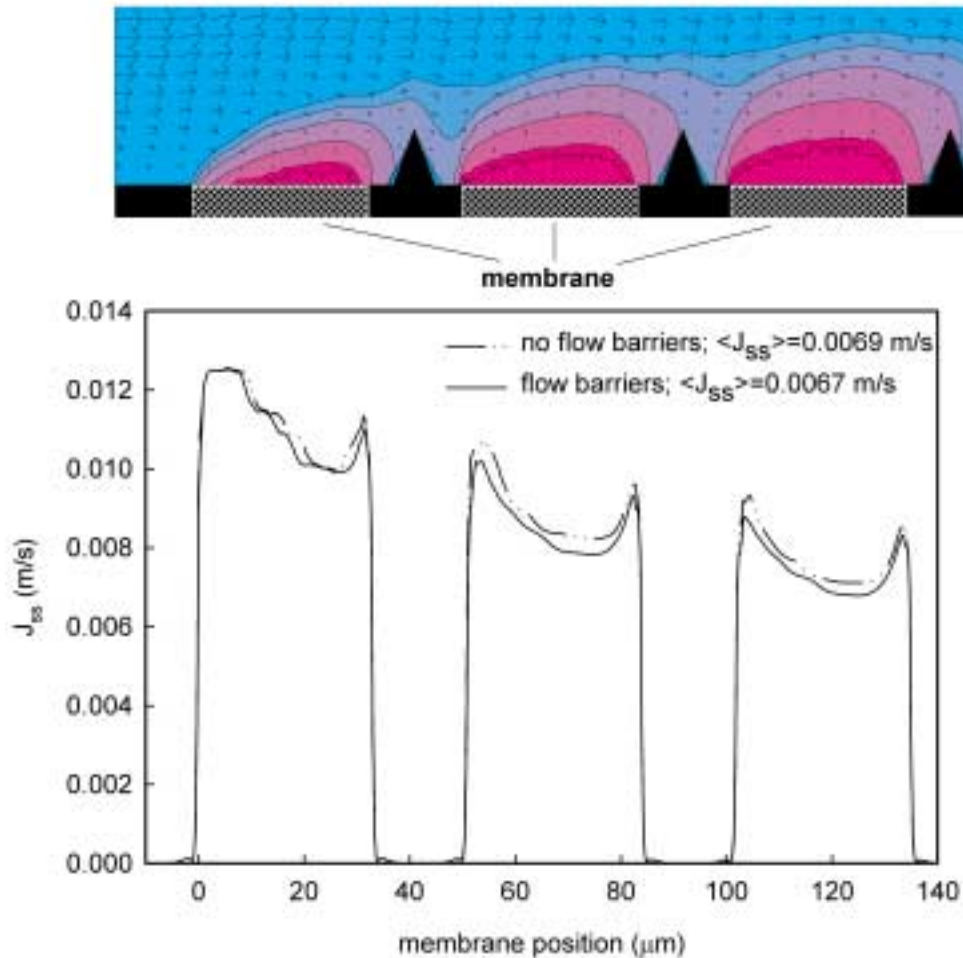


Figure 8.8: Steady-state flux as a function of position along the membrane for two different membranes: 1) a membrane with a total membrane length of $135 \mu\text{m}$, which is divided into three evenly distributed pore fields with a length of $33 \mu\text{m}$ and two solid walls with a length of $18 \mu\text{m}$ and 2) the same membrane but with flow barriers placed at the solid walls (see figure above graph). The flow barriers had a triangular form, with a width of $9.9 \mu\text{m}$ at the bottom side to $0.3 \mu\text{m}$ at the top side. The height was $2.7 \mu\text{m}$. Three flow barriers were placed in total, each with the center at a distance of $9 \mu\text{m}$ after a piece of membrane. Also indicated is the length-averaged steady-state flux for both situations. The figure on top shows the concentration distribution and the flow field for the membrane with flow barriers (settings as in 8.6). Other system parameters as in figure 8.1.

δ_m	thickness of the membrane, m
ε_c	porosity of the cake
η_0	viscosity of the particle free medium, Pa s
η_b	viscosity in the bulk of the suspension, Pa s
ρ	fluid density, kg/m^3
ϕ	particle volume fraction
ϕ_b	particle volume fraction in bulk suspension

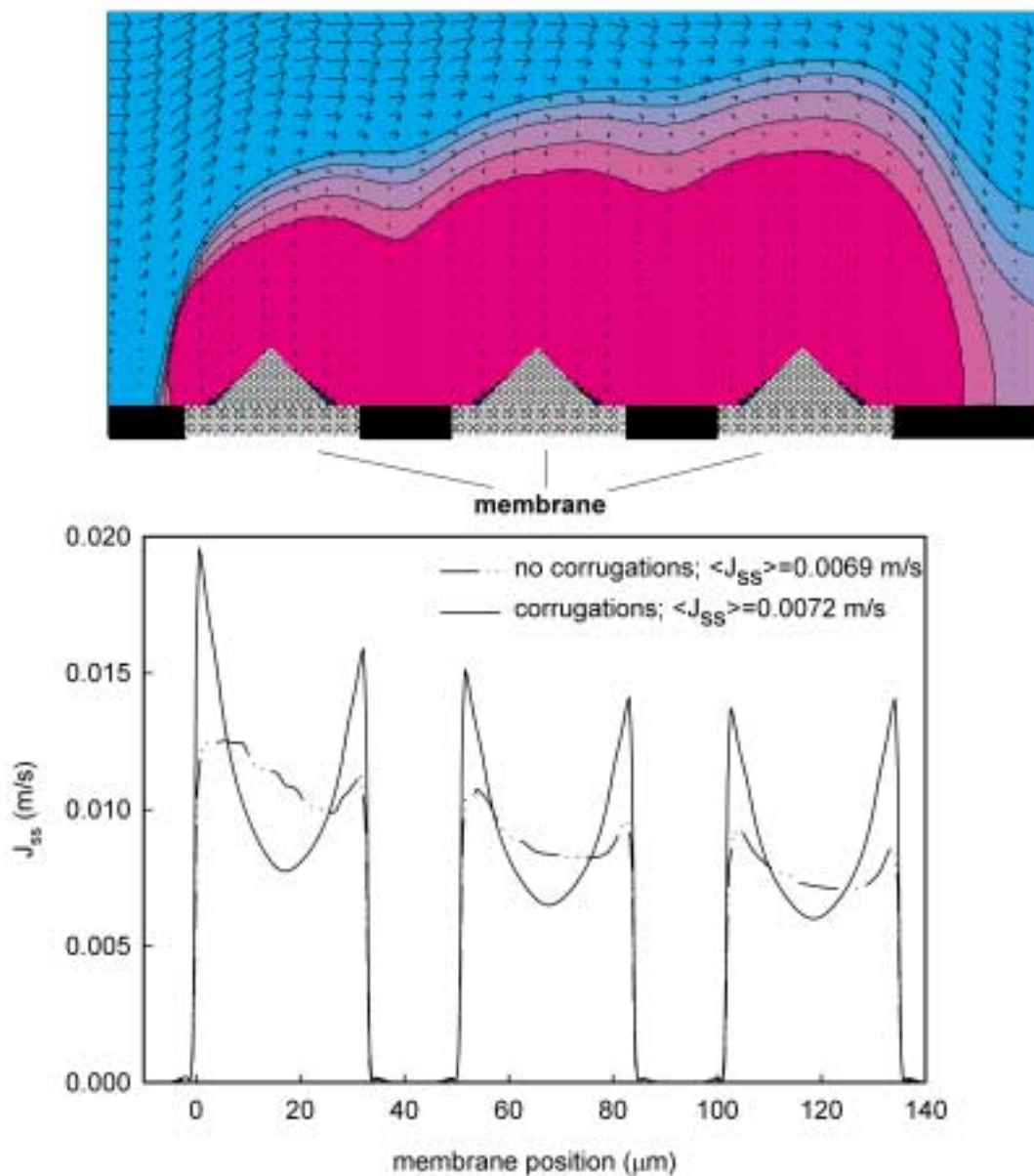


Figure 8.9: Steady-state flux as a function of position along the membrane for two different membranes: 1) a membrane with a total membrane length of 135 μm , which is divided into three evenly distributed pore fields with a length of 33 μm and two solid walls with a length of 18 μm and 2) the same membrane but with a corrugated structure (see figure above graph). The corrugations consist of triangular pieces of membrane which are put on top of the pore fields. The triangular pieces had a width of 24.3 μm at the bottom side to 0.3 μm at the top side. The height was 2.7 μm . Three triangular pieces were placed in total, each with the center at a distance of 16.5 μm from the beginning of a pore field. Also indicated is the length-averaged steady-state flux for both situations. The figure on top shows the concentration distribution and the flow field for the membrane with corrugations (settings as in 8.6, but the height is 20.2 μm). Other system parameters as in figure 8.1.

Acknowledgements

Friesland Foods is greatly acknowledged for supporting this research. The authors would like to acknowledge the support of the Dutch Ministries of Economic Affairs, Education, Culture and Sciences and of Housing, Spatial Planning and the Environment through a grant of the Dutch Program Economy, Ecology and Technology.

9

References

- [1] C.J. King, Separation processes, McGraw-Hill, New York, 1971, 26-31.
- [2] R.W. Rousseau (Ed.), Handbook of separation process technology, John Wiley Sons, 1971.
- [3] G. Brans, C.G.P.H. Schroën, R.G.M. van der Sman, R.M. Boom, Membrane fractionation of milk: state of the art and challenges, *J. Membr. Sci.* 243, 2004, 263-272.
- [4] M.C. Porter, Ultrafiltration of colloidal suspensions, In: Recent advances in separation techniques, AIChE Symp. Ser. No. 120, 1972, 21-30.
- [5] G. Green, G. Belfort, Fouling of ultrafiltration membranes: lateral migration and the particle trajectory model, *Desalination* 35, 1980, 129-147.
- [6] D.A. Drew, J.A. Schonberg, G. Belfort, Lateral inertial migration of a small sphere in fast laminar flow through a membrane duct, *Chem. Eng. Sci.* 46, 1991, 3219-3224.
- [7] R.H. Davis, D.T. Leighton, Shear-induced transport of a particle layer along a porous wall, *Chem. Eng. Sci.* 42, 1987, 275-281.
- [8] C.A. Romero, R.H. Davis, Global model of crossflow microfiltration based on hydrodynamic particle diffusion, *J. Membr. Sci.* 39, 1988, 157-185.
- [9] C.A. Romero, R.H. Davis, Transient model of crossflow microfiltration, *Chem. Eng. Sci.* 45, 1990, 13-25.
- [10] G. Belfort, R.H. Davis, A.L. Zydney, The behavior of suspensions and macromolecular solutions in crossflow microfiltration, *J. Membr. Sci.* 96, 1994, 1-58.
- [11] A.G. Fane, C.J.D. Fell, M.T. Nor, Ultrafiltration in the presence of suspended matter, In: *Ind. Chem. Eng. Jubilee Symp.* 73, 1982, C1-C12.
- [12] R.G. Gutman, The design of membrane separation plant: Part 2 - Fouling of RO membranes, *The Chemical Engineer* 322, 1977, 521-523.
- [13] H. Ebner, Die kontinuierliche Microfiltration von Essig, *Chem. Ing. Tech.* 53, 1981, 25-31.
- [14] E.C. Eckstein, D.G. Bailey, A.H. Shapiro, Self-diffusion of particles in shear flow of a suspension, *J. Fluid Mech.* 79 (1), 1977, 191-208.
- [15] D. Leighton, A. Acrivos, The shear-induced migration of particles in concentrated suspensions, *J. Fluid Mech.* 181, 1987, 415-439.
- [16] R.J. Phillips, R.C. Armstrong, R.A. Brown, A.L. Graham, J.R. Abbott, A constitutive equation for concentrated suspensions that accounts for shear-induced particle migration, *Phys. Fluids A* 4, 1992, 30-40.
- [17] V. Breedveld, D. van den Ende, A. Tripathi, A.A. Acrivos, The measurement of the shear-induced particle and fluid tracer diffusivities in concentrated suspensions by a novel method, *J. Fluid Mech.* 375, 1998, 297-318.
- [18] V. Breedveld, D. van den Ende, M. Bosscher, R.J.J. Jongschaap, J. Mellema, Measuring shear-induced self-diffusion in a counterrotating geometry, *Phys. Rev. E* 63 (021403), 2001, 1-10.
- [19] V. Breedveld, D. van den Ende, M. Bosscher, R.J.J. Jongschaap, J. Mellema, Measurement of the full shear-induced self-diffusion tensor of noncolloidal suspensions, *J. Chem. Phys.* 116, 2002, 10529-10535.

- [20] A. Acrivos, G.K. Batchelor, E.J. Hinch, D.L. Koch, R. Mauri, Longitudinal shear-induced diffusion of spheres in a dilute suspension, *J. Fluid Mech.* 240, 1992, 651-657.
- [21] F.R. Da Cunha, E.J. Hinch, Shear-induced dispersion in a dilute suspension of rough spheres, *J. Fluid Mech.* 309, 1996, 211-223.
- [22] Y. Wang, R. Mauri, A. Acrivos, The transverse shear-induced liquid and particle tracer diffusivities of a dilute suspension of spheres undergoing a simple shear flow, *J. Fluid Mech.* 327, 1996, 255-272.
- [23] Y. Wang, R. Mauri, A. Acrivos, Transverse shear-induced gradient diffusivity of a dilute suspension of spheres, *J. Fluid Mech.* 357, 1998, 279-287.
- [24] J.F. Morris, J.F. Brady, Self-diffusion in sheared suspensions, *J. Fluid Mech.* 312, 1996, 223-252.
- [25] M. Marchioro, A. Acrivos, Shear-induced particle diffusivities from numerical simulations. *J. Fluid Mech.* 443, 2001, 101-128.
- [26] G. Drazer, J. Koplik, B. Khusid, A. Acrivos, Deterministic and stochastic behaviour of non-Brownian spheres in sheared suspensions, *J. Fluid Mech.* 460, 2002, 307-335.
- [27] A. Sierou, J.F. Brady, Shear-induced self-diffusion in non-colloidal suspensions, *J. Fluid Mech.* 506, 2004, 285-314.
- [28] A.M. Leshansky, J.F. Brady, Dynamic structure factor study of diffusion in strongly sheared suspensions, *J. Fluid Mech.* 527, 2005, 141-169.
- [29] A.J.C. Ladd, Numerical simulations of particulate suspensions via a discretized Boltzmann equation. Part 1. Theoretical foundation, *J. Fluid Mech.* 271, 1994, 285-309.
- [30] A.J.C. Ladd, Numerical simulations of particulate suspensions via a discretized Boltzmann equation. Part 2. Numerical results, *J. Fluid Mech.* 271, 1994, 311-339.
- [31] C.J.M. van Rijn, M.C. Elwenspoek, Micro filtration membrane sieve with silicon micro machining for industrial and biomedical applications, *Proc. IEEE* 1995, 83-87.
- [32] A. Komnik, J. Harting, Transport phenomena and structuring in shear flow of suspensions near solid walls, *Cond. Mat.* 0408029, 2004, 1-13.
- [33] A.J.C. Ladd, R. Verberg, Lattice-Boltzmann simulations of particle-fluid suspensions, *J. Stat. Phys.* 104 (5/6), 2001, 1191-1251.
- [34] S. Succi, *The Lattice Boltzmann equation for fluid dynamics and beyond*, Oxford University Press, New York, 2001.
- [35] S. Chapman, T.G. Cowling, *The mathematical theory of non-uniform gases*, Cambridge University Press, 1960.
- [36] U. Frisch, B. Hasslacher, Y. Pomeau, Lattice-gas automata for the Navier-Stokes equation, *Phys. Rev. Lett.* 56 (14), 1986, 1505-1508.
- [37] Y.H. Qian, D. d'Humières, P. Lallemand, Lattice BGK models for the Navier-Stokes equation, *Europhys. Lett.* 17, 1992, 479-484.

- [38] O. Behrend, Solid-fluid boundaries in particle suspension simulations via the lattice Boltzmann method, *Phys. Rev. E* 52 (1), 1995, 1164-1175.
- [39] J. Kromkamp, D.T.M. van den Ende, D. Kandhai, R.G.M. van der Sman, R.M. Boom, Shear-induced self-diffusion and microstructure in non-Brownian suspensions at non-zero Reynolds numbers, *J. Fluid Mech.* 529, 2005, 253-278.
- [40] N.-Q. Nguyen, A.J.C. Ladd, Lubrication corrections for Lattice-Boltzmann simulations of particle suspensions, *Phys. Rev. E* 66 (046708), 2002, 1-12.
- [41] R.C. Ball, J.R. Melrose, Lubrication breakdown in hydrodynamic simulations of concentrated colloids, *Adv. Coll. Int. Sci.* 59, 1995, 19-30.
- [42] H. Nirschl, H.A. Dwyer, V. Denk, Three-dimensional calculations of the simple shear flow around a single particle between two moving walls, *J. Fluid Mech.* 283, 1995, 273-285.
- [43] G.I. Taylor, The viscosity of a fluid containing small drops of another fluid, *Proc. R. Soc. Lond. A* 138 (834), 1932, 41-48.
- [44] G.K. Batchelor, J.T. Green, The hydrodynamic interaction of two small freely-moving spheres in a linear flow field, *J. Fluid Mech.* 56 (2), 1972, 375-400.
- [45] N.A. Frankel, A. Acrivos, On the viscosity of a concentrated suspension of solid spheres, *Chem. Eng. Sci.* 22, 1967, 847-853.
- [46] I.M. Krieger, Rheology of monodisperse lattices, *Adv. Coll. Int. Sci.* 3, 1972, 111-136. I.M. Krieger, T.J. Dougherty, A mechanism for non-Newtonian flow in suspensions of rigid spheres, *Trans. Soc. Rheol.* 3, 1959, 137-152.
- [47] A. Shakib-Manesh, P. Raiskinmki, A. Koponen, M. Kataja, J. Timonen, Shear stress in a Couette flow of liquid-particle suspensions, *J. Stat. Phys.* 107 (1/2), 2002, 67-84.
- [48] M.W. Heemels, M.H.J. Hagen, C.P. Lowe, Simulating solid colloidal particles using the Lattice-Boltzmann method, *J. Comp. Phys.* 164, 2000, 48-61.
- [49] R.S. Farr, J.R. Melrose, R.C. Ball, Kinetic theory of jamming in hard-sphere startup flows, *Phys. Rev. E* 55 (6), 1997, 7203-7211.
- [50] L.V.A. Breedveld, Shear-induced self-diffusion in concentrated suspensions, Ph.D. thesis University of Twente, The Netherlands, 2000.
- [51] B.K. Chapman, D.T. Leighton, Dynamic viscous resuspension, *Int. J. Multiphase Flow* 17 (4), 1991, 469-483.
- [52] M.K. Lyon, L.G. Leal, An experimental study of the motion of concentrated suspensions in two-dimensional channel flow. Part 1. Monodisperse systems, *J. Fluid Mech.* 363, 1998, 25-56.
- [53] J.F. Brady, J.F. Morris, Microstructure of strongly sheared suspensions and its impact on rheology and diffusion, *J. Fluid Mech.* 348, 1997, 103-139.
- [54] Y. Yurkovetsky, I. Statistical mechanics of bubbly liquids; II. Behavior of sheared suspensions of non-Brownian particles, Dissertation Californian Institute of Technology, United States of America, 1998.
- [55] D.R. Foss, J.F. Brady, Self-diffusion in sheared suspensions by dynamic simulation, *J. Fluid Mech.* 401, 1999, 243-274.

- [56] A. Sierou, J.F. Brady, Accelerated Stokesian Dynamics simulations, *J. Fluid Mech.* 448, 2001, 115-146.
- [57] P. Bhatnagar, E.P. Gross, M.K. Krook, *Phys. Rev.* 94 , 1954, 511-525.
- [58] J. Feng, H.H. Hu, D.D. Joseph, Direct simulation of initial value problems for the motion of solid bodies in a Newtonian fluid. Part 2. Couette and Poiseuille flows, *J. Fluid Mech.* 277, 1994, 271-301.
- [59] J. Feng, H.H. Hu, D.D. Joseph, Direct simulation of initial value problems for the motion of solid bodies in a Newtonian fluid. Part 1. Sedimentation, *J. Fluid Mech.* 261, 1994, 95-134.
- [60] C.K. Aidun, Y. Lu, Lattice Boltzmann simulation of solid particles suspended in fluid. *J. Stat. Phys.* 81 (1/2), 1995, 49-61.
- [61] J.F. Brady, G. Bossis, The rheology of concentrated suspensions of spheres in simple shear flow by numerical simulation, *J. Fluid Mech.* 155, 1985, 105-129.
- [62] R.L. Hoffman, Explanations for the cause of shear thickening in concentrated colloidal suspensions, *J. Rheol.* 42, 1998, 111-123.
- [63] M.D. Haw, W.C.K. Poon, P.N. Pusey, Structure factors from cluster-cluster aggregation simulation at high concentration, *Physica A* 208, 1994, 8-17.
- [64] D.T. Leighton, A.A. Acrivos, Viscous resuspension, *Chem. Eng. Sci.* 41(6), 1986, 1377-1384.
- [65] G.P. Krishnan, S. Beimfohr, D.T. Leighton, Shear-induced radial segregation in bidisperse suspensions, *J. Fluid Mech.* 321, 1996, 371-393.
- [66] K. Höfler, S. Schwarzer, B. Wachmann, Simulation of hindered settling in bidisperse suspensions of rigid spheres, *Comp. Phys. Comm.* 121-122, 1999, 268-269.
- [67] G.P. Krishnan, D.T. Leighton, Dynamic viscous resuspension of bidisperse suspensions - I. Effective diffusivity, *Int. J. Multiphase Flow* 21(5), 1995, 721-732.
- [68] M.K. Lyon, L.G. Leal, An experimental study of the motion of concentrated suspensions in two-dimensional channel flow. Part 2. Bidisperse systems, *J. Fluid Mech.* 363, 1998, 57-77.
- [69] A.W. Chow, R.D. Hamlin, Size segregation of concentrated, bidisperse and polydisperse suspensions during tube drawing, *IUTAM Symposium on Hydrodynamic Diffusion of Suspended Particles*, Estes Park, CO, 1995.
- [70] D.M. Husband, L.A. Mondy, E. Ganani, A.L. Graham, Direct measurements of shear-induced particle migration in suspensions of bimodal spheres, *Rheol. Acta* 33, 1994, 185-192.
- [71] A. Shauly, A. Wachs, A. Nir, Shear-induced particle migration in a polydisperse concentrated suspension, *J. Rheol.* 42, 1998, 1329-1348.
- [72] C. Chang, R.L. Powell, Dynamic simulation of bimodal suspensions of hydrodynamically interacting spherical particles, *J. Fluid Mech.* 253, 1993, 1-25.
- [73] C. Chang, R.L. Powell, Effect of particle size distributions on the rheology of concentrated bimodal suspensions, *J. Rheol.* 38(1), 1994, 85-98.

- [74] A.P. Shapiro, R.F. Probstein, Random packings of spheres and fluidity limits of monodisperse and bidisperse suspensions, *Phys. Rev. Lett.* 68, 1992, 1422-1425.
- [75] R.F. Probstein, M.Z. Sengun, T.-C. Tseng, Bimodal model of concentrated suspension viscosity for distributed particle sizes, *J. Rheol.* 38, 1994, 811-829.
- [76] J.S. Chong, E.B. Christiansen, A.D. Baer, Rheology of concentrated suspensions, *J. Appl. Polym. Sci.* 15, 1971, 2007-2021.
- [77] G. Bossis, J.F. Brady, The rheology of Brownian suspensions, *J. Chem. Phys.* 91, 1989, 1866-1874.
- [78] Kromkamp, J., D. Kandhai, R.G.M. van der Sman, R.M. Boom, Lattice Boltzmann simulation of 2D and 3D non-Brownian suspensions in Couette flow, Submitted for publication.
- [79] G. Daufin, J.-P. Escudier, H. Carre, S. Brot, L. Fillaudeau, M. Decloux, Recent and emerging applications of membrane processes in the food and dairy industry, *Trans IChemE* 79, 2001, 89-102.
- [80] D.T. Leighton, A.A. Acrivos, Measurement of the shear-induced coefficient of self-diffusion in concentrated dispersions of spheres, *J. Fluid Mech.* 177, 1987, 109-131.
- [81] R.H. Davis, J.D. Sherwood, A similarity solution for steady-state crossflow microfiltration, *Chem. Eng. Science* 45, 1990, 3203-3209.
- [82] H. Bechhold, Kolloidstudien mit der Filtrationsmethode, *Z. Phys. Chem.* 60, 1907, 257-318.
- [83] P. Bacchin, P. Aimar, V. Sanchez, Model for colloidal fouling of membranes, *AIChE Journal* 41, 1995, 368-376.
- [84] N.N. Kramadhati, M. Mondor, C. Moresoli, Evaluation of the shear-induced diffusion model for the microfiltration of polydisperse feed suspension, *Sep. Pur. Techn.* 27, 2002, 11-24.
- [85] J. Kromkamp, M. Domselaar, K. Schroën, R. van der Sman, R. Boom, Shear-induced diffusion model for microfiltration of polydisperse suspensions, *Desalination* 146, 2002, 63-68.
- [86] S. Chellam, M.R. Wiesner, Evaluation of crossflow filtration models based on shear-induced diffusion and particle adhesion: Complications induced by feed suspension polydispersity, *J. Membr. Sci.* 138, 1998, 83-97.
- [87] H. Li, A.G. Fane, H.G.L. Coster, S. Vigneswaran, Direct observation of particle deposition on the membrane surface during crossflow microfiltration, *J. Membr. Sci.* 149, 1998, 83-97.
- [88] A. Ould-Dris, M.Y. Jaffrin, D. Si-Hassen, Y. Neggaz, Effect of cake thickness and particle polydispersity on prediction of permeate flux in microfiltration of particulate suspensions by a hydrodynamic diffusion model, *J. Membr. Sci.* 164, 2000, 211-227.
- [89] S. Kim, S.-H. Cho, H. Park, Effects of particle size distribution on the cake formation in crossflow microfiltration, *Water Sci. Techn.: Water supply* 2, 2002, 305-311.
- [90] R.M. Sandblom (Alfa-Laval), Filtering Process, Swedish Pat. 7416257, 1974.

- [91] H. Goudédranche, J.L. Maubois, J. Fauquant, Produits, en particulier laitiers, comprenant des fractions sélectionnés de globules gras, obtention et applications, Brevet FR. 2.776.208.-A1, 1998.
- [92] J.-L. Maubois, New applications of membrane technology in the dairy industry, *Aus. J. Dairy Technol.* 46, 1991, 91-95.
- [93] C.-C. Ho, A.L. Zydney, Effect of membrane morphology on the initial rate of protein fouling during microfiltration, *J. Membr. Sci.* 155, 1999, 261-275.
- [94] C.-C. Ho, A.L. Zydney, A combined pore blockage and cake filtration model for protein fouling during microfiltration, *J. Coll. Int. Sci.* 232, 2000, 389-399.
- [95] M. Hlavacek, F. Bouchet, Constant flowrate blocking laws and an example of their application to dead-end microfiltration of protein solutions, *J. Membr. Sci.* 82, 1993, 285-295.
- [96] E.M. Tracey, R.H. Davis, Protein fouling of track-etched polycarbonate microfiltration membranes, *J. Coll. Int. Sci.* 167, 1994, 104-106.
- [97] C. Guell, R.H. Davis, Membrane fouling during microfiltration of protein mixtures, *J. Membr. Sci.* 119, 1996, 269-284.
- [98] T.C. Arnot, R.W. Field, A.B. Koltuniewicz, Cross-flow and dead-end microfiltration of oily-water emulsions. Part II. Mechanisms and modelling of flux decline, *J. Membr. Sci.* 169, 2000, 1-15.
- [99] J. Hermia, Constant pressure blocking filtration laws—application to power law non-Newtonian flows, *Trans. Inst. Chem. Eng.* 60, 1982, 183-187.
- [100] A. Flippov, V.M. Starov, D.R. Lloyd, S. Chakravarti, S. Glaser, Sieve mechanism of microfiltration, *J. Membr. Sci.* 89, 1994, 199-213.
- [101] D.E. Smiles, J.M. Kirby, Aspects of one-dimensional filtration, *Sep. Sci. Technol.* 22, 1987, 1405-1423.
- [102] J.R. Philip, D.E. Smiles, Macroscopic analysis of the behaviour of colloidal suspensions, *Adv. Coll. Int. Sci.* 17, 1982, 83-103.
- [103] D.E. Smiles, P.A.C. Raats, J.H. Knight, Constant pressure filtration: The effect of a filter membrane, *Chem. Eng. Sci.* 37, 1982, 707-714.
- [104] P. Walstra, T.J. Geurts, A. Noomen, A. Jellema, M.A.J.S. van Boekel, *Dairy Technology: Principles of milk properties and processes*, Marcel Dekker, New York, 1999.
- [105] R. H. Davis, D.C. Grant, Theory for deadend microfiltration, In: *Membrane Handbook*, W.S. Ho, K. Sirkar (Ed.), Van Nostrand Reinhold, New York, 1992.
- [106] D.M.E. Thies-Weesie, A.P. Philipse, Liquid permeation of bidisperse colloidal hard-sphere packings and the Kozeny-Carman scaling relation, *J. Coll. Int. Sci.* 162, 1994, 470-480.
- [107] S. Kosvintsev, R.G. Holdich, I.W. Cumming, V.M. Starov, Modelling of dead-end microfiltration with pore blocking and cake formation, *J. Membr. Sci.* 208, 2002, 181-192.

- [108] R.W. Hartel, K.E. Kaylegian, Advances in milk fat fractionation, In: Crystallization processes in fats and lipid systems, N. Garti, K. Sato (Ed.), Marcel Dekker, New York, 2001.
- [109] P. Walstra, R. Jenness, Dairy chemistry and physics, Wiley, New York, 1984.
- [110] A.L. Zydney, C.K. Colton, A concentration polarization model for the filtrate flux in cross-flow microfiltration of particulate suspensions, Chem. Eng. Comm. 47, 1986, 1-21.
- [111] N. Pelekasis, A convection-shear induced resuspension model for crossflow microfiltration, Chem. Eng. Sci. 53, 1998, 3469-3481.
- [112] D.E. Wiley, D.F. Fletcher, Techniques for computational fluid dynamics modelling of flow in membrane channels, J. Membr. Sci. 211, 2003, 127-137.
- [113] C.J. Richardson, V. Nassehi, Finite element modelling of concentration profiles in flow domains with curved porous boundaries, Chem. Eng. Sci. 58, 2003, 2491-2503.
- [114] X. He, S. Chen, G.D. Doolen, A novel thermal model for the Lattice Boltzmann method in incompressible limit, J. Comp. Phys. 146, 1998, 282-300.
- [115] S. Hou, J. Sterling, S. Chen, G.D. Doolen, A Lattice Boltzmann subgrid model for high Reynolds number flows, Fields Inst. Commun. 6, 1996, 151-166.
- [116] R.G.M. van der Sman, M.H. Ernst, Convection-diffusion lattice Boltzmann scheme for irregular lattices, J. Comp. Phys. 160, 2000, 766-782.
- [117] Q. Zou, X. He, On pressure and velocity flow boundary conditions for the lattice Boltzmann BGK model, Phys. Fluids 9, 1997, 1591-1598.
- [118] S. Kuiper, R. Brink, W. Nijdam, G.J.M. Krijnen, M.C. Elwenspoek, Ceramic microsieves: influence of perforation shape and distribution on flow resistance and membrane strength, J. Membr. Sci. 196, 2002, 149-157.
- [119] K. Scott, A.J. Mahmood, R.J. Jachuck, B. Hu, Intensified membrane filtration with corrugated membranes, J. Membr. Sci. 173, 2000, 1-16.

Summary

Microfiltration (MF) is a process that is used for the separation or fractionation of particles (0.02-20 μm) in a suspension. A suspension is pressed through a MF membrane; larger particles are retained by the membrane and a size-selective separation is obtained, which can be applied for e.g. water treatment and the manufacture of many products in biotechnological, food and medical applications.

In general, accumulation and deposition of retained particles in and onto the membrane, often referred to as concentration polarisation and cake layer formation respectively, severely limit the flux and selectivity of MF processes. This is especially the case for MF of complex suspensions such as milk, which contains a high volume fraction of dispersed matter ($\pm 15\%$) with a broad particle size distribution (1 nm - 20 μm). In this thesis, factors affecting the flux and selectivity of MF processes for milk separation are studied on various levels of detail. The initial focus was at a microscopic scale by studying suspension flow at conditions relevant to MF (Chapter 2, 3 and 4) and then gradually shifted to a macroscopic scale, studying the filtration behaviour of complex suspensions (Chapter 5, 6 and 7), for which a computer simulation model was developed to support the design of MF processes (Chapter 8).

In Chapter 2, a computer simulation model for suspension flow is presented, based on the Lattice Boltzmann (LB) method. With this model, the flow behaviour of two-dimensional (2D) and three-dimensional (3D) suspensions in Couette systems are compared. Scaling relations were found for the translation of 2D computer simulation results to 3D real systems therewith reducing the computational effort considerably.

Chapter 3 discusses the effect of non-zero Reynolds numbers on Couette flow of 2D suspensions. Shear-induced diffusion, a diffusion mechanism that reduces concentration polarisation and cake layer formation in cross-flow MF systems, is found to increase with the Reynolds number. A similar effect is found for the suspension viscosity. These effects correlated with the occurrence of particle clustering in the suspensions, which can not only be achieved by increasing the Reynolds number but also by increasing the attraction between particles.

Shear-induced diffusion in suspensions with a bimodal particle size distribution is described in Chapter 4, as studied by computer simulations with the LB method. In monodisperse suspensions, shear-induced diffusivity scales with the squared particle radius, which stresses the importance of particle size. In bidisperse suspensions, the larger particles behave as “master particles” when they are present in a sufficient amount: the shear-induced diffusivity is totally determined by these larger particles. The smaller “slave particles” acquire a shear-induced diffusivity similar to the large particles, but larger than in the respective monodisperse suspension (equal total volume fraction, same particle size). Moreover, it is found that the larger particles can enhance the effects of non-zero Reynolds number as found in Chapter 3, since these particles experience a larger

shear intensity. The results clearly demonstrate that the particle size distribution affects the shear-induced diffusion coefficients of the individual particles in the suspension.

Chapter 5 reports on an experimental study on the steady-state flux in cross-flow MF of latex suspensions with a bimodal size distribution. For monodisperse suspensions, the steady-state flux is known to relate to $a^{4/3}$, where a is the particle radius. In bidisperse suspensions with various concentration ratios of small to large particles but with a constant total volume fraction, it turned out that the steady-state flux is similar to the steady-state flux of a monodisperse suspension of the small particles. The influence of the presence of the large particles on the shear-induced diffusivity of the smaller particles could be explained with a model for shear-induced particle migration of polydisperse suspensions, which is also relevant in practice.

In Chapter 6, the study of the MF behaviour of suspensions with a particle size distribution is extended towards particle deposition onto the membrane, and towards particle fractionation. In the transient flux regime, particle deposition is the net result of transport of particles towards the membrane by the flux through the membrane and the back-transport of particles from the membrane towards the bulk phase by shear-induced diffusion. By monitoring the particle deposition onto the membrane during MF by means of Confocal Scanning Laser Microscopy, it was found that only the small particles in the bidisperse suspension deposit on the membrane. These results can be explained by the occurrence of particle size segregation in the feed flow, which leads to an enrichment of the smaller particles near the membrane. The findings are also shown to be relevant to particle fractionation processes by MF as was demonstrated with the fractionation of milk fat globules in milk. This polydisperse suspension could be fractionated using a membrane having a pore size larger than the largest particles present. The separation characteristics of the process, such as particle size and fat content of the permeate, could be totally controlled by the cross-flow velocity and permeate flux. This demonstrates that the fractionation is not due to size exclusion by the membrane, but instead due to segregation effects in the feed channel.

Some particle deposition is often inevitable in MF processes. For the purpose of process design, it is important to know the relevant properties of these deposition layers. For many complex suspensions, these cannot be predicted easily. In Chapter 7, the properties of particle deposition layers from micellar casein and milk fat globule suspensions are studied. By following a differential approach, it was possible to evaluate the particle deposition layers during their formation in a dead-end filtration process. Both micellar casein and milk fat globules were able to form layers with a very high hydrodynamic resistance. While the permeability of layers of micellar casein was independent of the pressure gradient applied, the layers of (liquid) milk fat globules were dependent on the pressure gradient. When the fat was partly crystallised, the compressibility was smaller, but the hydrodynamic resistance of the deposition layers was still very high, probably because of the occurrence of partial coalescence of the fat globules. The parameters identified in this study are considered essential for the rational design of UF and MF processes of milk.

Process models that predict the flux and selectivity as a function of system and process parameters, are important tools in the design of MF processes. Chapter 8 presents a newly developed MF model which predicts concentration polarisation and cake layer formation, and which is, unlike other MF models, suited for MF processes of complex suspensions and in MF systems with complex membrane or module geometries or process conditions.

The so-called suspension flow model is a computer simulation model, in which the hydrodynamics and convection-diffusion are resolved simultaneously, using an Euler-Euler approach. This model, which is based on the LB method, allows the complete solution of the flow field (including calculation of the actual local shear rate) and the application of a pressure gradient over the feed flow channel as well as over the membrane. The general applicability of the suspension flow model as a design tool for MF membranes, systems and processes is demonstrated with computations on concentration polarisation and cake layer formation in MF systems with complex geometries, such as feed flow channels with flow barriers and corrugated membranes. The suspension flow model is a practical tool for the design of MF processes of complex suspensions such as milk.

Samenvatting

Microfiltratie (MF) is een proces dat wordt gebruikt om deeltjes ($0.02\text{-}20\ \mu\text{m}$) in een suspensie af te scheiden of te fractioneren. De suspensie wordt hierbij door een MF membraan geperst; grotere deeltjes worden tegengehouden door het membraan, zodat een scheiding op grootte wordt verkregen. Deze scheiding kan bijvoorbeeld worden ingezet voor waterbehandeling en voor de vervaardiging van producten voor biotechnologische, voedings- en medische toepassing.

In het algemeen wordt de flux en selectiviteit van MF processen ernstig beperkt door ophoping en afzetting van de tegengehouden deeltjes aan en op het membraan, verschijnselen die vaak aangeduid worden met respectievelijk concentratiepolarisatie en koeklaagvorming. Dit treedt in het bijzonder op tijdens MF van suspensies met een complexe samenstelling, zoals melk, dat een hoge volumefractie aan gedispergeerd materiaal bevat ($\pm 15\%$) met een brede grootteverdeling ($1\ \text{nm} - 20\ \mu\text{m}$). Dit proefschrift beschrijft een onderzoek waarin op verschillende detailniveaus factoren zijn bestudeerd die de flux en selectiviteit van MF processen voor de scheiding van melk beïnvloeden. Het begin van dit proefschrift focuseert op de microscopische schaal, met een studie van het stromingsgedrag van suspensies onder condities die relevant zijn voor MF (Hoofdstuk 2, 3 en 4), waarna de focus geleidelijk verschuift naar macroscopische schaal, met een studie van het filtratiegedrag van suspensies met een complexe samenstelling (Hoofdstuk 5, 6 en 7). Het laatste Hoofdstuk beschrijft een computersimulatiemodel dat is ontwikkeld om het ontwerp van MF processen te ondersteunen (Hoofdstuk 8).

In Hoofdstuk 2 wordt een computersimulatiemodel gepresenteerd, dat is gebaseerd op de Lattice Boltzmann (LB) methode. Aan de hand van dit model is een vergelijking gemaakt tussen het stromingsgedrag van twee-dimensionale (2D) en drie-dimensionale (3D) suspensies in Couette systemen. Er zijn schalingsrelaties gevonden voor de vertaling van 2D computersimulatie resultaten naar 3D reële systemen, waarmee de benodigde computercapaciteit voor het berekenen van het stromingsgedrag aanzienlijk gereduceerd kan worden.

Hoofdstuk 3 bediscussieert het effect van Reynolds getallen groter dan nul op Couette stroming van 2D suspensies. Shear-induced diffusie, een diffusiemechanisme dat concentratiepolarisatie en koeklaagvorming in cross-flow MF systemen reduceert, bleek toe te nemen met een toenemend Reynolds getal. Een vergelijkbare toename werd gevonden voor de viscositeit van de suspensie. Deze effecten correleerden met het optreden van clustering van deeltjes in de suspensie, hetgeen niet alleen optrad met een toename van het Reynolds getal maar ook met een toename van de attractie tussen deeltjes.

Shear-induced diffusie in suspensies met een bimodale deeltjesgrootteverdeling, bestudeerd door middel van computersimulaties met de LB methode, is beschreven in Hoofdstuk 4. In monodisperse suspensies schaalde de shear-induced diffusiviteit met het kwadraat van de deeltjesstraal. Het belang van de grootteverdeling wordt duidelijk in bidisperse

suspensies, waar de grotere deeltjes, wanneer aanwezig in voldoende hoeveelheid, hun gedrag volledig opleggen aan de kleinere deeltjes: de shear-induced diffusiviteit is dan volledig bepaald door deze grotere deeltjes. De kleinere deeltjes nemen een shear-induced diffusiviteit aan die gelijk is aan die van de grotere deeltjes, en daardoor groter dan in een monodisperse suspensie van alleen de kleinere deeltjes (met gelijke totale volumefractie). De grotere deeltjes blijken bovendien de effecten van toenemende Reynolds getallen, zoals gevonden in Hoofdstuk 3, te kunnen versterken, doordat deze deeltjes in een bidisperse suspensie een groter shear Reynolds getal ervaren dan de kleinere deeltjes. De resultaten tonen duidelijk aan dat de deeltjesgrootteverdeling van invloed is op de shear-induced diffusiecoëfficiënten van de individuele deeltjes in de suspensie.

Hoofdstuk 5 doet verslag van een experimentele studie naar de *steady-state flux* tijdens cross-flow MF van latex suspensies met een bimodale grootteverdeling. Voor monodisperse suspensies is het bekend dat de *steady-state flux* lineair schaalte met $a^{4/3}$, waar a gelijk is aan de deeltjesstraal. Voor bidisperse suspensies met verschillende concentratieverhoudingen van kleine tot grote deeltjes, maar met een constante totale volumefractie, bleek de *steady-state flux* gelijk te zijn aan die van een monodisperse suspensie van alleen de kleine deeltjes. De invloed van de aanwezigheid van grote deeltjes op de shear-induced diffusiviteit van kleine deeltjes kon worden verklaard met een model voor polydisperse suspensies, dat shear-induced migratie van individuele deeltjes in een polydisperse suspensie beschrijft in aanwezigheid van een concentratie-gradiënt. Hiermee is een stap gemaakt naar de beschrijving van shear-induced diffusie gedrag zoals relevant voor MF van polydisperse suspensies.

In Hoofdstuk 6 is de studie naar het MF gedrag van suspensies met een deeltjesgrootteverdeling uitgebreid naar deeltjesdepositie op het membraan en deeltjesfractionering. In het dynamische flux regime is deeltjesdepositie het netto resultaat van enerzijds het transport van deeltjes naar het membraan, veroorzaakt door de flux door het membraan, en anderzijds het terugtransport van deeltjes vanaf het membraan naar de bulkfase, veroorzaakt door shear-induced diffusie. Door de deeltjesdepositie op het membraan tijdens MF te volgen door middel van Confocal Scanning Laser Microscopie is gevonden dat alleen de kleinere deeltjes van de bidisperse suspensie zich afzetten op het membraan. Deze resultaten kunnen worden verklaard met het optreden van deeltjessegregatie in de crossflow, gedreven door grootteverschillen tussen de deeltjes, die leidt tot een verrijking met kleinere deeltjes van de suspensie bij het membraan. Met een studie naar de fractionering van melkvetbollen in melk is aangetoond dat de bovengenoemde resultaten ook relevant zijn voor deeltjesfractioneringsprocessen middels MF. De polydisperse melkvetbolsuspensie kon worden gefractioneerd met gebruik van een membraan waarvan de poriegrootte groter was dan de grootste deeltjes in de suspensie. De scheidingseigenschappen van het proces, waaronder de deeltjesgrootte en het vetgehalte van het permeaat, kon volledig ingesteld worden met de crossflow snelheid en de permeaatflux. Dit maakt duidelijk dat de fractionering niet toegeschreven kan worden aan uitsluiting door het membraan op basis van afmetingen, maar dat deze toegeschreven kan worden aan segregatie effecten in het stromingskanaal.

Enige mate van deeltjesdepositie blijkt vaak onvermijdbaar in MF processen. In het kader van procesontwerp is het belangrijk om de relevante eigenschappen van deze depositielagen te kennen. In Hoofdstuk 7 zijn de eigenschappen van deeltjesdepositielagen van suspensies van micellair caseïne en melkvetbollen bestudeerd. Door een differentiële benadering te gebruiken was het mogelijk om de deeltjesdepositielagen te bestuderen tijdens

hun vorming in een dead-end filtratieproces. Zowel micellair caseïne als melkvetbollen vormden lagen met een zeer grote hydrodynamische weerstand. Terwijl de permeabiliteit van lagen van micellair caseïne onafhankelijk was van de toegepaste drukgradiënt, vertoonden lagen van (vloeibare) melkvetbollen wel een afhankelijkheid van de drukgradiënt. Wanneer het vet gedeeltelijk gekristalliseerd was, was de drukafhankelijkheid, en daarmee de compressibiliteit van de lagen, kleiner. De hydrodynamische weerstand van de depositielagen was dan echter nog steeds zeer hoog, waarschijnlijk vanwege het optreden van partiële coalescentie van de vetbollen. De parameters die zijn vastgesteld in deze studie, zijn van belang voor het rationeel ontwerpen van UF en MF processen van melk.

Procesmodellen die de flux en selectiviteit voorspellen als functie van systeem en proces parameters vormen belangrijke instrumenten voor het ontwerp van MF processen. Hoofdstuk 8 presenteert een nieuw ontwikkeld MF model, dat concentratiepolarisatie en koeklaagvorming voorspelt en dat, in tegenstelling tot andere MF modellen, geschikt is voor MF processen van complexe suspensies en voor MF systemen met complexe membraan of module geometriën of procescondities. Dit zogenoemde suspensie flow model is een computersimulatie model, waarin de hydrodynamica en convectie-diffusie gelijktijdig worden opgelost, gebruikmakend van een Euler-Euler benadering. Het model is gebaseerd op de LB methode en maakt het volledig oplossen van het stromingsveld mogelijk (inclusief het berekenen van de actuele lokale afschuifsnelheid) in aanwezigheid van een drukgradiënt over zowel het crossflow kanaal als het membraan. De algemene toepasbaarheid van het suspensie flow model als een ontwerpinstrument voor MF membranen, systemen en processen is gedemonstreerd met berekeningen van concentratiepolarisatie en koeklaagvorming in MF systemen met complexe geometriën, zoals crossflow kanalen met flow barrières en gecorrigeerde membranen. Het suspensie flow model is daarmee een praktisch instrument voor het ontwerp van MF processen van complexe suspensies zoals melk.

Nawoord

Het nawoord: de plek om iedereen te bedanken die op enigerlei wijze heeft bijgedragen aan de totstandkoming van dit proefschrift. En dat zijn er veel! Allereerst wil ik mijn werkgever Friesland Foods van harte bedanken dat zij mij de gelegenheid heeft geboden dit promotie-onderzoek uit te voeren. Voor mij betekende dit onderzoek een prachtige kans mijn kennis te verdiepen en uit te breiden, en daarbij tegelijk een optimale bijdrage aan innovatie binnen Friesland Foods te leveren.

Voor dit promotie-onderzoek ben ik op part-time basis gedetacheerd geweest bij de sectie Proceskunde aan de Landbouwniversiteit in Wageningen, waar ik begeleid werd door Remko Boom, Karin Schroën (eerst nog even door Albert van der Padt, maar die besloot al snel collega bij Friesland Foods in Deventer te worden) en Ruud van der Sman. Allereerst wil ik Remko bedanken voor zijn enthousiaste en inspirerende begeleiding. Onze besprekingen heb ik altijd als zeer prettig ervaren en ik ging altijd weer met nieuwe ideeën jouw deur uit. Karin, met veel plezier hebben we samen studenten begeleid bij hun afstudeeronderzoek. Bovendien werden mijn artikelen door jouw correcties zienderogen sterker. Ruud heeft mij geïntroduceerd in de wereld van computersimulaties, mijn grootste avontuur in mijn promotie-onderzoek. Dit is mij niet alleen erg goed bevallen, maar ik heb er ook heel veel van geleerd. Ook jullie van harte bedankt!

Ook buiten de sectie Proceskunde zijn er een aantal mensen geweest die een belangrijke rol hebben gespeeld. Allereerst wil ik Drona Kandhai (destijds) van het Kramers Laboratorium voor Fysische Technologie van de TU Delft noemen. Drona, jij hebt jouw computercode voor Lattice Boltzmann simulaties aan suspensies ter beschikking gesteld en mij daarin wegwijs gemaakt. Daarnaast heb jij mij geweldig geholpen door als klankbord te fungeren voor mijn onderzoek op dit gebied. Dirk van den Ende van Science and Technology van de UT Twente heeft mij een stuk verder gebracht op het gebied van de fysica van suspensies en met een analytisch model voor shear-induced diffusie. During my thesis, I have worked for a period of seven weeks at the University of Edinburgh, under the terms of the European program for Training and Research on Advanced Computing Systems. I was impressed by the large knowledge and research infrastructure at the Department of Physics and Astronomy and the Edinburgh Parallel Computing Centre, and acknowledging the pleasant supervision by Mike Cates and Kevin Stratford, I have learnt a lot more of physics and computer science, and on top of that, thanks to the Burns supper, about Scottish traditional poetry and food (haggis, tatties and neeps with whiskey). During my stay in Edinburgh, I have shared a student flat with Fatima Lucas. Fatima, your company was always very nice, not only in our flat, but also during our weekend trips in Scotland and in our meetings with so many other people! Joost van Opheusden van de leerstoelgroep Wiskundige en Statistische Methoden van Wageningen Universiteit heeft

me goed op weg geholpen met het analyseren van deeltjesaggregatie en microstructuren in suspensies. John Brady, due to your part-time professorship at the UT Twente, I had the unique opportunity to discuss my work with you on several occasions. These discussions have been very interesting and clarifying for me, so I have really appreciated them.

Ook aan de studenten heb ik veel te danken. Mark, Jeroen, Rob, Annet, Jan, Nienke, Bieuwe, Frits, Sarah en Sylvia, het was een plezier met jullie samen te werken. Jullie hebben een belangrijke bijdrage geleverd, welke jullie in meer of mindere mate terug kunnen zien in de hoofdstukken 5 t/m 8. Andere mensen die een rechtstreekse bijdrage aan dit proefschrift hebben geleverd zijn Henk Streppel, Miriam Krijgsman en Anno Koning (al- len van Friesland Foods Corporate Research) en Harry Rollema (NIZO Food Research). En natuurlijk de mensen van de technische werkplaats van het Biotechnion van Wageningen Universiteit, en in het bijzonder Hans, die heel wat ideeën in mooie meetopstellingen heeft omgezet. Mijn dank daarvoor!

Mijn onderzoek was onderdeel van een groot samenwerkingsproject, D-Force genaamd. Het projectteam, met mensen van verschillende expertise en achtergrond, kwam op regelmatige basis bij elkaar, wat meestal leidde tot levendige en interessante discussies. Meningsverschillen werden overbrugd of juist niet (computersjoemulaties!). Hoewel de samenwerking zowel ups als downs heeft gekend, vind ik dat er de afgelopen jaren veel is bereikt. Aan de basis van het D-Force project ligt de samenwerking tussen Friesland Foods en Aquamarijn, met Cees van Rijn als de uitvinder van de microzeven. Cees, ondanks jouw initiële scepsis over de toepasbaarheid van microzeven voor melk, denk ik dat het nut van microzeven ondertussen meer dan bewezen is. Rolf, bedankt dat je als projectleider van het D-Force project mijn promotie-onderzoek altijd hebt ondersteund. Miriam en Gerben waren collega-promovendi binnen het D-Force project. Bedankt voor de fijne samenwerking en jullie vriendschap! Bij Friesland Foods voerden we ondertussen onderzoek aan microfiltratie van melk uit. En dat was weer heel andere koek dan onderzoek aan keurige modelsystemen. Reinier, Bas, Henk, Frank, Albert, Kees, Gerrit en Rolf, wat hebben we geploeterd met z'n allen, maar wat mogen we trots zijn op het resultaat!

Voor mijn promotie-onderzoek is er een Friesland Foods begeleidingscommissie in het leven geroepen, bestaande uit verschillende “kennisiconen”. Tjeerd, Geert, Albert, Hans, Ger, Evert en Tom, bedankt voor jullie betrokkenheid, opbouwende kritiek en ideeën. Tjeerd, jij bent altijd een belangrijke motor geweest achter het D-Force project en hebt daarmee ook een onmisbare rol gespeeld in de totstandkoming van dit boekje. Rolf en Albert, bedankt voor jullie inbreng in de bilaterale besprekingen. Daarnaast was er ook de Technology Circle “Separations” met collega’s van verschillende werkmaatschappijen van Friesland Foods. Sytze, Gerard, Marc, Krin, Cor, Evert, Bert, Tjeerd en Albert, bedankt voor jullie belangstelling voor het onderzoek en de goede besprekingen, ondermeer over de praktische toepassing van microfiltratie.

Door mijn part-time detachering bij de sectie Proceskunde kreeg ik opeens veel extra collega’s. En dat heeft veel voordelen. Pieter en Olivier, bedankt voor het aan de gang krijgen en houden van het rekencluster, Gerrit, bedankt voor het oplossen van computer- en netwerkproblemen, en Jos, voor de ondersteuning op het lab. Ik heb genoten van de AIO-reis

naar Zuid-Afrika (hoewel wel erg kort voor mij) en vooral Canada, de verschillende feestjes en borrels, wielrentochten in België en Duitsland en natuurlijk de dagelijkse sfeer en gein op de afdeling. Kamergenoten te over voor serieuze en minder serieuze kletspraatjes (in wat soms ook wel het kippenhok werd genoemd): Marieke, Rolf, Marcel, Nick, Hadi, Julita, Judy en Jan (die na zijn afstudeeronderzoek terugkwam als promovendus).

En dan natuurlijk het thuisfront. Allereerst de sportclubjes (wielrennen en korfbal), voor de broodnodige lichamelijke inspanning en geestelijke ontspanning! Familie en vrienden, bedankt voor de gezelligheid tijdens feestjes, etentjes, ski-vakanties, fietskampeerweekenden en wat al niet meer. Lieve ouders en schoonouders, bedankt voor jullie onvoorwaardelijke liefde en steun. Mam, het was kanteboord drie jaar geleden, maar ik ben blij dat je er nog bent en dat ik alles wat nu gebeurt met je kan delen!

Lieve George, bij niemand voel ik me zo thuis als bij jou! Je geloof in mij heeft me gesterkt bij het uitvoeren van dit onderzoek. Hopelijk hebben we samen nog een mooie tijd te gaan.

Curriculum vitae

Janneke Kromkamp werd geboren op 4 november 1965 in de zuid-Friese gemeente Ooststellingwerf. In 1984 behaalde zij het Gymnasium- β diploma aan de Rijksscholengemeenschap te Heerenveen. Daarna volgde zij de studie Levensmiddelentechnologie aan de Agrarische Hogeschool Friesland in Bolsward. Deze studie werd in 1988 met goed gevolg afgerond.

Van 1 augustus 1988 tot 1 november 1997 was zij werkzaam bij NIZO te Ede, waar zij als onderzoeksmedewerkster achtereenvolgens werkzaam was op de gebieden bioprocetechnologie, membraanfiltratie en eiwittechnologie. Tijdens deze periode volgde zij in 1989 en 1990 de post-HBO cursus Bioprocetechnologie van de Stichting PHTO Hogeschool Heerlen, die zij met lof afrondde. Van 1993 tot en met 1996 volgde ze de studie Levensmiddelentechnologie aan de Landbouwniversiteit in Wageningen. In het kader van haar afstudeervak (oriëntatie Zuivelkunde) voerde zij een onderzoek uit naar de denaturatie van het eiwit β -lactoglobuline onder invloed van hoge isostatische druk. In januari 1997 slaagde zij met lof.

Sinds 1 november 1997 is ze werkzaam bij Friesland Foods Corporate Research in Deventer. Als researcher Process Technology voerde zij van 1 oktober 2000 tot 1 oktober 2004 het in dit proefschrift beschreven promotie-onderzoek uit. Dit onderzoek is tot stand gekomen onder begeleiding van Prof. R.M. Boom, Dr. C.P.G.H. Schroën en Dr. R.G.M. van der Sman van de sectie Proceskunde van Wageningen Universiteit. Tijdens het promotie-onderzoek was Janneke Kromkamp op part-time basis gedetacheerd in deze sectie.

List of publications

Articles

Timmer, J.M.K., Kromkamp, J., Robbertsen, T., Lactic acid separation from fermentation broths by reverse osmosis and nanofiltration, *J. Membr. Sci.* 92 (1994) 185-197.

Timmer, J.M.K., Kromkamp, J., Efficiency of lactic acid production by *Lactobacillus helveticus* in a membrane cell recycle reactor, *FEMS Microbiology Reviews* 14 (1994) 29-38.

Kromkamp, J., Moreira, R.M., Langeveld, L.P.M., Mil, P.J.J.M., Microorganisms in milk and yoghurt: selective inactivation by high hydrostatic pressure, In: *Proceedings of the IDF Symposium Heat treatments and alternative methods*, Vienna, 1995, 267-271.

Kromkamp, J., Domselaar, M. van, Schroën, K., Sman, R. van der, Boom, R., Shear-induced diffusion model for microfiltration of polydisperse suspensions, *Desalination* 146 (2002) 63-68.

Kromkamp, J., Cross flow microfiltration of polydisperse suspensions: concentration polarisation and shear-induced diffusion, In: *Nano and micro engineered membrane technology*, 10, Rijn, C.J.M. van, Elsevier, 2004, ISBN 0-444-51489-9.

Kromkamp, J., Ende, D.T.M. van den, Kandhai, D., Sman, R.G.M. van der, Boom, R.M., Shear-induced self-diffusion and microstructure in non-Brownian suspensions at non-zero Reynolds numbers, *J. Fluid Mech.* 529 (2005) 253-278.

Kromkamp, J., Bastiaanse, A., Swarts, J., Brans, G., Sman, R.G.M. van der, Boom, R.M., A suspension flow model for hydrodynamics and concentration polarisation in crossflow microfiltration, *J. Membr. Sci.* 253 (2005) 67-79.

Kromkamp, J., Faber, F., Schroën, K., Boom, R., Effects of particle size segregation on crossflow microfiltration performance: control mechanism for concentration polarisation and particle fractionation, accepted for publication by *J. Membr. Sci.*

Kromkamp, J., Rijnsent, S., Huttenhuis, R., Schroën, K., Boom, R., Differential analysis of particle deposition layers from micellar casein and milk fat globule suspensions, submitted 2005.

Kromkamp, J., Ende, D.T.M. van den, Kandhai, D., Sman, R.G.M. van der, Boom, R.M., Lattice Boltzmann simulation of 2D and 3D non-Brownian suspensions in Couette flow, submitted 2005.

Kromkamp, J., Kandhai, D., Sman, R.G.M. van der, Boom, R.M., Shear-induced self-diffusion in bidisperse suspensions, submitted 2005.

Brans, G., Kromkamp, J., Pek, N., Gielen, J., Heck, J., Schroën, C.P.G.H., Sman, R.G.M. van der, Boom, R.M., Evaluation of microsieve membrane design with particle filtration experiments and lattice Boltzmann CFD calculations, submitted 2005.

Patents

Kromkamp, J., Rijn, C.J.M. van, Method for filtering milk, Patent WO 02/09527 (2002).

Kromkamp, J., Padt, A. van der, Vorst, C. van der, Inrichting en werkwijze voor micro-of ultrafiltratie, Patent P67278NL00 (2004).

Kromkamp, J., Padt, A. van der, Schroën, C.G.P.H., Boom, R.M., Shear-induced fractionation of suspensions, Patent application 04078536.2 (2004).